

THE MINISTRY OF EDUCATION AND SCIENCE OF THE RUSSIAN FEDERATION



**ST. PETERSBURG STATE
POLYTECHNICAL UNIVERSITY
JOURNAL**

Physics
and Mathematics

VOLUME 11, No. 2
2018

Polytechnical University Publishing House
Saint Petersburg
2018

ST. PETERSBURG STATE POLYTECHNICAL UNIVERSITY JOURNAL. PHYSICS AND MATHEMATICS

JOURNAL EDITORIAL COUNCIL

Zh.I. Alferov – full member of RAS, head of the editorial council;
A.I. Borovkov – vice-rector for perspective projects;
V.A. Glukhikh – full member of RAS;
D.A. Indeitsev – corresponding member of RAS;
V.K. Ivanov – Dr. Sci.(phys.-math.), prof.;
A.I. Rudskoy – full member of RAS, deputy head of the editorial council;
R.A. Suris – full member of RAS;
D.A. Varshalovich – full member of RAS;
A.E. Zhukov – corresponding member of RAS, deputy head of the editorial council.

JOURNAL EDITORIAL BOARD

V.K. Ivanov – Dr. Sci. (phys.-math.), prof., SPbPU, St. Petersburg, Russia, – editor-in-chief;
A.E. Fotiadi – Dr. Sci. (phys.-math.), prof., SPbPU, St. Petersburg, Russia, – deputy editor-in-chief;
V.M. Kapralova – Candidate of Phys.-Math. Sci., associate prof., SPbPU, St. Petersburg, Russia, – executive secretary;
V.I. Antonov – Dr. Sci. (phys.-math.), prof., SPbPU, St. Petersburg, Russia;
I.B. Bezprozvanny – Dr. Sci. (Biology), prof., The University of Texas Southwestern Medical Center, Dallas, TX, USA;
A.V. Blinov – Dr. Sci. (phys.-math.), prof., SPbPU, St. Petersburg, Russia;
A.S. Cherepanov – Dr. Sci. (phys.-math.), prof., SPbPU, St. Petersburg, Russia;
D.V. Donetski – Dr. Sci. (phys.-math.), prof., State University of New York at Stony Brook, NY, USA;
D.A. Firsov – Dr. Sci. (phys.-math.), prof., SPbPU, St. Petersburg, Russia;
A.S. Kheifets – Ph.D., prof., Australian National University, Canberra, Australia.
O.S. Loboda – Candidate of Phys.-Math. Sci., associate prof., SPbPU, St. Petersburg, Russia;
J.B. Malherbe – Dr. Sci. (Physics), prof., University of Pretoria, Republic of South Africa;
V.M. Ostryakov – Dr. Sci. (phys.-math.), prof., SPbPU, St. Petersburg, Russia;
V.E. Privalov – Dr. Sci. (phys.-math.), prof., SPbPU, St. Petersburg, Russia;
E.M. Smirnov – Dr. Sci. (phys.-math.), prof., SPbPU, St. Petersburg, Russia;
A.V. Solov'yov – Dr. Sci. (phys.-math.), prof., MBN Research Center, Frankfurt am Main, Germany;
A.K. Tagantsev – Dr. Sci. (phys.-math.), prof., Swiss Federal Institute of Technology, Lausanne, Switzerland;
I.N. Toptygin – Dr. Sci. (phys.-math.), prof., SPbPU, St. Petersburg, Russia;
E.A. Tropp – Dr. Sci. (phys.-math.), prof., SPbPU, St. Petersburg, Russia.

The journal is included in the List of leading peer-reviewed scientific journals and other editions to publish major findings of theses for the research degrees of Doctor of Sciences and Candidate of Sciences.

The publications are presented in the VINITI RAS Abstract Journal and Ulrich's Periodical Directory International Database.

The journal is published since 2008 as part of the periodical edition 'Nauchno-tekhnicheskie vedomosti SPb-GPU'.

The journal is registered with the Federal Service for Supervision in the Sphere of Telecom, Information Technologies and Mass Communications (ROSKOMNADZOR). Certificate ПИ № ФС77-52144 issued December 11, 2012.

The journal is distributed through the CIS countries catalogue, the «Press of Russia» joint catalogue and the «Press by subscription» Internet catalogue. The subscription index is **71823**.

The journal is in the Russian Science Citation Index (RSCI) database.

© Scientific Electronic Library (<http://www.elibrary.ru>).

No part of this publication may be reproduced without clear reference to the source.

The views of the authors may not represent the views of the Editorial Board.

Address: 195251 Politekhnicheskaya St. 29, St. Petersburg, Russia.

Phone: (812) 294-22-85.

<http://ntv.spbstu.ru/physics>

МИНИСТЕРСТВО ОБРАЗОВАНИЯ И НАУКИ РОССИЙСКОЙ ФЕДЕРАЦИИ



НАУЧНО-ТЕХНИЧЕСКИЕ ВЕДОМОСТИ

САНКТ-ПЕТЕРБУРГСКОГО ГОСУДАРСТВЕННОГО
ПОЛИТЕХНИЧЕСКОГО УНИВЕРСИТЕТА

Физико-математические
науки

ТОМ 11, № 2
2018

Издательство Политехнического университета
Санкт-Петербург
2018

**НАУЧНО-ТЕХНИЧЕСКИЕ ВЕДОМОСТИ САНКТ-ПЕТЕРБУРГСКОГО
ГОСУДАРСТВЕННОГО ПОЛИТЕХНИЧЕСКОГО УНИВЕРСИТЕТА.
ФИЗИКО-МАТЕМАТИЧЕСКИЕ НАУКИ**

РЕДАКЦИОННЫЙ СОВЕТ ЖУРНАЛА

Алферов Ж.И., академик РАН – председатель;
Боровков А.И., проректор по перспективным проектам;
Варшалович Д.А., академик РАН;
Глухих В.А., академик РАН;
Жуков А.Е., чл.-кор. РАН – зам. председателя;
Иванов В.К., д-р физ.-мат. наук, профессор;
Индейцев Д.А., чл.-кор. РАН;
Рудской А.И., академик РАН – зам. председателя;
Сурис Р.А., академик РАН.

РЕДАКЦИОННАЯ КОЛЛЕГИЯ ЖУРНАЛА

Иванов В.К., д-р физ.-мат. наук, профессор, СПбПУ, СПб., Россия, – главный редактор;
Фотиади А.Э., д-р физ.-мат. наук, профессор, СПбПУ, СПб., Россия, – зам. главного редактора;
Капралова В.М., канд. физ.-мат. наук, доцент, СПбПУ, СПб., Россия – ответственный секретарь;
Антонов В.И., д-р физ.-мат. наук, профессор, СПбПУ, СПб., Россия;
Безпрозванный И.Б., д-р биол. наук, профессор, Юго-Западный медицинский центр
Техасского университета, Даллас, США;
Блинов А.В., д-р физ.-мат. наук, профессор, СПбПУ, СПб., Россия;
Донецкий Д.В., д-р физ.-мат. наук, профессор, университет штата Нью-Йорк в Стоуни-Брук, США;
Лобода О.С., канд. физ.-мат. наук, доцент, СПбПУ, СПб., Россия;
Малерб Й.Б., Dr.Sc. (Physics), профессор, университет Претории, ЮАР;
Остряков В.М., д-р физ.-мат. наук, профессор, СПбПУ, СПб., Россия;
Привалов В.Е., д-р физ.-мат. наук, профессор, СПбПУ, СПб., Россия.
Смирнов Е.М., д-р физ.-мат. наук, профессор, СПбПУ, СПб., Россия;
Соловьёв А.В., д-р физ.-мат. наук, профессор, Научно-исследовательский центр
мезобионаносистем (MBN), Франкфурт-на-Майне, Германия;
Таганцев А.К., д-р физ.-мат. наук, профессор, Швейцарский федеральный институт технологий,
Лозанна, Швейцария;
Топтыгин И.Н., д-р физ.-мат. наук, профессор, СПбПУ, СПб., Россия;
Тропп Э.А., д-р физ.-мат. наук, профессор, СПбПУ, СПб., Россия;
Фирсов Д.А., д-р физ.-мат. наук, профессор, СПбПУ, СПб., Россия;
Хейфец А.С., Ph.D. (Physics), профессор, Австралийский национальный университет,
Канберра, Австралия;
Черепанов А.С., д-р физ.-мат. наук, профессор, СПбПУ, СПб., Россия.

Журнал с 2002 г. входит в Перечень ведущих рецензируемых научных журналов и изданий, в которых должны быть опубликованы основные результаты диссертаций на соискание ученых степеней доктора и кандидата наук.

Сведения о публикациях представлены в Реферативном журнале ВИНТИ РАН, в международной справочной системе «Ulrich's Periodical Directory».

С 2008 года выпускается в составе сериального периодического издания «Научно-технические ведомости СПбГПУ».

Журнал зарегистрирован Федеральной службой по надзору в сфере информационных технологий и массовых коммуникаций (Роскомнадзор). Свидетельство о регистрации ПИ № ФС77-52144 от 11 декабря 2012 г.

Распространяется по Каталогу стран СНГ, Объединенному каталогу «Пресса России» и по Интернет-каталогу «Пресса по подписке». Подписной индекс **71823**.

Журнал включен в базу данных «Российский индекс научного цитирования» (РИНЦ), размещенную на платформе Научной электронной библиотеки на сайте <http://www.elibrary.ru>

При перепечатке материалов ссылка на журнал обязательна.

Точка зрения редакции может не совпадать с мнением авторов статей.

Адрес редакции и издательства: Россия, 195251, Санкт-Петербург, ул. Политехническая, д. 29.
Тел. редакции (812) 294-22-85.
<http://ntv.spbstu.ru/physics>

Contents

Condensed matter physics

- Meredelina T.A., Stukova E.V., Baryshnikov S.V., Milinskiy A.Yu.** *The ferroelectric phase transition in the ammonium iodate embedded into the alumina porous matrix* 9
- Dyubo D.B., Tsybin O.Yu.** *The relation of volume and surface effects with a charge barrier height in a dynamic p-i-n-photodiode* 16
- Romanov N.M., Zakharova I.B., Elistratova M.A., Lähderanta E.** *The structure of ZnTPP, ZnTPP-C₆₀ thin films and X-ray effect on their photoluminescence* 26
- Romanov N.M., Musikhin S.F.** *Gamma-induced effect on the luminescence of nanocomposites of MEH-PPV conductive polymer with lead sulphide quantum dots* 41

Simulation of physical processes

- Zaborova D.D., Petritchenko M.R., Musorina T.A.** *The Dupuis paradox and mathematical simulation of unsteady filtration in a homogeneous closing dike* 49

Mathematical physics

- Anikonov D.S., Konovalova D.S.** *Direct and inverse problems for a wave equation with discontinuous coefficients* 61

Physical electronics

- Korenyugin D.G., Martsinovskiy A.M.** *An asymmetrical dielectric barrier discharge in the pulsed mode* 73
- Kozhevnikov V.A., Privalov V.E.** *The geometrical effect of an active element cross-section on the laser gain* 84

Physical materials technology

- Borisova M.E., Kamalov A.M., Orlov I.D., Smirnova V.E.** *Charge relaxation in partially crystalline R-BAPB polyimides under conditions of elevated humidity* 96
- Pakhotin V.A., Zakrevskii V.A., Sudar N.T., Apaseyev A.A.** *The ion emission during the fracture of polymers* 106

Nuclear physics

- Radzevich P.V., Berdnikov A.Ya., Berdnikov Ya.A., Zharko S.V., Kotov D.O.** *PHENIX experiment: Study of the jet quenching effect in the ultrarelativistic U + U collisions* 119

Radiophysics

- Dikiy D.V., Akimov V.P., Sochava A.A., Cherepanov A.S.** *Phase shift control using waveguide-slot phase shifter* 130

Theoretical physics

Agapev K.B., Ivanov V.K., Korol A.V., Solov'yov A.V. *Channeling of ultrarelativistic particles in a diamond crystal*..... 139

Mechanics

Gusakov A.A., Grekov M.A., Seroshtanov V.V. *Aerodynamics and heat transfer over the surface of a single circular fin*..... 151

Author index..... 165

Содержание

Физика конденсированного состояния

Меределина Т.А., Стукова Е.В., Барышников С.В., Милинский А.Ю. <i>Сегнетоэлектрический фазовый переход в иодате аммония, внедренного в пористую матрицу оксида алюминия</i>	9
Дюбо Д.Б., Цыбин О.Ю. <i>Связь объемных и поверхностных эффектов с высотой зарядового барьера в динамическом р-і-п-фотодиоде</i>	16
Романов Н.М., Захарова И.Б., Елистратова М.А., Лахдеранта Э. <i>Структура тонких пленок ZnTPP, ZnTPP-C₆₀ и влияние рентгеновского излучения на их фотолюминесценцию</i>	26
Романов Н.М., Мусихин С.Ф. <i>Воздействие гамма-излучения на люминесценцию нанокompозитов проводящего полимера МЕН-PPV с квантовыми точками сульфида свинца</i>	41

Математическое моделирование физических процессов

Заборова Д.Д., Петриченко М.Р., Мусорина Т.А. <i>Парадокс Дюпюи и математическое моделирование нестационарной фильтрации в однородной перемычке</i>	49
--	----

Математическая физика

Аниконов Д.С., Коновалова Д.С. <i>Прямая и обратная задачи для волнового уравнения с разрывными коэффициентами</i>	61
---	----

Физическая электроника

Коренюгин Д.Г., Марциновский А.М. <i>Асимметричный барьерный разряд в пульсирующем режиме</i>	73
Кожевников В.А., Привалов В.Е. <i>Влияние геометрии сечения активного элемента лазера на усиление его излучения</i>	84

Физическое материаловедение

Борисова М.Э., Камалов А.М., Орлов И.Д., Смирнова В.Е. <i>Релаксация заряда в частично-кристаллических полиимидах Р-ОДФО в условиях повышенной влажности</i>	96
Пахотин В.А., Закревский В.А., Сударь Н.Т., Апасеев А.А. <i>Эмиссия ионов при разрушении полимеров</i>	106

Ядерная физика

Радзевич П.В., Бердников А.Я., Бердников Я.А., Жарко С.В., Котов Д.О. <i>Изучение эффекта гашения струй в системе ультрарелятивистских столкновений ядер урана на эксперименте ФЕНИКС</i>	119
--	-----

Радиофизика

Дикий Д.В., Акимов В.П., Сочава А.А., Черепанов А.С. <i>Управление фазовым сдвигом с помощью волноводно-щелевого фазовращателя</i>	130
---	-----

Теоретическая физика

Агапьев К.Б., Иванов В.К., Король А.В., Соловьев А.В. <i>Каналирование ультрарелятивистских частиц в кристалле алмаза</i>	139
--	-----

Механика

Гусаков А.А., Греков М.А., Сероштанов В.В. <i>Аэродинамика и теплообмен на поверхности одиночного кольцевого ребра</i>	151
---	-----

<i>Авторский указатель</i>	165
----------------------------------	-----

THE FERROELECTRIC PHASE TRANSITION IN THE AMMONIUM IODATE EMBEDDED INTO THE ALUMINA POROUS MATRIX

T.A. Meredelina¹, E.V. Stukova², S.V. Baryshnikov¹, A.Yu. Milinskiy¹

¹ Blagoveshchensk State Pedagogical University, Blagoveshchensk, Russian Federation;

² Amur State University, Blagoveshchensk, Russian Federation

The temperature dependences of the linear permittivity ϵ' and the harmonic coefficient γ of composite materials obtained by embedding the ferroelectric NH_4IO_3 into the porous alumina (Al_2O_3) matrix with a pore diameter of 60 nm have been studied. It was found out that the phase transition was diffused and the Curie temperature shifted to a low-temperature region $T \sim 25$ K. The results obtained were interpreted within the framework of the phenomenological Landau theory and the Ising model. On the basis of these theoretical descriptions, it was shown that the phase transition temperature in a nanocomposite was consequence of dimensional effects. At the same time, the electrical interaction between particles in adjacent pores does not play an important role, due to the low spontaneous polarization of ammonium iodate and significant distances between neighboring pores.

Key words: ferroelectric; dielectric permittivity; nanocomposite; phase transition

Citation: T.A. Meredelina, E.V. Stukova, S.V. Baryshnikov, A.Yu. Milinskiy, The ferroelectric phase transition in the ammonium iodate embedded into the alumina porous matrix, St. Petersburg State Polytechnical University Journal. Physics and Mathematics. 11 (2) (2018) 5 – 10. DOI: 10.18721/JPM.11201

Introduction

The dielectric properties of nanocomposites based on porous matrices filled with ferroelectrics are currently the focus of considerable attention. The physical properties of such structures are affected by the size and geometry of the porous network. The greatest number of studies are dedicated to nanocomposites with sodium nitrite, Rochelle salt, potassium nitrate and triglycine sulfate embedded into the pores (see [1 – 3] and references therein). Exploring the factors governing the changes in the properties of the ferroelectric component of nanocomposites is one of the key goals of modern physics of low-dimensional systems and solid-state electronics.

In this paper, we have studied the dielectric properties of nanocomposites based on ammonium iodate embedded in porous alumina (Al_2O_3) films.

Samples and experimental procedure

Ammonium iodate (NH_4IO_3) consists of colorless crystals of ammonium salt and iodic acid, soluble in water. Japanese researchers Oka, Mitsui, Shiroishi and Sawada discovered the ferroelectric properties of ammonium iodate in 1976 [4]. Ammonium iodate is in the cubic α phase at temperatures above 393 K. Below this temperature, the crystal transforms into the orthorhombic piezoelectric β phase ($Pc2_1n$) with lattice constants $a = 6.426$ Å, $b = 9.104$ Å, $c = 6.466$ Å. A transformation into the ferroelectric γ phase ($Pm2_1b$), which is also orthorhombic with lattice constants $a = 6.413$ Å, $b = 9.156$ Å, $c = 6.411$ Å occurs with a further decrease in temperature in the region of about 358 K. The structural transformation between the nonpolar piezoelectric β phase and the ferroelectric γ phase near 358 K is caused by a change in the tilt of the IO_6^- octahedra

in the perovskite-like structure. At the same time, small shifts of the ammonium ion NH_4^+ along the polar axis b and spontaneous polarization occur (the magnitude of the spontaneous polarization vector at room temperature is $P_s \approx 1.8 \mu\text{C}/\text{cm}^2$). Although the space group of the high-temperature β phase is polar, the dipole moment of the cell is equal to zero. The phase transition is of the first-order type with anomalies of the dielectric, the piezoelectric, and the elastic constants.

Porous anodized aluminum oxide films with a cell size of 125 nm and a pore diameter of 60 nm were used in the experiment. The pore depth was about 50 μm . Aluminum oxide films were manufactured by TopMembranes Technology using two-step electrochemical anodizing of aluminum in an aqueous solution of oxalic acid at a voltage of 35 V. The structure of the film is shown in Fig. 1. The porous film was filled with ammonium iodate from a saturated aqueous solution under vacuum at 353 – 363 K. The sample was then slowly cooled, with NH_4IO_3 nanocrystals forming in the pores as a result. The procedure was repeated ten times, the pores were then filled and NH_4IO_3 nanorods were formed within them. The degree of pore filling, determined from the change in the mass of the films, was about 60%. Vacuum drying was used to remove the remaining water.

A digital E7-25 LCR meter with a frequency range of 25 Hz – 1 MHz was used for measuring the linear dielectric properties of the samples. The experimental setup for studying the harmonics included a sinusoidal oscillator with an operating frequency of 2 kHz. The field strength was approximately 750 V/cm for the bulk sample and 500 V/cm for the alumina film filled with ammonium iodate. The signal was taken from a resistor that was series-connected with the sample and fed to a digital spectrum analyzer (a computer with a ZET-230 24-bit analog-to-digital converter and ZetLab software). The amplitudes of the second ($U_{2\omega}$) and third ($U_{3\omega}$) harmonics were recorded in the experiment. The harmonic coefficient γ was calculated by the formula

$$\gamma = \frac{\sqrt{U_{2\omega}^2 + U_{3\omega}^2}}{U_{\omega}^2}.$$

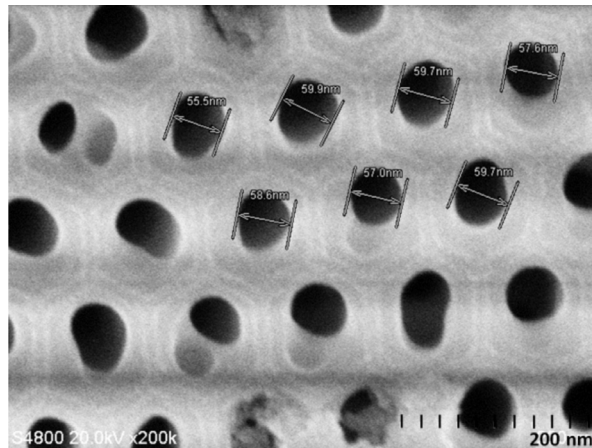


Fig. 1. Surface morphology of the Al_2O_3 film with pore sizes of 60 nm, obtained with an electron microscope

The technique of nonlinear measurements is described in more detail in [5].

The measurements were carried out in the temperature range of 80 – 500 K under continuous heating and cooling at a rate of 1 K/min. The temperature was measured with a digital TC-6621 thermometer with an accuracy of about 0.1 K. The silver paste was used as electrodes.

Experimental results and discussion

The temperature dependence of the dielectric constant for bulk ammonium iodate exhibited low-frequency dispersion (Fig. 2). It is evident from the inset in Fig. 2 that the phase transition temperatures for bulk ammonium iodate determined from the $\epsilon'(T)$ and $\gamma(T)$ dependences coincide. It should be borne in mind that the dielectric permittivity reaches its maximum at the Curie point, while the harmonic coefficient value is minimal at this point.

It also follows from the $\epsilon'(T)$ dependence for the $\text{NH}_4\text{IO}_3/\text{Al}_2\text{O}_3$ composite (Fig. 3) that the dielectric constant decreases with increasing frequency; however, no anomaly in the behavior of this dependence is observed in the Curie temperature region for NH_4IO_3 .

Nevertheless, the studies, which were carried out by nonlinear dielectric spectroscopy, indicate an anomaly in the region of 343 K, which suggests the presence of a phase transition in NH_4IO_3 in nanopores with a diameter of

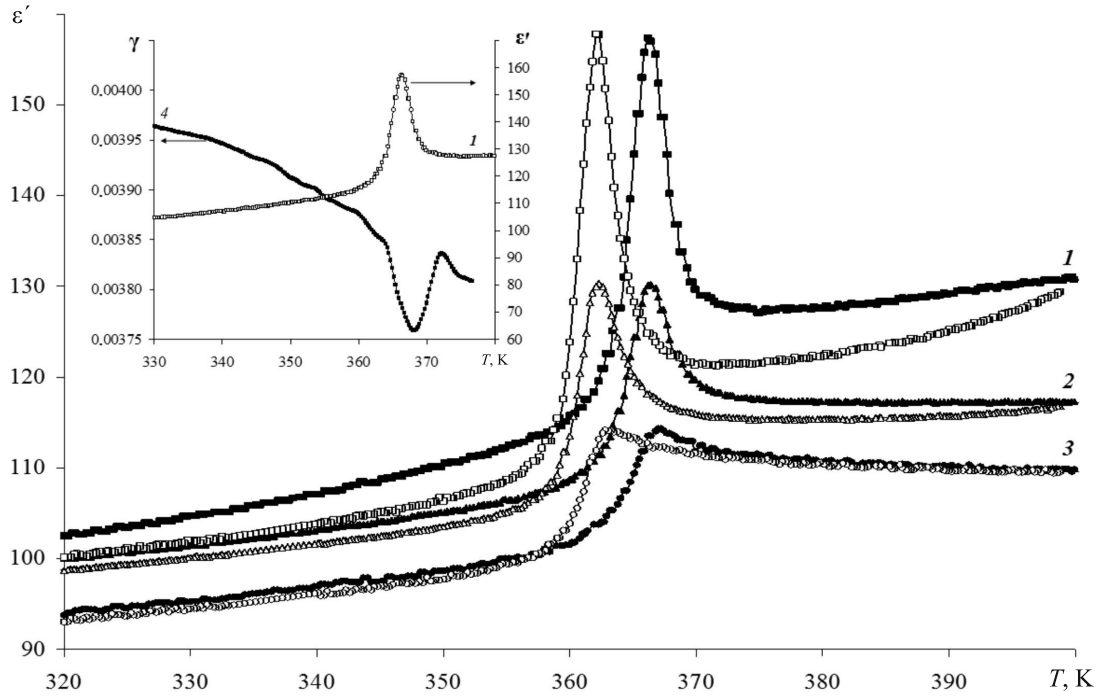


Fig. 2. Temperature dependences of the dielectric constant of bulk NH_4IO_3 at different frequencies, kHz: 1 (curve 1), 100 (2), 1000 (3); obtained under sample heating (shaded symbols) and cooling (open symbols). The inset shows the $\epsilon'(T)$ (1) and $\gamma(T)$ (4) dependences at a frequency of 1 kHz

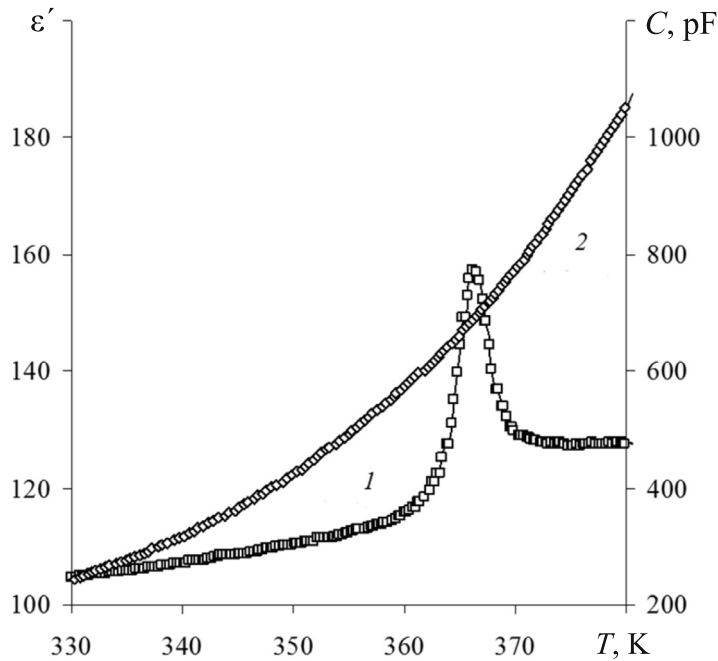


Fig. 3. Temperature dependences of the dielectric permittivity (1) and the capacitance (2) of the $\text{NH}_4\text{IO}_3/\text{Al}_2\text{O}_3$ composite at a frequency of 1 kHz, obtained under sample cooling

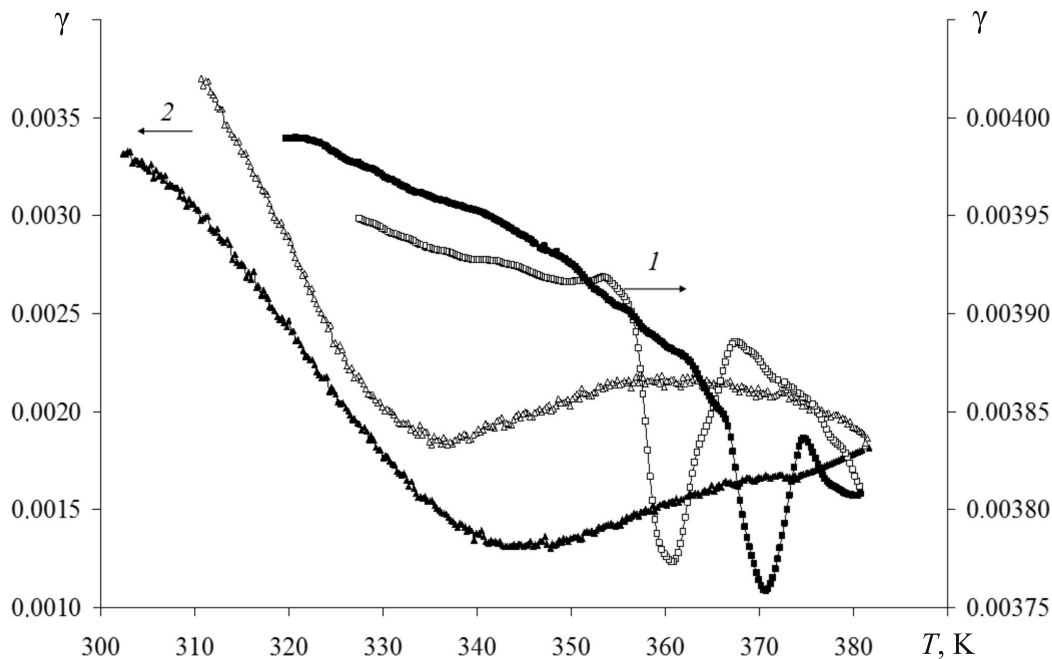


Fig. 4. Temperature dependences of the harmonic coefficient for a bulk NH_4IO_3 sample (1) and a $\text{NH}_4\text{IO}_3/\text{Al}_2\text{O}_3$ composite (2); obtained under heating (shaded symbols) и under cooling (open symbols)

60 nm. Fig. 4 shows the temperature dependences of the harmonic coefficient for the bulk sample and for the $\text{NH}_4\text{IO}_3/\text{Al}_2\text{O}_3$ composite, pointing to a diffused phase transition and to a shift of the Curie temperature toward the low temperature region by $\Delta T \approx 25$ K.

The decrease in the phase transition temperature in ammonium iodate embedded into alumina pores agrees with the conclusions of theoretical models developed on the basis of Landau's phenomenological theory and the Ising model [6 – 8]. These models predict that the structural phase transition temperature for small isolated particles of spherical or cylindrical shapes shifts deeper into the ferroelectric phase as the particle size decreases. The conclusions of these models were also confirmed experimentally for individual small particles of ferroelectrics such as barium titanate (see [9] and references therein). Theoretical analysis [10] established that the interaction between ferroelectric particles in the pores, which is electrical in nature, can significantly weaken the dimensional effects. The interaction with the walls of the pores can play an additional role for small particles in porous matrices,

leading to a change in the sign of the phase transition shift [11]. A significant decrease in the ferroelectric transition temperature in ammonium iodate embedded into alumina pores indicates that the size effects are predominant for such a nanocomposite. The electrical interaction between particles in adjacent pores does not play a substantial role, due to low spontaneous polarization of ammonium iodate and significant distances between adjacent pores.

The issue of diffused phase transition in ferroelectrics embedded into nanoscale matrices is not new: it was discussed from a theoretical standpoint in a number of studies [12, 13]. Some reasons that can lead to this effect are that the deformation of the particles in the pores and the values of the effective internal electric field are distributed non-uniformly. A similar picture is observed both in bulk disordered ferroelectric structures and in solid solutions. These substances are characterized by a gradual diffused transition from the paraelectric to the ferroelectric phase (observed in a wide temperature range, usually called the Curie region), instead of a sharp structural one. The ferroelectric properties, such as spontaneous

polarization, piezoelectric coefficients, anomalous specific heat capacity and others change gradually within the Curie region.

Conclusion

This study has revealed a decrease in the temperature of the ferroelectric phase transition in nanostructured ammonium iodate em-

bedded into the pores of aluminum oxide. The temperature of the phase transition has been found to decrease by 25 K. The shift of the phase transition to the region of lower temperatures for nanostructured ammonium iodate agrees with the theoretical descriptions of the Landau and Ising models for isolated small particles.

REFERENCES

- [1] **C. Tien, E.V. Charnaya, D.Yu. Podorozhkin, et al.**, Ferroelectricity and gradual melting in NaNO_2 particles confined within porous alumina, *Physica Status Solidi (b): Basic Solid State Physics*. 246 (10) (2009) 2346–2351.
- [2] **S.V. Baryshnikov, A.Yu. Milinskiy, E.V. Charnaya, Y.V. Patrushev**, Phase transitions in KNO_3 embedded in MCM-41 films with regular nanopores, *Physics of the Solid State*. 55 (12) (2013) 2566–2570.
- [3] **A.Y. Milinskii, S.V. Baryshnikov, A.A. Antonov**, Phase transition of $\text{Sc}(\text{NH}_2)_2$ ferroelectrics in Al_2O_3 -based nanoporous matrices, *Physics of the Solid State*. 59 (9) (2017) 1783–1788.
- [4] **T. Oka, T. Mitsui, Y. Shiroishi, Sh. Sawada**, Ferroelectricity in NH_4IO_3 , *J. Phys. Soc. Japan*. 40 (3) (1976) 913–914.
- [5] **A.Yu. Milinskiy, Yu.A. Shatskaya, A.A. Antonov, S.V. Baryshnikov**, Metod nelineynoy dielektricheskoy spektroskopii dlya issledovaniya segnetoelektrikov v sluchaye silnykh poley [Nonlinear dielectric spectroscopy for studies of ferroelectrics in the high-field region], *Izvestiya Samarskogo nauchnogo tsentra RAN*. 16 (4) (2014) 83–89.
- [6] **W.L. Zhong, Y.G. Wang, P.L. Zhang, B.D. Qu**, Phenomenological study of the size effect on phase transitions in ferroelectric particles, *Phys. Rev. B*. 50 (2) (1994) 698–703.
- [7] **Y.G. Wang, W.L. Zhong, P.L. Zhang**, Size driven phase transition in ferroelectric particles, *Solid State Commun.* 90 (5) (1994) 329–332.
- [8] **C.L. Wang, Y. Xin, X.S. Wang, P.L. Zhang**, Size effects of ferroelectric particles described by the transverse Ising model, *Phys. Rev. B*. 62 (17) (2000) 11423–11427.
- [9] **V.A. Shchukin, D. Bimberg**, Spontaneous ordering of nanostructures on crystal surfaces, *Rev. Mod. Phys.* 71 (4) (1999) 1125–1171.
- [10] **E.V. Charnaya, A.L. Pirozerskii, C. Tien, M.K. Lee**, Ferroelectricity in an array of electrically coupled confined small particles, *Ferroelectrics*. 350 (1) (2007) 75–80.
- [11] **P. Sedykh, D. Michel**, Ferroelectric phase transition in barium titanate nanoparticles, *Phys. Rev. B*. 79 (13) (2009) 134119.
- [12] **B.N. Rolov, V.E. Yurkevich**, Termodinamika fazovykh perekhodov v segnetoaktivnykh tverdykh rastvorakh [Thermodynamics of phase transitions in ferroelectric solid solutions] Riga, Zinatne, 1976.
- [13] **Ya.I. Frenkel**, *Statisticheskaya fizika* [Statistical physics], Moscow, Leningrad, Izd-vo AN SSSR, 1948.

Received 09.01.2018, accepted 29.01.2018.

THE AUTHORS

MEREDELINA Tatiana A.

Blagoveshchensk State Pedagogical University

104, Lenina St., Blagoveshchensk, 675000, Russian Federation
biofirm@mail.ru

STUKOVA Elena V.

Amur State University

21 Ignatievskoe HW, Blagoveshchensk, 675027, Russian Federation
lenast@bk.ru

BARYSHNIKOV Sergey V.

Blagoveshchensk State Pedagogical University

104 Lenina St., Blagoveshchensk, 675000, Russian Federation
svbar2003@list.ru

MILINSKIY Aleksey Yu.

Blagoveshchensk State Pedagogical University

104 Lenina St., Blagoveshchensk, 675000, Russian Federation

a.milinskiy@mail.ru

THE RELATION OF VOLUME AND SURFACE EFFECTS WITH A CHARGE BARRIER HEIGHT IN A DYNAMIC $p-i-n$ -PHOTODYODE

D.B. Dyubo, O.Yu. Tsybin

Peter the Great St. Petersburg Polytechnic University, St. Petersburg, Russian Federation

The characteristics of the microelectronic dynamic operational $p-i-n$ -photodetector have been analyzed. These features are determined by the interaction of volume effects with particles adsorbed on the SiO_2 film surface. The temperature characteristics in the visible light irradiation regime, the anomalous characteristics of the temperature hysteresis, the processes in the adsorbed layer and the charge carriers' transport through the potential barrier in the Si substrate bulk were considered. The photocurrent sensitivity of the device was found to depend nonlinearly on temperature. We proposed a theoretical model that related the processes of thermal- and photo-generation of the charge carriers with the potential barrier parameters. The effects resulted from the formation of the surface charges were revealed. The optimal conditions and regimes for measuring the photocurrent were determined.

Key words: dynamic $p-i-n$ -diode; temperature hysteresis; volume effect; charge barrier

Citation: D.B. Dyubo, O.Yu. Tsybin, The relation of volume and surface effects with a charge barrier height in a dynamic $p-i-n$ -photodyode, St. Petersburg Polytechnical State University Journal. Physics and Mathematics. 11 (2) (2018) 11 – 18. DOI: 10.18721/JPM.11202

Introduction

Effective photodetectors of electromagnetic radiation in the visible spectral region are in great demand in science and technology, with stringent requirements imposed on their sensitivity, stability, noise level, size and other characteristics. Developing semiconductor devices that meet these requirements is an important task for electronics.

Vacuum photomultipliers are highly sensitive but have no microelectronic equivalent and possess a number of drawbacks, such as high noise level, narrow dynamic range, and no mode for obtaining two-dimensional images; in addition, their photocathodes are prone to degradation. Photomultipliers also have insufficient shock and vibration resistance, and require high-voltage power supplies.

Electron multipliers with microchannel plates are smaller, but their characteristics are unstable under vibrations and are not resistant against ionizing radiation; these devices also require a high-voltage power supply.

Ordinary semiconductor photodetectors and CCD arrays also have their own flaws: they need high-sensitivity broadband preamplifiers and signal integrators, which actually introduce additional high levels of noise and can lose weak signals.

New $p-i-n$ -photodiodes [1] are equipped with a metal-oxide semiconductor (CMOS) gate around the built-in p -type depletion region in silicon (CMOS is a complementary metal – oxide – semiconductor structure). The spectral sensitivity of the diode is sufficiently high in the visible range of the electromagnetic spectrum (400 – 800 μm). The device operates in dynamic mode with a voltage pulse switching between reverse and forward bias. The measured quantity characterizing the incident light is not the amplitude of the signal applied to the device but the switching time, which depends on the energy dose of the absorbed light. In the initial state and during the delay τ after switching, the electrons and holes are trapped by electrostatic potential barriers corresponding to the Boltzmann equilibrium of drift-diffusion near the boundaries of the depletion regions. After switching from reverse to forward bias, the device keeps operating in a blocking state for a certain delay time τ , for as long as the mobile charge carriers remain trapped by potential barriers. The injected current increases upon irradiation with visible light that generates electron-hole pairs in silicon. The switching time depends on space charge neutralization of the barriers upon injection of charge carriers: electrons into the cathode and holes into the anode region. The carriers produced

via thermal generation generate additional injection current. The total current ensures that the depletion region is occupied and the barriers are neutralized over time τ . As current flows and the depletion regions are occupied, potential barriers become lower and narrower. Switching from a state with a low-amplitude current output to a high-current state occurs with a sharp edge, presumably due to tunneling breakdown in a narrowing barrier, and this process is amplified by positive feedback due to reverse transfer of holes to the cathode.

The new $p-i-n$ -photodiodes hold promise for applications in devices for detecting low-level emission in the visible spectral range, including luminometers, spectrum analyzers and other photosensitive devices [1, 2].

However, the characteristics of the device and the physical processes underlying its operation have not been sufficiently studied this far. For instance, the temperature characteristics have to be obtained to correctly describe the processes occurring in the device, as well as to determine its operating conditions and application parameters.

The temperature dependences of the self-triggering time of a diode without external illumination were measured in [2]. A theoretical current flow model was also offered, allowing to interpret the experimental characteristics. It was assumed that only the carriers capable of overcoming the potential barrier due to thermal energy could participate in neutralization processes in self-triggering mode. In the absence of external irradiation, the density J_0 of the current of thermally generated charge carriers, flowing over the potential barrier, was estimated by integrating the Fermi function over the above-barrier energy E_b . A relation describing the dependence of the neutralized part $Q(t)$ of the total barrier charge on time t , temperature T and the current barrier height $E_b(t)$ was obtained as a result:

$$Q(t) \sim \int_0^t dt \cdot T^2 \exp(-E_b(t) / kT). \quad (1)$$

The barrier height $E_b(t)$ depends on the time for two reasons: due to neutralization of the charge by the thermal current and due to a decrease in the barrier height by a thermally

generated carrier charge. The diode switches quickly when $Q(t)$ reaches a critical value Q_c with $t = \tau$. This simple model allowed to approximate the experimental temperature dependences rather accurately, but did not yield the temperature characteristics of switching under photodiode illumination by incident light and adsorption of particles from the external environment on the photosensitive layer.

The goal of this study was to further develop the model describing the temperature-dependent processes occurring in the device, and to determine the mechanisms by which external factors affect these processes, including changes in the concentration of the adsorbed layer on the surface of the silicon oxide film in the outer region between the cathode and the gate.

Methods of investigation

The diode was placed in a light-protected thermostat where the temperature was varied and controlled in the range from 275 to 305 K at natural humidity for the duration of the measurements. The temperature was varied under quasi-equilibrium conditions: slowly (by less than 1 deg/min) and in small steps; each step involved a long pause until the new temperature settled, so that the temperature change rate would not affect the results obtained. As photon illumination started, external illumination of the diode surface by visible daylight was controlled by changing the size of the aperture stop in the wall of the thermostat. The effect of humidity on the device was studied as well; the device was not hermetically sealed for this purpose.

Absolute values of the incident light intensity were not measured in the experiments, since relative values were sufficient for our purposes. Non-zero minimum illuminance corresponded to the mode with room temperature and minimal photocurrent, which was undetectable against the thermally generated current. Light intensity was increased in a dynamic range to values exceeding this level by one or two orders of magnitude.

A programmable control circuit with an integrated microelectronic chip was used for supplying power to the diode and for measurements. The diode's self-triggering



time and its switching time under illumination were determined from the counts of the circuit and simultaneously controlled with a TDS520 digital oscilloscope.

The processes in the diode were simulated with the COMSOL package, used to determine the potential per unit volume. The geometrical parameters of the diode, the impurity concentrations and the voltages at the diode electrodes were set for the simulations, and the presence of adsorbed water molecules on the outer surface of silicon oxide film in the region between the cathode and the gate was taken into account.

Experimental results and discussion

Typical dependences of normalized inverse triggering time of the diode (plotted on a logarithmic scale) versus temperature are shown in Fig. 1 in three modes: self-triggering by ther-

mally generated charge carriers and switching in two modes under illumination by a constant (time-independent) photon flux ($\Phi = \text{const}$). The normalizing value of the maximum time τ_{max} was taken to be constant. It is obvious (see Fig. 1) that the curves obtained for irradiation with visible light differ from those recorded in the thermal generation mode where approximation by formula (1) is possible. The dependences obtained for photogeneration of charge carriers cannot be simulated by linear displacements of curve 1. The behavior of the quantity τ_{max} / τ as a function of the temperature T under irradiation with an extremely low flux Φ_2 (barely detectable by the device), in curve 2, indicates two competing types of generation. Curves 2 and 3 remain approximately exponential with different exponents in separate segments: low (about 0.49) with the photocurrent prevailing over the thermal generation cur-

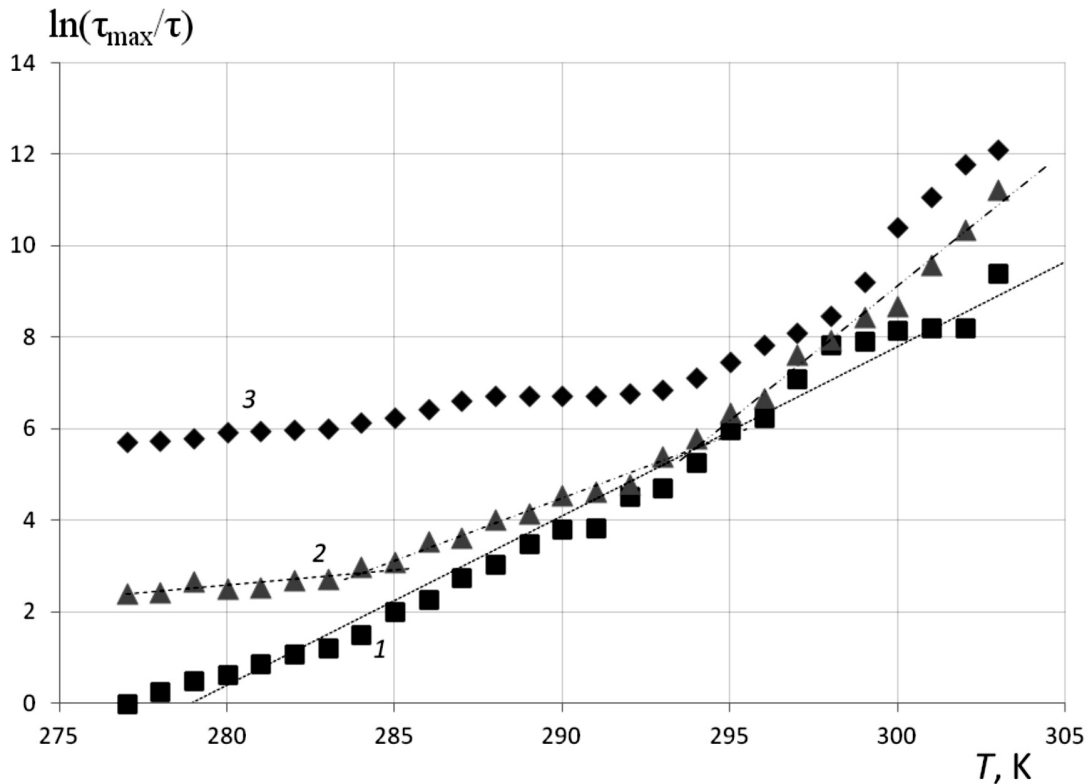


Fig. 1. Temperature dependences of logarithmic inverse switching time of the diode without illumination (1) and with illumination (2, 3) by visible light with different photon fluxes Φ : 1: charge carriers are generated thermally ($\Phi_1 = 0$); 2: two competing types of generation for an extremely low photon flux ($\Phi_2 > 0$); 3: the photogeneration process is predominant but thermal generation occurs at higher temperatures ($\Phi_3 > \Phi_2$); $\tau_{\text{max}} = \text{const}$

rent that is substantial in the temperature range $T > 285$ K; rather small (about 2.11) at 285 K $< T < 295$ K and, finally, increased (about 4.61) with the prevailing thermal generation current, when $T > 295$ K.

As the photocurrent increases (curve 3 in Fig. 1), the exponent remains approximately constant and small (about 0.52) with $T < 295$ K, i.e., the switching time in this mode is less dependent on the temperature than in thermal generation mode under zero illumination. The slope of curve 3 becomes considerably steeper with an increase in temperature in the region $T > 295$ K, indicating a greater contribution of the thermally generated current. The incident light Φ_2 was chosen to be extremely low in intensity, but still detectable with respect to the thermally generated current; its signal-to-noise ratio SNR is determined as follows:

$$\text{SNR} = P_{ph} / P_{th},$$

where P_{ph} and P_{th} are the powers of the total photogeneration signal and the thermal generation signal, respectively.

The SNR value is close to 1 at $T > 290$ K; $\text{SNR} > 1$ at $T < 290$ K, and this segment of the temperature dependence can be regarded as optimal for using the photodiode. However, as we shall discuss below, there are also limitations in the low-temperature region.

The reasons why the temperature dependence of the switching time changes under irradiation with visible light may include nonequilibrium generation of electron-hole pairs that receive an initial excess energy with respect to the lattice temperature in the silicon substrate. The effective height of the confining potential barrier decreases for photogenerated carriers in the region above the equilibrium thermodynamic energy kT . In this case, the flow of the total thermal generation and photogeneration currents can be described by the relation refining formula (1):

$$Q(\tau) \sim \int_0^\tau dt \cdot T^2 \exp\left(\frac{-E_b(t) - \Delta E_b(\Phi, T)}{kT}\right), \quad (2)$$

where $\Delta E_b(\Phi, T)$ is the effective decrease in the height of the barrier due to space charge neutralization by photogenerated carriers (Φ is the irradiation dose).

The photocurrent flowing above the barrier is proportional to the irradiation dose, i.e., $I_\Phi(\Phi) \sim \text{const} \cdot \Phi$.

The model corresponding to formula (2) describes the photocurrent entirely from the standpoint of the changes in the barrier height. This model takes into account the contribution of the photocurrent to barrier charge neutralization, modulation of the barrier height by photogenerated carrier charge and the dependence of the barrier height on temperature, allowing to interpret the dependences shown in Fig. 1 more accurately. If divided into segments, the experimental curves can be well approximated by exponential curves with different exponents. This is likely evidence that the change in the effective barrier height $\Delta E_b(\Phi, T)$ depends on temperature. The barrier parameters were determined from the dependences in Fig. 1 for the voltages at the diode electrodes corresponding to the computations using the COMSOL package (see the data in Fig. 3 below). The obtained values of the parameters in formula (2) are in agreement with both the adopted model and with the computational result:

$$W_1 = E_b = 2,62 \text{ B};$$

$$W_2 = E_b + \Delta E_b(\Phi, T_{<295}) = 0,52 \text{ B};$$

$$\Delta E_b(\Phi, T_{<295}) = -2,10 \text{ B},$$

where W_1 , W_2 are the barrier heights at $\Phi = 0$ irrespective of the temperature and at $\Phi = \Phi_3$ for the temperature region $T < 295$ K, respectively; $\Delta E_b(\Phi, T_{<295})$ is the change in the barrier height under the conditions established for the W_2 quantity.

To further refine the temperature characteristics in the low-temperature region, we performed measurements under cyclic cooling and heating. The first hysteresis loop was observed in the temperature range of about $270 - 280$ K, near the computed dew point. It can be seen from Fig. 2 that the diode switching time corresponding to the heating cycle was increased compared with the switching time corresponding to the cooling cycle. The observed hysteresis may be attributed to the dependence of the concentration of adsorbed particles on temperature. Indeed, the particle fluxes incident on the surface and leaving it are equalized under quasi-equilibrium conditions.

However, the concentration of the particles trapped on the surface due to adsorption forces depends on the thermal history even in quasi-equilibrium processes. As the temperature increases, the processes are governed by the increased concentration of the adsorbate, obtained at lower temperatures.

Condensation of water vapor from the surrounding atmospheric volume naturally occurred at a lower temperature on the silicon dioxide layer and a sufficiently adsorbed surface film consisting of water molecules was accumulated. This film gradually thinned under heating, changing the diode switching time, but with a different pattern compared with the temperature dependence of this quantity under cooling.

A possible mechanism by which the hysteretic processes manifest in the measured parameters of the diode is that the surface charges in the film distort the potential distribution and the height of the barriers along charge carrier paths in the near-surface region of the silicon substrate. The charge state of the adsorbed layer is a complicated issue discussed in very few literary sources. The emergence of a charged layer near the surface may be caused by the separation of charges in the film due to

their different mobilities [3, 4]. Protons have an abnormally high mobility and are capable of producing H_3O^+ ions and stable complexes [5 – 7]. In addition, such ions can form on the surface during the self-ionization reaction of water [3 – 5]:



The NO^+ cation, capable of forming strong bonds with water molecules, and, accordingly, stable $\text{NO}^+ + (\text{H}_2\text{O})_n$ clusters, is another active ion [8].

Water molecules bonding with the surface and the corresponding ions forming in the film can also be interpreted in terms of a simple acid-base interaction according to the Lewis theory [9, 10]: the water molecule acts as the electron donor (Lewis base), and the substrate as the electron acceptor (Lewis acid).

While the specifics of this phenomenon have not been explained, the very fact of charging in the presence of water molecules agrees with modern concepts of the adsorbed layer. Surface charges generate an electric field that changes the form of potential barriers in the silicon-based photodiode. Similar phenomena are known in semiconductor biosensors [11].

Computer simulation in the COMSOL

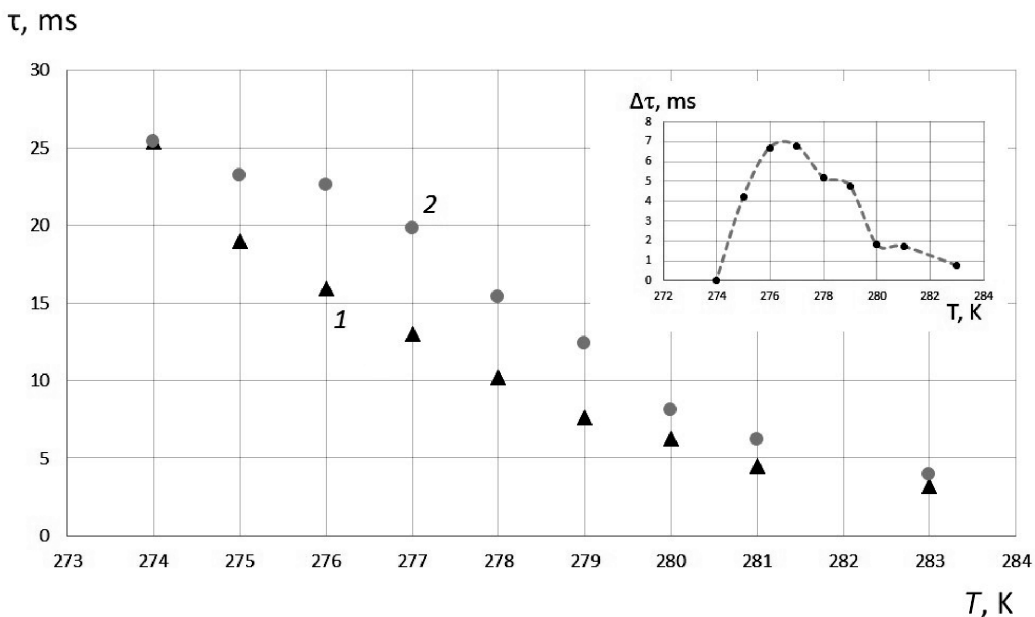


Fig. 2. Temperature dependences of the diode's self-triggering time under initial cooling (1) and subsequent heating (2). The inset shows the differences in curves 2 and 1 plotted along the vertical axis

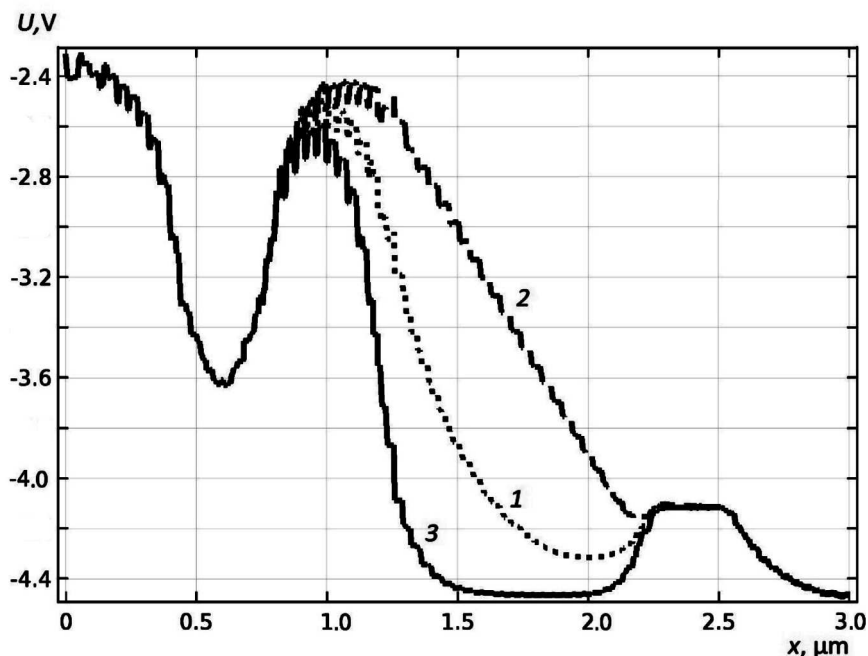


Fig. 3. Computed distributions of static potential along the charge carrier path for different charge states of the adsorbed layer:
 1 without adsorbed film; 2, 3 with the film generating, respectively a positively and a negatively charged layer (the surface charge was taken equal to 0.01 C/m²)

package was used to further interpret the results. We computed the heights and modulations of potential barriers for the given acceptable values of surface and space charges. We assumed that the molecular film had a small charge with a surface concentration corresponding to an approximately 10% ionic component in the neutral Langmuir monolayer, which can be considered close to the measurement conditions.

We have also determined the profile of the electrostatic potential of the barriers confining the space charge in the switching mode of the *p-i-n*-diode with an integrated metal-oxide semiconductor gate around the *p*-region. The simulation yielded static spatial distributions of the potential values for different temperatures and different films of adsorbed particles on the outer surface of the SiO₂ film in the region between the cathode and the gate. Fig. 3 shows the potential distribution for forward bias (the anode and the gate have a positive potential with respect to the cathode), computed in a plane located at a distance of tenths of microns from the upper surface of the diode, where

the possible particle paths lie. The potential distribution was computed along the charge carrier path.

Evidently (see Fig. 3), there are electrostatic barriers trapping charges in potential wells along carrier paths. The magnitude of the electric field strength rapidly decreases outside the depletion region. The charge carrier mobility is low due to a lack of a sufficiently strong electric field. The molecular film forms a charged layer near the surface; this layer's electric field changes the height and shape of potential barriers, controlling the neutralizing carrier fluxes. Computations of barrier heights based on the data in Fig. 3 are given above for estimating the temperature dependences and parameters according to formula (2) and were also used to determine the ratio of the barrier height E_{bs} with the surface film to the barrier height E_b without the film:

$$\gamma = (E_{bs} / E_b) \cong 1, 2.$$

Conclusion

The experimental and theoretical study we



have carried out yielded the following results:

the temperature characteristics of a $p-i-n$ diode with an integrated metal-oxide semiconductor gate have been determined in dynamic mode, under conditions close to real life, i.e., with an external atmospheric environment affecting the sample during photocurrent measurements;

the sensitivity of the device with respect to the photocurrent was found to be nonlinearly dependent on temperature, which is to say that the temperature curves have segments with different slopes;

we have offered a theoretical model linking the processes of thermal generation and photogeneration of charge carriers with the change in the height of potential barriers that depends on temperature and on modulation by mobile carrier charge;

we have found the conditions and modes optimal for measuring the photocurrent;

we have found the effects that may be due to surface charges forming when particles from an external environment are deposited on a silicon dioxide film or on the elements of the optical system, for example, when the device is operating in a humid environment or is depressurized.

The theoretical and experimental results obtained allowed to gain more insight into the dynamic scenarios of the processes occurring in the device, as well as to estimate the device's potential applications and operating parameters in measuring equipment. The effects discovered can be taken into account when developing technical devices with the new photodetector.

Acknowledgment

We express our gratitude to the employees of ActLight SA (Lausanne, Switzerland) for providing a sample of the $p-i-n$ -diode for our study.

REFERENCES

- [1] S. Okhonin, M. Gureev, D. Sallin, et al., A dynamic operation of a PIN photodiode, *Appl. Phys. Lett.* 106 (3) (2015) 031115.
- [2] D. Dyubo, O.Y. Tsybin, Nano communication device with an embedded molecular film. Electromagnetic signals integration with dynamic operation photodetector, *Lecture Notes in Computer Science (including subseries Lecture Notes in Artificial Intelligence and Lecture Notes in Bioinformatics)*. 10531 (2017) 206–213.
- [3] O.Yu. Tsybin, A.V. Grigoryev, Issledovaniye molekulyarnoy desorbtsii iz adsorbirovannogo sloya ostatochnykh gazov elektrodinamicheskim i lazernym metodami [Investigation of the molecular desorption from the adsorbed residual gases layer using electrodynamic and laser methods], *Vakuumnaya tekhnika i tekhnologiya*. 17(2) (2007) 73–81.
- [4] O.Yu. Tsybin, Elektrodinamicheskaya desorbtsiya/ionizatsiya chastits s poluprovodnikovyykh podlozhek [Electrodynamic desorption / ionization of the particles from the semiconductor substrates], *Vakuumnaya tekhnika i tekhnologiya*. 21 (1) (2011) 17–20.
- [5] V.L. Voeikov, Biological significance of active oxygen-dependent processes in aqueous systems, In: G.H. Pollack, I.L. Cameron, and D.N. Wheatley (Eds.) *Water and the Cell*, Springer, Dordrecht (2006) 285–298.
- [6] D.M. Camaioni, C.A. Schwerdtfeger, Accurate experimental values for the free energies of hydration of H^+ , OH^- , and H_3O^+ , *J. Phys. Chem. A*. 109 (47) (2005) 10795–10797.
- [7] N. Agmon, Mechanism of hydroxide mobility, *Chem. Phys. Lett.* 319 (3–4) (2000) 247–252.
- [8] E. Hammam, E.P.F. Lee, J.M. Dyke, *Ab initio* molecular orbital calculations on NO^+ (H_2O)_n cluster ions, Part I: Minimum-energy structures and possible routes to nitrous acid formation, *J. Phys. Chem. A*. 104 (19) (2000) 4571–4580.
- [9] A.M. Kuznetsov, Adsorbtsiya parov vody na metallicheskih poverkhnostyakh [The adsorption of water vapor on metal surfaces], *Sorosovskiy obrazovatelnyy zhurnal*. 6 (5) (2000) 45–51.
- [10] K.-H. Sun, A. Silverman, Lewis acid-base theory applied to glass, *J. Am. Cer. Soc.* 28 (1) (1945) 1–32.
- [11] M. Barbaro, A. Bonfiglio, L. Raffo, A charge-modulated FET for detection of biomolecular processes: conception, modeling, and simulation, *IEEE Transactions on Electron Devices*. 53 (1) (2006) 158–166.

Received 12.01.2018, accepted 17.04.2018.

THE AUTHORS

DYUBO Dmitry B.

Peter the Great St. Petersburg Polytechnic University

29 Politechnicheskaya St., St. Petersburg, 195251, Russian Federation

doobinator@rambler.ru

TSYBIN Oleg Yu.

Peter the Great St. Petersburg Polytechnic University

29 Politechnicheskaya St., St. Petersburg, 195251, Russian Federation

otsybin@rphf.spbstu.ru

THE STRUCTURE OF ZnTPP, ZnTPP-C₆₀ THIN FILMS AND X-RAY EFFECT ON THEIR PHOTOLUMINESCENCE

N.M. Romanov^{1,2}, I.B. Zakharova¹, M.A. Elistratova³, E. Lähderanta²

¹ Peter the Great St. Petersburg Polytechnic University, St. Petersburg, Russian Federation;

² Lappeenranta University of Technology, Lappeenranta, Finland;

³ Ioffe Institute of RAS, St. Petersburg, Russian Federation

The paper presents the results of studies in properties of ZnTPP and nanocomposite ZnTPP-C₆₀ films prepared under quasi-equilibrium conditions. The films' composition, structure and surface morphology have been investigated. Inequality in the optical absorption and photoluminescence (PL) spectra of ZnTPP solution and ZnTPP film was testimony to the formation of a regulated phase with the 745 nm-phosphorescence at room temperature. The X-ray effect on the PL spectra of ZnTPP and ZnTPP-C₆₀ films was considered. The former was rather stable to the used X-ray doses. The dose dependences of electronic and electron-vibrational contributions to the PL emission intensity were different for the latter. A decrease in the emission intensity due to the electronic transition in the composite was caused by a probability increase in an excitation transfer from the carrier to the fullerene C₆₀ and, correspondingly, by PL suppression.

Key words: metalloporphyrin; nanocomposite; fullerene; photoluminescence; X-radiation; scanning electron microscopy; X-ray diffractometry

Citation: N.M. Romanov, I.B. Zakharova, M.A. Elistratova, E. Lähderanta, The structure of ZnTPP, ZnTPP-C₆₀ thin films and X-ray effect on their photoluminescence, St. Petersburg State Polytechnical University Journal. Physics and Mathematics. 11 (2) (2018) 19 – 30. DOI: 10.18721/JPM.11203

Introduction

Recent studies in organic nanoelectronics have paid much attention to nanocomposites with bulk heterojunctions [1, 2]. Vacuum deposition (thermal evaporation in vacuum) of thin films from initial mixtures is an industrial method of obtaining structures with bulk heterojunctions [3]. Different molecular components of porphyrins and phthalocyanins are successfully used as initial materials [4]; one example is tetraphenylporphyrin (H₂TPP), a derivative compound of porphin (C₂₀H₁₄N₄). The latter consists of four pyrrole rings with methine bridges. Pyrrole rings are five-membered aromatic nitrogen heterocycles.

Chelates (metal complexes of porphyrins, or MeTPP) are some of the most promising materials from the porphyrin group for applications in organic optoelectronics. A metal ion replacing two hydrogen atoms is located at the core of a tetrapyrrolic macrocycle. This macrocyclic structure has a high degree of π -conjugation, which regulates its main properties, for example, absorption of light in different spectral regions and fluorescence; the

chelate has a strong donor effect [5].

Porphyrins play an important role in fabrication of electroluminescent [6] and photonic [7] devices used for photodynamic therapy [8], as well as for synthesis of materials with controllable magnetic properties [12]. Porphyrins can be incorporated into photochromic compounds used to store data [9] and to manufacture solar cells [10] and gas analyzers [11].

The porphyrin – fullerene pair is one of the optimal combinations for creating a bulk heterojunction. The C₆₀ fullerene acts as a strong acceptor and is a widely available and inexpensive initial material for producing thin films by vacuum deposition [13]. Notably, thin films of pure porphyrin and porphyrin – fullerene nanocomposite are capable of supramolecular self-assembly and formation of molecular ensembles or aggregates [5, 14].

To date, the properties of porphyrins and various porphyrin-containing compounds have been studied mainly in solutions; however, it is solid structures and not solutions that have industrial applications [15]. One of the draw-

backs of organic structures, including fullerenes [16] and porphyrins [17], is that external factors can change their properties, mostly leading to degradation: photopolymerization occurs as a result of UV irradiation, exposure to oxygen or water vapor causes oxidation or photostimulated oxidation. The characteristics of the layers making up the structure are transformed in these cases [18].

There are practically no studies dealing with the effect of X-ray radiation (as an external factor) on the properties of composite porphyrin-fullerene films. This problem is rather poorly understood; for example, an increase in optical absorption below the edge of the Soret band was confirmed in [19] for CoMTPP films. On the other hand, the change in the properties of organic materials exposed to irradiation can lead not only to deterioration of the parameters that are important for practical applications, but also to modification and generating new useful characteristics [20].

A few more papers have reported on the effect of ionizing radiation on fullerenes; a number of studies confirmed the stability of their properties despite the effect of gamma irradiation [21]. The effect of various types of ionizing radiation on nanocomposite materials incorporating C_{60} fullerenes was considered in [22 – 24]. These studies found that adding fullerene improves the absolute stability of nanocomposites. Both an increase in crosslink density and an improvement in thermal stability of the nanocomposites incorporating fullerene were established in [23].

Ref. [24] is dedicated to applications of organic photovoltaic elements in outer space, where the elements are exposed to ionizing radiation. Changes in the characteristics depending on the irradiation dose for the P3HT:PCBM composite (polymer – fullerene) were attributed to the decay of the main chain and the reduction of π -conjugation in the P3HT polymer. The stability of the nanocomposites based on fullerenes with inorganic donors exposed to X-rays was demonstrated in [25].

In general, it can be argued that fullerene, due to its symmetry and the presence of a delocalized π -electron cloud, has enhanced stability against various types of ionizing radiation.

The study of degradation of the properties

of porphyrin and fullerene – porphyrin films is an important task. This paper presents the comprehensive findings of an investigation of self-assembly processes and their effect on the structure of thin films of zinc tetraphenylporphyrin (ZnTPP) and nanocomposite films of zinc tetraphenylporphyrin with fullerene ($ZnTPP - C_{60}$). We have analyzed the changes in photoluminescence (degradation processes) in these films after exposure to X-ray radiation.

Sample preparation and methods of investigation

Sample preparation. A mixture consisting of both pure ZnTPP and a combination of ZnTPP и C_{60} in weight ratio of 1 : 1 was used to synthesize the films (both compounds were from Sigma-Aldrich, USA). BDS-10 grade boron-doped (111) silicon, freshly cleaved muscovite mica and potassium bromide (KBr) were used as substrates.

While most studies use molecular beam epitaxy to grow organic films, we chose hot-wall epitaxy in quasi-equilibrium. This method allows to synthesize molecular crystals and obtain uniform nanocomposite films whose properties are highly reproducible under identical technological conditions. According to the data in [5, 14], film thickness ranges from 100 to 600 nm. The advantages of this method, in contrast to molecular beam epitaxy, are that it facilitates self-assembly and makes it possible for ordered structures of organic complexes to form.

The choice of temperature conditions was limited by the following factors. Firstly, the temperatures of the evaporator and the substrate were tailored to ensure minimal supersaturation of vapor in order to obtain self-assembling crystalline films. The condensation temperature of the films was chosen as close as possible to the evaporator temperature for this purpose. At the same time, the substrate temperature had to be maintained at a level below the evaporator temperature by 100 K in order to sustain the required growth rate and obtain pure films in a technical vacuum instead of an ultra-high one. Using a technical vacuum considerably simplifies the technology of growing the films and reduces the energy costs for synthesis.

Surface morphology studies. A JEOL JSM-6390 scanning electron microscope with the ultimate resolution of 3 nm was used for studying the self-assembly processes and the morphology of the surface and near-surface layers of the samples grown on Si (111) substrates.

Transfer processes and film composition in the selected local regions were investigated using an Oxford INCA Energy EDS microanalysis system for scanning electron microscopes with the ultimate sensitivity of 0.1 wt %. Samples grown on dielectric substrates, for example, on mica, cannot be studied by this method.

Film structure studies. The structure of the film samples was studied by X-ray diffractometry (XRD) for both silicon and dielectric substrates. The X8 PROTEUM diffractometer (Bruker, USA) was used.

Luminescence studies. Photoluminescence spectra were measured with an automated system consisting of a Horiba Jobin Yvon spectrometer and an FHR monochromator equipped with a Symphony II 1024*256 Cryogenic Open-Electrode CCD detector with a light yellow filter. Photoluminescence was excited by stabilized radiation of a semiconductor laser operating in continuous mode at a wavelength of 408 nm.

X-ray radiation. The samples were irradiated with different doses of X-rays from a tungsten-rhenium X-ray tube with the operating parameters of 40 kV and 90 mA. A tungsten-rhenium

anode allowed to irradiate the samples with $K_{\alpha 1}$ and $K_{\beta 1}$ X-rays with the energies of 59.3 and 67.2 keV, respectively. The X-ray source was calibrated by changing the threshold voltage for MOS structures relative to that for the gamma radiation source.

The exposure doses were (in 10^5 R):

1.20; 2.65 and 4.51 for ZnTPP;

0.62; 1.45 and 2.69 for ZnTPP- C_{60} .

Irradiation and all measurements were carried out at room temperature (about 300 K).

Results and discussion

Scanning electron microscopy data. The surface morphology of the initial films is shown in Fig. 1. ZnTPP films exhibit a well-developed near-surface relief; their surface layer is an ordered, dense and clearly visible set of crystallites. Analysis of the film morphology in both secondary and elastically reflected electron fluxes revealed no impurity inclusions or inhomogeneities, with good reproducibility of the results.

It can be seen from Fig. 1, *b* that ZnTPP- C_{60} films have a more developed surface compared with ZnTPP and are a two-phase system with surface inclusions of the second phase in the form of nanorods. The second phase appears as the characteristic habit of porphyrin crystals and follows the laws of crystallography. The obtained surface morphology can be explained by the temperature conditions in which the films were synthesized and by the differ-

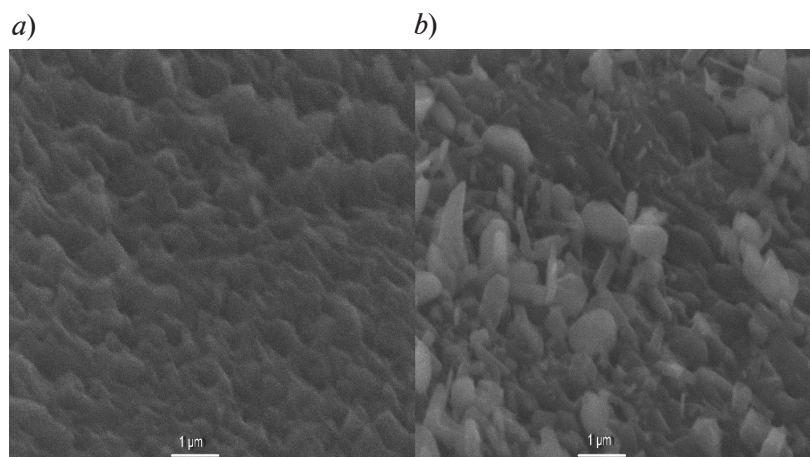


Fig. 1. Surface morphology of ZnTPP (*a*) and ZnTPP- C_{60} (*b*) films obtained by scanning electron microscopy

Table

Compositions determined for the studied compounds

Compound	Elemental composition, arb. units		
	Zn	C	N
ZnTPP	0,99	1,05	0,99
ZnTPP-C ₆₀	1,24	0,95	1,52

Notes. 1. EDX was used. 2. The table lists the ratios of the obtained experimental values to the stoichiometric compositions of the thin-film samples studied.

ence in the evaporation temperatures of the C₆₀ fullerene and ZnTPP. Since the evaporator and substrate heater is a rather massive graphite structure in the hot wall method, the films cooled down slowly after heating stopped. All the while, porphyrin, whose evaporation temperature is lower, kept evaporating from the remaining mixture. Crystallization in the form of nanorods was accompanied by weak interaction with the substrate and occurred with a small number of crystalline nuclei, which was facilitated by a persistently high temperature of the substrate.

Sample composition studies. The experimental results obtained by energy-dispersive X-ray microanalysis (EDX) confirm the above explanations. The data found were renormalized to exclude the contribution from the silicon substrate. A characteristic Si peak caused by this substrate is present in the spectral images with accelerating voltages of the primary electron beam of the order of 8 keV, since the penetrating power of such a beam is much greater than the thickness of the films in question. There was no point in using accelerating voltages of the primary electron beam below 8 keV, since the sensitivity of the method decreases sharply as a result. This method cannot be used to detect either hydrogen (since there are no electronic transitions in its atom) present in the composition of the organic materials under consideration or its weight contribution to the final result; thus, a systematic error is inevitably introduced into the measurements. For convenience, the experimental results obtained by EDX were normalized to the stoichiometric composition (see Table).

The normalization used allows to analyze the deviations of the experimental results from

the values calculated from the initial mixture compositions; the results that fully coincide with the stoichiometric composition should yield a value of 1.00 in the table. Deviations towards depletion yield values less than unity, while enrichment is characterized by values greater than unity. It can be concluded from the data given in the table that the obtained ZnTPP film is practically stoichiometric, which means that nondestructive transfer of the composition of the initial mixture to the film occurs during the synthesis of the films.

An insignificant oxygen content (about 0.041 wt% for ZnTPP and 0.088 wt% for the composite) is not shown in the table and can be associated with free oxygen or oxygen in the water vapor adsorbed on the surface of the freshly grown film after it is removed from the vacuum chamber; this result does not necessarily indicate oxidation of the samples. The higher oxygen content in composite films may be due to a more developed surface of the sample.

Substantial deviations from the composition calculated from the initial mixture are observed for the ZnTPP-C₆₀ nanocomposite film. The data point to carbon depletion of the obtained films with simultaneous zinc and nitrogen enrichment, i.e., enrichment in the porphyrin phase, which corresponds to SEM observations of porphyrin crystals in the second phase (see Fig. 1, *b*). According to calculations, the film contains approximately 38 % of fullerene instead of the 50 % weight in the initial composition. These results agree with the data for other types of composite films that we obtained earlier [14].

XRD analysis. More data on the structure of the films were obtained by analyzing

the samples grown on a silicon substrate (Fig. 2, *a*), on an oriented layered substrate of freshly cleaved muscovite mica (Fig. 2, *b*) and on potassium bromide (Fig. 2, *c*). It was established in [26, 27] that a molecular crystal of ZnTPP can have a different structure, that is, exhibit polymorphism. According to the data in [28], the initial polycrystalline mixture consists of crystals with a triclinic system. However, the films obtained by the authors of that study under

non-equilibrium conditions had an amorphous structure, and haloes were detectable in their XRD patterns only at scattering angles 2θ from 7° to 20° .

The processes of formation of polymorphic phases were studied in [29], where it was revealed that the activation energies of crystalline phases for different crystal systems can be classified in the following way by descending absolute values of crystal lattice energies:

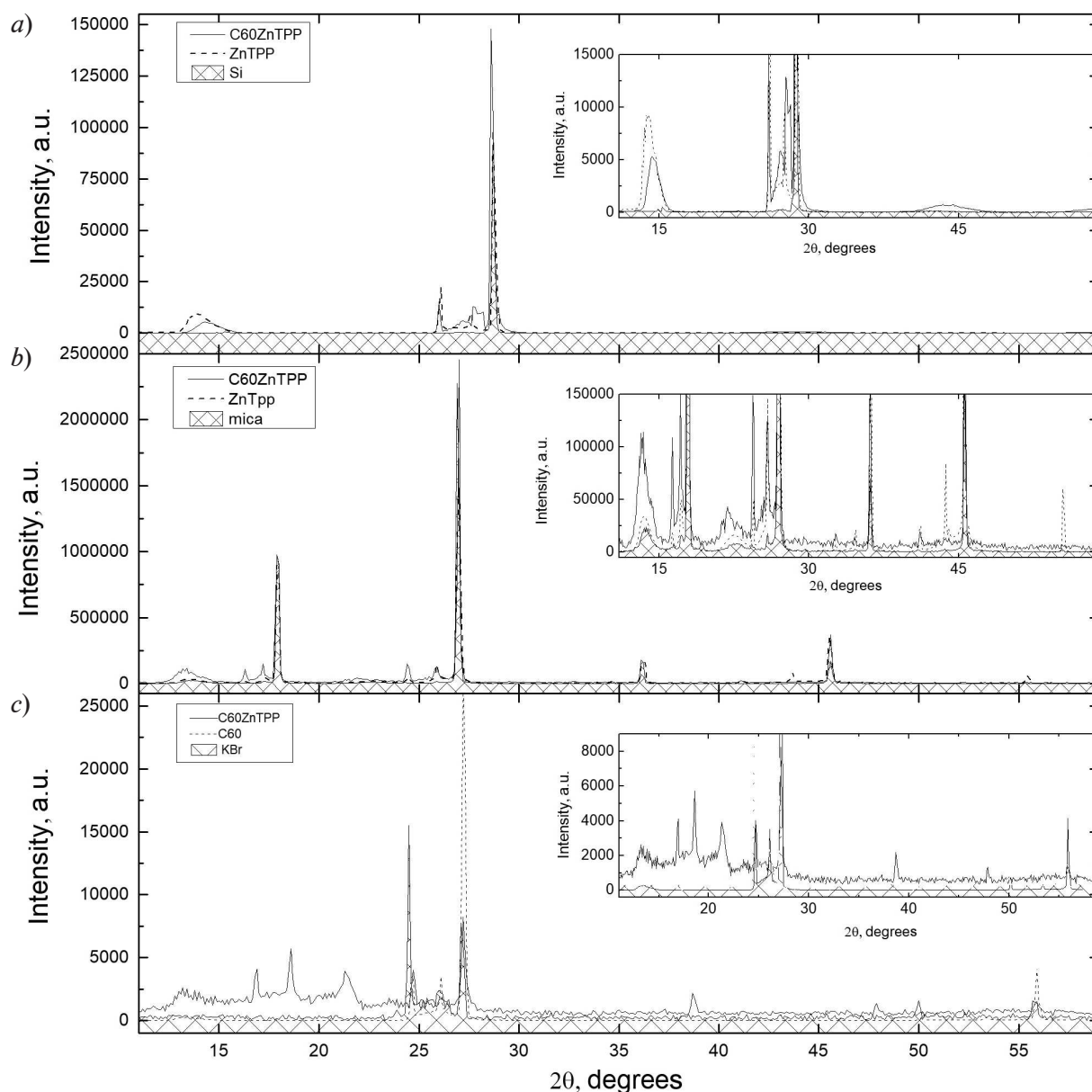


Fig. 2. XRD patterns of ZnTPP and ZnTPP- C_{60} films grown on different substrates: silicon (*a*), muscovite mica (*b*) and KBr (*c*). The background and the peaks caused by X-ray diffraction from the substrates are shaded

$$P1 > I4/m > P2_1/n,$$

and the energies of the first two structural modifications are close and are significantly (by 15 kJ/mol) higher than the third one corresponding to the monoclinic system. Nucleation and growth of the $P2_1/n$ crystalline phase occur in the initial sample with the structure $I4/m$ in the temperature range of 443 – 493 K. Thus, we can expect structurally perfect ordered objects that correspond to a minimum energy to form in our samples.

Fig. 2, *a* shows the experimental XRD patterns of the film samples on Si (111) substrate. As the film's thickness is small, the main contribution is made by the peaks corresponding to the substrate; for silicon this is the peak with a scattering angle 2θ equal to 28.6° . A broad peak is observed in the XRD patterns of ZnTPP films in the range of $13 - 14^\circ$, which corresponds to the nanocrystalline component of the film, while a peak at 26.1° corresponds to ZnTPP crystals.

The position of the peaks is somewhat shifted for the composite, the prevailing type of crystal lattice cannot be determined reliably due to small intensities and a limited number of detected peaks; however, a large number of lines in the range of 2θ values from 25° to 27° likely corresponds to the $P1$ cell. The thin structure up to the intense silicon peak may be caused by the presence of various crystalline components in the ZnTPP- C_{60} film.

Analysis of the structure of dielectric oriented substrates of muscovite mica and potassium bromide was performed to refine the results obtained, and the degree of crystallinity of the films turned out to be higher in these cases. The number of spectral lines was much larger for the mica substrate than for the silicon and KBr substrates, and these lines largely overlapped the weaker peaks corresponding to the thin film; however, a set of lines from the nanocomposite can be detected after subtraction (the substrate peaks are shaded in Fig. 2): 10.9° ; 13.2° ; 16.3° ; 17.2° , 21.9° and 24.4° . The set of lines corresponding to the crystalline structure of the composite is as follows for the KBr substrate: 13.2° ; 16.8° ; 17.2° ; 21.3° ; 38.7° ; 47.8° .

The relative peak intensity is more difficult

to estimate with the Debye – Scherrer method in the case of a thin film, since, in contrast to the powder, potential texturing of this film should be taken into account. However, a peak observed on dielectric substrates at 2θ values equal to $16 - 17^\circ$ most likely excludes the presence of a phase with the $P2_1/n$ structure, as the intensity of the line is minimal for this phase in this region [29]. Apparently, the crystalline phase is deposited on the substrates in our experimental conditions but it may possibly belong to the $P1$ crystal system that is rather energetically unfavorable.

Spectral dependences of photoluminescence.

It was established in the above-mentioned study [19] that X-ray irradiation changes the absorption spectrum below the HOMO-LUMO gap, so the photoluminescence method was chosen to investigate the changes in the electron spectrum.

Fig. 3, *a* shows the optical density spectra for ZnTPP both for the toluene solution and for the solid (film). The features of the spectra of ZnTPP solutions in Fig. 3 have already been well-studied [30, 31]. In addition to a strong band (the Soret band or the B band at a wavelength of $350 - 400$ nm) due to allowed electronic transitions (the matrix element is not equal to zero), the so-called Q band, which is a set of bands in the visible region, is contained in the absorption spectra of porphyrins. In the case of D_{4h} molecular symmetry (metalloporphyrin), this region should consist of two bands. The Q band is quasi-forbidden, not on account of symmetry, but on account of cyclic conjugation [32], and is weak as a consequence. Two bands are present in the experimental absorption spectra in the Q region: their wavelengths are 550 and 590 nm. The first one is due to electron-vibronic (vibronic) replicas and is more intense because the oscillations act as a perturbing factor, removing the quasi-prohibition. A weak band at 590 nm in the absorption spectrum is caused by an electronic transition. The frequency difference in the absorption spectrum (590 and 550 nm in Fig. 3, *a*) should always be smaller than in the emission spectrum (600 and 650 nm in Fig. 3, *b*).

The positions of the absorption peaks in the spectrum remained the same for films, with the

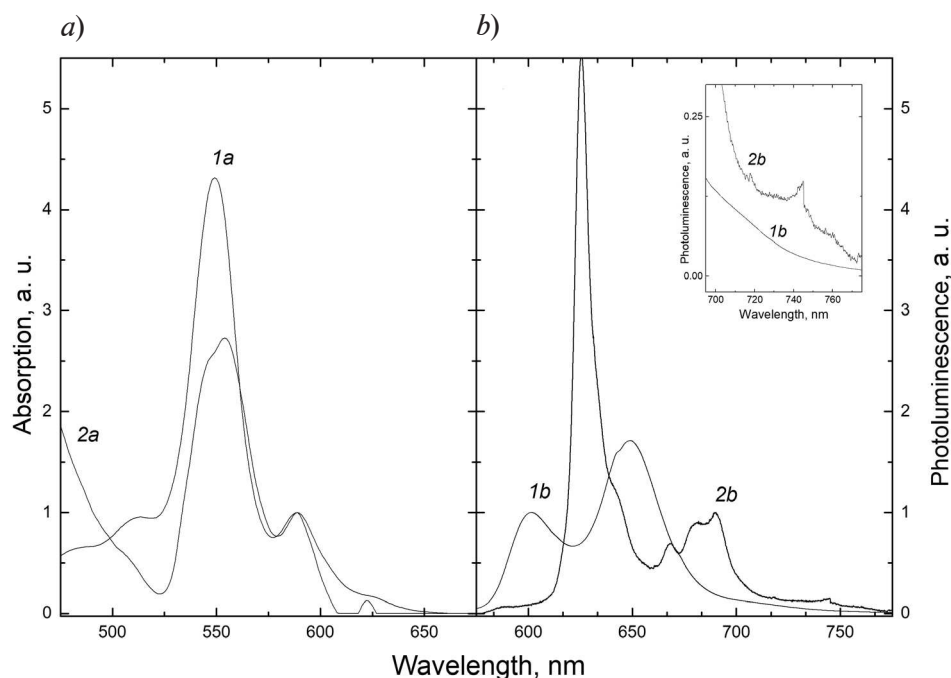


Fig. 3. Optical density (a) and photoluminescence (b) of ZnTPP solutions in toluene (1a, 1b) and 300-nm-thick ZnTPP films on Si (111) substrate (2a, 2b)

vibronic peak splitting into two components at 550 nm. Fig. 3, b shows the photoluminescence spectra of the films and the solution in toluene. Notably, there is a mirror symmetry in the position and intensity of the absorption and emission spectra for solutions, because the absorption and emission bands belong to the same electronic transition on which oscillations are superimposed; in other words, both spectra belong to the vibrational structure of one electronic transition [32].

However, the position and shape of the photoluminescence peaks for thin films do not correspond to those for the ZnTPP solution peaks.

Firstly, the photoluminescence spectrum of the films is shifted toward the long-wave region by approximately 30 nm. According to [33], the bathochromic shift is related to the stacking π - π interaction in the delocalized system of macrocyclic electrons during the formation of the ordered phase of porphyrin, mainly in the form of non-covalently bound $(\text{ZnTPP})_2$ dimers.

Secondly, mirror symmetry breaks down for the intensities of the emission and absorption spectra in the solid-state phase, and the line as-

sociated with the electronic transition that was previously quasi-forbidden becomes the most intense in the emission spectrum.

Thirdly, the photoluminescence spectrum of films, in comparison with solutions, exhibits a new long-wave emission peak at 745 nm, apparently associated with phosphorescence. It was observed earlier that metalloporphyrin solutions possess phosphorescence, but only at low temperatures. Introducing a heavy or a paramagnetic atom into an organic molecule leads to a “mixing” of the wave functions of the singlet and triplet states, removing the rule forbidding intercombination, and, as a consequence, to an increase in the probability of singlet-triplet transitions. A molecule can relax from the excited state not only by conversion to the ground state, but also nonradiatively to a metastable triplet state [32]. In this case, spin-orbital interaction violates the rule forbidding intercombination. It can be concluded from the data obtained that the prohibition against intercombination can be violated due to formation of different kinds of structures, for example, porphyrin dimers.

The effect of X-ray radiation on the photoluminescence of samples. Photoluminescence

spectra of porphyrin and composite samples, recorded before and after irradiation with the respective doses, are shown in Fig. 4. It can be seen that the photoluminescence intensity is higher for the pure ZnTPP sample of (Fig. 4, *a*) than for the ZnTPP-C₆₀ nanocomposite sample (Fig. 4, *b*). This is explained by fullerene's strong acceptor properties and the transfer of the photoexcited charge to the fullerene molecule in the ZnTPP-C₆₀ nanocomposite [5]. A weaker change in the photoluminescence intensity than that obtained in [5] is in this case due to the formation of the second phase and fullerene depletion of the nanocomposite, compared with its stoichiometric composition. A decrease in photoemission intensity was observed after the first X-ray irradiation dose for all the samples studied, while the posi-

tions of the lines and their shapes remained in the spectrum. In order to clarify the behavior of photoluminescence intensity of the samples upon further irradiation, the obtained spectra were decomposed into the components of the Lorentz-type line and the dose dependences of the total relative intensity of the spectral fluorescence lines, caused by both electronic and vibronic transitions on energy scales, were plotted (Fig. 5), along with phosphorescence lines.

It can be seen from the graphs that the dose dependences of photoluminescence differ for the electronic and electron-vibrational components of the spectrum, both for pure ZnTPP films and for the composite. The intensity of the electron-vibrational component gradually decreases by 10 – 15 % as the

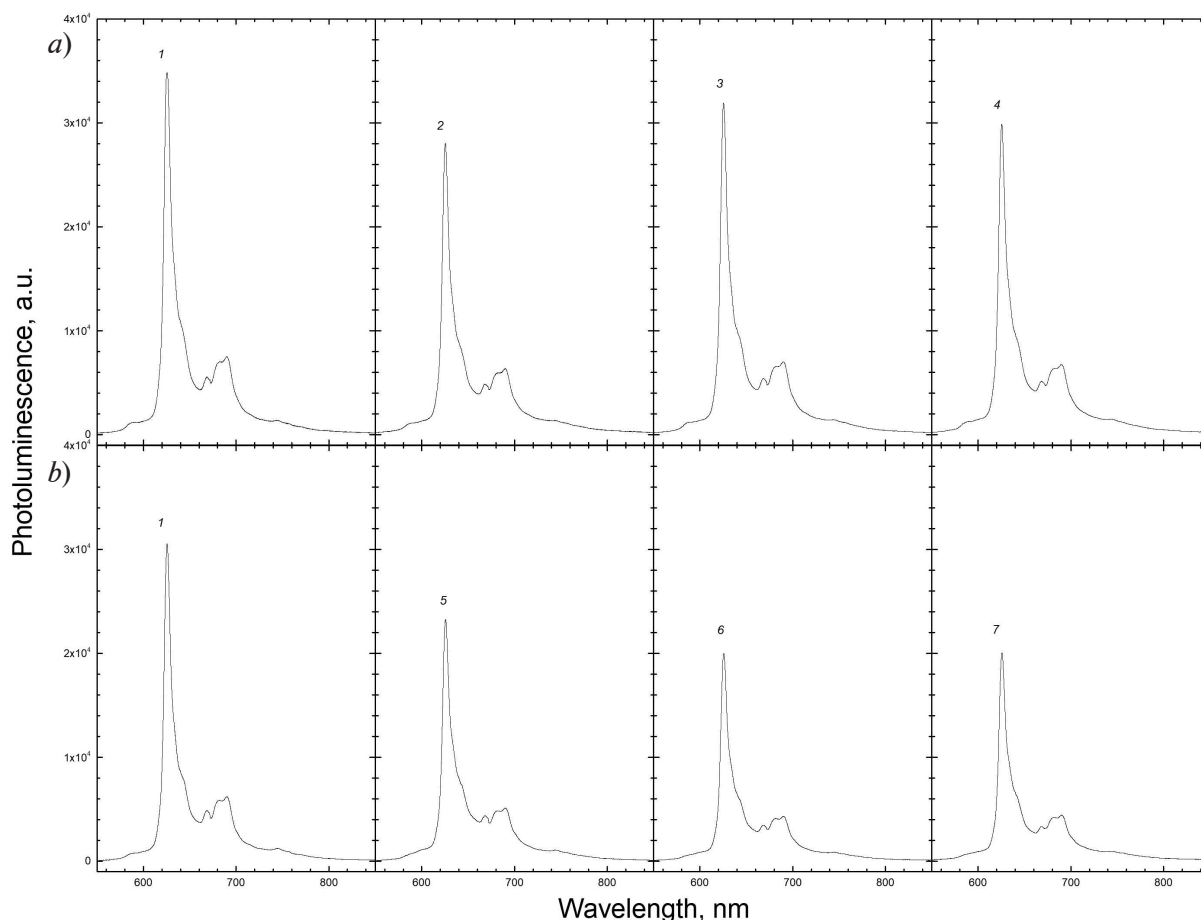


Fig. 4. Photoluminescence spectra of ZnTPP (*a*) and ZnTPP-C₆₀ (*b*) films before irradiation (1) and after irradiation with different doses of X-rays (in 10⁵ R): 1.20 (2); 2.65 (3); 4.51 (4); 0.62 (5); 1.45 (6); 2.69 (7)

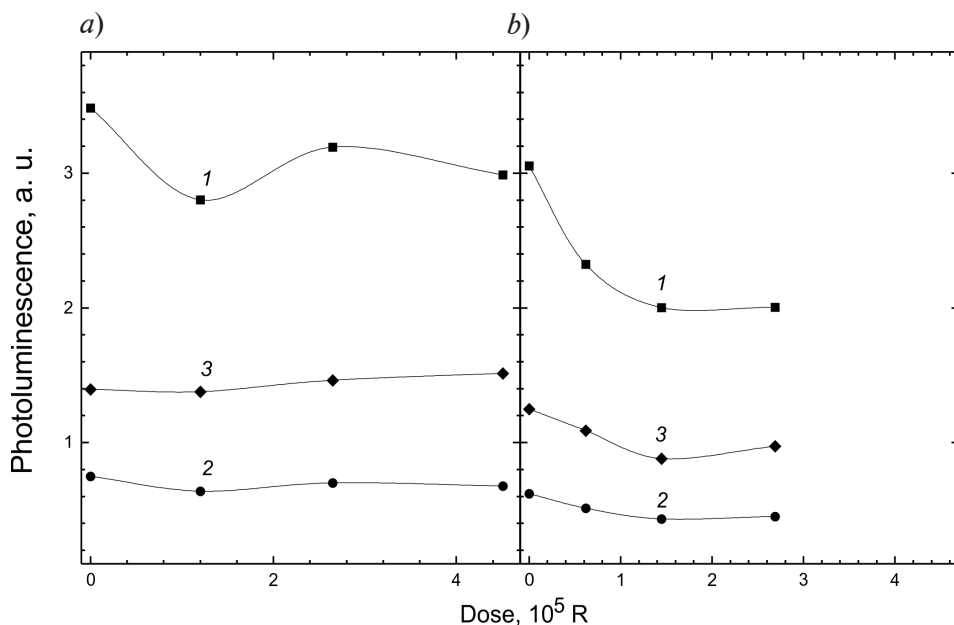


Fig. 5. Dependences of relative intensity of fluorescence (1, 2) and phosphorescence (3) bands on the dose of X-rays for ZnTPP (a) and ZnTPP-C₆₀ (b) samples. The figure includes data for the peaks caused by electronic (1) and electron-vibrational (2) transitions

radiation dose increases. As for the electronic component of the fluorescence band, the dose dependence of its relative intensity is weaker for pure ZnTPP than for the composite material. While the intensity of the radiative electronic transition is practically restored after a 20 % drop for ZnTPP films, the decrease in intensity is more significant (by 50%) and monotonic for composite films.

The following assumptions have to be made to explain this form of the obtained dose dependences.

The effect of X-ray radiation for pure ZnTPP turns out to be weak in this range of doses and leads to an overall slight decrease in photoemission intensity associated with the growth of defects that contribute to nonradiative recombination. In this case, the relative contribution of phosphorescence slightly increases.

A stronger decrease in fluorescence intensity due to radiative electronic transition (up to 50 %) is observed for composite films, which is apparently because irradiation leads to an increased probability of luminescence quenching due to the energy transfer of carrier photoexcitation to fullerene.

Thus, it can be assumed that radiation defects developing in the composite compound under consideration (upon irradiation in the chosen dose range) lead to an increased probability of both intercombination transition and carrier photoexcitation transfer to the acceptor fullerene molecule. The effect should be more pronounced when the surface of the interface between the two phases increases.

Conclusion

This paper presents the results of investigations of thin films of zinc tetraphenylporphyrin (ZnTPP) and nanocomposite films of zinc tetraphenylporphyrin with fullerene (ZnTPP-C₆₀) synthesized under quasi-equilibrium conditions.

We have studied the surface morphology of the samples by scanning electron microscopy and the structure of the films by X-ray diffraction. Combining these methods, we were able to establish that a crystalline ZnTPP film formed on the silicon substrate and that a two-phase system was present in ZnTPP-C₆₀ films at a phase ratio of 1.3 : 1.0 by weight.

Partial losses of the fullerene phase, compared with the calculated value, were discov-

ered in the ZnTPP-C₆₀ composite films by energy-dispersive microanalysis.

The differences in the optical absorption and photoluminescence spectra in ZnTPP solutions and in the ZnTPP film synthesized indicate that an ordered phase is established. We have obtained data on the crystalline structure of the films with a *P1*-type lattice forming. Phosphorescence could be observed in crystalline ZnTPP films even at room temperature.

We have examined the changes in the photoluminescence spectra of thin films of ZnTPP and nanocomposite films of ZnTPP-C₆₀ after X-ray irradiation with doses ranging from $1 \cdot 10^5$ до $3 \cdot 10^5$ R. We have found that films of pure ZnTPP with a coarse crystalline structure are sufficiently stable against these doses of X-ray

radiation.

The dose dependences for composite ZnTPP-C₆₀ films differ by the electronic and electron-vibrational contributions to photoluminescence intensity. A significant decrease (up to 50 %) in the intensity of the photoluminescence band due to electronic transfer is most likely linked to an increased probability of carrier photoexcitation transfer to fullerene molecules and, correspondingly, to an increased probability of photoluminescence quenching. In this case, the relative intensity of the electron-vibrational band in the photoluminescence spectrum of composite films only weakly depends on the irradiation dose, which can be explained by sufficiently high time constants of these processes.

REFERENCES

- [1] **G. Dennle, M.C. Scharber, C.J. Brabec**, Polymer-fullerene bulk-heterojunction solar cells, *Advanced Materials*. 21 (13) (2009) 1323–1338.
- [2] **P. Peumans, A. Yakimov, S.R. Forrest**, Small molecular weight organic thin-film photodetectors and solar cells, *J. Appl. Phys.* 93 (7) (2003) 3693–3723.
- [3] **E.A. Katz**, Nanostructured materials for solar energy conversion, Ed. T. Soga, Elsevier, Amsterdam, 2006.
- [4] **G. Mazzone, M.E. Alberto, B.C. de Simone, et al.**, Porphyrins and phthalocyanines in solar photovoltaic cells, *J. Porphyrins Phthalocyanines*. 14 (7) (2010) 759–792.
- [5] **M.A. Elistratova, I.B. Zakharova, N.M. Romanov, et al.**, Photoluminescence spectra of thin films of ZnTPP-C₆₀ and CuTPP-C₆₀ molecular complexes, *Semiconductors*. 50 (9) (2016) 1191–1197.
- [6] **Z. Guolun, J. Wu, Y. Wang, et al.**, Photo- and electroluminescent properties of 5,10,15,20-tetra-*p*-tolyl-21H,23H-porphine doped poly[2-methoxy-5-(2'-ethylhexyloxy)-1,4-phenylenevinylene] films, *Thin Solid Films*. 517 (11) (2009) 3340–3344.
- [7] **D. Wrobel, A. Siejak, P. Siejak**, Photovoltaic and spectroscopic studies of selected halogenated porphyrins for their application in organic solar cells, *Solar Energy Materials and Solar Cells*. 94 (3) (2010) 492–500.
- [8] **Y. Chen, G. Li, R.K. Pandey**, Synthesis of bacteriochlorins and their potential utility in photodynamic therapy (PDT), *Current Organic Chemistry*. 8 (12) (2004) 1105–1134.
- [9] **J. Durantini, G.M. Marisa, S.M. Funes, et al.**, Synthesis and characterization of porphyrin electrochromic and photovoltaic electropolymers, *Organic Electronics*. 13 (4) (2012) 604–614.
- [10] **K.D. Seo, M.J. Lee, H. MinSong, et al.**, Novel *D-π-A* system based on zinc porphyrin dyes for dye-sensitized solar cells: Synthesis, electrochemical, and photovoltaic properties, *Dyes and Pigments*. 94 (1) (2012) 143–149.
- [11] **P. Muthukumar, J.S. Abraham**, Highly sensitive detection of HCl gas using a thin film of mesotetra(4-pyridyl)porphyrin coated glass slide by optochemical method, *Sensors and Actuators. B. Chemical*. 159 (1) (2011) 238–244.
- [12] **M.A. Elistratova, I.B. Zakharova, O.E. Kvyatkovskii, et al.**, Electronic structure, optical and magnetic properties of tetraphenylporphyrins-fullerene molecular complexes, *J. Phys., Conference Series*. 690 (2016) 012012.
- [13] **I.B. Zakharova, V.M. Ziminov, N.M. Romanov, et al.**, Optical and structural properties of fullerene films doped with cadmium telluride, *Physics of the Solid State*. 56 (5) (2014) 1064–1070.
- [14] **N.M. Romanov, I.B. Zakharova**, The composition and the structure of thin films based on metalporphyrin complexes, *St. Petersburg Polytechnical University Journal, Physics and Mathematics*. (2) (2016) 1–7.
- [15] **I. Fratoddi, C. Battocchio, R. D'Amato, et al.**, Diethynyl-Zn-porphyrin-based assemblies: optical and morphological studies of nanostructured thin films, *Mat. Sci. Eng.* 23 (6) (2003) 867–871.
- [16] **R. Konenkamp, G. Priebe, B. Pietzak**, Carrier mobilities and influence of oxygen in C₆₀ films, *Phys. Rev. B. Condensed Matter and Materials*

Physics. 60 (16) (1999) 11804–11808.

[17] **E.V. Antina, E.V. Balantseva, M.B. Berezin**, Oxidative degradation of porphyrins and metalloporphyrins under polythermal conditions, Russian Journal of General Chemistry. 81 (6) (2011) 1222–1230.

[18] **H. Kim, W. Kim, Y. Mackeyev, et al.**, Selective oxidative degradation of organic pollutants by singlet oxygen-mediated photosensitization: tin porphyrin versus C₆₀ aminofullerene systems, Environ Sci. Technol. 46 (17) (2012) 9606–9613.

[19] **M.M. El-Nahass, A.H. Ammar, A.A. Atta, et al.**, Influence of X-ray irradiation on the optical properties of CoMTPP thin films, Optics Commun. 284 (9) (2011) 2259–2263.

[20] **D. Manas, M. Manas, M. Stanek, et al.**, Micromechanical properties of surface layer of HDPE modified by beta irradiation, Intern. J. Mech. 8 (2014) 150–157.

[21] **V.A. Basiuk, G. Albarrón, E.V. Basiuk, J.-M. Saniger**, Stability of interstellar fullerenes under high-dose γ -irradiation: new data, Advances in Space Research. 36 (2) (2005) 173–177.

[22] **M.A. Elistratova, I.B. Zakharova, N.M. Romanov**, X-ray radiation influence on photoluminescence spectra of composite thin films based on C₆₀<CdTe>, J. Phys., Conf. Ser. 586 (2015) 012002.

[23] **F. Cataldo, O. Ursinib, G. Angelinib**, Radiation-cured polyisoprene/C₆₀ fullerene nanocomposite, Part 2, Synthesis in decalin, Rad. Phys. Chem. 77 (6) (2008) 742–750.

[24] **A.M. Todd, T. Zhua, F. Zhang, et al.**, Performance degradation of P3HT:PCBM polymer/fullerene photovoltaic cells under gamma irradiation, ECS Trans. 25 (11) (2009) 103–111.

[25] **N.M. Romanov, I.B. Zakharova, E. Lähderanta**, Diagnostics of thin films of fullerene

/ cadmium telluride and their stability under X-ray radiation by IR spectroscopy // Optical Journal. 84 (12) (2017) 50–55.

[26] **G.L. Perlovich, O.A. Golubchikov, M.E. Klueva**, Thermodynamics of porphyrin sublimation, J. Porphyrins Phthalocyanines. 4 (8) (2000) 699–706.

[27] **M.P. Byrn, C.J. Curtis, Y. Hsiou, et al.**, Porphyrin sponges: conservative of host structure in over 200 porphyrin-based lattice clathrates, J. Am. Chem. Soc. 115 (21) (1993) 9480–9497.

[28] **H.M. Zeyada, M.M. Makhlof, M.A. Ali**, Structural, optical and dispersion properties of 5,10,15,20-tetraphenyl-21H,23H-porphyrin zinc thin films, J. Appl. Phys. 55 (2) (2016) 022601–022608.

[29] **G.L. Perlovich, W. Zielenkiewicz, Z. Kaszkur, et al.**, Thermophysical and structural properties of crystalline solvates of tetraphenylporphyrin and their zinc, copper and cadmium metallo-complexes, Thermochimica Acta. 311 (1-2) (1998) 163–171.

[30] **R.T. Kuznetsova, E.G. Ermolina, R.M. Gadirov, et al.**, Luminescence of metal complexes of chelate substituted tetraphenylporphyrin, High Energy Chemistry. 44 (2) (2010) 134–138.

[31] **M. Gouterman**, Optical spectra and electronic structure of porphyrins and related rings, The Porphyrins, Vol. 3, Ed. D. Dolphin, Academic Press, New York (1978) 161–165.

[32] **G.P. Gurinovich, A.N. Sevchenko, K.N. Solov'ev**, The spectroscopy of the porphyrins, Soviet Physics Uspekhi. 6 (1) (1963) 67–105.

[33] **X.-L. Zhang, J.-W. Jiang, Y.-T. Liu, et al.**, Identifying the assembly configuration and fluorescence spectra of nanoscale zinc-tetraphenylporphyrin aggregates with scanning tunneling microscopy, Sci. Rep. 6 (2016) 227561–227567.

Received 06.02.2018, accepted 03.03.2018.

THE AUTHORS

ROMANOV Nikolay M.

Peter the Great St. Petersburg Polytechnic University
29 Politechnicheskaya St., St. Petersburg, 195251, Russian Federation
nikromanov.90@gmail.com

ZAKHAROVA Irina B.

Peter the Great St. Petersburg Polytechnic University
29 Politechnicheskaya St., St. Petersburg, 195251, Russian Federation
zakharova@rphf.spbstu.ru

ELISTRATOVA Marina A.

Ioffe Institute of RAS
26 Politechnicheskaya St., St. Petersburg, 195251, Russian Federation
marina.elistratova@mail.ioffe.ru

LÄHDERANTA Erkki
Lappeenranta University of Technology
Skinnarilankatu 34, 53850 Lappeenranta, Finland
Erkki.Lahderanta@lut.fi

GAMMA-INDUCED EFFECT ON THE LUMINESCENCE OF NANOCOMPOSITES OF MEH-PPV CONDUCTIVE POLYMER WITH LEAD SULPHIDE QUANTUM DOTS

N.M. Romanov^{1,2}, S.F. Musikhin¹

¹ Peter the Great St. Petersburg Polytechnic University, St. Petersburg, Russian Federation;

²Lappeenranta Technological University, Lappeenranta, Finland

Gamma radiation effect on the photoluminescence of thin films of conductive polymer MEH-PPV, PbS quantum dots (QDs) and MEH-PPV–PbS (QDs) nanocomposite have been studied. Thin films were obtained by centrifugation. Samples were irradiated with exposure doses (in Gy): 0; $1.84 \cdot 10^4$; $4.18 \cdot 10^4$; $6.73 \cdot 10^4$. Photoluminescence of the polymer MEH-PPV was established to change nonmonotonically with an increase in doses, which might be due to running the oppositely directed, competing processes under the action of gamma quanta, namely destruction and cross-linking of polymer chains. Significant polymer's restructuring took place under gamma rays. Photoluminescence intensity of PbS QDs fell approximately twofold after irradiation with doses mentioned above, the intensity maximum shifting to the short-wavelength region. This behavior was due to a change in the energy structure of the QDs. The effect of gamma quanta on the QDs photoluminescence was analyzed.

Key words: conductive polymer; quantum dot; MEH-PPV; PbS; photoluminescence; gamma quantum

Citation: N.M. Romanov, S.F. Musikhin, Gamma-induced effect on the luminescence of nanocomposites of MEH-PPV conductive polymer with lead sulphide quantum dots, St. Petersburg State Polytechnical University Journal. Physics and Mathematics. 11 (2) (2018) 31 – 36. DOI: 10.18721/JPM.11204

Introduction

Nanocomposites based on conductive polymers and semiconductor nanocrystals show promise for use in optoelectronic devices with flexible parameter settings [1].

Different combinations of conductive polymers and semiconductor nanoparticles (quantum dots (QDs)) make it possible to customize the optical properties of nanocomposites [2 – 4]. At the same time, varying the size of QDs of different materials allows to generate the required optical spectrum of the nanocomposite and its properties. The optical properties of nanocomposites can be further altered by exposure to ionizing radiation, in particular, gamma radiation. Gamma rays can affect both the material of the polymer matrix and the semiconductor nanoparticles. Due to the physical properties of gamma radiation, its penetrating power is strong. Interactions between gamma rays and matter include electronic excitation, electron ionization and electron-hole pair generation [5].

The effect of gamma-ray irradiation on CdS, CdSe/ZnS and CsPbBr₃ quantum dots was considered in [6 – 8], with analysis of possible

degradation mechanisms. It was established in [6] that irradiation with gamma rays affected the sizes of the reverse micellar systems used to synthesize the QDs and of their aqueous cores, with the changes in size due to irradiation depending on the conditions in which the specific QDs were obtained. QDs were shown to decrease in size as a function of the level of micelle hydration and the irradiation dose. The authors concluded that γ -irradiation could change the size of CdS quantum dots and, as a consequence, consistently change their parameters and properties (intensity, lifetime, and fluorescence band position).

Ref. [7] considered the effect of gamma radiation from a ¹³⁷Cs source on the photoluminescence properties of colloidal CdSe/ZnS quantum dots. Optical degradation was estimated depending on the irradiation dose. The authors linked the decrease in the photoluminescence decay time constants with recombination of exciton states. At the same time, the deterioration in quantum efficiency was attributed to nonradiative processes that did not involve exciton states and consisted in the trapping of excited carriers by irradiation-induced defects. In general, these quantum dots

were found to exhibit poor radiation hardness.

Ref. [8] examined the effect of gamma radiation from a ^{137}Cs source on perovskite CsPbBr_3 QDs. It was revealed that CsPbBr_3 QDs were significantly more stable with respect to γ -radiation than commercial samples of CdSe/ZnS QDs traditionally used for the same tasks. The observed degradation processes were described assuming that a dose-dependent drop in photoluminescence was related not only to a change in the particle size distribution but also to the formation of nonradiative recombination centers as a result of the material's exposure to high energy. The authors proposed using CsPbBr_3 nanocrystals as potential *in vivo* biosensors under increased radiation background during antitumor therapy.

Some studies explored the effect of gamma irradiation on various polymers. Ref. [9] confirmed that it was possible to fabricate a thermally stable polymer by means of radiation cross-linking, with a modified polymer formed by cross-linking of short monomer units of the initial polymer. The study determined the threshold doses causing irreversible changes and the doses of complete oxidation of fragmented units, and described the changes in the fundamental physical and chemical properties of the polymers, such as the band gap value.

Ref. [10] studied the changes in the molecular weight of a polymer exposed to gamma irradiation that were induced by cross-linking (elongation) and degradation (shortening) of the main polymer chain depending on the irradiation dose. The findings of this paper were rather controversial, yet important. Both processes were shown to occur simultaneously, but with different probabilities. This complicates quantitative assessment and prediction of the final properties of the material. Notably, the technology of radiation cross-linking of polymers is currently used in industry for insulation of deep-water cables with the required performance characteristics, as well as for orthopedic applications [11].

In turn, the effect of gamma irradiation on polymer – QD nanocomposites is rather poorly understood at present and needs a more in-depth approach.

In this study, we have investigated for the first time the degradation of the photolumi-

nescent properties of the MEH-PPV polymer nanocomposites with lead sulfide (PbS) quantum dots, exposed to gamma irradiation and the effect of this irradiation on PbS QDs.

Experimental procedure

The samples were prepared from the commercially available MEH-PPV (Poly[2-methoxy-5-(2-ethylhexyloxy)-1,4-phenylenevinylene]) polymer powder from Sigma Aldrich with a number-average molecular weight of about 40,000 – 70,000. PbS QDs were synthesized by a method identical to that used in [4] from an organometallic solution based on lead oxide (PbO) dissolved in oleic acid ($\text{C}_{18}\text{H}_{34}\text{O}_2$). Bis-trimethylsilyl sulfide in trioctylphosphine was introduced into this solution.

We should note that Ref. [4] proved that it was possible to use these QDs to create a polymer-QD nanocomposite, and also considered the potential applications of nanocomposites.

In our study, a toluene solution was prepared to obtain thin films of the MEH-PPV polymer, the PbS QDs, and their composite. The solution was deposited on glass substrates by centrifugation (the spin-coating technology). It is known that centrifugation should not lead to noticeable destruction of macromolecules [12]. The spinner's parameters (rotation rate, acceleration, etc.) can be changed with high precision, so that thin films of a given thickness can be obtained.

The initial industrial MEH-PPV polymer powder (weight about 10 mg) was dissolved in toluene (the solution was immersed in an ultrasonic bath for 20 minutes to completely dissolve the polymer). The PbS QDs and the composite (MEH-PPV + PbS QD) were prepared in toluene. The glass substrates were pretreated in the ultrasonic bath filled with isopropyl alcohol for 10 minutes. The MEH-PPV and PbS QD films and their composites were deposited on glass substrates by spin-casting.

Photoluminescence of the samples was excited by a semiconductor laser with a wavelength $\lambda = 405$ nm and a power of 50 mW, operating in continuous mode. The photoluminescence spectra were recorded using the Horiba Jobin

Yvon automated system including a FHR 640 monochromator with a 1200 gr/mm diffraction grating and a Symphony II 1024*256 Cryogenic Open-Electrode CCD detector.

The gamma radiation source was a ^{137}Cs radionuclide with a photon energy of 661 keV. The samples were irradiated in a quasi-closed oxygen-containing chamber by a monochromatic gamma-ray flux, which was achieved by using 84 radiation sources. In our case, a cesium source of gamma rays (^{137}Cs) has a number of advantages compared with a cobalt source (^{60}Co), primarily a lower gamma energy and less penetrating power; this allows to generate more single interactions. In other words, other things being equal, the linear attenuation coefficient is higher for the cesium isotope than for the cobalt isotope.

The thin films we have examined were exposed to the following irradiation doses, Gy: 0; $1.84 \cdot 10^4$; $4.18 \cdot 10^4$; $6.73 \cdot 10^4$.

All irradiations and measurements were performed at room temperature.

Experimental results and discussion

The photoluminescence spectrum for the conductive polymer – QD nanocomposite contains both the luminescence spectrum of the conductive polymer and the luminescence spectrum of quantum dots, as well as their combined energy band diagram. Fig. 1 shows the luminescence spectra of the MEH-PPV polymer, PbS QDs and MEH-PPV – PbS QD films (deposited on a glass substrate), recorded after exposure to different doses of gamma radiation.

Irradiation of the pure MEH-PPV polymer with gamma rays results in various changes in polymer chains, which in turn changes the luminescence spectra. Gamma irradiation randomly breaks the C – C and C – H bonds, and also leads to oxidative degradation with different functional groups forming in the presence of oxygen [10].

Fig. 1, *a* shows the photoluminescence spectra of the gamma-irradiated MEH-PPV polymer. Evidently, the luminescence intensity decreases sharply at an irradiation dose of $1.84 \cdot 10^4$ Gy, and increases as the dose is further increased, with a subsequent slight decrease in intensity. Additionally, a broadening of

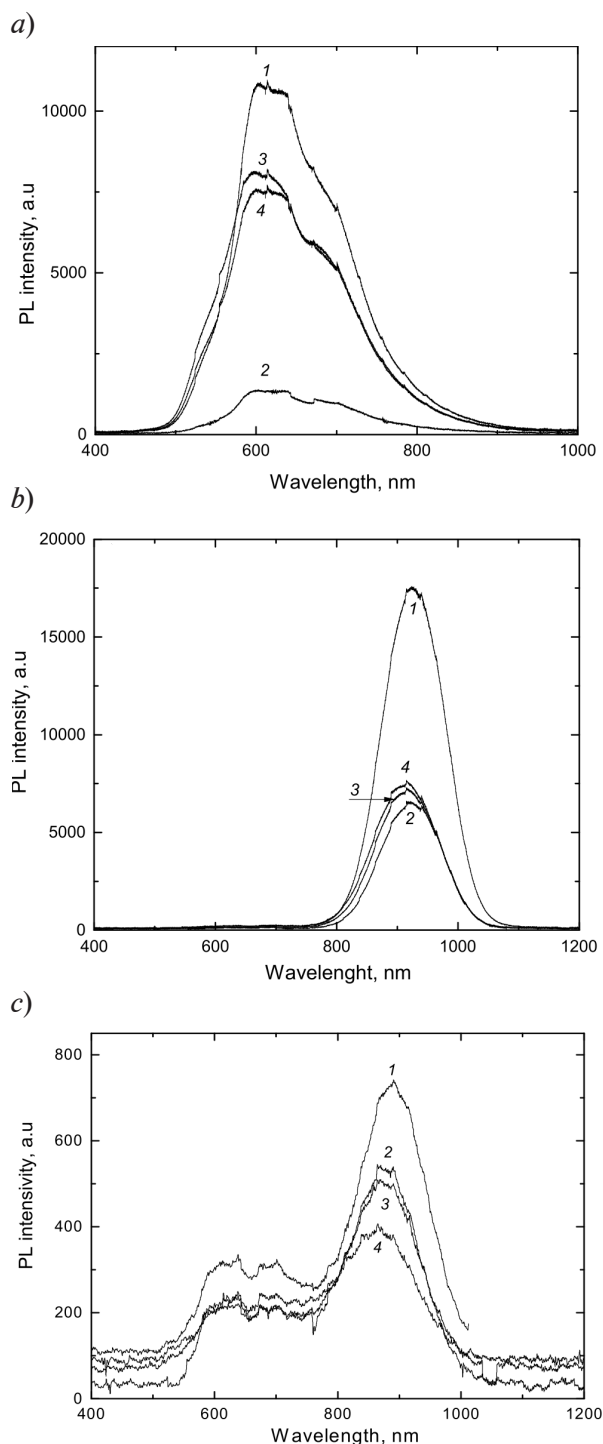


Fig. 1. Photoluminescence spectra for a pure MEH-PPV polymer (*a*), PbS QDs (*b*), and a MEH-PPV – PbS QD polymer nanocomposite (*c*), deposited on glass substrates; recorded after exposure to different doses of gamma irradiation, Gy: 0 (1); $1.84 \cdot 10^4$ (2); $4.18 \cdot 10^4$ (3); $6.73 \cdot 10^4$ (4)

the spectrum is observed with a shift in the intensity maximum toward short wavelengths and with an insignificant broadening toward long wavelengths at the doses of $4.18 \cdot 10^4$ and $6.73 \cdot 10^4$ Gy.

This behavior of the luminescence spectrum can be attributed to structural changes occurring in the polymer. At low irradiation doses, the key role is played by cross-linking of polymer chains [9] that promotes the decay of the exciton excited during activation. Cross-linking facilitates the transition of an electron or a hole to an adjacent polymer chain with the corresponding exciton decay and subsequent nonradiative recombination. Besides, the arising defects contribute to the formation of nonradiative recombination centers, which electrons and holes reach rather quickly via long conjugated chain segments. A further increase in the irradiation dose leads to a shortening of the conjugated chain segments, which is manifested in the luminescence intensity maximum shifting toward short wavelengths. This also hinders the decay of excitons due to transition of electrons or holes to adjacent conjugated sites or adjacent polymer chains and to increased luminescence intensity. Since the transfer of electrons and holes from one conjugated site to another or to an adjacent chain occurs via a hopping mechanism, this process is hampered by an increase in the length distribution of the conjugated segments and a corresponding increase in the energy distribution [13]. Luminescence intensity increases as a result. The number of defects and, consequently, the number of nonradiative recombination centers increase with a further increase in the dose, and luminescence intensity gradually decreases.

Fig. 1, *b* shows the luminescence spectra of PbS QDs with different irradiation doses. With increasing irradiation dose, the luminescence peak shifts toward the shortwave region of the spectrum, and the peak width increases. The luminescence intensity decreases significantly with an irradiation dose of $1.84 \cdot 10^4$ Gy, and then increases slightly with an increase in the irradiation dose. This can be attributed to a whole range of processes occurring in colloidal QDs irradiated with gamma rays. Gamma irradiation can affect the size of the QDs [6].

Defects leading to an increase in nonradiative recombination can form within QDs. Defects similar to defects in polymer chains can occur in the organic molecules surrounding the QD. In combination with oxygen atoms, this process can lead to the formation of charge trapping centers. As a result, an electric charge is generated around the QD. Regardless of the sign of the charge, this leads to a shift in the quantum confinement subbands of the QD and an increase in the effective band gap, which in turn causes the luminescence peak to shift toward the short wavelengths. The broadening of the spectrum is due either to an increase in the size distribution of the QD, or in the distribution of the electric charge surrounding the QD.

Fig. 1, *c* shows the luminescence spectra of the MEH-PPV – PbS QD nanocomposite. The luminescence intensity of the polymer decreases substantially when the nanocomposite is formed, while the luminescence intensity of the QD remains rather high.

This effect is due to the specifics of the energy band diagram of the nanocomposite (Fig. 2). Electrons and holes excited in the polymer matrix are trapped into quantum dots and recombine with the emission of infrared rays. As a result, the luminescence intensity of the polymer matrix decreases, while that of the QD increases. Irradiation with gamma rays most significantly affects the luminescence intensity of the QD, which decreases with increasing irradiation dose, dropping by half compared to the unirradiated sample at a dose of $6.73 \cdot 10^4$ Gy. The luminescence intensity of the polymer matrix also decreases with an increasing dose of gamma irradiation but not so considerably as in the case of the QDs. A significant drop in the luminescence intensity of the QD is due not only to enhanced nonradiative recombination in the QD, but also to a change in the factors affecting the trapping of electrons and holes from the polymer matrix. The shift of the luminescence peak of the QD toward the short-wavelength region of the spectrum indicates a shift in the quantum confinement energy levels of the QD toward higher energies and a decrease in the depth of the quantum well for electrons and holes. This depth for holes can be reduced

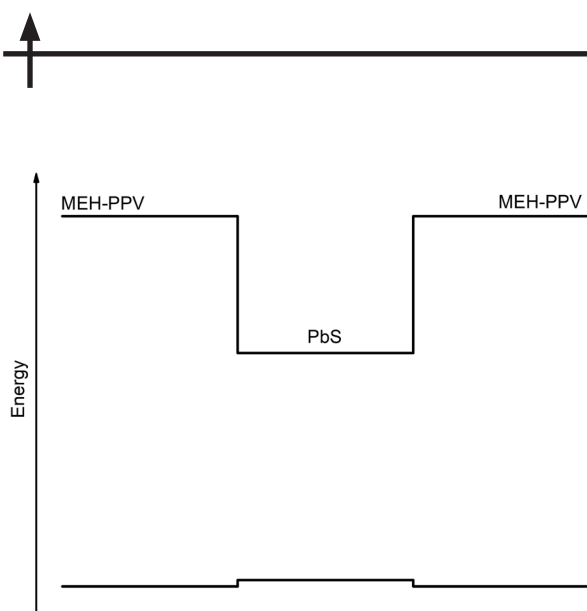


Fig. 2. Energy band structure for the MEH-PPV – PbS QD nanocomposite

until it either becomes a very small value or the well disappears altogether.

Let us analyze the band diagram of the nanocomposite in Fig. 2 in more detail. A quantum well corresponding to the PbS QDs is located at its center, and the lines to the right and left of the well correspond to the LUMO and HOMO levels of the MEH-PPV polymer. Reducing the depth of the quantum well significantly reduces the probability of trapping and confinement of holes within the QD. The probability of trapping one of the types of carriers in the QD is also reduced due to the presence of an electric charge surrounding the QD. Due to these factors, the luminescence of the QD is considerably reduced. Decreased luminescence of the polymer matrix is due to both an increase in the number of defects and

an increase in the intersystem transition between the singlet and triplet exciton states in the polymer. The probability of this transition increases if heavy impurity atoms (with a large atomic number Z) are present in the polymer matrix [14]. These atoms, in particular, lead, can appear if the absorption of gamma rays by the quantum dot causes the release of such an atom from the QD into the polymer matrix.

Conclusion

Photoluminescence spectra of gamma-irradiated samples (the MEH-PPV – PbS QD nanocomposite and its components) were recorded and analyzed in this study. The following conclusions can be drawn based on our findings.

Gamma irradiation leads to a nonmonotonic decrease in the photoluminescence of the MEH-PPV polymer, which may be due to competing oppositely directed processes occurring in it, namely, degradation and cross-linking of polymer molecular chains. Significant structural changes occur in the polymer during these processes.

The photoluminescence of the PbS quantum dot irradiated with different doses in the range of $(1.84 - 6.73) \cdot 10^4$ Gy decreases approximately by half, with its intensity maximum shifting to the short-wavelength region; this points to a change in the energy structure of the QD.

The luminescence of a gamma-irradiated nanocomposite is determined by its energy band structure, which varies depending on the irradiation dose absorbed.

REFERENCES

- [1] L. Bakueva, S. Musikhin, E.H. Sargent, et al., Luminescence and photovoltaic effects in polymer-based nanocomposites, Handbook of Organic-Inorganic Hybrid Materials and Nanocomposites, Vol. 2, American Scientific Publishers, USA (2003) 181–215.
- [2] S.A. McDonald, P.W. Cyr, L. Levina, E.H. Sargent, Photoconductivity from PbS-nanocrystal/semiconducting polymer composites for solution-processible, quantum-size tunable infrared photodetectors, Appl. Phys. Lett. 85 (11) (2004) 2089–2091.
- [3] J.Y. Kim, O. Voznyy, D. Zhitomirsky, E.H. Sargent, 25th Anniversary article: colloidal quantum dot materials and devices: A quarter century of advances, Adv. Mater. 25 (3) (2013) 4986–5010.
- [4] L. Bakueva, S. Musikhin, M.A. Hines, et al., Size-tunable infrared 1000–1600 nm electroluminescence from PbS quantum-dot nanocrystals in a semiconducting polymer, Appl. Phys. Lett. 82 (17) (2003) 2895–2897.
- [5] R. El-Mallawany, A. Abousehly, A.A. El-Rahamani, F. Yousef, Radiation effect on the ultrasonic attenuation and internal friction of tellurite glasses, Materials Chemistry and Physics. 52 (2) (1998) 161–165.
- [6] O.D. Bekasova, A.A. Revina, A.L. Rusanov, et al., Effect of gamma-ray irradiation on the size

and properties of CdS quantum dots in reverse micelles, *Radiation Phys. and Chem.* 92 (Nov.) (2013) 87–92.

[7] **N.J. Withers, K. Sankar, B.A. Akins, et al.**, Rapid degradation of CdSe/ZnS colloidal quantum dots exposed to gamma irradiation, *Applied Physics Letters*. 93 (17) (2008) 173101.

[8] **L.B. Matyushkin, N.M. Romanov**, Gamma-irradiation influence on photoluminescence of CsPbBr₃ and CdSe/ZnS nanocrystals, *Journal of Optical Technology*. 85 (2) (2018) 72–74.

[9] **S.A. Siddhartha, K. Dev, S.K. Raghuvanshi, et al.**, Effect of gamma radiation on the structural and optical properties of Polyethyleneterephthalate (PET) polymer, *Radiation Phys. and Chem.* 81 (4) (2012) 458–462.

[10] **A. Tidjani, Y. Watanabe**, The dose-rate effect of irradiation on chemical and physical modifications. Gamma-oxidation of linear low-density polyethylene, *J. Polym. Sci. A: Polym. Chem.* 33 (3) (1995) 1455–1460.

[11] **E. Oral, O.K. Muratoglu**, Radiation cross-linking in ultra-high molecular weight polyethylene for orthopaedic applications, *Nuclear Instruments and Methods in Physics Research. B.* 265 (2007) 18–22.

[12] **V.I. Vettegren, V.A. Zakrevskii, A.N. Smirnov, N.T. Sudar'**, Electric-field-induced formation of a conducting channel in a dielectric polymer film, *Physics of the Solid State*. 52(8) (2010) 1774–1779.

[13] **S.D. Baranovskii, O. Rubel, F. Jansson, R. Österbacka**, Description of charge transport in disordered organic materials, In: Grasser T., Meller G., Li L. (eds), *Organic Electronics*, 2009, *Advances in Polymer Science*, Vol. 223, Springer, Berlin, Heidelberg.

[14] **L. Bakueva, D. Matheson, S. Musikhin, E.H. Sargent**, Luminescence of pure and iodine doped PPV: internal energetic structure revealed through spectral signatures, *Synthetic Metals*. 126 (2–3) (2002) 207–211.

Received 19.01.2018, accepted 24.01.2018.

THE AUTHORS

ROMANOV Nikolay M.

Peter the Great St. Petersburg Polytechnic University
29 Politechnicheskaya St., St. Petersburg, 195251, Russian Federation
nikromanov.90@gmail.com

MUSIKHIN Sergey F.

Peter the Great St. Petersburg Polytechnic University
29 Politechnicheskaya St., St. Petersburg, 195251, Russian Federation
musihin.sf@spbstu.ru

THE DUPUIS PARADOX AND MATHEMATICAL SIMULATION OF UNSTEADY FILTRATION IN A HOMOGENEOUS CLOSING DIKE

D.D. Zaborova, M.R. Petritchenko, T.A. Musorina

Peter the Great St. Petersburg Polytechnic University, St. Petersburg, Russian Federation

The aim of this study is to determine a flow rate and a shape of a depression curve in conditions of filtration through a rectangular closing dike using aperiodic solutions of the Boussinesq limit problem. We have established that the formation of this curve and the seepage area (the final jump of continuity or interruption of the curve at the minimum pressure point) on the border of the downstream and porous medium, in the closing dike of finite length, occurs for a finite amount of time proportional to the square of the closing dike length. Therefore, in the short closing dike, a cut-out point does not have time to fall into the downstream during the time, it takes for the depression curve to touch the water level in the upstream. The continuous curve without seepage area always reaches the steady state in the semi-infinite closing dike for a finite amount of time.

Key words: filtration of subsoil water; porous medium; depression curve; seepage area

Citation: D.D. Zaborova, M.R. Petritchenko, T.A. Musorina, The Dupuis paradox and mathematical simulation of unsteady filtration in a homogeneous closing dike, St. Petersburg Polytechnical State University Journal. Physics and Mathematics. 11 (2) (2018) 50 – 58. DOI: 10.18721/JPM.11205

Introduction

Seepage problems have major importance for power engineering and construction, with a wide range of applications extending from hydraulic engineering and melioration [1 – 6] to construction technologies (rapid pumping of groundwater from the pit, drainage of construction sites) [8 – 12]. Seepage theory as a section of fluid mechanics includes two branches: hydromechanical and hydraulic. These branches overlap in solving stationary problems [4, 6, 7, 13 – 18].

Hydromechanical seepage theory encompasses methods for solving mixed limit problems of theory of analytic functions in regions with free boundaries [1]. An important result of hydromechanical theory is Devison's conclusion on the interruption of the limiting boundary streamline in the location (the cut-out point) where it falls into the tailwater (the waters downstream from a hydraulic structure). The magnitude of this interruption is called the seepage area (δh in Fig. 1). The limiting streamline separating the saturated medium from the unsaturated one is called the depression curve. In other words, the depression curve is a line characterizing the level of groundwater in the plane of water movement.

Instead of density distributions (vector

bundles) of the velocity fields, hydraulic seepage theory uses trivial (scalar) bundles obtained as cross-section-averaged distribution values (fluid flow rate and its average velocity instead of a velocity layer, flow instead of a streamline bundle). This theory is based on Dupuit equations for the mean rates of seepage and flow in steady-state problems [12]. This theory does not have the concepts of a discontinuous depression curve and a seepage area, since in this case the depression curve is smooth, i.e., differentiable at each point.

Implicit techniques are used to calculate the height of the seepage area at the boundaries of this region. For this reason, it is natural to use the stabilization problem for finding the solution of the unsteady Boussinesq problem in order to determine the shape of the depression curve and the fluid flow rate through the closing dike.

Depression curve

Dupuit's theory considers the seeping motion of water with an instantaneous mean velocity v , which, according to the Dupuit formula, is expressed as

$$v = kJ,$$

where k is the hydraulic conductivity ($k = \text{const}$

The Dupuit depression curve (see formula (1)) intersects the cross-section $s = 0$ at the elevation level $h = h_e$ ($u = u_e$) and the straight line $h = H$ ($u = 1$) in the cross-section $s = L$.

In other words, the following conditions are fulfilled on the Dupuit parabola (1):

a) no seepage area;

b) at the point $s = L, h = H$ (point C in Fig. 1), the Dupuit depression curve does not touch the straight line $h = H$ (the dashed line in Fig. 1), so this curve cannot be a streamline orthogonally intersecting the flow area $s = L$.

Both of these conditions have to be fulfilled for seepage flow to exist. This is precisely what the Dupuit paradox is.

Explaining the paradox by the singular character (singularity) of the point $s = L, h = H$ seems untenable.

In this study we propose an alternative scheme that explains the instantaneous configuration of the depression curve by the variable character of the instantaneous seepage rate over the length of the porous medium.

The explanation is as follows.

Let the seepage flow depth in a semi-enclosed body $s > 0$ filled with a porous medium be equal to H ($h = H$) before the initial time $t = 0$. At time $t = 0$, the fluid level in the tailwater $s < 0$ instantly drops from $h = H$ to $h = h_e$. The fluid starts to flow out of the porous

medium, where $s > 0$, to the tailwater, where $s < 0$. The depression curve is deformed (Fig. 2). Its initial length is equal to zero and increases with time. At any time $t > 0$, the left end of the depression curve intersects the vertical slope $s = 0$ on the ordinate $h = h_0$ (the h_0 value lies in the region $h_e < h_0 \leq H$), where $dh_0/dt < 0$, and the right end of this curve touches the straight line $h = H$ at the cross-section $s = L > 0$, with $dL/dt > 0$. The left end of the depression curve falls down at a rate $c_0 = -dh_0/dt$, and the right end touches the straight line $h = H$ at a velocity $c_\lambda = dL/dt$.

In other words, the depression curve acts as a flexible (deformable) impermeable “piston” that squeezes the fluid out of the porous medium by turning counterclockwise around the point $s = L, h = H$. If the right end of the depression curve reaches the cross-section $s = L_\infty$ (L_∞ is the length of the closing dike) at the time $t = t_\lambda$, further movement of the right end stops, the depression curve stabilizes (the semi-infinite closing dike is cut off by the abscissa $s = L_\infty$). Two possible scenarios can happen at this time at the left end of the depression curve:

1. The value $h_0 > h_e$, and a final discontinuity is formed at the left end of the depression curve (seepage area);
2. $h_0 \rightarrow h_e + 0$, and the seepage area is small.

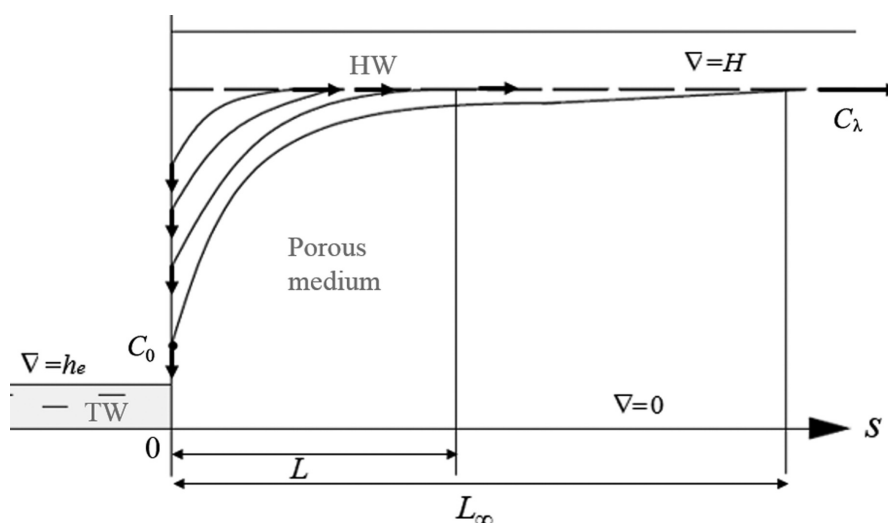


Fig. 2. The system under consideration, showing the deformation of the depression curve over time: its right end slides along the straight line $h = H$ from the tailwater (TW) to the highwater (HW), and the left slides down (L_∞ is the length of the closing dike); C_0, C_λ are the velocities of the left and right ends of the depression curve



The first case happens if the cut-out point does not have time to descend (fall) to the water level downstream. This is possible if the time T_{Δ} is small, the closing dike is short and the initial level difference $H - h_e$ is a finite value.

For the second case to happen, it is sufficient for the closing dike to be long and the initial difference of the levels $H - h_e$ to be small. Sufficient conditions for the existence of the seepage area correspond to the results of hydromechanical seepage theory.

Indeed, if other conditions are unchanged, the height of the seepage area is the greater, the shorter the closing dike. If the length of the closing dike is invariant, the height of the seepage area decreases together with the $H - h_e$ value, and the height of the seepage area $\Delta := h_0 - h_e$ for an infinitely thin closing dike is equal to $H - h_0$ ($\Delta = H - h_0$), i.e., $h_0 = H$.

Thus, we suggest to regard seepage through the closing dike as unsteady motion in the porous medium bounded by a moving (descending and stretching) depression curve.

If the motion of the depression curve stops, steady seepage develops.

The goal of the study is to determine the flow rate and the instantaneous shape of the depression curve under unsteady seepage through a rectangular closing dike.

The solutions of the Boussinesq limit problem

The Boussinesq equation of unsteady seepage has to be integrated to calculate the integral characteristics of seepage (the flow rate, the height of the seepage area, and the shape of the depression curve). For plane one-dimensional flow, the continuity condition is fulfilled:

$$\frac{\partial h}{\partial t} + \frac{\partial}{\partial s}(vh) = 0.$$

It is assumed that the Dupuit formula

$$v = -k \cdot \partial h / \partial s$$

is valid for unsteady motion, and the equality

$$\frac{\partial h}{\partial t} = \frac{\partial}{\partial s} \left(k \frac{\partial h}{\partial s} \right) \quad (2)$$

is satisfied in this case.

Eq. (2) is considered in the region

$0 < s < L \leq L_{\infty}$, $t > 0$, and the boundary conditions have the form

$$h(0, s) - H = h(t, 0) - h_0 = \left(\frac{\partial h}{\partial s} \right)_{s=0} = 0. \quad (3)$$

If we start using dimensionless coordinates

$$u := h / H, u_e < u_0 < u < 1,$$

$$\tau = kt / H > 0, \sigma = s / H, 0 < \sigma < \lambda \leq \lambda_{\infty},$$

$$\lambda := L / H, \lambda_{\infty} = L_{\infty} / H,$$

then we obtain, instead of Eq. (2), the equation

$$\frac{\partial u}{\partial \tau} = \frac{\partial}{\partial \sigma} \left(u \frac{\partial u}{\partial \sigma} \right), \quad (2a)$$

and, instead of boundary conditions (3), boundary conditions of the form

$$u(0, \sigma) - 1 = u(\tau, 0) - u_0(\tau) = \left(\frac{\partial u}{\partial \sigma} \right)_{\sigma=\lambda} = 0. \quad (3a)$$

Boundary problem (2a), (3a) can be complicated if we assume that the hydraulic conductivity is a function of the pressure head, for example,

$$k = k_0 f(u) / u$$

with an arbitrary function $f(u)$.

In this case, Eq. (2a) takes the form

$$\frac{\partial u}{\partial \tau} = \frac{\partial}{\partial \sigma} \left(f(u) \frac{\partial u}{\partial \sigma} \right). \quad (2b)$$

It can be proved that boundary problem (2b), (3a) is equivalent to the following typical Crocco boundary problem:

$$2\varphi \frac{d^2 \varphi}{du^2} + f(u) = 0, \varphi(u) := \int_u^1 \zeta dz, \zeta := \frac{\sigma}{2\sqrt{\tau}},$$

$$\mathfrak{D}(\varphi) = (u : u_0 < u < 1), \left(\frac{d\varphi}{du} \right)_{u=u_0} = \varphi(1) = 0.$$

The solutions of the typical Crocco boundary problem are known in terms of weak solutions (or weak approximations of solutions). For example, let $u_0 = 0$. Then we obtain that

$$\varphi^2(u) = \int_u^1 F(v) dv + \int_0^u \ln \frac{u}{v} \cdot F(v) dv - \int_0^1 \ln \frac{1}{v} F(v) dv,$$

where

$$F(u) := \int_0^u f(v)dv$$

is the antiderivative for $f(u)$.

In particular, if $f(u) = u$ (the classical case, the hydraulic conductivity is a constant), then it follows from the previous formula that

$$\varphi(u) = 1 / 3\sqrt{1 - u^3},$$

and then the following expression is obtained for the instantaneous depression curve:

$$\zeta := -\frac{d\varphi}{du} = \frac{u^2}{2\sqrt{1 - u^3}}. \quad (4)$$

Let $c = c(\tau, \sigma) := -\partial u / \partial \tau \geq 0$ be the descent rate of the depression curve and $c_0 = c(\tau, 0) := -du_0 / d\tau \geq 0$ the descent (falling) rate of the left end of this curve (in fractions of the hydraulic conductivity k).

Let us set the descent rate distribution of the depression curve along its length in the form of a binomial:

$$c(\tau, \sigma; \lambda) = c_0(\tau)(1 - \sigma / \lambda)^\alpha. \quad (4a)$$

Instead of Eq. (2a), taking into account expression (4a), we obtain the following equation:

$$\frac{d}{d\sigma} \left(u \frac{du}{d\sigma} \right) = -c_0(1 - \sigma / \lambda)^\alpha, \quad (2c)$$

whose solution has the form

$$\theta(\tau, \sigma) := u \frac{\partial u}{\partial \sigma} = \frac{c_0 \lambda}{\alpha + 1} (1 - \sigma / \lambda)^{\alpha+1}, \quad (5)$$

where $\theta = \theta(\tau, \sigma)$ is the dimensionless fluid flow (in fractions of kH^2/L).

The second integration leads to the expression

$$u^2 / 2 = u_0^2 / 2 + \frac{c_0 \lambda^2}{(\alpha + 1)(\alpha + 2)} \times (1 - (1 - \sigma / \lambda)^{\alpha+2}). \quad (5a)$$

Consequently, the instantaneous depression curve (5a) differs from the Dupuit parabola and coincides with the Dupuit parabola (1) for $\alpha = -1$

For the flow rate θ , we obtain, due to the solution of (5), the following expression:

$$\theta(\tau, \sigma) = \frac{1 - u_0^2}{2\lambda} (\alpha + 2)(1 - \sigma / \lambda)^{\alpha+1}. \quad (5b)$$

As a result, the flow rate varies from the maximum $\theta(\tau)$ value in the cross-section $\sigma = 0$ which is expressed as

$$\theta_0(\tau) := \theta(\tau, 0) = \frac{(\alpha + 2)(1 - u_0^2)}{2\lambda},$$

to zero in the cross-section $\sigma = \lambda$.

The mean flow rate $\theta_m(\tau)$ over the length of the closing dike, due to expression (5b), has the form

$$\theta_m(\tau) = \frac{1 - u_0^2}{2\lambda} \quad (6)$$

and coincides with the value of the Dupuit flow rate, if $u_0 = u_e$ and $\lambda = \Lambda$.

Thus, we have established that the mean flow rate does not depend on the value of the parameter α and formally coincides with the Dupuit flow rate.

The following technique is important for further calculations. Let us introduce the thickness of the seepage boundary layer as a thickness of a porous medium layer adjacent to the cross-section $\sigma = 0$ ($\zeta = 0$), where a finite change in the pressure is localized, namely, let δ be the thickness of the seepage boundary layer:

$$\delta = \frac{\lambda}{2\sqrt{\tau}}.$$

Therefore, by definition, the thickness of the seepage boundary layer is determined as follows:

$$\forall \zeta > \delta, \exists \varepsilon(\zeta) > 0 \Rightarrow 1 - \varepsilon < u < 1.$$

Fig. 3 shows the thickness of the seepage boundary layer for the case $u_0 > 0$.

So, according to the definition and using Crocco's equation, we obtain:

$$\begin{aligned} \delta &:= \int_0^\infty (1 - u) d\zeta = (1 - u_0)\lambda(\tau) = \\ &= \int_0^1 (1 - u)(-\varphi''(u)) du = \frac{1}{2} \int_0^1 \frac{f(u)(1 - u)}{\varphi(u)} du. \end{aligned}$$

It can be proved that the thickness of the seepage boundary layer $\delta < \infty$ for any summa-

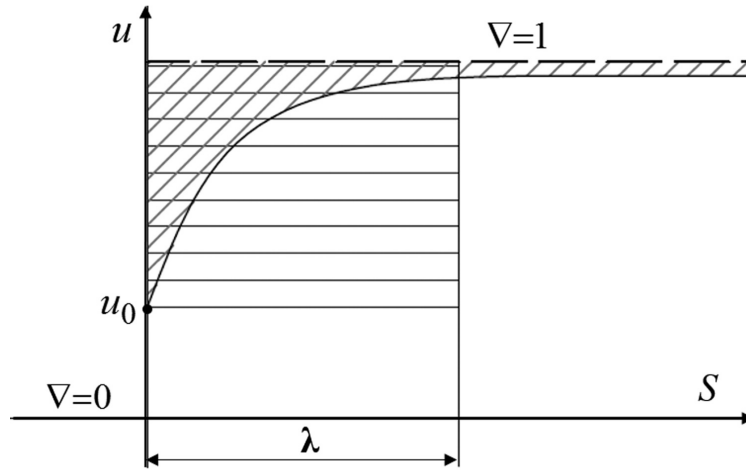


Fig. 3. Thickness of the seepage boundary layer λ (the shaded area between the dashed line and the depression curve is equal to the area of the rectangle with the sides $1 - u_0$ and λ);
 $u_0 = h_0/H$, $\lambda = L/H$ is the dimensionless length of the closing dike

ble and bounded function f . Hence, the dimensionless length of the closing dike

$$\lambda = 2\delta\sqrt{\tau} = a\sqrt{\tau}, a = O(1),$$

and then

$$\Lambda = a\sqrt{T_\Lambda}.$$

The constant a is bounded, i.e., $a = O(1)$, therefore, due to expression (6), the flow rate takes the form

$$\begin{aligned} \theta_m(\tau) &= \frac{1 - u_0^2}{2a\sqrt{\tau}} = \\ &= \frac{1 - (1 - c_0\tau)^2}{2a\sqrt{\tau}} \xrightarrow{\tau \rightarrow T_\Lambda} \frac{2c_0T_\Lambda - c_0^2T_\Lambda^2}{2\Lambda}. \end{aligned}$$

If $c_0 = 1/T_\Lambda$, this expression reaches maximum in the form

$$\theta_m(T_\Lambda) = \frac{1}{2\Lambda}, \quad (6a)$$

which coincides with the Dupuit flow rate.

Therefore, we can draw the following conclusions:

the mean instantaneous flow rate $\theta_m(\tau)$ over the length of the closing dike does not depend on the parameter α , i.e., on the instantaneous shape of the depression curve;

the limit expression (i.e., with $\tau \rightarrow T_\Lambda - 0$) for the mean flow rate over the length of the closing dike coincides with the Dupuit rate;

The Dupuit formula for flow rate is applicable only under conditions of steady-state seepage.

The main integral relations

The Dupuit equation (2a) implies an integral identity expressing the flow rate balance (the entire fluid forced out from the closing dike by the descending depression curve flows through the cross-section $s = 0$):

$$\frac{d}{d\tau} \int_0^\lambda (1 - u) d\sigma = \theta_0(\tau) = \frac{c_0\lambda}{\alpha + 1}. \quad (7)$$

Let us approximately suppose, somewhat overestimating the $\lambda(\tau)$ value, that

$$\int_0^\infty (1 - u) d\sigma = \frac{1 - u_0(\tau)}{2} \lambda(\tau).$$

Then we obtain a simple equation for λ^2 :

$$\frac{d\lambda^2}{d\tau} = n(1 + u_0), n(\alpha) = (1 - \alpha)(2 + \alpha) > 0, \quad (8)$$

$$-2 < \alpha < 1,$$

where $\lambda(0) = 0$.

The value of the parameter $n(\alpha)$ varies from zero at $\alpha = 1, -2$ to the maximum value $n = 9/4$ at $\alpha = -1/2$; the arithmetic mean of $n(\alpha)$ is $3/2$.

Then solution (8) takes the following form:

$$\lambda^2(\tau) = n(\alpha) \left(2\tau - \int_0^\tau c_0(\omega)(\tau - \omega) d\omega \right). \quad (9)$$

Let $\lambda = \Lambda$, then the quantity τ reaches the value $\tau = T_\Lambda$. Due to expression (9), the parameters Λ, T_Λ and the velocity $c_0(\tau)$ are related by the following condition:

$$\Lambda^2 = n(\alpha) \left(2T_\Lambda - \int_0^{T_\Lambda} c_0(\tau)(T_\Lambda - \tau) d\tau \right); \quad (9a)$$

and if $u_0 = u_e$, then $\tau = T_\Lambda$.

Consequently,

$$1 - u_e - \int_0^{T_\Lambda} c_0(\tau) d\tau = 0. \quad (9b)$$

Obviously, $c_0 \leq 1$; then we obtain the following from formulae (9a), (9b), respectively:

$$\begin{aligned} \Lambda^2 / n &= 2T_\Lambda - 1 / 2T_\Lambda^2, T_\Lambda = 2 - \sqrt{4 - \frac{2\Lambda^2}{n}}, \\ T_\Lambda &= 2 \left(1 - \sqrt{1 - \frac{\Lambda^2}{2n}} \right) = \frac{\Lambda^2}{2n}, \\ T_\Lambda &= 1 - u_e \leq 1, \end{aligned} \quad (10)$$

and then, due to expression (6a), the limit value of the mean flow rate over the length of

the closing dike takes the form

$$\lim_{\tau \rightarrow T_\Lambda} \theta_m = \frac{2}{\Lambda} - \sqrt{\frac{4}{\Lambda^2} - \frac{2}{n}} \leq \frac{\Lambda}{2n} = \frac{1 - u_0^2(T_\Lambda)}{2\Lambda}.$$

For the final expression, the ordinates of the left end of the depression curve are:

$$u_0(T_\Lambda) = \sqrt{1 - \Lambda^2 / n}. \quad (6b)$$

Formulae (10) make sense if the inequality

$$\Lambda \leq \sqrt{2n} \leq \sqrt{9/2} = 2.121$$

holds true.

Otherwise, the closing dike is assumed to be long, i.e., $T_\Lambda = \infty$, and $u_0 \rightarrow u_e + 0$.

If $\Lambda \ll 1$, then

$$T_\Lambda = \frac{\Lambda^2}{2n} < T_\Lambda = 1 - u_e.$$

Therefore, the right end of the depression curve in a short closing dike reaches the headwater level faster than the cut-out point of the depression curve falls to the tailwater level.

Let $\tau = T_\Lambda = \Lambda^2 / (2n)$, and then the following expression holds true:

$$u_0(T_\Lambda) = 1 - \Lambda^2 / (2n),$$

$$\Delta(T_\Lambda) := u_0(T_\Lambda) - u_e = 1 - u_e - \Lambda^2 / (2n).$$

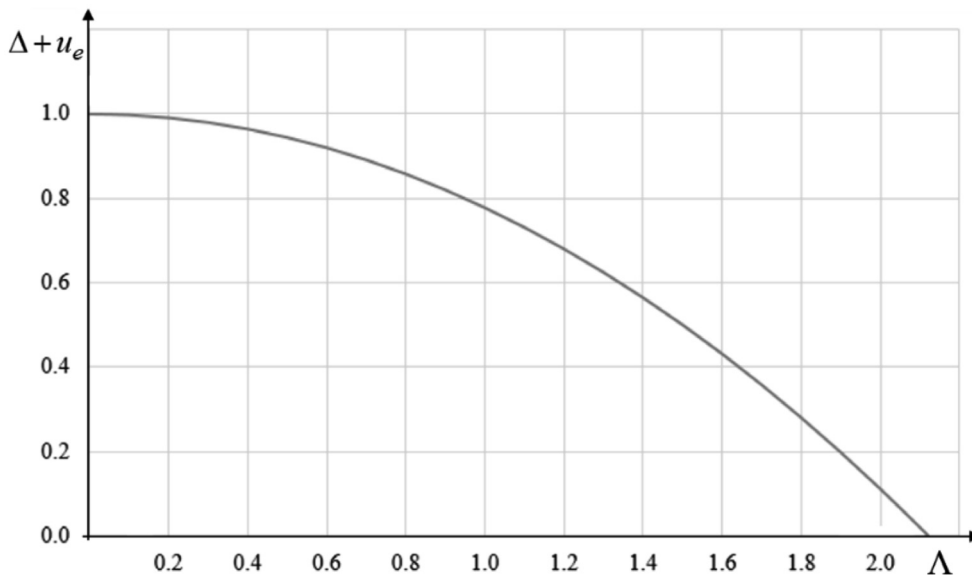


Fig. 4. Dependence of the height of the seepage area Δ on the length of the closing dike $\Lambda = L_\infty / H$ with a fixed level of u_e



Finally, we obtain the formula

$$\Delta = 1 - u_e - \Lambda^2 / (2n) = 1 - u_e - 2 / 9\Lambda^2.$$

Let $\Lambda \rightarrow +0$, then $\Delta = 1 - u_e$. The graph of function $\Delta = \Delta(\Lambda)$ is shown in Fig. 4. We assume that $\Delta = 0$ for the value $\Lambda > (9 / 2)^{1/2}$.

We should note that it is possible to improve the estimates. Namely, since solution (9) is valid, we have:

$$\lambda^2 = n(2\tau - \tau^2 / 2). \quad (11)$$

Let $\tau = 2 = T_\Lambda$. Then the length λ of the closing dike reaches its maximum value $\lambda = \Lambda$, while $\Lambda^2 = 2n = 9 / 2$. This Λ estimate coincides with the previous one. If we formally set $T_\Lambda = 2$ in formula (11), then we obtain that $\Lambda^2 = 4n = 9$.

So, the closing dike is considered to be long if

$$9 / 2 < \Lambda^2 < 9, \text{ i.e., } 2,12 < \Lambda < 3,00,$$

and the mean value of $\Lambda = 2,52$. These estimates are close to the ones obtained in hydro-mechanical theory, where with $\Lambda \approx 2,7, \dots, 2,8$, the seepage area disappears for nearly all values of u_e [12, 16].

Conclusions

The following conclusions can be drawn

[1] **E.V. Gubkina, V.N. Monakhov**, Filtration of a liquid with free boundaries in unbounded regions, *J. Appl. Mech. Tech. Phys.* 41 (5(243)) (2000) 930–936.

[2] **V.M. Margolin**, Study of key parameters of impervious structures, *Industrial and Civil Engineering.* (12) (2014) 73–76.

[3] **D.V. Purgina, L.A. Strokova, K.I. Kuzevanov**, Modeling hydrogeological conditions for antilandslide measures justification on the plot of the Kama river embankment in Perm, *Bulletin of the Tomsk Polytechnic University, Geo Assets Engineering.* 327 (1) (2016) 116–127.

[4] **A.K. Strelkov, D.Yu. Teplykh, N.S. Bukhman, A.M. Sargsyan**, Analysis and specifications of filtration of surface runoff from railway track ballast section, *Water Supply and Sanitary Technique.* (12) (2015) 63–72.

[5] **V.V. Terleev, A. Nikonorov, I. Togo, et al.**, Nysteretic water-retention capacity of sandy soil, *Magazine of Civil Engineering.* (2 (70)) (2017) 84–92.

[6] **V.T. Orlov, O.I. Zaytsev, E.A. Loktionova,**

based on determining the flow rate and the shape of the depression curve under seepage through a rectangular closing dike:

the height of the seepage area Δ is uniquely determined by the length of the closing dike. The height of the seepage area in a short closing dike, when $\Delta = 1 - u_e$, is determined only by the upstream water level;

the seepage area stabilizes during the time $T_\Lambda = O(\Lambda^2)$, so in a short closing dike this time is less than the time T_Λ that it takes for the cut-out point to fall downstream, i.e., $T_\Lambda < T_\Lambda$;

the cut-out point in a long closing dike succeeds in falling downstream in time T_Λ shorter than the time T_Λ that it takes for the right end of the depression to touch the top-water;

the height of the seepage area monotonically decreases during stabilization from the value $1 - u_e$ at the time $\tau = 0$ to the value $\Delta(T_\Lambda) \geq 0$.

The proposed alternative scheme explaining the instantaneous configuration of the depression curve by the variable nature of unsteady seepage flow along the porous medium is fully justified and allows to obtain new important results, in particular, the seepage area, the instantaneous local and mean seepage flow.

REFERENCES

Assessment of pollution area's sizes natural ground waters infiltration stream, *Construction of Unique Buildings and Structures.* 2013. (6 (11)) (2013) 28–33.

[7] **Yu.M. Kosichenko**, Razvitiye issledovaniy v oblasti primeneniya novykh materialov dlya protivofiltratsionnykh tseley [The progress of studies in advance materials applications for impervious purpose], *Puti povysheniya effektivnosti oroshayemogo zemledeliya* [The ways for improving the efficiency of irrigated farming]. (58-2) (2015) 21–27.

[8] **A.V. Ishchenko, A.S. Sokolov**, Gidravlicheskaya model vodopronitsayemosti betonoplenochnogo protivofiltratsionnogo pokrytiya kanala [A hydraulic model of the water permeability of a concrete-film impervious coating of a canal], *In: Melioratsiya i vodnoye khozyaystvo. Materialy nauchno-prakticheskoy konferentsii* [Reclamation and water industry, Conference proceedings] (2016) 73–77.

[9] **A.A. Kuvayev, I.S. Pashkovsky, S.P.**

Pozdnyakov, A.A. Roshal, V.M. Shestakov and the development of modern hydrogeodynamic ideas, Moscow University Geology Bulletin. (1) (2009) 54–58.

[10] **S.V. Solsky, D.P. Samofalov, E.V. Bulganin, E.P. Semanina**, Justification of the method to assess the parameters of ablation of the slopes of deep pits, Bull. of B.E. Vedeneev VINIG. (278) (2015) 95–106.

[11] **Yu.M. Brumshteyn**, Analysis of possible approaches to methods of computer modelling for some special geofiltration problems, Izvestiya Volgogradskogo gosudarstvennogo tekhnicheskogo universiteta. 2014. 22 (25 (152)) 5–11.

[12] **A.D. Girgidov**, The time of groundwater free surface lowering before foundation pit construction, Magazine of Civil Engineering. (4(30)) (2012) 52–56.

[13] **V.A. Podolsky**, Primneniye metoda konechnykh elementov dlya resheniya profilnoy zadachi rascheta izmeneniya polozheniya depressionnoy krivoy [An application of the finite element method to a solution of a profile problem on a changing position of a depression curve], Gornyy informatsionno-analiticheskiy byulleten (nauchno-tekhnicheskii zhurnal) [The Mining Informational-Analytical Bulletin]. (4) (2007) 58–60.

[14] **A.A. Afonin**, Matematicheskoye

modelirovaniye realnykh nelineynykh zadach filtratsii so svobodnoy granitsey [Mathematical simulation of real nonlinear problems on filtration with a free boundary], Izvestiya YuFU. Tekhnicheskiiye nauki. 2006. (3 (58)) (2006) 260–264.

[15] **V.A. Podolsky**, Raschet polozheniya svobodnoy poverkhnosti pri nestatsionarnoy filtratsii metodom konechnykh elementov [The calculation of a free surface position in the non-stationary filtration using the finite element method], Gornyy informatsionno-analiticheskiy byulleten (nauchno-tekhnicheskii zhurnal) [The Mining Informational-Analytical Bulletin]. (4) (2007) 63–67.

[16] **M.E. Memarianfard, N.A. Aniskin**, Raschet filtratsii v gruntovykh plotinakh i osnovaniyakh s uchetom anizotropii [The calculation of filtration in the earth dams and bases with allowance for anisotropy], Vestnik MGSU. (S1) (2009) 125–128.

[17] **P.S. Chagirov, V.V. Kadet**, A New method for determining the applicability of the Darcy law, Vestnik Nizhegorodskogo universiteta im. N.I. Lobachevskogo. (4-3) (2011) 1243–1244.

[18] **V.V. Kadet, A.A. Maksimenko**, Printsipy analiticheskogo opisaniya techeniya zhidkosti v reshetochnykh modelyakh poristyykh sred [Principles of analytical description of a flow in lattice models of porous media], Fluid Dynamics. 35 (1) (2000) 79–83.

Received 12.02.2018, accepted 01.03.2018.

THE AUTHORS

ZABOROVA Dariya D.

Peter the Great St. Petersburg Polytechnic University
29 Politechnicheskaya St., St. Petersburg, 195251, Russian Federation
zaborova-dasha@mail.ru

PETRITCHENKO Mikhail R.

Peter the Great St. Petersburg Polytechnic University
29 Politechnicheskaya St., St. Petersburg, 195251, Russian Federation
fonpetrich@mail.ru

MUSORINA Tatiana A.

Peter the Great St. Petersburg Polytechnic University
29 Politechnicheskaya St., St. Petersburg, 195251, Russian Federation
flamingo-93@mail.ru

DIRECT AND INVERSE PROBLEMS FOR A WAVE EQUATION WITH DISCONTINUOUS COEFFICIENTS

D.S. Anikonov, D.S. Konovalova

Sobolev Institute of Mathematics, Novosibirsk, Russian Federation

The present article is devoted to the studies in solutions of partial differential equations with discontinuous coefficients for the highest derivatives. This line of investigation is not only of purely academic interest for mathematicians, but plays an important part in the theory of sounding of unknown media composed of various substances. The direct and inverse problems have been considered. The theorem of existence and of the solution-uniqueness was proved for the first of them. For inverse problems, the uniqueness of the solution was proved.

The integro-differential equation, which is a consequence of the physical laws, was used for solving the direct problem in the derivation of formulae. The meaning of the inverse problems lies in determination of a junction point of different materials and a wave velocity. The used nature of the proof allows us to construct an appropriate numerical algorithm.

Key words: differential equation; discontinuous coefficient; sounding of unknown media; direct and inverse problems

Citation: D.S. Anikonov, D.S. Konovalova, Direct and inverse problems for a wave equation with discontinuous coefficients, St. Petersburg State Polytechnical University Journal. Physics and Mathematics. 11 (2) (2018) 59 – 68. DOI: 10.18721/JPM.11206

Introduction

To date, partial differential equations with discontinuous coefficients have not been sufficiently studied. Yet, a number of works have been dedicated to this subject [1 – 12].

In this study, we consider a half-plane

$$R_2^+ = ((x, t), -\infty < x < \infty, t > 0)$$

with the Cauchy problem:

$$\alpha(x) \frac{\partial^2 U(x, t)}{\partial t^2} - \beta(x) \frac{\partial^2 U(x, t)}{\partial x^2} = f(x, t), \quad (1)$$

$$(x, t) \in R_2^+, \alpha(x), \beta(x) > 0,$$

$$U(x, 0) = \varphi(x), U_t(x, 0) = \psi(x). \quad (2)$$

We assume that the function $\varphi(x)$ has continuous derivatives up to and including the second order, while $\psi(x)$ has a continuous first derivative. The function $f(x, t)$ has continuous first-order partial derivatives with $(x, t) \in R_2^+$.

The direct problem (1), (2) consists

in finding $U(x, t)$ for the given functions $\alpha(x), \beta(x), \varphi(x), \psi(x), f(x, t)$. Its physical meaning is in describing the process of transverse vibrations of a string or longitudinal vibrations of a rod.

The solution of this problem for constant values of α and β is well-known and is represented by d'Alembert's formula. We consider the case of discontinuous coefficients $\alpha(x), \beta(x)$, which corresponds to a string or a rod composed of different materials.

In the particular case when $f = 0$, our results for the direct problem are similar to those presented in [8, 9]. Refs. [10 – 12] also contain various generalizations of d'Alembert's formula. In our study, we use only [10, pp. 75 – 77], where a problem of type (1), (2) is written in the form of an integro-differential equation for a generalized solution in the class of piecewise smooth functions. As for the inverse problems described in this paper, so far we have been unable to uncover similar results by other authors.

While this study contains a substantial amount of cumbersome calculations, we formulate only the fundamental ones in detail, and confine ourselves to outlining the corresponding analysis schemes for other similar actions.

Notations, definitions and direct problem statement

In Eq. (1), functions $\alpha(x), \beta(x)$ are assumed to be piecewise constant, that is,

$$\alpha(x) = \alpha_1, \beta(x) = \beta_1, \quad x < x_0;$$

$$\alpha(x) = \alpha_2, \beta(x) = \beta_2, \quad x \geq x_0,$$

where x_0 is a fixed number; $\alpha_i, \beta_i \quad i=1,2$, are positive numbers.

We will use the following notations below:

$$\gamma_i = \sqrt{\alpha_i \beta_i}, \quad a_i = \sqrt{\beta_i} / \sqrt{\alpha_i},$$

$$i = 1, 2, \quad a(x) = \sqrt{\beta(x)} / \sqrt{\alpha(x)}.$$

The notation $\partial_1 \omega(x, t), \partial_2 \omega(x, t)$ will be used for first derivatives of an arbitrary function $\omega(x, t)$ with respect to x and t in addition to the traditional notation. The left-hand side of Eq. (1) is denoted as $LU(x, t)$ in short.

Let us select the following subsets in the half-plane R_2^+ : G_1 is the domain between the straight lines $t = 0$ and $x = x_0 - a_1 t$; G_2 is the domain between the straight lines $t = 0$ and $x = x_0 + a_2 t$; G_3 is the domain between the straight lines $x = x_0 + a_2 t$ and $x = x_0$; G_4 is the domain between the straight lines $x = x_0$ and $x = x_0 - a_1 t$; $G_0 = G_1 \cup G_2 \cup G_3 \cup G_4$.

Let us write the coupling conditions for the boundaries between the domains $G_i, i = 1, \dots, 4$:

$$\lim_{x \rightarrow x_0 - 0} \partial_2 U(x, t) = \lim_{x \rightarrow x_0 + 0} \partial_2 U(x, t), \quad (3)$$

$$\lim_{x \rightarrow x_0 - 0} \beta_1 \partial_1 U(x, t) = \lim_{x \rightarrow x_0 + 0} \beta_2 \partial_1 U(x, t), \quad (4)$$

$$\{\partial_2 U(x, t) - a_1 \partial_1 U(x, t)\} = 0, \quad x = x_0 - a_1 t, \quad (5)$$

$$\{\partial_2 U(x, t) + a_2 \partial_1 U(x, t)\} = 0, \quad x = x_0 + a_2 t. \quad (6)$$

The braces in conditions (5), (6) and below denote the jumps of the functions at the boundary points, when the limit value for $(x, t) \in G_i$ is obtained by subtracting the limit value of the same function at $(x, t) \in G_j, i > j$. Below we shall establish that conditions (3) – (6) are a

consequence of Hooke’s law and the law of conservation of momentum.

The solution of problem (1), (2) is sought in the class of functions that are continuous in R_2^+ and piecewise smooth, such that $U(x, t)$ has in G_0 all partial derivatives up to and including the second order, uniformly continuous at the intersection of each domain $G_i, i = 1, \dots, 4$ with a circle of any radius and a center at the origin. Let us regard a function of this class as a generalized solution of problem (1), (2) if it satisfies Eq. (1) in G_0 and conditions (2) – (6).

Below, we use curvilinear integrals of the second kind only. The notation (PQ) is used for a curve starting at point P and ending at point Q . If the curve is the boundary of a simply-connected bounded domain, the orientation adopted is such that the domain is located on the left for a point moving along the curve.

Let us agree to denote the current points of the domains $G_i, i = 1, \dots, 4$ as $M_i = (x, t)$ and construct the following scheme. Taking an arbitrary point $M_1 = (x, t) \in G_1$ and using the current variables (ξ, τ) , we draw through M_1 two straight lines:

$$\xi - x = a_1(\tau - t),$$

$$\xi - x = -a_1(\tau - t).$$

The first line intersects the horizontal axis of the coordinate system at point $A_1 = (0, x - a_1 t)$, and the second at point $B_1 = (0, x + a_2 t)$. The triangle with the vertices A_1, M_1, B_1 is denoted as $G(M_1)$. Similarly, for an arbitrary point $M_2 = (x, t) \in G_2$ let us use straight lines

$$\xi - x = a_2(\tau - t),$$

$$\xi - x = -a_2(\tau - t)$$

and obtain points

$$A_2 = (0, x - a_2 t), \quad B_2 = (0, x + a_2 t)$$

and a triangle $G(M_2)$.

Construction is more complicated in domains G_3, G_4 . Let $M_3 = (x, t) \in G_3, X_0 = (x_0, 0)$ (Fig. 1). Let us consider the straight lines

$$\xi - x = -a_2(\tau - t),$$

$$\xi - x = a_2(\tau - t).$$

The first line intersects the Ox axis at point $B_3 = (0, x + a_2 t)$ and the second intersects

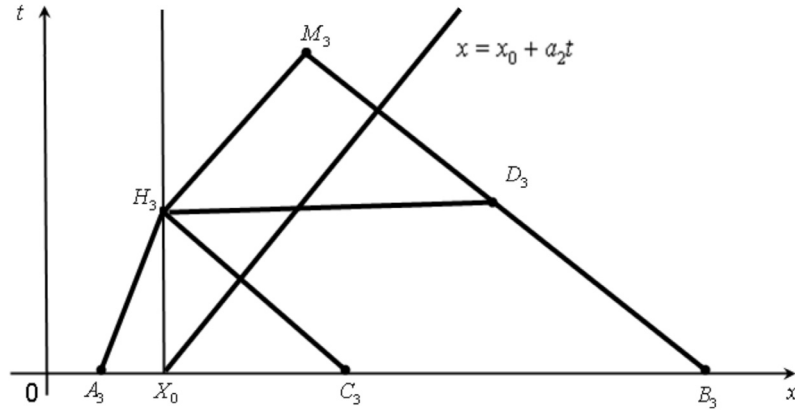


Fig. 1. Illustration to constructing the function $U(x, t)$ for an arbitrary point $M_3 = (x, t) \in G_3$

the line $\xi = x_0$ at point $H_3 = (x_0, h_3)$, where $h_3 = t - (x - x_0)/a_2$. Next, we draw through point H_3 a straight line

$$\xi - x_0 = a_1(\tau - h_3),$$

intersecting the Ox axis at point $A_3 = (0, x_0 - a_1 h_3)$.

The quadrangle with the vertices A_3, H_3, M_3, B_3 is denoted as $G(M_3)$. We draw a horizontal line from point H_3 , intersecting the line

$$\xi - x = -a_2(\tau - t)$$

at point $D_3 = (2x - x_0, h_3)$.

In addition, we draw a line

$$\xi - x_0 = -a_2(\tau - h_3),$$

intersecting the Ox axis at point $C_3 = (0, x_0 + a_2 h_3)$.

The triangle with the vertices A_3, C_3, H_3 is denoted as $G(H_3)$. The construction is similar in domain G_4 for an arbitrary point $M_4 = (x, t) \in G_4$ (Fig. 2). Namely, we use lines

$$\xi - x = a_1(\tau - t),$$

$$\xi - x = -a_1(\tau - t).$$

The first line intersects the Ox axis at point $A_4 = (0, x - a_1 t)$ and the second one intersects the line $\xi = x_0$ at point $H_4 = (x_0, h_4)$, where $h_4 = t + (x - x_0)/a_1$.

Next, we draw through point H_4 a straight line

$$\xi - x_0 = -a_2(\tau - h_4),$$

intersecting the Ox axis at point $B_4 = (0, x_0 + a_2 h_4)$. The quadrangle with the vertices A_4, M_4, H_4, B_4 is denoted as $G(M_4)$. In addition, we draw a line

$$\xi - x_0 = a_1(\tau - h_4),$$

intersecting the Ox axis at point $C_4 = (0, x_0 - a_1 h_4)$. The triangle with the vertices C_4, H_4, B_4 is denoted as $G(H_4)$.

The existence and uniqueness of the solution for the direct problem

Let us denote the values of the function $U(x, t)$ in G_i as $U_i(x, t)$, $i = 1, \dots, 4$.

Theorem 1. *Under all the assumptions made, there exists a unique generalized solution of problem (1), (2), represented by formulae*

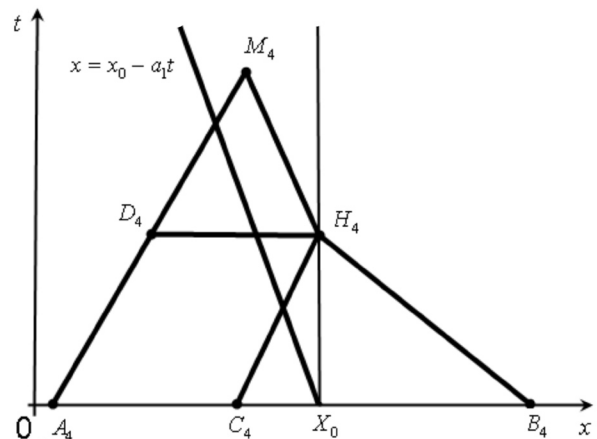


Fig. 2. Illustration to constructing the function $U(x, t)$ for an arbitrary point $M_4 = (x, t) \in G_4$

$$U_i(M_i) = \frac{U(A_i) + U(B_i)}{2} + \int_G f(\xi, \tau) d\xi d\tau = 0. \quad (10)$$

$$+ \frac{1}{2\gamma_i} \int_{(A_i B_i)} \alpha_i \psi(\xi) d\xi + \frac{1}{2\gamma_i} \int_{G(M_i)} f(\xi, \tau) d\xi d\tau, \quad (7)$$

$$i = 1, 2,$$

$$U_3(M_3) = \frac{1}{2} \left[\frac{2\gamma_1}{\gamma_1 + \gamma_2} U(A_3) + U(B_3) + \frac{\gamma_2 - \gamma_1}{\gamma_1 + \gamma_2} U(C_3) \right] +$$

$$+ \frac{1}{2\gamma_2} \left[\frac{\gamma_2 - \gamma_1}{\gamma_1 + \gamma_2} \int_{(A_3 B_3)} \alpha(\xi) \psi(\xi) d\xi + \int_{(A_3 B_3)} \alpha(\xi) \psi(\xi) d\xi \right] + \frac{1}{2\gamma_2} \left[\frac{\gamma_2 - \gamma_1}{\gamma_1 + \gamma_2} \times \right.$$

$$\left. \times \int_{G(H_3)} f(\xi, \tau) d\xi d\tau + \int_{G(M_3)} f(\xi, \tau) d\xi d\tau \right]; \quad (8)$$

$$U_4(M_4) = \frac{1}{2} \left[\frac{2\gamma_1}{\gamma_1 + \gamma_2} U(A_4) + U(B_4) + \frac{\gamma_1 - \gamma_2}{\gamma_1 + \gamma_2} U(C_4) \right] +$$

$$+ \frac{1}{2\gamma_1} \left[\frac{\gamma_1 - \gamma_2}{\gamma_1 + \gamma_2} \int_{(A_4 B_4)} \alpha(\xi) \psi(\xi) d\xi + \int_{(A_4 B_4)} \alpha(\xi) \psi(\xi) d\xi \right] + \frac{1}{2\gamma_1} \left[\frac{\gamma_1 - \gamma_2}{\gamma_1 + \gamma_2} \times \right.$$

$$\left. \times \int_{G(H_4)} f(\xi, \tau) d\xi d\tau + \int_{G(M_4)} f(\xi, \tau) d\xi d\tau \right]. \quad (9)$$

Proof. The theorem is proved in three stages

1. *Obtaining formulae (7) – (9).* We should note that the solution in domains G_1 and G_2 is given by d'Alembert's classical formula. Now let us focus on domain G_3 . A problem coinciding in meaning with problem (1), (2) was considered in [10, pp. 75 – 77], but under different restrictions. Namely, an integro-differential equation with respect to the function $u(x, t)$ was studied instead of Eq. (1):

$$\int_{\partial G} \alpha(\xi) \partial_2 u(\xi, \tau) d\xi + \beta(\xi) \partial_1 u(\xi, \tau) d\tau + \quad (10)$$

Additionally, the initial conditions are given:

$$u(x, 0) = \varphi(x), \quad u_t(x, 0) = \psi(x). \quad (11)$$

G in equality (10) is an arbitrary bounded simply-connected domain in R_2^+ , and its boundary ∂G is a piecewise smooth curve of class C^1 . The function $u(x, t)$ is continuous in R_2^+ , and its partial derivatives $\partial_1 u(x, t)$, $\partial_2 u(x, t)$, are piecewise continuous with possible discontinuities of the first kind on certain lines. In this case, discontinuities are allowed within G and it is also possible that the line of discontinuities coincides with a part of ∂G , and then the derivatives $\partial_1 u(\xi, \tau)$, $\partial_2 u(\xi, \tau)$ are substituted in Eq. (10) by their limit values within domain G . We should note that Eq. (10) is a consequence of Hooke's law and the law of conservation of momentum. Accordingly, the conclusions obtained from (10) are also a consequence of these laws.

Let us take an arbitrary point $M_3 = (x, t) \in G_3$ and use Eq. (10) with respect to quadrangle $G(M_3)$ (see Fig. 1). The curvilinear integrals along the lines $(M_3 H_3)$, $(H_3 A_3)$, $(A_3 B_3)$, $(B_3 M_3)$ are denoted, respectively, as I_1, I_2, I_3, I_4 . Via direct and simple calculations, we obtain the equalities

$$I_1 = \gamma_2(u(H_3) - u(M_3)),$$

$$I_2 = \gamma_1(u(A_3) - u(H_3)),$$

$$I_3 = \int_{(A_3 B_3)} \alpha(\xi) \psi(\xi) d\xi, \quad I_4 = \gamma_2(u(B_3) - u(M_3)).$$

Additionally, let us use equality (10) for triangle $G(H_3)$. Let us denote the curvilinear integrals along the lines $(H_3 A_3)$, $(A_3 C_3)$, $(C_3 H_3)$ as J_1, J_2, J_3 and, similar to the above, we have:

$$J_1 = \gamma_1(u(A_3) - u(H_3)), \quad J_2 = \int_{(A_3 C_3)} \alpha(\xi) \psi(\xi) d\xi,$$

$$J_3 = \gamma_2(u(C_3) - u(H_3)).$$

Next, we use equality (10) for $G(M_3)$ and $G(H_3)$, and taking into account the calculations for $I_1, I_2, I_3, I_4, J_1, J_2, J_3$, we obtain for $u(M_3)$ the expression coinciding with the right-

hand side of the equality for $U_3(M_3)$. Identifying $u(x,t)$ with $U_3(x,t)$, we obtain formula (8). $U_4(x,t)$ is obtained in much the same way. In this case, quadrangle $G(M_4)$ and triangle $G(H_4)$ are used in equality (10).

2. *Existence of a solution for the direct problem.* Let us calculate the limits for $U(x,t)$ with the arguments tending to points on the lines

$$x - x_0 = a_2 t, \quad x - x_0 = -a_1 t, \quad x = x_0.$$

If we use the expressions for $A_i, B_i, C_i, H_i, i = 1, \dots, 4$, via (x,t) , it is evident that the limits of the functions $U_i(x,t)$ coincide at these points, i.e., the function $U(x,t)$ represented by formulae (7) – (9) is continuous in R_2^+ .

Now let us verify that $U_i(x,t)$ satisfy Eq. (1) in $G_i, i = 1, \dots, 4$. We should note that this does not have to be verified for functions $U_1(x,t)$ and $U_2(x,t)$, as they are represented by d'Alembert's classical formulae, which also means that conditions (2) are satisfied for $U(x,t)$. It is convenient for us to examine separate parts of formula (8),

$$U_3(x,t) = U_{3,\varphi}(x,t) + U_{3,\psi}(x,t) + U_{3,f}(x,t),$$

where

$$U_{3,\varphi}(x,t) = \frac{1}{2} \left[\frac{2\gamma_1}{\gamma_1 + \gamma_2} \varphi(x_0 - a_1 h_3) + \varphi(x + a_2 t) + \frac{\gamma_2 - \gamma_1}{\gamma_1 + \gamma_2} \varphi(x_0 + a_2 h_3) \right],$$

$$h_3 = t - (x - x_0) / a_2, \quad (x,t) \in G_3; \quad (12)$$

$$U_{3,\psi}(x,t) = \frac{1}{2\gamma_2} \left[\frac{\gamma_2 - \gamma_1}{\gamma_1 + \gamma_2} \int_{(A_3 C_3)} \alpha(\xi) \psi(\xi) d\xi + \int_{(A_3 B_3)} \alpha(\xi) \psi(\xi) d\xi \right]; \quad (13)$$

$$U_{3,f}(x,t) = \frac{1}{2\gamma_2} \left[\frac{\gamma_2 - \gamma_1}{\gamma_1 + \gamma_2} \int_{G(H_3)} f(\xi, \tau) d\xi d\tau + \int_{G(M_3)} f(\xi, \tau) d\xi d\tau \right]. \quad (14)$$

Let us calculate the derivatives of the function $U_{3,\varphi}(x,t)$:

$$\begin{aligned} \frac{\partial U_{3,\varphi}(x,t)}{\partial t} &= \\ &= \frac{1}{2} \left[\frac{-2\gamma_1 a_1}{\gamma_1 + \gamma_2} \varphi'(x_0 - a_1 h_3) + a_2 \varphi'(x + a_2 t) + \frac{\gamma_2 - \gamma_1}{\gamma_1 + \gamma_2} a_2 \varphi'(x_0 + a_2 h_3) \right], \end{aligned} \quad (15)$$

$$\begin{aligned} \frac{\partial^2 U_{3,\varphi}(x,t)}{\partial t^2} &= \\ &= \frac{1}{2} \left[\frac{2\gamma_1 a_1^2}{\gamma_1 + \gamma_2} \varphi''(x_0 - a_1 h_3) + a_2^2 \varphi''(x + a_2 t) + \frac{\gamma_2 - \gamma_1}{\gamma_1 + \gamma_2} a_2^2 \varphi''(x_0 + a_2 h_3) \right]; \end{aligned} \quad (16)$$

$$\begin{aligned} \frac{\partial U_{3,\varphi}(x,t)}{\partial x} &= \\ &= \frac{1}{2} \left[\frac{2\gamma_1 a_1}{(\gamma_1 + \gamma_2) a_2} \varphi'(x_0 - a_1 h_3) + \varphi'(x + a_2 t) - \frac{\gamma_2 - \gamma_1}{\gamma_1 + \gamma_2} \varphi'(x_0 + a_2 h_3) \right]; \end{aligned} \quad (17)$$

$$\begin{aligned} \frac{\partial^2 U_{3,\varphi}(x,t)}{\partial x^2} &= \\ &= \frac{1}{2} \left[\frac{2\gamma_1 a_1^2}{(\gamma_1 + \gamma_2) a_2^2} \varphi''(x_0 - a_1 h_3) + \varphi''(x + a_2 t) + \frac{\gamma_2 - \gamma_1}{\gamma_1 + \gamma_2} \varphi''(x_0 + a_2 h_3) \right]. \end{aligned} \quad (18)$$

Using equalities (16), (18), we write

$$\begin{aligned} LU_{3,\varphi}(x,t) &= \\ &= \varphi''(x_0 - a_1 h_3) \left[\frac{\gamma_1 a_1^2 \alpha_2}{\gamma_1 + \gamma_2} - \frac{\gamma_1 a_1^2 \beta_2}{(\gamma_1 + \gamma_2) a_2^2} \right] + \\ &+ \varphi''(x + a_2 t) \left[\frac{a_2^2 \alpha_2}{2} - \frac{\beta_2}{2} \right] + \\ &+ \varphi''(x_0 + a_2 h_3) \left[\frac{a_2^2 \alpha_2 (\gamma_2 - \gamma_1)}{2(\gamma_1 + \gamma_2)} - \frac{\beta_2 (\gamma_2 - \gamma_1)}{2(\gamma_1 + \gamma_2)} \right]. \end{aligned}$$

It is easy to verify that all the expressions in square brackets on the right-hand side of the last equality are equal to zero, i.e., $LU_{3,\varphi}(x,t) = 0, (x,t) \in G_3$.

Next, let us calculate the partial derivatives of the function $U_{3,\psi}(x,t)$:

$$\frac{\partial U_{3,\psi}(x,t)}{\partial t} = \frac{1}{2\gamma_2} \left[\frac{\gamma_2 - \gamma_1}{\gamma_1 + \gamma_2} (\alpha_1 a_1 \psi(x_0 - a_1 h_3) + \alpha_2 a_2 \psi(x_0 + a_2 h_3)) + \alpha_1 a_1 \psi(x_0 - a_1 h_3) + \alpha_2 a_2 \psi(x + a_2 t) \right]; \quad (19)$$

$$\frac{\partial^2 U_{3,\psi}(x,t)}{\partial t^2} = \frac{1}{2\gamma_2} \left[\frac{\gamma_2 - \gamma_1}{\gamma_1 + \gamma_2} (-\alpha_1 a_1^2 \psi'(x_0 - a_1 h_3) + \alpha_2 a_2^2 \psi'(x_0 + a_2 h_3)) \right] + \quad (20)$$

$$+ \frac{1}{2\gamma_2} [-\alpha_1 a_1^2 \psi'(x_0 - a_1 h_3) + \alpha_2 a_2^2 \psi'(x + a_2 t)],$$

$$\frac{\partial U_{3,\psi}(x,t)}{\partial x} = \frac{1}{2\gamma_2} \left[\frac{\gamma_2 - \gamma_1}{\gamma_1 + \gamma_2} \left(-\frac{\alpha_1 a_1}{a_2} \psi(x_0 - a_1 h_3) - \alpha_2 \psi(x_0 + a_2 h_3) \right) - \frac{\alpha_1 a_1}{a_2} \psi(x_0 - a_1 h_3) + \alpha_2 \psi(x + a_2 t) \right]; \quad (21)$$

$$\frac{\partial^2 U_{3,\psi}(x,t)}{\partial x^2} = \frac{1}{2\gamma_2} \left[\frac{\gamma_2 - \gamma_1}{\gamma_1 + \gamma_2} \times \left(-\alpha_1 \frac{a_1^2}{a_2^2} \psi'(x_0 - a_1 h_3) + \alpha_2 \psi'(x_0 + a_2 h_3) \right) \right] + \quad (22)$$

$$+ \frac{1}{2\gamma_2} \left[-\alpha_1 \frac{a_1^2}{a_2^2} \psi'(x_0 - a_1 h_3) + \alpha_2 \psi'(x + a_2 t) \right].$$

It follows from equalities (20), (22) that $LU_{3,\psi}(x,t) = 0$. Now let us focus on the expression $U_{3,f}(x,t)$. Firstly, let us consider the integral $F(x,t)$, representing it as a sum of two terms:

$$F(x,t) = F_1(x,t) + F_2(x,t),$$

where $F_1(x,t)$ is the integral with respect to $f(\xi,\tau)$ over a triangle with the vertices H_3, M_3, D_3 , and $F_2(x,t)$ is the integral with respect to the same function over the remaining part of $G(M_3)$. Consequently,

$$F_1(x,t) = \int_{h_3}^t \int_{x-a_1(h_3-\tau)}^{x+a_2(t-\tau)} f(\xi,\tau) d\xi d\tau, \quad (23)$$

$$F_2(x,t) = \int_{t-x-a_1(h_3-\tau)}^{h_3} \int_{x+a_2(t-\tau)}^{x+a_2(t-\tau)} f(\xi,\tau) d\xi d\tau. \quad (24)$$

Let us calculate the partial derivatives of $F_1(x,t)$ and $F_2(x,t)$:

$$\frac{\partial F_1(x,t)}{\partial t} = - \int_{x-a_2(t-h_3)}^{x+a_2(t-h_3)} f(\xi,h_3) d\xi + \int_{h_3}^t [a_2 f(x+a_2(t-\tau),\tau) + a_2 f(x-a_2(t-\tau),\tau)] d\tau; \quad (25)$$

$$\frac{\partial^2 F_1(x,t)}{\partial t^2} = - \int_{x_0}^{2x-x_0} \partial_2 f(\xi,h_3) d\xi + 2a_2 f(x,t) - a_2 f(2x-x_0,h_3) - a_2 f(x_0,h_3) + \int_{h_3}^t [a_2^2 [\partial_1 f(x+a_2(t-\tau),\tau) - \partial_1 f(x-a_2(t-\tau),\tau)] d\tau; \quad (26)$$

$$\frac{\partial F_2(x,t)}{\partial t} = \int_{x_0}^{2x-x_0} f(\xi,h_3) d\xi + \int_0^{h_3} [a_2 f(x+a_2(t-\tau),\tau) + a_1 f(x_0-a_1(h_3-\tau),\tau)] d\tau; \quad (27)$$

$$\frac{\partial^2 F_2(x,t)}{\partial t^2} = - \int_{x_0}^{2x-x_0} \partial_2 f(\xi,h_3) d\xi + a_2 f(2x-x_0,h_3) + a_1 f(x_0,h_3) + \int_0^{h_3} [a_2^2 \partial_1 f(x+a_2(t-\tau),\tau) - a_1^2 \partial_1 f(x-a_1(t-\tau),\tau)] d\tau.$$

It follows from the last equality and formula (26) that

$$\frac{\partial^2 F(x,t)}{\partial t^2} = 2a_2 f(x,t) + (a_1 - a_2) f(x_0,h_3) + \int_{h_3}^t [a_2^2 [\partial_1 f(x+a_2(t-\tau),\tau) - \partial_1 f(x-a_2(t-\tau),\tau)] d\tau +$$

$$\begin{aligned}
 & + \int_0^{h_3} [a_2^2 \partial_1 f(x + a_2(t - \tau), \tau) - \\
 & - a_1^2 \partial_1 f(x - a_1(h_3 - \tau), \tau)] d\tau.
 \end{aligned}$$

By similar direct calculations we obtain the equality

$$\begin{aligned}
 \frac{\partial^2 F(x, t)}{\partial x^2} &= \left[\frac{a_1}{a_2^2} - \frac{1}{a_2} \right] f(x_0, h_3) + \\
 & + \int_{h_3}^t [\partial_1 f(x + a_2(t - \tau), \tau) - \\
 & - \partial_1 f(x - a_2(t - \tau), \tau)] d\tau + \\
 & + \int_0^{h_3} \left[a_2^2 \partial_1 f(x + a_2(t - \tau), \tau) - \right. \\
 & \left. - \frac{a_1^2}{a_2} \partial_1 f(x - a_1(h_3 - \tau), \tau) \right] d\tau.
 \end{aligned}$$

Using the formulae obtained for the second derivatives of the function $F(x, t)$, we verify that $LF(x, t) = f(x, t)$.

Now let us consider the integral $\Phi(x, t)$ with respect to $f(\xi, \tau)$ over triangle $G(H_3)$, i.e.,

$$\Phi(x, t) = \int_0^{h_3 x_0 + a_2(h_3 - \tau)} \int_{x_0 - a_1(h_3 - \tau)} f(\xi, \tau) d\xi d\tau.$$

Let us calculate the derivatives of the function $\Phi(x, t)$:

$$\begin{aligned}
 \frac{\partial \Phi(x, t)}{\partial t} &= \int_0^{h_3} [a_2 f(x_0 + a_2(h_3 - \tau), \tau) + \\
 & + a_1 f(x_0 - a_1(h_3 - \tau), \tau)] d\tau; \\
 \frac{\partial^2 \Phi(x, t)}{\partial t^2} &= (a_1 + a_2) f(x_0, h_3) + \\
 & + \int_{h_3}^t [a_2^2 \partial_1 f(x_0 + a_2(h_3 - \tau), \tau) - \\
 & - a_1^2 \partial_1 f(x_0 - a_1(h_3 - \tau), \tau)] d\tau; \\
 \frac{\partial^2 \Phi(x, t)}{\partial x^2} &= \left(\frac{a_1}{a_2^2} + \frac{1}{a_2} \right) f(x_0, h_3) + \\
 & + \int_0^{h_3} \left[\partial_1 f(x_0 + a_2(h_3 - \tau), \tau) - \right. \\
 & \left. - \frac{a_1^2}{a_2} \partial_1 f(x_0 - a_1(h_3 - \tau), \tau) \right] d\tau.
 \end{aligned} \tag{28}$$

It follows from here that $L\Phi(x, t) = 0$, $(x, t) \in G_3$.

Combining the results of the calculations, we obtain the equality

$$LU_{3,f}(x, t) = f(x, t), \quad (x, t) \in G_3.$$

In view of the equations

$$LU_{3,\varphi}(x, t) = 0, \quad LU_{3,\psi}(x, t) = 0,$$

which we have obtained earlier, we now obtain $LU_3(x, t) = f(x, t)$.

We similarly obtain the equality

$$LU_4(x, t) = f(x, t), \quad (x, t) \in G_4.$$

The same conclusion can be reached by replacing the variable $x' = 2x_0 - x$ and using the results we have already obtained. Thus, we have proved that the function $U(x, t)$ satisfies Eq. (1) in G_0 and conditions (2).

It is easy to derive properties (3) – (6) from the equalities obtained for $\partial_1 U(x, t)$ and $\partial_2 U(x, t)$. Therefore, the function $U(x, t)$ represented by formulae (7) – (9) is a generalized solution of problem (1), (2).

3. *Uniqueness of the solution of the direct problem.* To prove this uniqueness, we take two solutions of problem (1), (2) and denote their difference as $V(x, t)$. Let us consider the functions

$$v_1(x, t) = \partial_2 V(x, t) + a(x) \partial_1 V(x, t),$$

$$v_2(x, t) = \partial_2 V(x, t) - a(x) \partial_1 V(x, t).$$

It is easy to verify that the following equalities are satisfied:

$$\partial_2 v_1(x, t) - a(x) \partial_1 v_1(x, t) = 0,$$

$$\partial_2 v_2(x, t) + a(x) \partial_1 v_2(x, t) = 0, \tag{29}$$

$$v_i(x, 0) = 0, \quad i = 1, 2, \quad (x, t) \in G_0.$$

Let us agree to denote $v_1(x, t), v_2(x, t), V(x, t)$ for $x < x_0$ as $v_1^-(x, t), v_2^-(x, t), V^-(x, t)$, and as $v_1^+(x, t), v_2^+(x, t), V^+(x, t)$ for $x \geq x_0$.

It follows from conditions (5), (6) that the functions $v_1^+(x, t), v_2^-(x, t)$ are continuous. Therefore, we obtain from system (29)

$$v_1^+(x, t) = v_2^-(x, t) = 0.$$

For an arbitrary point H on the half-axis $(x_0, t), t > 0$, the following equalities are satisfied:

$$v_1^+(H) = \partial_2 V^+(H) + a_2 \partial_1 V^+(H) = 0,$$

$$v_2^-(H) = \partial_2 V^-(H) - a_1 \partial_1 V^-(H) = 0.$$

Then, since $\partial_2 v_2(x, t)$ is continuous with $x = x_0$ and taking into account condition (4), it follows that $v_1(x, t)$ and $v_2(x, t)$ are continuous at point H . Thus, we obtain the equalities

$$v_1(x, t) = v_2(x, t) = 0,$$

$$\partial_1 V(x, t) = 0, \partial_2 V(x, t) = 0,$$

where $V(x, t) = \text{const}$.

Therefore, due to the condition $V(x, 0) = 0$, we have $V(x, t) = 0, (x, t) \in R_2^+$, which actually means that the solution of the direct problem is unique.

Theorem 1 is proved.

Statement and investigation of inverse problems

Two inverse problems are considered in the study.

Problem 1. With the given solution of the direct problem $U(x, t)$ on rays $(x_1, t), (x_2, t), (x_3, t), t > 0$, where the fixed points $x_i, i = 1, 2, 3$, satisfy the inequalities $x_1 < x_0, x_2, x_3 > x_0$, find the values x_0, a_1, a_2 .

Problem 2. With the given values of, $i = 2, 3$ and fixed points $x_2, x_3 > x_0$, find x_0, a_2 .

Both problems have applications in theory on sounding unknown media and determining some of their parameters. In this case, the junction point of different materials (x_0) and the wave propagation velocities (a_i) are unknown. The second problem differs from the first by the smaller amount of the known data and, correspondingly, smaller amount of the data to be determined.

Theorem 2. Each of the inverse problems 1, 2 has at most one solution if the following condition is satisfied:

$$\varphi'(x_0)(\beta_1 - \beta_2) \neq 0. \quad (30)$$

Proof. First of all, let us analyze the derivative $\partial_2 U(x, t)$ with a fixed $x, x \neq x_0, t > 0$. Let us assume to be definite that $x > x_0$. Then the ray $(x, t), t > 0$, lies in domains G_2 and G_3 , intersecting the boundary between them at the point

$$P = (x, (x - x_0) / a_2).$$

We have already carried out an analysis of $\partial_2 U(x, t)$ for $(x, t) \in G_3$ in proving Theorem 1, and the results are represented by formulae (15), (19), (25), (27).

Now let us carry out a similar analysis of $\partial_2 U(x, t), (x, t) \in G_2$. Using equality (7) for $i = 2$, let us represent $U_2(x, t)$ as a sum

$$U_2(x, t) = U_{2,\varphi}(x, t) + U_{2,\psi}(x, t) + U_{2,f}(x, t),$$

where

$$U_{2,\varphi}(x, t) = \frac{\varphi(x - a_2 t) + \varphi(x + a_2 t)}{2};$$

$$U_{2,\psi}(x, t) = \frac{1}{2\gamma_2} \int_{x - a_2 t}^{x + a_2 t} \alpha_2 \psi(\xi) d\xi;$$

$$U_{2,f}(x, t) = \frac{1}{2\gamma_2} \int_0^t \int_{x - a_2(t-\tau)}^{x + a_2(t-\tau)} f(\xi, \tau) d\xi d\tau.$$

Calculating the derivatives of these functions with respect to t and using the limit $(x, t) \rightarrow P$, we obtain:

$$\frac{\partial U_{2,\varphi}(P)}{\partial t} = \frac{a_2}{2} (\varphi'(2x - x_0) - \varphi'(x_0)); \quad (31)$$

$$\frac{\partial U_{2,\psi}(P)}{\partial t} = \frac{1}{2} (\psi(2x - x_0) + \psi(x_0)); \quad (32)$$

$$\frac{\partial U_{2,f}(P)}{\partial t} = \frac{a_2}{2\gamma_2} \int_0^{(x-x_0)/a_2} [f(2x - x_0 - a_2\tau, \tau) + f(x_0 + a_2\tau, \tau)] d\tau. \quad (33)$$

Using equalities (25), (27), (28), we obtain the limit value of $\partial_2 U_{3,f}(x, t)$ at point P :

$$\frac{\partial U_{3,f}(P)}{\partial t} = \frac{a_2}{2\gamma_2} \int_0^{(x-x_0)/a_2} [f(2x - x_0 - a_2\tau, \tau) + f(x_0 + a_2\tau, \tau)] d\tau. \quad (34)$$

Using limit $(x, t) \rightarrow P, (x, t) \in G_3$ in equalities (15), (19), (25), (27), (28) and comparing the obtained expressions in the right-hand sides of equalities (15) and (31), (19) and (32), (33) and (34), we reach the following conclusion:

$$\partial_2 U_{3,\psi}(P) = \partial_2 U_{2,\psi}(P),$$

$$\partial_2 U_{3,f}(P) = \partial_2 U_{2,f}(P);$$

$$\begin{aligned} \partial_2 U_{3,\varphi}(P) - \partial_2 U_{2,\varphi}(P) &= \\ &= \varphi'(x_0)(\beta_2 - \beta_1) / (\gamma_2 + \gamma_1). \end{aligned}$$

Thus, the terms of the function $U(x, t)$ that contain $\psi(x)$, and $f(x, t)$ have continuous derivatives with respect to t . The term containing the function $\varphi(x)$ has a discontinuous derivative with respect to t at point P , i.e.,

$$\left\{ \frac{\partial U}{\partial t}(P) \right\} = \varphi'(x_0) \frac{\beta_2 - \beta_1}{\gamma_2 + \gamma_1}. \quad (35)$$

In a similar manner, we can verify for the case $x < x_0$ that the following equality is satisfied:

$$\left\{ \frac{\partial U}{\partial t}(Q) \right\} = \varphi'(x_0) \frac{\beta_1 - \beta_2}{\gamma_2 + \gamma_1}, \quad (36)$$

where Q is the point of intersection of the ray (x, t) , $t > 0$ and the straight line $\xi - x_0 = -a_1\tau$.

We should note that, as in Theorem 1, we can replace the variable $x' = 2x_0 - x$ and derive equality (36) from equality (35).

Let us denote the intersection points of the straight line $\xi - x_0 = -a_2\tau$ and the rays (x_2, t) , (x_3, t) , $t > 0$ as P_2 , P_3 . It follows from property (35) that $\partial_2 U(x_2, t)$, $\partial_2 U(x_3, t)$ have discontinuities only if $(x_2, t) = P_2$, $(x_3, t) = P_3$, respectively. Thus, points P_2 , P_3 are uniquely determined from the data of the problem, and consequently, x_0 and a_2 are uniquely determined as well, which means that the solution of problem 2 is unique.

Using the representation $U(x_1, t)$, $t > 0$ and equality (36), we verify that $\partial_2 U(x_1, t)$ has a discontinuity only at point P_1 , which is the intersection of the line $\xi - x_0 = -a_1\tau$ and the ray (x_1, t) , $t > 0$. Since P_1 and x_0 are uniquely deter-

mined, it follows that a_0 is uniquely determined as well.

Thus, Theorem 2 is proved.

We should bear in mind that if condition (30) is satisfied, then, using the proof of Theorem 2, it is easy to construct the corresponding algorithms.

Note. Since the function $\varphi(x)$ is not given in inverse problems but the inequality $\varphi'(x_0) \neq 0$ has to hold true, Theorem 2 is conditional. To give this theorem a constructive form, it is sufficient to postulate the inhomogeneity of the medium ($\beta_1 \neq \beta_2$) and additionally set the function $\varphi(x)$.

Conclusion

In this study, we have considered a one-dimensional wave equation describing the transverse vibrations of an inhomogeneous string or longitudinal vibrations of an inhomogeneous rod. We have formulated a direct problem on determining the vibration function in the general case, when the initial state, the initial velocity, and the external force are known and sufficiently arbitrary. We have proved that the solution for this problem exists and is unique, and provided simple and explicit formulae for this solution. In addition, we have considered two inverse problems on finding the junction point of different materials and wave propagation velocities. We have proved that inverse problems have a unique solution if a certain inequality is satisfied.

REFERENCES

- [1] G. Petrova, B. Popov, Linear transport equations with discontinuous coefficients, Communications in Partial Differential Equations. 24 (9–10) (1999) 1849–1873.
- [2] F. Bouchut, F. Jame, One-dimensional transport equations with discontinuous coefficients, Journal Nonlinear Analysis, Theory, Methods and Applications. 32 (7) (1998) 891–933.
- [3] A.G. Kulikovskiy, E.I. Sveshnikova, A.P. Chugaynova, Matematicheskiye metody izucheniya razryvnykh resheniy nelineynykh giperbolicheskikh sistem uravneniy [Mathematical methods of studies in discontinuous solutions of systems of nonlinear hyperbolic equations], SEC lecture course, Iss. 16 (2010), MIAN, Moscow.
- [4] E. Tadmor, Local error estimates for discontinuous solutions of nonlinear hyperbolic equations, SIAM J. Numer. Anal. 28 (4) (1991) 891–906.
- [5] N.N. Kalitkin, Chislennyye metody [Numerical methods], Nauka, Moscow, 1978.
- [6] I.M. Gel'fand, Some problems of analysis and differential equations, Uspekhi Mat. Nauk. 14 (2(86)) (1959) 87–158.
- [7] A.F. Filippov, Differentsialnyye uravneniya s razryvnoy pravoy chastyu [Differential equations with discontinuous right-hand parts], Nauka, Moscow, 1985.
- [8] V.A. Il'in, A d'Alembert-type formula for longitudinal oscillations of an infinite rod consisting of two segments with different densities and elasticities, Doklady Mathematics. 80 (1) (2009)

613–615.

[9] **V.A. Ilin**, A d'Alembert-type formula for transverse oscillations of an infinite rod consisting of two segments with different densities, *Doklady Mathematics*. 80 (1) (2009) 624–626.

[10] **A.N. Tikhonov, A.A. Samarskiy**, *Uravneniya matematicheskoy fiziki* [Mathematical physics

equations], Nauka, Moscow, 1977.

[11] **G.S. Salekhov**, A generation of formulas of d'Alembert and Poisson, *Uspekhi Mat. Nauk*. 2 (4(20)) (1947) 175–182.

[12] **A.G. Sveshnikov, A.N. Bogolyubov, V.V. Kravtsov**, *Lektsii po matematicheskoy fizike* [Lectures on mathematical physics], MSU, Moscow, 2004.

Received 20.02.2018, accepted 01.03.2018.

THE AUTHORS

ANIKONOV Dmitriy S.

Sobolev Institute of Mathematics

4 Acad. Koptug Ave., Novosibirsk, 630090, Russian Federation

anik@math.nsc.ru

KONOVALOVA Dina S.

Sobolev Institute of Mathematics

4 Acad. Koptug Ave., Novosibirsk, 630090, Russian Federation

dsk@math.nsc.ru

AN ASYMMETRICAL DIELECTRIC BARRIER DISCHARGE IN THE PULSED MODE

D.G. Korenyugin¹, A.M. Martsinovsky²

¹ Peter the Great St. Petersburg Polytechnic University, St. Petersburg, Russian Federation;

² The Ioffe Institute of the Russian Academy of Sciences, St. Petersburg, Russian Federation

The paper presents the results of an investigation of an asymmetric dielectric barrier discharge (DBD) in the air at atmospheric pressure. The discharge system consisted of a plane electrode and semispherical short-radius one, and the both were coated with dielectric. The discharge was excited by a train of almost sinusoidal damped oscillations which was applied to electrodes with a frequency of 1 kHz. It has been found that the preferable to biological applications homogeneous avalanche form of the DBD is always realized in the investigated voltage range 7 – 15 kV, whereas the streamer form of the discharge is excited under identical conditions in the case of a conducting semisphere. It was also established that the positive and negative (according to the voltage sign of the first pulse of the train onto the small electrode) discharge differed greatly in their characteristics. An explanation for this difference has been proposed.

Key words: dielectric barrier discharge; pulse train; avalanche; streamer form; discharge mode

Citation: D.G. Korenyugin, A.M. Martsinovsky, An asymmetrical dielectric barrier discharge in the pulsed mode, St. Petersburg State Polytechnical University Journal. Physics and Mathematics. 11 (2) (2018) 69 – 76. DOI: 10.18721/JPM.11207

Introduction

A barrier discharge is a gas discharge occurring in the gap between electrodes, where at least one of the electrodes is coated with a dielectric. Such discharges are traditionally used for various purposes, and, as a rule, their discharge systems have a plane-parallel electrode configuration. If the interelectrode gap is narrow enough (on the order of millimeters), the distribution of the electric field in the discharge region can be considered homogeneous, so this type of barrier discharge is symmetrical, and this subject has been well understood. However, more complex asymmetrical barrier discharges with an inhomogeneous electric field distribution are being actively studied for some practical applications, primarily, plasma technologies in medicine. The discharge systems of such barrier discharges are usually cells where one of the electrodes is flat and the other can have an arbitrary shape. The most frequently

used electrode systems are the sphere–plane and the tip–plane types.

The main form that an asymmetrical barrier discharge takes in air under atmospheric pressure is a coronal streamer [1, 2]; this is the form typically involved for practical applications. However, sometimes this type of discharge should not be used, in particular, in medicine and biology, when treating (sterilizing) relatively large open wounds or bacterial samples for a short time with a discharge [3 – 5]. The streamer form is insufficiently homogeneous for these purposes, and streamers can actually damage living tissues. In view of this, finding a more stable form of homogeneous avalanche discharge is of great interest. For example, according to the data in [6], a homogeneous form of an asymmetrical discharge in air, excited by high-voltage trains, evolved in the pulse frequency range $f \approx 10$ MHz with an interelectrode gap $L \leq 0.4$ cm. However,

the discharge always changed into streamer form at lower pulse frequencies and larger gaps (which substantially simplifies practical applications). For this reason, searching for modes of a homogeneous asymmetrical barrier discharge that are convenient for practical use is an important problem, as is exploring the conditions (and causes) for the existence of the avalanche and streamer forms.

The goal of this study was to find the optimal modes of an asymmetrical barrier discharge with a homogeneous form.

This work continues the study of this type of discharge started in 2008 for a discharge system with a single dielectric electrode [2, 7]. In accordance with our main goal, we have set the task of examining a system with two dielectric electrodes and comparing the characteristics and patterns of the discharge for the two cases.

Experimental procedures

An asymmetrical barrier discharge in air under atmospheric pressure was studied in a discharge cell (Fig. 1). While previous studies [2, 7] used a metal or liquid-phase (conducting) electrode as the small electrode above the surface of this cell, in this experiment, a non-conductive polymer coating was applied to

the surface of a spherical metal electrode 2 of radius $r = 0.3$ cm (cellulose acetate butyrate CAB-308) and 0.075 cm thick. The second electrode was a 0.25 cm thick glass plate 1 with a translucent conductive coating applied to its lower surface. The distance from the sphere to the plate was $L = 0.25$ cm. A camera capturing images of the discharge from the end-face was placed below the plate.

Fig. 1, *b* shows a typical distribution of the electric field along the shortest distance from the sphere to the plate (in the interelectrode gap) for the voltages used in the experiment. Of course, the field is extremely inhomogeneous, so in general the field strength E_{br} for static breakdown ($E_{br} \approx 30$ kV/cm for air [8]) is reached in the interelectrode gap at a distance z_{ed} from the surface of the spherical electrode.

A sequence of high-voltage damped trains with oppositely polarized almost sinusoidal voltages was applied to the electrodes of the discharge system (see Fig. 3); the parameters of these voltages are given in the table. The pulse voltage generator provided train sequences with both $U_1 > 0$ and $U_1 < 0$ values relative to the grounded non-planar electrode.

The voltage across the discharge gap was measured with a calibrated antenna connected to an oscilloscope; the low-voltage values of

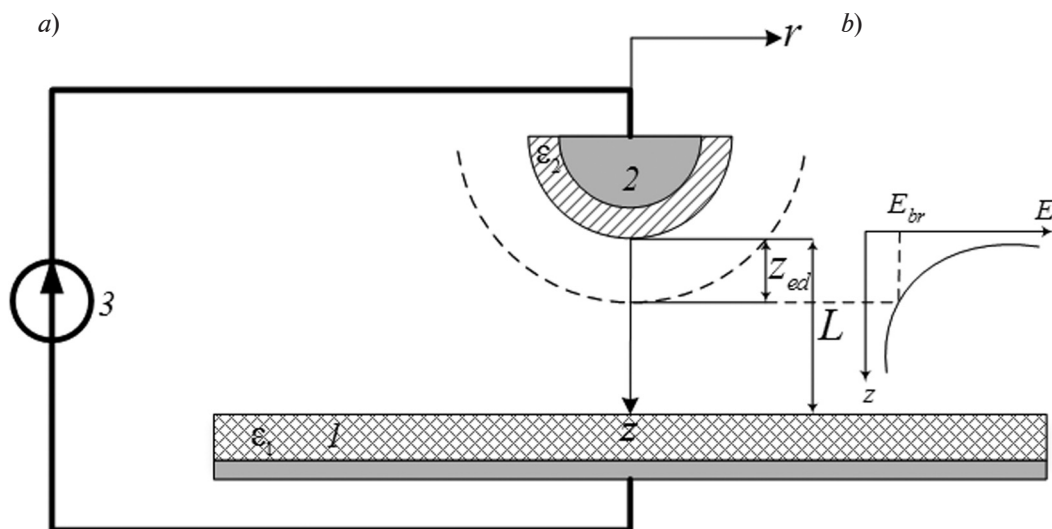


Fig. 1. Schematic of the discharge cell (*a*) and the electric field distribution in the interelectrode gap (*b*): flat glass plate 1 with conductive coating, spherical metal electrode 2 with non-conductive polymer coating, source 3 of high-voltage damped trains with oppositely polarized almost sinusoidal voltages; L , z_{ed} , E_{br} are the characteristic parameters of the barrier discharge; z , r is the coordinate system; E is the electric field strength; ϵ_1 , ϵ_2 are the dielectric permittivities of electrode coatings



Table

Parameter values of high voltages applied to the electrodes

Parameter	Notation	Unit	Value
Train duration	τ_t	μs	≈ 150
Train repetition rate	T_t	ms	1
Oscillation frequency of pulses in a train	f	kHz	55
Pulse duration	first pulse	μs	4
	subsequent pulses		8 – 9
Voltage of first pulse	U_1	kV	7 – 15
Pulse damping	$U_1 : U_2 : U_3$	–	1.0 : 0.8 : 0.7

the antenna signal were then converted to high-voltage (using the calibration curve). The voltage could be additionally adjusted with the volts/div knob, usually with sufficient accuracy (± 0.2 kV). The discharge current was measured with a 5- Ω non-inductive resistive shunt connected between the spherical electrode and the ground. The setup is described in more detail in [2, 7].

Experimental results and discussion

We have discovered in the course of the experiment that while using a polymer coating on the spherical electrode eliminated charge flow from the discharge gap to the external circuit and further impeded avalanche current (as the bias current had to be maintained in this dielectric layer), this also radically changed the discharge shape. Only a streamer form of an asymmetrical discharge could be generated in the experiments described in [2, 7] for a metallic or liquid conductive semi-sphere, virtually throughout the entire range of its parameters; however, a homogeneous avalanche shape of an asymmetrical discharge was steadily observed in a sphere with a dielectric coating with a wide range of pulse voltages from 7 to 15 kV for both polarities.

Fig. 2 shows typical integral images for the shapes of discharges with opposite polarities for a coated semisphere and for a semispherical surface of a droplet of a conductive liquid. Fig. 2, *a* shows the image obtained for a negative

barrier discharge, i.e., for the case when a negative voltage was applied to the sphere and a positive voltage was applied to the plate.

Fig. 2, *b* shows the image obtained for a positive barrier discharge, i.e., with the reverse polarity voltage applied. Fig. 2, *c* shows the image for the experiment described in [2, 7] for the case of a negative asymmetrical barrier discharge. The voltage U_1 of the first pulse on the drop was about 13 kV. In the latter case, the discharge existed in a streamer form.

We should note that the polarity of the corona discharge (positive and negative corona) is typically determined by the sign of the voltage in the tip (the electrode with a small area), since the processes near it play a key role and depend on the voltage sign. The same is largely true for an asymmetrical barrier discharge. Therefore, it is logical to follow the same principle in determining the positive and negative asymmetrical barrier discharges by the sign of the voltage on the sphere relative to the plane electrode. In our experimental conditions, a voltage was applied as a train of oppositely polarized pulses, and it was assumed that the polarity was determined by the most intense first pulse, during which avalanche breakdown develops most often.

Observing the discharge from the side, we have established that it is a luminous cone from the semisphere to the plate, with an angle of about 30° for a negative discharge and about 15° for a positive one. In the first case, bright glow

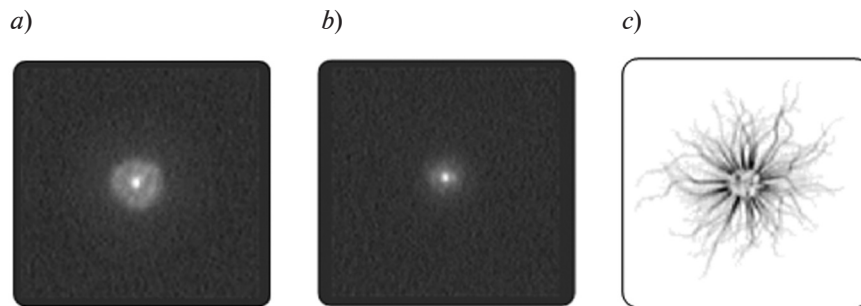


Fig. 2. Comparison of integral images of the shapes of oppositely polarized discharges for a coated semisphere (*a*, *b*) and for a semispherical surface of a droplet of a conductive liquid (*c*). The images shown are for the negative (*a*, *c*) and the positive (*b*) asymmetrical barrier discharges. The characteristic geometric parameters of the discharge system are the same in all cases.

propagated up to the surface of the plate, while in the second case the glow became noticeably dimmer towards the plate and increasing the interelectrode gap leads to the glow “breaking away” from the surface of the plate.

The observed picture of the discharges clearly indicates that the field strength is high enough to not only ensure the propagation of avalanches but also initiate them in the entire discharge gap for the given experimental conditions; respectively, the distribution profile of the electric field, shown in Fig. 1, *b*, should apparently decrease to E_{br} more smoothly.

We should also note that the avalanche is actually a quasi-homogeneous or an integrally homogeneous form of discharge. Indeed, a lot of avalanches manage to develop during the exposure time (≈ 20 ms) with a train repetition rate of 1 kHz, and their total glow generates a homogeneous picture registered by the detector. However, from a practical point of view, even this form of discharge fully satisfies all the necessary requirements (for example, when used for rapid sterilization).

Our studies have revealed that while discharges of opposite polarities are close in form and type of glow, the conditions in which these discharges form turn out to be different.

Fig. 3 shows the electrical characteristics of a negative asymmetrical barrier discharge (the waveforms of the voltage $U(t)$ and pulse current $I(t)$ with different sweep speeds) typical of the range of voltages U_1 from 7 to 12 kV. Some explanation is required for the waveforms obtained. Since the spherical electrode was grounded in the circuit used, the oscilloscope

recorded the voltage on the plate relative to this electrode (the ground). To determine the voltage on the spherical electrode itself relative to the plate, the polarity of the voltages and currents on the waveforms had to be changed.

Thus, it can be seen from Fig. 3 that on a millisecond scale steady discharge current is a sequence of individual short pulses of opposite polarities, differing in amplitude by an order of magnitude. Not every pulse train is accompanied by a current pulse.

The waveform with a nanosecond sweep of individual pulses (see Fig. 3, *d*) has the form typical for avalanche discharge [9]. This result, along with the range of maximum pulse currents (1 – 40 mA), also typical for avalanches, conclusively proves that it is the avalanche (Townsend) discharge form we are dealing with. Most avalanches are formed during the first pulses of the train, which are the most intense; in this case, either a pair of current pulses (first with a negative, then with a positive polarity, see Fig. 3, *b*), or one pulse of the corresponding polarity (Fig. 3, *c*) is observed.

In a negative discharge, avalanches move from the spherical electrode to the plate, into the region with the decreasing field. However, as we have pointed out above, the character of the discharge glow indicates that almost all of the avalanches reach the dielectric surface of the electrode in the given conditions, depositing a negative electron charge on it. This charge generates an electric field inverse to the external field, which prevents the formation of new avalanches, even when breakdown occurs before the high-voltage pulse reaches a maxi-

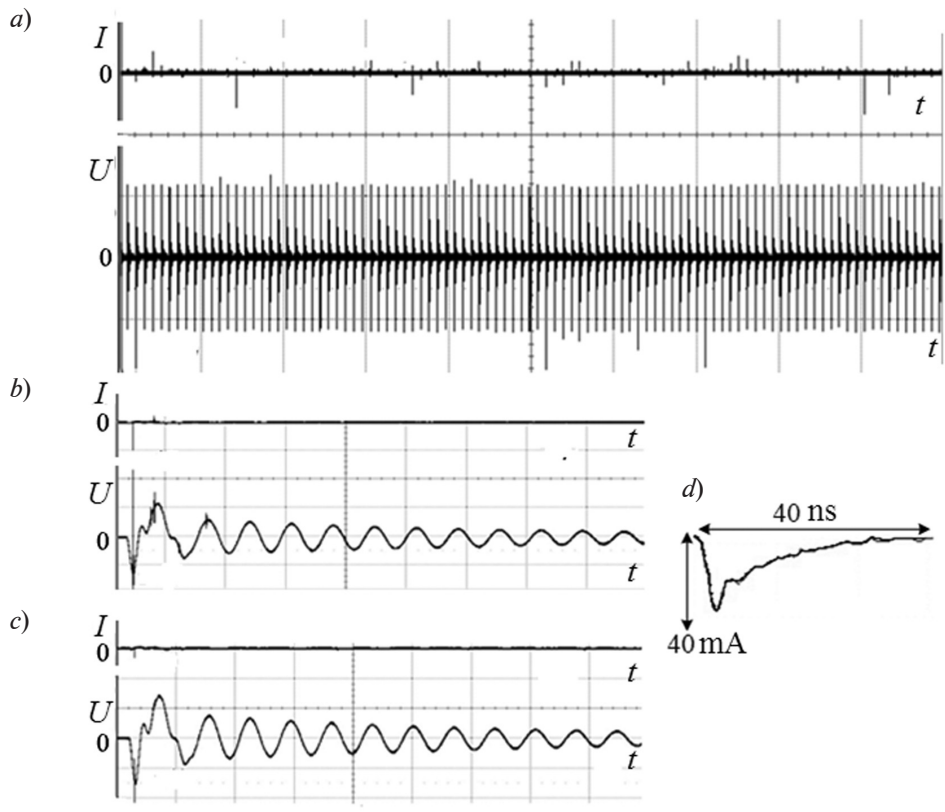


Рис. 3. Current and voltage waveforms of a negative asymmetrical barrier discharge evolving in the small spherical electrode, with different sweep speeds $\Delta t/n$. The waveforms were recorded for a sequence of pulse trains (a), and for a single pulse train: with a pair of pulses (b) and with a single current pulse (c); the shape of a single discharge current pulse ($U_1 \approx 11.8$ kV) (d) is also shown; $\Delta t/n = 10$ ms/div (a), 10 μ s/div (b, c)

mum, and the voltage continues to increase after this breakdown (Fig. 3, c). This is because the amplitudes of the overvoltage pulses are small for the range considered.

With a positive pulse, the electric field of the surface charge is summed with the external field, and thus the resultant field strength in the gap reaches the breakdown value. This leads to the positive breakdown immediately after the negative in almost every case (see Fig. 3, b). Fig. 3, a shows that a positive pulse is observed for all relatively large negative current pulses, even if it is substantially smaller. There is no positive breakdown immediately after the negative only in very rare cases (see Fig. 3, c). This is most likely due to the statistical nature of initiation of avalanches by free electrons.

It can be seen from the waveforms in Fig. 3, b that an avalanche developing results in a spike

in the voltage waveform. The short duration of the spikes indicates that they are actually caused by avalanches, and do not represent random electromagnetic interference. A spike can have the same and the opposite sign as the current pulse. No correlation was observed between the amplitude of the current pulse and the width of the spike, and in some cases, spikes were also observed in the absence of current pulses (for example, in the second positive half-cycle of the waveform, see Fig. 3, b). In this regard, such spikes can be considered to be indicators of low-intensity avalanches. Avalanche noise is the apparent reason for a small fluctuation in the voltage amplitude of the first pulse of the train, observed in the waveform in Fig. 3, a.

Fig. 4 shows the electrical characteristics of a positive asymmetrical barrier discharge, which is approximately the same as the negative one (see

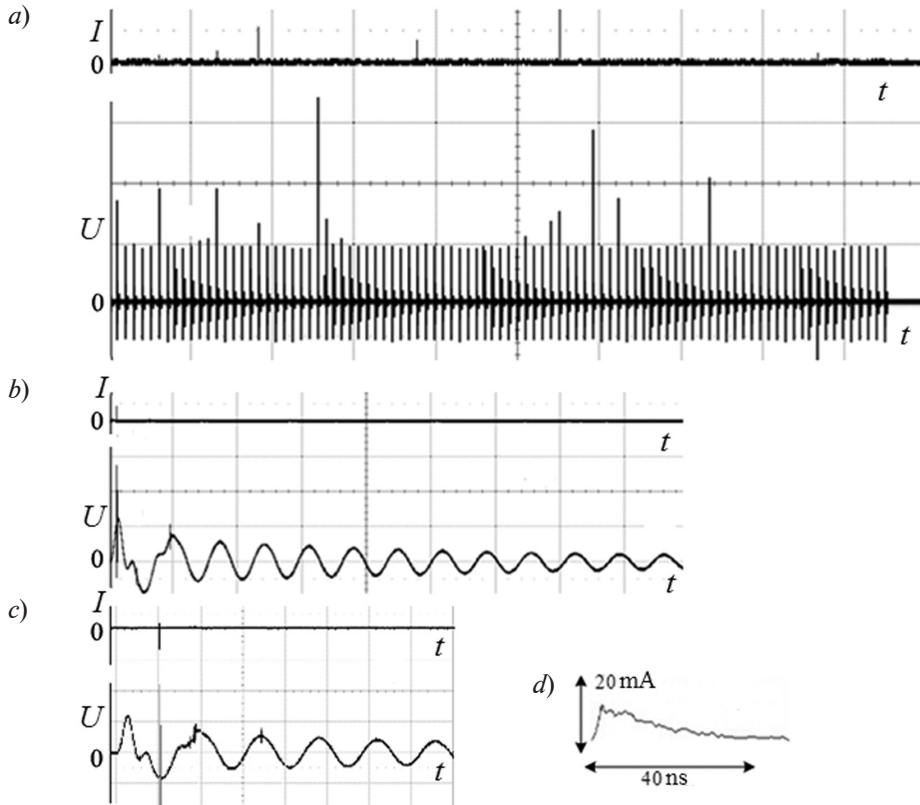


Fig. 4. Current and voltage waveforms with a positive asymmetrical barrier discharge evolving, for different sweep speeds $\Delta t/n$. The waveforms were recorded for a sequence of pulse trains (a) and for a single pulse train (b, c); the shape of a single discharge current pulse ($U_1 \approx 13.2$ kV) (d) is also shown;
 $\Delta t/n = 10$ ms/div (a), 10 μ s/div (b), 5 μ s/div (c)

Fig. 3), but with an external voltage exceeded by 0.5 kV. It can be seen from the figure that for a discharge excited by positive pulses, the discharge current is a sequence consisting almost entirely of positive pulses, similar in their parameters to the current pulses for a negative discharge. Pulses of negative polarity could be “caught” in the millisecond range very rarely (once per dozen waveforms), and only in the second, negative pulse of a train (Fig. 4, c). The waveform in Fig. 4, a shows that current pulses exist only for some high-voltage trains of the sequence, even though voltage spikes (without a current pulse) can also be observed in subsequent negative half-periods (see Fig. 4). Very large spikes are also present on the voltage waveform with no current spikes at all, which was not observed for the negative discharge.

Thus, there is a significant difference between negative and positive asymmetrical

barrier discharges. It should be emphasized here that, generally speaking, breakdowns in the same direction, observed for a positive discharge, contradict the very principle of the barrier discharge: current flow in the presence of dielectric layers on the electrodes is ultimately due to charges accumulating on these layers, and a reverse current phase is necessary in continuous mode to neutralize these charges and to accumulate charges of the opposite sign [8, 10].

We could hypothesize that such a difference is due to the difference in the relaxation processes of surface and space charges in both cases, but even rough estimates indicate that these processes should be close. Indeed, with a positive barrier discharge evolving, a “positive” avalanche, developed from the first pulse of a train while moving from the flat electrode to the spherical one and depositing its negative electron



charge on the sphere, should leave the same distributed positive ion charge (the avalanche's "ion sheath") in the interelectrode gap.

During the remainder of the first pulse ($\approx 2 \mu\text{s}$, see Fig. 4, *b*), positive ions are moved by the field in the direction opposite from the sphere. Assuming (for a rough estimate) that the space- and time-averaged field strength at the surface is about 20 kV/cm , and the mobility of positive ions is $1.25 \text{ cm}^2/(\text{V}\cdot\text{s})$ [11], we obtain a drift velocity value of approximately $2.5 \cdot 10^4 \text{ cm/s}$ and a sufficiently large ($\approx 0.05 \text{ cm}$) distance of the front of the sheath (with the highest ion concentration) from the surface of the sphere. Accordingly, the "tail" of the ion sheath falls on the surface of the flat electrode, if the avalanche was initiated near it, and charges the electrode positively. However (see Fig. 4, *b*), the second, negative pulse (that has almost the same amplitude as the positive one) lasts two times longer, so when the ions move back to the surface of the sphere during this pulse, the corresponding distance must be substantially larger, equal to $\approx 0.2 \text{ cm}$. Thus, by that time, the majority of the positive space charge of ions should fall on the surface of the sphere and neutralize the part of the electron charge that was deposited there.

Subsequently, the positive and the negative pulses of the train last the same time, and the remaining small ion cloud makes damped oscillations, spreading due to diffusion, primarily in the radial direction. For the above ion mobility value at $T = 300 \text{ K}$, the diffusion coefficient $D = 0.032 \text{ cm}^2/\text{s}$, and the characteristic spreading time (over which the cloud size increases by $\sqrt{2}$) with an initial cloud radius of $50 \mu\text{m}$ is $t \approx 20 \mu\text{s}$, i.e., of the order of the train duration. The spread then grows as \sqrt{t} , and the size $\approx 0.1 \text{ cm}$ will be reached in a time $t \approx 20 \text{ ms}$. It is likely that a small number of ions neutralizing the negative surface charge will be added to the spherical electrode during this process of diffused spreading of the initial positive avalanche.

Thus, the charge of a single avalanche is mostly but not completely (this is of the essence) neutralized on the electrodes and in the interelectrode gap during the period between the trains. So subsequent avalanches of the same polarity increase the charge, until

the charge that has increased after the latest avalanche increases the field of the negative pulse so that a breakdown with a "negative" avalanche (moving towards the plate and carrying a negative electron charge) occurs, with a current pulse of negative polarity (see Fig. 4, *c*) neutralizing the accumulated charges. The fact that such breakdowns were extremely rare in the given conditions gives us grounds to conclude that, due to a good combination of the amplitude and the form of the train pulses (short first pulse), the neutralization of charges occurs quite effectively on its own.

The picture observed for a negative barrier discharge, when a negative avalanche formed during the first negative pulse of the train moves towards the plate and transfers its electronic charge to it, and the avalanche's ion sheath shifts towards the spherical electrode, is only slightly more complex. In this case, as noted above, a "positive" avalanche moving towards the spherical electrode is formed, usually in the middle of the second, positive pulse (while the surface charge field is still large). After the avalanche has transferred its electron charge to the electrode, its ionic sheath, together with the remainder of the sheath from the first avalanche, moves towards the plate under the action of the field during the second half of the positive pulse ($\approx 4 \mu\text{s}$), and then to the spherical electrode again during the third pulse ($\approx 8 \mu\text{s}$). As a result of the movement of the second sheath, the majority of its ions must reach the spherical electrode and neutralize the main part of the negative charge of the second avalanche during the third pulse.

A more complex picture should be observed in those modes of negative barrier discharge when the avalanches moving towards the flat electrode do not reach it because ionization stops in a weak field in this part of the discharge gap. In this case, the avalanche current is generated by the drift motion of the electrons that have already formed towards the plate. But since the probability that electrons attach to oxygen and nitrogen in air under atmospheric pressure is high (the attachment rate is $2 \cdot 10^8 \text{ s}^{-1}$ [8, 12]), they quickly turn into negative ions. In general, the presence of a space charge of slow negative ions considerably complicates the picture of charge relaxation in all cases when

such ions are formed.

However, since the glow from the avalanches is typically adjacent to the surface of the flat electrode in both positive and negative asymmetrical barrier discharges for the modes under consideration, the neutralization efficiencies of the charges should not differ greatly. It is more likely that the reason for the observed difference is due to their asymmetry. In a negative discharge, the electron charge is deposited on the plate, where the field of the applied voltage pulse is minimal, and the additional field generated by the charge, which is summed with the field of the second, negative pulse, is the factor determining avalanche breakdown during this pulse. Conversely, the avalanche in a positive discharge carries an

electron charge to the spherical electrode, where the field strength of the applied pulse is maximal and the addition from the surface charge has little effect on the formation of avalanches.

Conclusion

The findings we have obtained on asymmetrical barrier discharges helped establish a number of important regularities in discharge evolution, indicating that a stable homogeneous (avalanche) form of these discharges, which has significant advantages for practical applications, can be generated. Avalanche discharge likely occurs with an appropriately selected type of voltage supply, which ensures effective mutual compensation of volume and surface charges, especially for a positive discharge.

REFERENCES

- [1] **J-S. Chang**, Corona discharge processes, *IEEE Trans. on Plasma Sci.* 19 (6) (1991) 1152–1166.
- [2] **D.G. Korenyugin, D.S. Nikandrov**, Influence of liquid electrode conductivity on dielectric barrier discharge characteristics, *St. Petersburg State Polytechnical University Journal. Computer Science. Telecommunications and Control Systems.* No. 2(55) (2008) 107–110.
- [3] **N.U. Babaeva, M.J. Kushner**, Intercellular electric fields produced by dielectric barrier discharge treatment of skin, *J. Phys. D: Appl. Phys.* 43 (18) (2009) 185–206.
- [4] **G. Fridman, G. Friedman, A. Gutsol, et al.**, Applied plasma medicine, *Plasma Process. Polym.* 5 (6) (2008) 503–533.
- [5] **M. Kuchenbecker, N. Bibinov, A. Kaemling, et al.**, Characterization of DBD plasma source for biomedical applications, *J. Phys. D: Appl. Phys.* 42 (4) (2009) 045213.
- [6] **H. Ayan, G. Fridman, A. Gutsol, V. Vasilets**, Nanosecond-pulsed uniform DBD, *IEEE Trans. on Plasma Sci.* 36 (2) (2008) 504–508.
- [7] **D.G. Korenyugin**, Dynamic characteristics of dielectric barrier discharge with liquid (nonmetallic) electrode, *St. Petersburg State Polytechnical University Journal. Computer Science. Telecommunications and Control Systems.* No. 4 (62) (2008) 116–119.
- [8] **Yu.P. Raizer**, Gas discharge physics, Springer-Verlag, Berlin, 1991.
- [9] **H. Raether**, Electron avalanches and breakdown in gases, Butterworths, Washington, 1964.
- [10] **D.S. Nikandrov, L.D. Tsendin**, Low frequency dielectric-barrier discharge in the Townsend mode, *Technical Physics.* 50 (10) (2005) 1284–1294.
- [11] **E.W. McDaniel, E.A. Mason**, The mobility and diffusion of ions in gases, Wiley, New York, 1973.
- [12] **H. Massey**, Negative ions, Cambridge U.P., Cambridge, 1976.

Received 12.01.2018, accepted 16.02.2018.

THE AUTHORS

KORENYUGIN Dmitriy G.

Peter the Great St. Petersburg Polytechnic University
29 Politechnicheskaya St., St. Petersburg, 195251, Russian Federation
polarisdsk@mail.ru

MARTSINOVSKY Artemiy M.

The Ioffe Institute of the Russian Academy of Sciences
26 Polytekhnicheskaya St., St. Petersburg, 194021, Russian Federation
amartsinovsky@gmail.com



THE GEOMETRICAL EFFECT OF AN ACTIVE ELEMENT CROSS-SECTION ON THE LASER GAIN

V.A. Kozhevnikov, V.E. Privalov

Peter the Great St. Petersburg Polytechnic University, St. Petersburg, Russian Federation

An improved method for calculating the dependence of a laser emission gain on the tube cross-section's geometry has been developed. In this connection the general solution of the Helmholtz equation was considered. But the solution in the form of an infinite series holds the potential for errors. In practice, a researcher has to replace the infinite series by a finite one. Some measures for solving the problems arising in this case were proposed. We have obtained an approximate solution of the Helmholtz equation that is convenient for practice, and a modified method for finding the coefficients of expansion has been developed. The method was tested for some cross-sectional forms that allowed independent theoretical calculation. As a result, the calculations accuracy was demonstrated to improve.

Key words: laser; active element; laser radiation gain; geometry of a tube cross-section

Citation: V.A. Kozhevnikov, V.E. Privalov, The geometrical effect of an active element cross-section on the laser gain, St. Petersburg Polytechnical State University Journal. Physics and Mathematics. 11 (2) (2018) 77 – 87. DOI: 10.18721/JPM.11208

Introduction

One of the tasks of laser studies is to provide maximum radiation power with a fixed length of the gain medium (GM). The latter usually has a cylindrical shape in gas-discharge lasers (GDL), due to the technology of glass production. The search for reserves of power for GDL has generated many different problems from the early years of the laser era. The question whether the cylindrical geometry of the GM was optimal from the standpoint of energy was one of them. The properties of a rectangular cross-section [1], then of an elliptic cross-section [2] were studied. Experiments with a helium-neon laser with a rectangular cross-section demonstrated an agreement between the model and the laser's actual properties [3]. The encouraging experimental results led to attempts to obtain a generalized theoretical model [4, 5]. Searches based on these generalizations continue in the present day [6, 7].

Notably, the Russian industry did not wait for reliable physical models to be created, starting to produce helium-neon lasers OKG-11 and OKG-12 not only with cylindrical but also with rectangular and elliptical GMs in the 1960s. The expectation was that radiation power would be increased due to higher types of oscillations in the resonator.

The search was not limited to choosing the optimal cross-section of the GM. The models of the optimal longitudinal cross-section were more successful [8, 9]. They were confirmed experimentally and yielded a noticeable increase in the lasing power [10]. However, more factors turned out to affect the power than previously believed. It is also clear from our present-day point of view that the models were not analytical, and the calculations were of an approximate nature. The modern level of computer technology should allow to develop new approaches and discover unexplored opportunities.

This article starts a new series of studies that should (as we hope) allow to gain deeper insight into the nature of the GDL and find additional power reserves.

The geometric part of the laser gain has the following form [1] (in this article we confine ourselves to a constant cross-section along the length of the GM):

$$k = \frac{1}{S_0} \int_V k_0 \cdot f \, dV; \quad (1)$$

the function $f(\mathbf{r})$ describing the spatial distribution of the gain coefficient satisfies the Helmholtz equation in the region V :

$$\Delta f + \lambda^2 f = 0 \quad (2)$$

with the boundary condition

$$f|_{\Gamma} = 0. \tag{3}$$

Here Γ is the boundary of the region in which the solution is sought; S_0 is the cross-sectional area of the tube; k_0 is the gain on the axis of the system.

General solution of the Helmholtz equation

Let us examine Eq. (2) in cylindrical coordinates (r, ϕ, z) , assuming from symmetry considerations that there is no dependence on the z coordinate. Using the variable separation method, we find that the general solution of the equation for polar angle periodicity and a solution bounded in the neighborhood of $r = 0$ is a set of functions

$$f(r, \phi) = a_{k1}J_k(\lambda r) \cdot \cos(k\phi) + a_{k2}J_k(\lambda r) \cdot \sin(k\phi),$$

where $J_k(\lambda r)$ are the Bessel functions of order k ; $k = 0, 1, 2, \dots$ (there is a single function $a_0J_0(\lambda r)$ for $k = 0$).

In this case, in general, boundary condition (3) with an arbitrary form of the boundary Γ of the region V (that is, with an arbitrary cross-section of the tube) is satisfied by a series of similar functions, rather than by any individual function for some fixed value of k , i.e., in the presence of condition (3), the general solution of Eq. (2) has the form

$$f(r, \phi) = \sum_{k=0}^{\infty} \{a_{k1}J_k(\lambda r) \cdot \cos(k\phi) + a_{k2}J_k(\lambda r) \cdot \sin(k\phi)\}. \tag{4}$$

A similar method for solving the boundary value problem in the form of expansions of the solution in exact solutions of the corresponding differential equation is often referred to as the Trefftz method in technical literature [11].

In this paper, we propose our own modification of this method, which allows to obtain solutions with a high accuracy and relatively low computational complexity.

Approximate solution of the Helmholtz equation

In practical calculations, we have to replace the infinite series with a finite one, taking a certain number of terms in expression (4) and

obtaining the function $f^n(r, \phi)$:

$$f^n(r, \phi) = \sum_{k=0}^n \{a_{k1}J_k(\lambda r) \cdot \cos(k\phi) + a_{k2}J_k(\lambda r) \cdot \sin(k\phi)\}. \tag{5}$$

Function (5), the same as function (4), satisfies Eq. (2) exactly (since each term satisfies this equation), but only approximately satisfies boundary condition (3).

Let us denote the corresponding functions from expression (5) as ξ_k , i.e.,

$$\zeta_k(\lambda r, \phi) = J_k(\lambda r) \cdot \cos(k\phi)$$

or

$$\zeta_k(\lambda r, \phi) = J_k(\lambda r) \cdot \sin(k\phi),$$

and normalize our function f (and, respectively, the function $f^n(r, \phi)$) by unity for $r = 0$ (Eq. (2) and boundary condition (3) are homogeneous).

Since $J_0(0) = 1$, $J_k(0) = 0$ with $k > 0$, then $a_0 = 1$ and

$$f^n(r, \phi) = \zeta_0(\lambda r, \phi) + \sum_{k=1}^n a_k \zeta_k(\lambda r, \phi). \tag{6}$$

Let us now formulate what we mean by stating that boundary condition (3) is satisfied approximately.

We choose some N points on the boundary Γ

$$\xi_1, \xi_2, \dots, \xi_N$$

and impose the condition that the sum of the values of the function f^n be equal to zero at these points:

$$\sum_{j=1}^N f^n(\xi_j) = 0, \xi_j \in \Gamma.$$

In practical calculations, we can also generally satisfy the latter equality only approximately, so we should rigorously formulate the condition in the following manner: the values of the parameter λ and the a_k coefficients in equality (6) should be chosen such that the absolute value of the sum is less than some given, very small value Δ :

$$|\sum_{j=1}^N f^n(\xi_j)| < \Delta, \xi_j \in \Gamma. \tag{7}$$

It is extremely ineffective to go through all

possible values of the parameter λ and the a_k coefficients, so we will search for them by the approximation method.

The first approximation for the parameter λ .

In the first approximation, we impose the following condition on λ :

$$\sum_{j=1}^N \zeta_0(\xi_j) \equiv \sum_{j=1}^N J_0(\lambda r_j) = 0, \quad (8)$$

where r_j is the corresponding value of the polar coordinate r of the point ξ_j .

In practice, we can either demand that the sum be equal to zero in condition (8) approximately with some accuracy, or replace the Bessel function J_0 with an approximate one, for which equation (8) can be solved exactly. For example, we can interpolate it with a second-degree polynomial (the second degree is convenient because in this case the equation is square and easily solvable; solution would be problematic for higher degrees). Interpolating the function with a polynomial of only the second degree is completely justified, since this is only the first approximation for the parameter λ , which will be refined further, and inappropriate choice of the first approximation can lead only to computational complexity of the algorithm, but will not worsen the final accuracy. So, if $[r_{\min}, r_{\max}]$ is the variation range of the coordinate r for the boundary Γ , we can construct, for example, the Lagrange interpolating polynomial of the second degree for the function $\zeta_0(r)$ in the nodes r_0, r_1, r_2 from the range $[r_{\min}, r_{\max}]$ [12]:

$$\begin{aligned} P(r) = & \zeta_0(r_0) \frac{(r-r_1)(r-r_2)}{(r_0-r_1)(r_0-r_2)} + \\ & + \zeta_0(r_1) \frac{(r-r_0)(r-r_2)}{(r_1-r_0)(r_1-r_2)} + \\ & + \zeta_0(r_2) \frac{(r-r_0)(r-r_1)}{(r_2-r_0)(r_2-r_1)} = ar^2 + br + c, \end{aligned}$$

where

$$\begin{aligned} a = & \frac{\zeta_0(r_0)}{(r_0-r_1)(r_0-r_2)} + \frac{\zeta_0(r_1)}{(r_1-r_0)(r_1-r_2)} + \\ & + \frac{\zeta_0(r_2)}{(r_2-r_0)(r_2-r_1)}; \\ b = & -\zeta_0(r_0) \frac{(r_1+r_2)}{(r_0-r_1)(r_0-r_2)} - \end{aligned}$$

$$\begin{aligned} & - \zeta_0(r_1) \frac{(r_0+r_2)}{(r_1-r_0)(r_1-r_2)} - \\ & - \zeta_0(r_2) \frac{(r_0+r_1)}{(r_2-r_0)(r_2-r_1)}; \end{aligned}$$

$$\begin{aligned} c = & \frac{\zeta_0(r_0) \cdot r_1 \cdot r_2}{(r_0-r_1)(r_0-r_2)} + \frac{\zeta_0(r_1) \cdot r_0 \cdot r_2}{(r_1-r_0)(r_1-r_2)} + \\ & + \frac{\zeta_0(r_2) \cdot r_0 \cdot r_1}{(r_2-r_0)(r_2-r_1)}. \end{aligned}$$

We can take the roots of the corresponding Chebyshev polynomials as interpolation nodes:

$$r_k = \frac{r_{\max} + r_{\min}}{2} + \frac{r_{\max} - r_{\min}}{2} \cos\left(\frac{2k+1}{2n+2} \pi\right),$$

where $k = 0, 1, 2, \dots, n$ and $n = 2$ in our case.

Substituting this into (9), we obtain an equation with respect to the parameter λ :

$$\lambda^2 \cdot a \sum_{j=1}^N r_j^2 + \lambda \cdot b \sum_{j=1}^N r_j + \sum_{j=1}^N c = 0, \quad (9)$$

from which we find the first approximation for λ as the value of the corresponding positive root.

If it turns out that Eq. (9) has no positive roots for a given choice of points $\xi_1, \xi_2, \dots, \xi_N$ on the boundary Γ (that is, the corresponding values of r_j), then, since the choice of the corresponding boundary points in the problem is not rigid, the above set of points can be changed and the algorithm can be repeated again. If, on the other hand, either the set of boundary points is rigidly fixed for some reason or we still cannot obtain the parameter λ after several changes of boundary points, then we can take, as a first approximation for λ , such a value that

$$J_0(\lambda r_{\text{mean}}) = 0,$$

where r_{mean} is the mean value of r in the cross-section of the tube, i.e., $\lambda = \lambda_1 / r_{\text{mean}}$, where $\lambda_1 = 2.4048$ is the first root of the function $J_0(x)$.

In this case, we simply have to increase the interval where we search for the next approximations of the parameter λ in subsequent calculations.

First approximation of the coefficients a_k .

It follows from boundary condition (3) that series (6)

$$\zeta_0(\lambda r, \phi) + \sum_{k=1}^n a_k \zeta_k(\lambda r, \phi)$$

is equal to zero on the boundary Γ , that is, the following equality should hold true on the boundary Γ :

$$-\zeta_0(\lambda r, \phi) = \sum_{k=1}^n a_k \zeta_k(\lambda r, \phi); (r, \phi) \in \Gamma. \quad (10)$$

Formula (10) can be interpreted as an approximation of the function $-\zeta_0$ on the boundary Γ by a linear combination of linearly independent functions ζ_k . However, it is more convenient to perform such an approximation through orthonormal (on the boundary Γ) functions, so let us move on from the set of linearly independent functions $\{\zeta_1, \zeta_2, \dots, \zeta_n\}$ to a set of functions $\{\Psi_1, \Psi_2, \dots, \Psi_n\}$ that are orthonormal on the boundary Γ (in fact, we only determine these functions on the boundary).

A transition to an orthonormal set can be made, for example, through the Gram – Schmidt process. In this case, the scalar product of the functions on the boundary Γ is naturally determined as

$$\langle \zeta_k, \zeta_s \rangle = \sum_{j=1}^N \zeta_k(\lambda r_j, \phi_j) \cdot \zeta_s(\lambda r_j, \phi_j);$$

$$\langle \Psi_k, \Psi_s \rangle = \sum_{j=1}^N \Psi_k(r_j, \phi_j) \cdot \Psi_s(r_j, \phi_j);$$

$$\langle \zeta_k, \Psi_s \rangle = \sum_{j=1}^N \zeta_k(\lambda r_j, \phi_j) \cdot \Psi_s(r_j, \phi_j),$$

and the norm of an arbitrary function Y on the boundary Γ is determined as follows:

$$\|Y\| = \sqrt{\langle Y, Y \rangle}.$$

The Gram – Schmidt process involves constructing non-normalized orthogonal functions $\{\tilde{Y}_k\}$ at first and then normalizing them:

$$\Psi_k(r, \phi) = \tilde{Y}_k(r, \phi) / \|\tilde{Y}_k\|.$$

The construction is carried out as follows. The first function ζ_1 is chosen as the first function \tilde{Y}_1 . More precisely, the values of this function \tilde{Y}_1 on the set of points $\xi_1, \xi_2, \dots, \xi_N$ on the boundary Γ are determined through the values of the first function ζ_1 on the same set of points:

$$\tilde{Y}_1(\xi_j) \equiv \tilde{Y}_1(r_j, \phi_j) = \zeta_1(\lambda r_j, \phi_j), \quad j = 1, 2, \dots, N;$$

$$\Psi_1(\xi_j) = \tilde{Y}_1(r_j, \phi_j) / \|\tilde{Y}_1\|.$$

The values of the next functions are found successively by the formulae:

$$\begin{aligned} \tilde{Y}_i(\xi_j) &\equiv \tilde{Y}_i(r_j, \phi_j) = \\ &= \zeta_i(\lambda r_j, \phi_j) - \sum_{k=1}^{i-1} \frac{\langle \zeta_i, \tilde{Y}_k \rangle}{\langle \tilde{Y}_k, \tilde{Y}_k \rangle} \tilde{Y}_k(r_j, \phi_j), \end{aligned} \quad (11)$$

$$j = 1, 2, \dots, N, \quad i = 2, \dots, n;$$

$$\Psi_i(\xi_j) = \tilde{Y}_i(r_j, \phi_j) / \|\tilde{Y}_i\|.$$

The resulting set of functions Ψ_i is orthonormal on the boundary Γ , and therefore any function, including the function $-\zeta_0$, can be expanded in a series (approximated by a linear combination) of these functions:

$$\begin{aligned} -\zeta_0(\lambda r_j, \phi_j) &= \sum_{k=1}^n \beta_k \Psi_k(r_j, \phi_j); \\ j &= 1, 2, \dots, N, (r_j, \phi_j) \in \Gamma. \end{aligned} \quad (12)$$

Since the system $\{\Psi_1, \Psi_2, \dots, \Psi_n\}$ is orthonormal, it is easy to find the expansion coefficients β_k :

$$\beta_k = -\langle \zeta_0, \Psi_k \rangle = -\sum_{j=1}^N \zeta_0(\lambda r_j, \phi_j) \cdot \Psi_k(r_j, \phi_j).$$

Comparing equations (10) and (12), we obtain the equality

$$\begin{aligned} \beta_1 \Psi_1(r_j, \phi_j) + \beta_2 \Psi_2(r_j, \phi_j) + \dots + \beta_n \Psi_n(r_j, \phi_j) &= \\ = a_1 \zeta_1(\lambda r_j, \phi_j) + a_2 \zeta_2(\lambda r_j, \phi_j) + \dots & \quad (13) \\ \dots + a_n \zeta_n(\lambda r_j, \phi_j), & \end{aligned}$$

which must be satisfied for all points $j = 1, 2, \dots, N$.

On the other hand, by virtue of their construction, each of the functions Ψ_k ($k = 1, 2, \dots, n$) is a linear combination of functions $\{\zeta_1, \zeta_2, \dots, \zeta_n\}$. Now, equating the coefficients for the same functions $\zeta_k(\lambda r, \phi)$ on the left-hand and on the right-hand sides in equality (13), we obtain expressions for the coefficients a_k . Substituting the first approximation for λ in these expressions, we obtain the first approximation for the coefficients a_k .

These expressions for the coefficients a_k are rather cumbersome and become more compli-

the coefficients a_k from equality (13). We find sum (7) from the new values of a_k ; this is Δ_2 . Then we repeat the whole process. Thus, by searching through the possible values of λ in the neighborhood of the first approximation, we finally choose the value with which sum (7) reaches the minimum. The number of points N on the boundary can also be changed (keeping in mind that the first approximation has to be found again in this case) to achieve the required accuracy.

We should note the following. According to theory, the solution of Eq. (2) with boundary condition (3) exists not for some single value, but for a set of values of λ (the so-called set of eigenvalues of the problem). The first eigenvalue of λ makes the main contribution to the gain. If we greatly increase the search interval for the first approximation, then in the subsequent approximations we risk obtaining not the first but the subsequent eigenvalues, since the approximate numerical value of sum (7) can be closer to zero for the subsequent eigenvalues than for the first one. In view of this, the dependence of sum (7) on the value of λ should be controlled to verify that the first eigenvalue has been obtained.

After we have determined the parameter λ and the coefficients a_k with the required accuracy, we can determine the gain coefficient (here and below we choose the tube length equal to unity):

$$\begin{aligned}
 k &= \frac{1}{S_0} \iint_S k_0 f^n(r, \phi) r dr d\phi = \\
 &= \frac{1}{S_0} \left(\iint_S k_0 \zeta_0(\lambda r, \phi) r dr d\phi + \right. \\
 &\quad \left. + \sum_{k=1}^n a_k \iint_S k_0 \zeta_k(\lambda r, \phi) r dr d\phi \right), \quad (15)
 \end{aligned}$$

where S is the cross-section of the tube with the area S_0 .

Let us demonstrate the application of this method for cross-sections of different shapes.

The case of a rectangular cross-section of the tube

Let the sides of the rectangle be equal to a and b , with $b \leq a$. We select the origin of the polar coordinate system at the center of the rectangle

and direct the polar axis (from which the polar angle ϕ is measured) parallel to the larger side. Let θ be half the smaller angle between the diagonals, and then the larger angle between the diagonals is equal to $\pi - 2\theta$. Obviously $\text{tg}\theta = b/a$. Then with the coordinate system we have chosen the coordinates (r, ϕ) of the vertices of the rectangle are expressed as

$$\begin{aligned}
 &\left(\frac{\sqrt{a^2 + b^2}}{2}, \text{arctg} \frac{b}{a} \right), \\
 &\left(\frac{\sqrt{a^2 + b^2}}{2}, \pi - \text{arctg} \frac{b}{a} \right), \\
 &\left(\frac{\sqrt{a^2 + b^2}}{2}, \pi + \text{arctg} \frac{b}{a} \right), \\
 &\left(\frac{\sqrt{a^2 + b^2}}{2}, -\text{arctg} \frac{b}{a} \right).
 \end{aligned}$$

Since in polar coordinates the equation of a straight line has the form

$$r = p / \cos(\phi - \alpha),$$

where p is the length of the perpendicular to the straight line from the origin, α is the polar angle of this perpendicular, then it follows from formula (15) that the gain coefficient has the form

$$\begin{aligned}
 k &= \frac{1}{ab} \left\{ \int_{-\text{arctg} \frac{b}{a}}^{\text{arctg} \frac{b}{a}} d\phi \int_0^{\frac{a}{2 \cos \phi}} r dr k_0 f^n(r, \phi) + \right. \\
 &\quad + \int_{\text{arctg} \frac{b}{a}}^{\pi - \text{arctg} \frac{b}{a}} d\phi \int_0^{\frac{b}{2 \sin \phi}} r dr k_0 f^n(r, \phi) + \\
 &\quad + \int_{\pi - \text{arctg} \frac{b}{a}}^{\pi + \text{arctg} \frac{b}{a}} d\phi \int_0^{\frac{a}{2 \cos \phi}} r dr k_0 f^n(r, \phi) + \\
 &\quad \left. + \int_{\pi + \text{arctg} \frac{b}{a}}^{2\pi - \text{arctg} \frac{b}{a}} d\phi \int_0^{\frac{b}{2 \sin \phi}} r dr k_0 f^n(r, \phi) \right\}.
 \end{aligned}$$

With the coordinate system we have chosen,



obviously, there is a symmetry when replacing ϕ with $-\phi$, which means that the function $f^n(r, \phi)$ must be even with respect to ϕ . Similarly, nothing should change in symmetry when replacing ϕ with $\pi - \phi$. This means that the expression

$$\zeta_k(\lambda r, \phi) = J_{2k}(\lambda r) \cdot \cos(2k\phi)$$

should be taken as the function $\zeta_k(\lambda r, \phi)$, i.e., formula (6) takes the following form:

$$f^n(r, \phi) = J_0(\lambda r) + \sum_{k=1}^n a_{2k} J_{2k}(\lambda r) \cdot \cos(2k\phi). \quad (16)$$

The results of the calculations based on the obtained formulae for the rectangular cross-section of the tube for different side ratios a/b ($b = 1$) for $N = 400$ points on the boundary are given in Table 1. For a square, with $a/b = 1$, there is additional symmetry when replacing ϕ with $\phi + \pi/2$, so only the coefficients a_{4k} differ from zero, which is well-confirmed by the calculation.

However, Eq. (2) with boundary condition (3) for a rectangle can be solved exactly in the Cartesian coordinate system. Writing boundary condition (3) in the form

$$\begin{aligned} f(a/2, y) &= f(-a/2, y) = f(x, b/2) = \\ &= f(x, -b/2) = 0 \end{aligned}$$

and using the variable separation method again, we obtain that for the spatial distribution of the gain $f(x, y)$ in the case of a tube with a rectangular cross-section, the general solution of Eq. (2) satisfying condition (3) is the function

$$f(x, y) = C \cos\left(\frac{n\pi}{a} x\right) \cdot \cos\left(\frac{m\pi}{b} y\right),$$

and obtain the following expression for the value of the parameter λ :

$$\lambda_{n,m}^2 = \frac{n^2\pi^2}{a^2} + \frac{m^2\pi^2}{b^2}, \quad n = 1, 2, 3, \dots; \quad m = 1, 2, 3, \dots$$

Normalizing the function f to unity at the center of the cross-section, we obtain $C = 1$. For comparison with the results of the above calculations (data for the first eigenvalue of λ), it is convenient to take the component for which $n = m = 1$. Then the gain coefficient for a tube with a rectangular cross-section can be calculated by formula (1):

$$\begin{aligned} k &= \frac{1}{ab} \int_{-\frac{a}{2}}^{\frac{a}{2}} \int_{-\frac{b}{2}}^{\frac{b}{2}} k_0 \cos\frac{\pi x}{a} dx \cdot \cos\frac{\pi y}{b} dy = \\ &= \frac{4}{\pi^2} k_0 = 0.405 k_0. \end{aligned}$$

Comparing the obtained value of the coefficient with that in Table 1 (bottom column) shows excellent agreement between the results of applying our method (finding both the gain coefficient and the parameter λ) and the exact solution.

The case of a circular cross-section of the tube

An exact solution can also be obtained for this cross-section. If the center of the circle is taken as the origin of the polar coordinate system, the sought-for function does not depend

Table 1

Calculated values of the main parameters of the system depending on the side ratio of the rectangular cross-section of the laser tube

a/b	λ	a_2	a_4	a_6	a_8	a_{10}	a_{12}
1.00	4.44	0.00	-2.00	0.00	2.00	0.00	-1.93
1.10	4.25	0.19	-1.96	-0.56	1.86	0.92	-1.69
1.25	4.02	0.44	-1.81	-1.23	1.27	1.79	-0.51
1.50	3.78	0.77	-1.41	-1.85	-0.02	1.84	1.41
1.75	3.62	1.02	-0.97	-2.00	-1.06	0.92	2.04
2.00	3.51	1.20	-0.56	-1.87	-1.69	-0.16	1.60

The normalized calculated value of the gain coefficient $k/k_0 = 0.405$ (k_0 is the gain on the axis of the system) for all given values of the ratio a/b

on the polar angle ϕ , and after replacing the argument $x = \lambda r$, Eq. (2) becomes an equation for the Bessel function of zero order. Its general solution has the form

$$f(r, \phi) = f(r) = a_0 J_0(\lambda r).$$

Let us normalize the function f to unity again at the center of the cross-section, and then we obtain that $f(r) = J_0(\lambda r)$.

Boundary condition (3) yields the value $J_0(\lambda a) = 0$ for a circle of radius a , and it follows then that the product λa takes the values

$$\lambda a = \lambda_1, \lambda_2, \lambda_3, \dots,$$

where λ_k is the k th root of the function $J_0(x)$.

Since the main contribution to the spatial distribution of the gain is made by the first eigenfunction, $\lambda a = \lambda_1 = 2.4048$. Then by formula (1) we obtain the following expression for the gain coefficient:

$$k = \frac{1}{\pi a^2} \int_0^{2\pi} d\phi \int_0^a r dr k_0 J_0\left(\frac{\lambda_1}{a} r\right) = \frac{2k_0}{\lambda_1^2} J_1\left(\frac{\lambda_1}{a} r\right) \cdot \frac{\lambda_1}{a} r \Big|_0^a = \frac{2k_0}{\lambda_1} J_1(\lambda_1) = 0.432k_0.$$

To test our algorithm, we performed calculations for a circular cross-section of the tube according to the general formula (15), which in this case has the form

$$k = \frac{1}{\pi a^2} \int_0^{2\pi} d\phi \int_0^a r dr k_0 f^n(r, \phi).$$

Since symmetry can be used again to replace the angle ϕ with the angle $-\phi$ and the angle $\pi + \phi$, we can once again take

$$\zeta_k(\lambda r, \phi) = J_{2k}(\lambda r) \cdot \cos(2k\phi),$$

as the function $\zeta_k(\lambda r, \phi)$, and use formula (16) for the function $f^n(r, \phi)$.

We should note that the circular cross-section is that very rare case when, obviously, the first approximation of λ cannot be found from formula (9); therefore, we choose the parameter $\lambda = \lambda_1 / a$ as the first approximation (based on the reasoning given above in the section "First approximation of λ ").

The results of the calculation for $N = 400$ points on the boundary are provided by the equalities

$$a_2 = a_4 = a_6 = a_8 = a_{10} = a_{12} = 0$$

being fulfilled with a high accuracy (the coefficients a_k are of the order of $10^{-16} - 10^{-21}$); the values of the parameter λ and the gain coefficient k also agree well with the theoretical values.

The case of the elliptical cross-section of the tube

An analytically exact expression for the laser gain coefficient cannot be obtained in this case. Let us use the method we propose.

We take the center of the ellipse as the origin of the polar coordinate system, and direct the polar axis along the ellipse's semi-major axis. Let c and d be the semi-axes of the ellipse ($d \leq c$), then the ellipse equation has the form

Table 2

Calculated values of the main parameters of the system as a function of the semi-axes ratio of the elliptical cross-section of the laser tube

c/d	k/k_0	λ	a_2	a_4	a_6	a_8	a_{10}
1.00	0.432	2.41	$<10^{-6}$	$<10^{-6}$	$<10^{-6}$	$<10^{-6}$	$<10^{-6}$
1.10	0.431	2.30	0.14	$2 \cdot 10^{-3}$	$2 \cdot 10^{-5}$	$<10^{-6}$	$<10^{-6}$
1.25	0.430	2.18	0.32	0.01	$2 \cdot 10^{-4}$	$<10^{-6}$	$<10^{-6}$
1.50	0.424	2.04	0.56	0.04	$2 \cdot 10^{-3}$	$3 \cdot 10^{-5}$	$<10^{-6}$
1.75	0.416	1.95	0.75	0.08	$4 \cdot 10^{-3}$	$1 \cdot 10^{-4}$	$<10^{-6}$
2.00	0.408	1.89	0.89	0.13	0.01	$4 \cdot 10^{-4}$	$1 \cdot 10^{-5}$

Notes. 1. The value $c/d = 1.00$ is for the circular cross-section of the tube. 2. All values of $a_{12} < 10^{-6}$. 3. The number of points on the boundary is $N = 400$.

$$r = \frac{cd}{\sqrt{c^2 \sin^2 \phi + d^2 \cos^2 \phi}}.$$

Then, according to formula (15), the gain coefficient follows the expression

$$k = \frac{1}{\pi cd} \int_0^{2\pi} d\phi \int_0^{\frac{cd}{\sqrt{c^2 \sin^2 \phi + d^2 \cos^2 \phi}}} r dr k_0 f^n(r, \phi).$$

Symmetry is again preserved for the ellipse when replacing the angle ϕ with the angle $-\phi$ and $\pi + \phi$, and therefore, we should once again take

$$\zeta_k(\lambda r, \phi) = J_{2k}(\lambda r) \cdot \cos(2k\phi)$$

as the function $\zeta_k(\lambda r, \phi)$ and use formula (16) for the function $f^n(r, \phi)$.

The results of the calculations for an elliptical cross-section of a laser tube with different semi-axes ratios c/d ($d = 1$) for $N = 400$ points on the boundary are given in Table 2 (also listing the result for the circular cross-section with $c/d = 1$).

Conclusion

In this study, we have proposed an improved method for calculating the gain coefficient of laser radiation as a function of the geometry of the tube's cross-section. The method allows to obtain more general and accurate results in comparison with the currently existing options. In the future, we plan to use this method to calculate this coefficient for other shapes of the cross-section of the laser gain medium.

Appendix 1

Expressions for the coefficients a_k with $n = 5$ for the classical Gram – Schmidt method

Let us introduce the following notations:

$$\begin{aligned} \alpha &= \frac{1}{\|\zeta_1\|}; \quad \varepsilon = \frac{\langle \zeta_2, \Psi_1 \rangle}{\|\Psi_1\|^2}; \quad \gamma_1 = \frac{\langle \zeta_3, \Psi_1 \rangle}{\|\Psi_1\|^2}; \\ \gamma_2 &= \frac{\langle \zeta_3, \tilde{Y}_2 \rangle}{\|\tilde{Y}_2\|^2}; \quad \delta_1 = \frac{\langle \zeta_4, \Psi_1 \rangle}{\|\Psi_1\|^2}; \quad \delta_2 = \frac{\langle \zeta_4, \tilde{Y}_2 \rangle}{\|\tilde{Y}_2\|^2}; \\ \delta_3 &= \frac{\langle \zeta_4, \tilde{Y}_3 \rangle}{\|\tilde{Y}_3\|^2}; \quad \omega_1 = \frac{\langle \zeta_5, \Psi_1 \rangle}{\|\Psi_1\|^2}; \quad \omega_2 = \frac{\langle \zeta_5, \tilde{Y}_2 \rangle}{\|\tilde{Y}_2\|^2}; \end{aligned}$$

$$\omega_3 = \frac{\langle \zeta_5, \tilde{Y}_3 \rangle}{\|\tilde{Y}_3\|^2}; \quad \omega_4 = \frac{\langle \zeta_5, \tilde{Y}_4 \rangle}{\|\tilde{Y}_4\|^2};$$

$$\beta_1 = -\langle \zeta_0, \Psi_1 \rangle; \quad \beta_2 = -\langle \zeta_0, \Psi_2 \rangle;$$

$$\beta_3 = -\langle \zeta_0, \Psi_3 \rangle; \quad \beta_4 = -\langle \zeta_0, \Psi_4 \rangle;$$

$$\beta_5 = -\langle \zeta_0, \Psi_5 \rangle.$$

With the above notations, the coefficients a_k take the following form:

$$a_5 = \frac{\beta_5}{\|\tilde{Y}_5\|}; \quad a_4 = \frac{\beta_4}{\|\tilde{Y}_4\|} - \frac{\beta_5 \omega_4}{\|\tilde{Y}_5\|};$$

$$a_3 = \frac{\beta_3}{\|\tilde{Y}_3\|} - \frac{\beta_4 \delta_3}{\|\tilde{Y}_4\|} + \frac{\beta_5 \omega_4 \delta_3 - \beta_5 \omega_3}{\|\tilde{Y}_5\|};$$

$$\begin{aligned} a_2 &= \frac{\beta_2}{\|\tilde{Y}_2\|} - \frac{\beta_3 \gamma_2}{\|\tilde{Y}_3\|} + \frac{-\beta_4 \delta_2 + \beta_4 \delta_3 \gamma_2}{\|\tilde{Y}_4\|} + \\ &+ (\beta_5 \omega_4 \delta_2 - \beta_5 \omega_4 \delta_3 \gamma_2 + \beta_5 \omega_3 \gamma_2 - \beta_5 \omega_2) / \|\tilde{Y}_5\|; \end{aligned}$$

$$a_1 = \beta_1 \alpha - \frac{\beta_2 \varepsilon \alpha}{\|\tilde{Y}_2\|} + \frac{-\beta_3 \gamma_1 \alpha + \beta_3 \gamma_2 \varepsilon \alpha}{\|\tilde{Y}_3\|} +$$

$$\begin{aligned} &+ (-\beta_4 \delta_1 \alpha + \beta_4 \delta_2 \varepsilon \alpha + \beta_4 \delta_3 \gamma_1 \alpha - \\ &- \beta_4 \delta_3 \gamma_2 \varepsilon \alpha) / \|\tilde{Y}_4\| + (\beta_5 \omega_4 \delta_1 \alpha - \beta_5 \omega_4 \delta_2 \varepsilon \alpha - \\ &- \beta_5 \omega_4 \delta_3 \gamma_1 \alpha + \beta_5 \omega_4 \delta_3 \gamma_2 \varepsilon \alpha - \beta_5 \omega_3 \gamma_2 \varepsilon \alpha + \\ &+ \beta_5 \omega_3 \gamma_1 \alpha + \beta_5 \omega_2 \varepsilon \alpha - \beta_5 \omega_1 \alpha) / \|\tilde{Y}_5\|. \end{aligned}$$

Appendix 2

Expressions for the coefficients a_k with $n = 6$ for the modified Gram – Schmidt method

Let us introduce the following notations:

$$\varepsilon = \frac{\langle \zeta_2, \tilde{Y}_1 \rangle}{\|\tilde{Y}_1\|^2}; \quad \gamma_1 = \frac{\langle \zeta_3, \tilde{Y}_1 \rangle}{\|\tilde{Y}_1\|^2}; \quad \gamma_2 = \frac{\langle \zeta_3^{(1)}, \tilde{Y}_2 \rangle}{\|\tilde{Y}_2\|^2};$$

$$\delta_1 = \frac{\langle \zeta_4, \tilde{Y}_1 \rangle}{\|\tilde{Y}_1\|^2}; \quad \delta_2 = \frac{\langle \zeta_4^{(1)}, \tilde{Y}_2 \rangle}{\|\tilde{Y}_2\|^2};$$

$$\delta_3 = \frac{\langle \zeta_4^{(2)}, \tilde{Y}_3 \rangle}{\|\tilde{Y}_3\|^2}; \quad \omega_1 = \frac{\langle \zeta_5, \tilde{Y}_1 \rangle}{\|\tilde{Y}_1\|^2};$$

$$\omega_2 = \frac{\langle \zeta_5^{(1)}, \tilde{Y}_2 \rangle}{\|\tilde{Y}_2\|^2}; \quad \omega_3 = \frac{\langle \zeta_5^{(2)}, \tilde{Y}_3 \rangle}{\|\tilde{Y}_3\|^2};$$

$$\omega_4 = \frac{\langle \zeta_5^{(3)}, \tilde{Y}_4 \rangle}{\|\tilde{Y}_4\|^2}; \quad \rho_1 = \frac{\langle \zeta_6, \tilde{Y}_1 \rangle}{\|\tilde{Y}_1\|^2};$$

$$\begin{aligned} \rho_2 &= \frac{\langle \zeta_6^{(1)}, \tilde{Y}_2 \rangle}{\|\tilde{Y}_2\|^2}; \rho_3 = \frac{\langle \zeta_6^{(2)}, \tilde{Y}_3 \rangle}{\|\tilde{Y}_3\|^2}; \\ \rho_4 &= \frac{\langle \zeta_6^{(3)}, \tilde{Y}_4 \rangle}{\|\tilde{Y}_4\|^2}; \rho_5 = \frac{\langle \zeta_6^{(4)}, \tilde{Y}_5 \rangle}{\|\tilde{Y}_5\|^2}; \\ \beta_1 &= -\langle \zeta_0, \Psi_1 \rangle; \beta_2 = -\langle \zeta_0, \Psi_2 \rangle; \\ \beta_3 &= -\langle \zeta_0, \Psi_3 \rangle; \beta_4 = -\langle \zeta_0, \Psi_4 \rangle; \\ \beta_5 &= -\langle \zeta_0, \Psi_5 \rangle; \beta_6 = -\langle \zeta_0, \Psi_6 \rangle. \end{aligned}$$

The notations introduced are similar to those in Appendix 1, with the exception that not only the functions $\zeta_k(\lambda r, \phi)$ but also $\zeta_k^{(i)}(\lambda r, \phi)$ are present in the corresponding scalar products.

With the above notations, the coefficients a_k take the following form:

$$\begin{aligned} a_6 &= \frac{\beta_6}{\|\tilde{Y}_6\|}; a_5 = \frac{\beta_5}{\|\tilde{Y}_5\|} - \frac{\beta_6 \rho_5}{\|\tilde{Y}_6\|}; \\ a_4 &= \frac{\beta_4}{\|\tilde{Y}_4\|} - \frac{\beta_5 \omega_4}{\|\tilde{Y}_5\|} + \frac{-\beta_6 \rho_4 + \beta_6 \rho_5 \omega_4}{\|\tilde{Y}_6\|}; \\ a_3 &= \frac{\beta_3}{\|\tilde{Y}_3\|} - \frac{\beta_4 \delta_3}{\|\tilde{Y}_4\|} + \frac{-\beta_5 \omega_3 + \beta_5 \omega_4 \delta_3}{\|\tilde{Y}_5\|} + \\ &+ (-\beta_6 \rho_3 + \beta_6 \rho_4 \delta_3 + \beta_6 \rho_5 \omega_3 - \end{aligned}$$

$$\begin{aligned} &- \beta_6 \rho_5 \omega_4 \delta_3) / \|\tilde{Y}_5\|; \\ a_2 &= \frac{\beta_2}{\|\tilde{Y}_2\|} - \frac{\beta_3 \gamma_2}{\|\tilde{Y}_3\|} + \frac{-\beta_4 \delta_2 + \beta_4 \delta_3 \gamma_2}{\|\tilde{Y}_4\|} + \\ &+ (-\beta_5 \omega_2 + \beta_5 \omega_3 \gamma_2 + \beta_5 \omega_4 \delta_2 - \\ &- \beta_5 \omega_4 \delta_3 \gamma_2) / \|\tilde{Y}_5\| + \\ &+ (-\beta_6 \rho_2 + \beta_6 \rho_3 \gamma_2 + \beta_6 \rho_4 \delta_2 - \beta_6 \rho_4 \delta_3 \gamma_2 + \\ &+ \beta_6 \rho_5 \omega_2 - \beta_6 \rho_5 \omega_3 \gamma_2 - \beta_6 \rho_5 \omega_4 \delta_2 + \\ &+ \beta_6 \rho_5 \omega_4 \delta_3 \gamma_2) / \|\tilde{Y}_6\|; \\ a_1 &= \frac{\beta_1}{\|\tilde{Y}_1\|} - \frac{\beta_2 \varepsilon}{\|\tilde{Y}_2\|} + \frac{-\beta_3 \gamma_1 + \beta_3 \gamma_2 \varepsilon}{\|\tilde{Y}_3\|} + \\ &+ (-\beta_4 \delta_1 + \beta_4 \delta_2 \varepsilon + \beta_4 \delta_3 \gamma_1 - \beta_4 \delta_3 \gamma_2 \varepsilon) / \|\tilde{Y}_4\| + \\ &+ (-\beta_5 \omega_1 + \beta_5 \omega_2 \varepsilon + \beta_5 \omega_3 \gamma_1 - \beta_5 \omega_3 \gamma_2 \varepsilon + \\ &+ \beta_5 \omega_4 \delta_1 - \beta_5 \omega_4 \delta_2 \varepsilon - \beta_5 \omega_4 \delta_3 \gamma_1 + \\ &+ \beta_5 \omega_4 \delta_3 \gamma_2 \varepsilon) / \|\tilde{Y}_5\| + (-\beta_6 \rho_1 + \beta_6 \rho_2 \varepsilon + \\ &+ \beta_6 \rho_3 \gamma_1 - \beta_6 \rho_3 \gamma_2 \varepsilon + \beta_6 \rho_4 \delta_1 - \beta_6 \rho_4 \delta_2 \varepsilon - \\ &- \beta_6 \rho_4 \delta_3 \gamma_1 + \beta_6 \rho_4 \delta_3 \gamma_2 \varepsilon + \beta_6 \rho_5 \omega_1 - \beta_6 \rho_5 \omega_2 \varepsilon - \\ &- \beta_6 \rho_5 \omega_3 \gamma_1 + \beta_6 \rho_5 \omega_3 \gamma_2 \varepsilon - \beta_6 \rho_5 \omega_4 \delta_1 + \\ &+ \beta_6 \rho_5 \omega_4 \delta_2 \varepsilon + \beta_6 \rho_5 \omega_4 \delta_3 \gamma_1 - \\ &- \beta_6 \rho_5 \omega_4 \delta_3 \gamma_2 \varepsilon) / \|\tilde{Y}_6\|. \end{aligned}$$

REFERENCES

[1] V.E. Privalov, S.A. Fridrikhov, Zavisimost moshchnosti izlucheniya He-Ne lazera ot geometrii secheniya razryadnogo promezhutki [The dependence of the He-Ne laser emission power on the cross-section geometry of a discharge gap], The Russian Journal of Applied Physics. 38 (12) (1968) 2080 – 2084.

[2] V.E. Privalov, S.F. Yudin, Influence of the shape of a discharge-gap cross section on the gas-laser gain // Quantum Electronics. 1 (11) (1974) 2484–2487.

[3] V.E. Privalov, V.A. Khodovoy, Eksperimentalnoye issledovaniye He-Ne lazera s razryadnym promezhutkom pryamougolnogo secheniya [An experimental investigation of a He-Ne laser with a rectangular cross-section discharge gap], Optics and Spectroscopy. 37 (4) (1974) 797–799.

[4] V.E. Privalov, S.F. Yudin, Vliyaniye granichnykh usloviy na usileniye aktivnoy sredy gazovogo lazera [Influence of boundary conditions on the active medium gain of the gas-laser], J. Appl. Spectr. 22 (1) (1975) 42–46.

[5] V.E. Privalov, S.F. Yudin, Zavisimost usileniya izlucheniya gazovogo lazera ot geometrii

secheniya razryada [Gas-laser emission gain as a function of discharge cross-section geometry], Optics and Spectroscopy. 45 (2) (1978) 340–345.

[6] V.E. Privalov, Gas-discharge geometry and studies in laser emission, Russian Physics Journal. 53 (5) (2010) 80 –90.

[7] V.E. Privalov, Some prospects for the development of gas-discharge lasers, Russian Physics Journal. 56 (2-2) (2013) 246–253.

[8] V.E. Privalov, S.A. Fridrikhov, The ring gas laser, Soviet Physics, Uspekhi. 12 (3) (1969) 153–167.

[9] V.E. Privalov, He-Ne lazerskombinirovannoy razryadnoy trubkoy [He-Ne laser with a combined discharge tube] Elektronnaya tekhnika, Ser. 3: Gas charge devices. No. 3(23) (1971) 29–31.

[10] A.A. Fedotov, V.V. Chernigovskiy, K opredeleniyu moshchnosti izlucheniya He-Ne OKG s konusoobraznoy trubkoy [About radiation power of He-Ne laser with a conic tube], Izvestiya LETI. (140) (1974) 74–77.

[11] S.G. Mikhlin, Variatsionnyye metody v matematicheskoy fizike [Variational methods in mathematical physics], Nauka, Moscow, 1970.



[12] **I.S. Berezin, N.P. Zhidkov**, *Metody vychisleniy* [Calculation methods, in 2 Vols]. Vol. 1, Fizmatlit, Moscow, 1962.

[13] **N.J. Higham**, *Accuracy and stability of numerical algorithms* (2nd ed.), Society for Industrial and Applied Mathematics, Philadelphia, 2002.

Received 26.02.2018, accepted 20.03.2018.

THE AUTHORS

KOZHEVNIKOV Vadim A.

Peter the Great St. Petersburg Polytechnic University
29 Politechnicheskaya St., St. Petersburg, 195251, Russian Federation
vadim.kozhevnikov@gmail.com

PRIVALOV Vadim E.

Peter the Great St. Petersburg Polytechnic University
29 Politechnicheskaya St., St. Petersburg, 195251, Russian Federation
vaepriv@yandex.ru

CHARGE RELAXATION IN PARTIALLY CRYSTALLINE R-BAPB POLYIMIDES UNDER CONDITIONS OF ELEVATED HUMIDITY

M.E. Borisova¹, A.M. Kamalov¹, I.D. Orlov¹, V.E. Smirnova²

¹ Peter the Great St. Petersburg Polytechnic University, St. Petersburg, Russian Federation;

² Institute of Macromolecular Compounds of RAS, St. Petersburg, Russian Federation

The charge relaxation processes in the films based on R-BAPB polyimide with different degree of crystallinity have been studied. The supramolecular structure effect on the charge relaxation processes in the films under elevated humidity conditions was revealed. The obtained experimental data was analyzed in the context of the present-day knowledge of the charge relaxation mechanism. The complex spectra of the thermally stimulated depolarization currents (TSDC) were resolved into individual components and described by the first-order kinetics equations using computer simulation. The TSDC activation energies were calculated and interpreted in terms of the mechanism of release of charge carriers. It was shown that the increment of crystallinity degree of the polyimide films lead to a decrease in the electret state stability at elevated temperature and high humidity.

Key words: polyimide; crystallinity; hygroscopicity; trap; simulation; coronoelectret

Citation: M.E. Borisova, A.M. Kamalov, L.D. Orlov, V.E. Smirnova, Charge relaxation in partially crystalline R-BAPB polyimides under conditions of elevated humidity, St. Petersburg State Polytechnical University Journal. Physics and Mathematics. 11 (2) (2018) 88 – 95. DOI: 10.18721/JPM.11209

Introduction

As polymer electrets are gaining wider applications, there is a continued effort to find methods for slowing down the charge relaxation processes in dielectrics and for increasing the stability of the electret state. The properties of polymers are typically adjusted by modifying their surface and structure and by introducing various fillers into the polymer [1 – 3]. The study of charge relaxation processes in polymer films presents an additional interest because the field of a charged dielectric affects the electrical properties of the entire insulation system in which it is used.

Polyimides are a class of polymers that has been in demand in industry for many years. Despite their high costs, polyimide films are widely used due to their heat resistance, high electrical and mechanical characteristics [4]. New types of polyimides are constantly developed, and the existing types are modified to enhance certain characteristics of the material.

One of the main problems of using polyimides in electrical insulators and electret devices is their low resistance to moisture [5, 6]. If polyimide insulation is in a humid environment for a long time, its electrical insulation properties deteriorate rapidly, increasing the conductivity of the insulation and the instability of the dielectric capacitance. A great deal of studies have been dedicated to investigating and improving the moisture-resistant characteristics of polyimides.

The goal of this study is to determine the effect of moisture on the charge relaxation process in R-BAPB polyimide films with different degrees of crystallinity, developed at the Institute of Macromolecular Compounds of the Russian Academy of Sciences in order to create thermally stable thermoplastic polyimides that compare favorably to foreign equivalents (PEEK, ULTEM, PPS).

Experimental procedure

The experimental samples were the films of

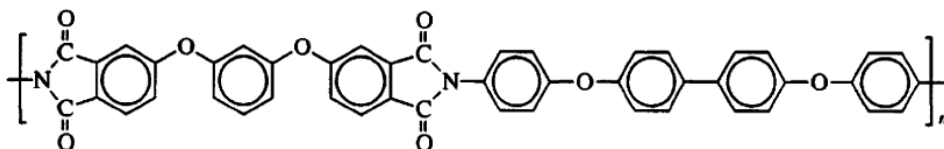


Fig. 1. The chemical formula of R-BAPB polyimide

R-BAPB polyimide (Fig. 1) based on 1,3-bis (3,3'-4,4'-dicarboxyphenoxy) benzene (R dianhydride) and 4,4'-bis (4-aminophenoxy) biphenyl (BAPB diamine) with the degrees of crystallinity of 0, 20 and 40%.

The effect of supramolecular structure of the R-BAPB material on the stability of the electret state under elevated humidity was studied in this paper.

A series of R-BAPB polyimide films with different degrees of crystallinity were heated to remove moisture and residual static charge for one hour at a temperature of 160 °C, and then kept in a desiccator at a humidity of 98% for 24 h. The second series of control samples were not hydrated. The films were then charged in air with a negative corona discharge under normal environmental conditions. An electret with a homocharge, where the charge carriers are localized at energy levels (traps) in the thin near-surface layer of the dielectric, is formed as a result of such charging [7, 8].

We studied electric charge relaxation in the

resulting electrets by the method of thermally stimulated depolarization currents (TSDC) with a constant heating rate $\beta = dT/dt = 2$ K/min maintained for the samples. The measurements were carried out with a blocking contact between the electrode and the sample. To achieve a blocking contact, an insulating layer made of a 40- μm -thick polytetrafluoroethylene film was placed on the charged surface of the film. In this case, the direction of the depolarization current coincided with the direction of motion of charged particles through the bulk of the sample.

The degree of hydration Γ of the samples was calculated from the increase in their mass (in percent) after exposure to 98% humidity for a certain time according to the following formula:

$$\tilde{A} = \frac{m - m_0}{m_0} \cdot 100\%,$$

where m_0 is the initial mass of the sample, m is the mass of the sample after hydration.

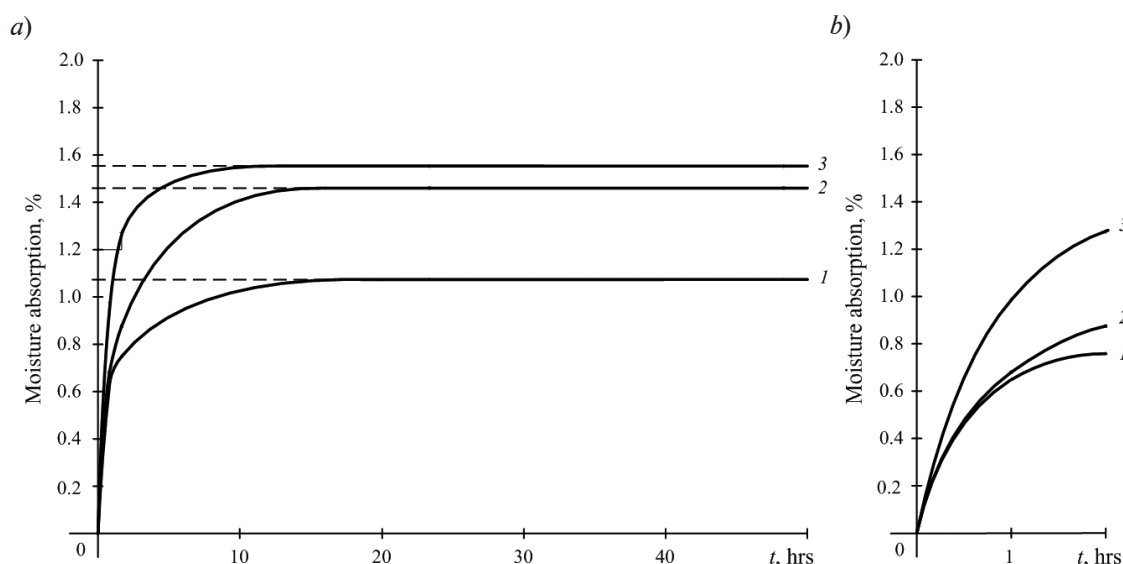


Fig. 2. Moisture absorption dependences of R-BAPB polyimide films with different degrees of crystallinity (DoC) versus the hydration time in the ranges (0 – 50) h (a) and (0 – 2) h (b); DoC, %: 0 (1 is the amorphous sample), 20 (2) and 40 (3)

Table 1

Maximum hygroscopicity values of R-BAPB polyimide samples with different degrees of crystallinity

Degree of crystallinity, %	0 (amorphous)	20	40
Maximum hygroscopicity, %	1.07	1.46	1.55

The humid environment was generated in a desiccator with an aqueous solution of copper sulfate.

Results and discussion

Hygroscopicity study. The curves obtained for the increase in the mass of films with different degrees of crystallinity depending on the hydration time are shown in Fig. 2. Evidently, hygroscopicity of polyimide films increases with increasing degree of crystallinity of the material. The maximum hydration levels of the samples are given in Table 1.

The maximum hygroscopicity values obtained were lower than for the samples of industrial PM polyimide, whose hygroscopicity is 2.3 – 3.0% [9].

Polyimide films absorb moisture within 10 – 18 h; samples with a higher degree of crystallinity reach the hydrated state faster and adsorb more moisture than amorphous samples. The increase in hygroscopicity can be explained by a larger interface between the crystalline and amorphous phases of the material. An additional free volume evolves in the region of this interface. Fig. 3 shows micrographs of the film surface for an amorphous sample and a polyimide sample with a degree of crystallinity of 40% (at two magnifications). It can be seen from the photographs that as the degree of crystallinity of polyimide increases, its structure loosens and the degree of heterogeneity of the material increases, which is accompanied by a growing amount of micropores.

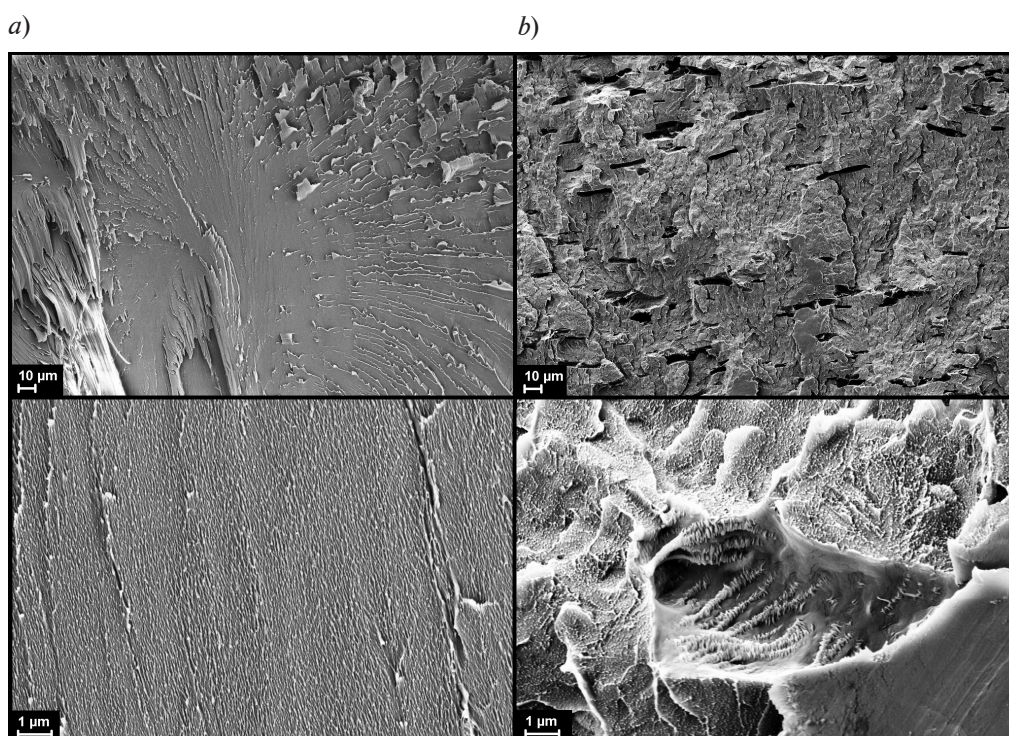


Fig. 3. Micrographs of the surface of R-BAPB polyimide films with different degrees of crystallinity: *a* is the amorphous sample, *b* is the sample with DoC = 40%; images with different magnifications are shown

Charge relaxation studies. Fig. 4 shows the TSDC spectra of the hydrated and non-hydrated polyimide films with different degrees of crystallinity. Comparing these spectra for two series of films indicates that hydration changes the behavior of the curve and leads to a shift in the temperature of the current maxima.

The obtained TSDC spectra, appearing to be curves with one or two peaks, have a complex character. As the degree of crystallinity of the material increases, the low-temperature peak grows. This maximum most likely due to the release of the charge from additional traps formed at the interface between the amorphous

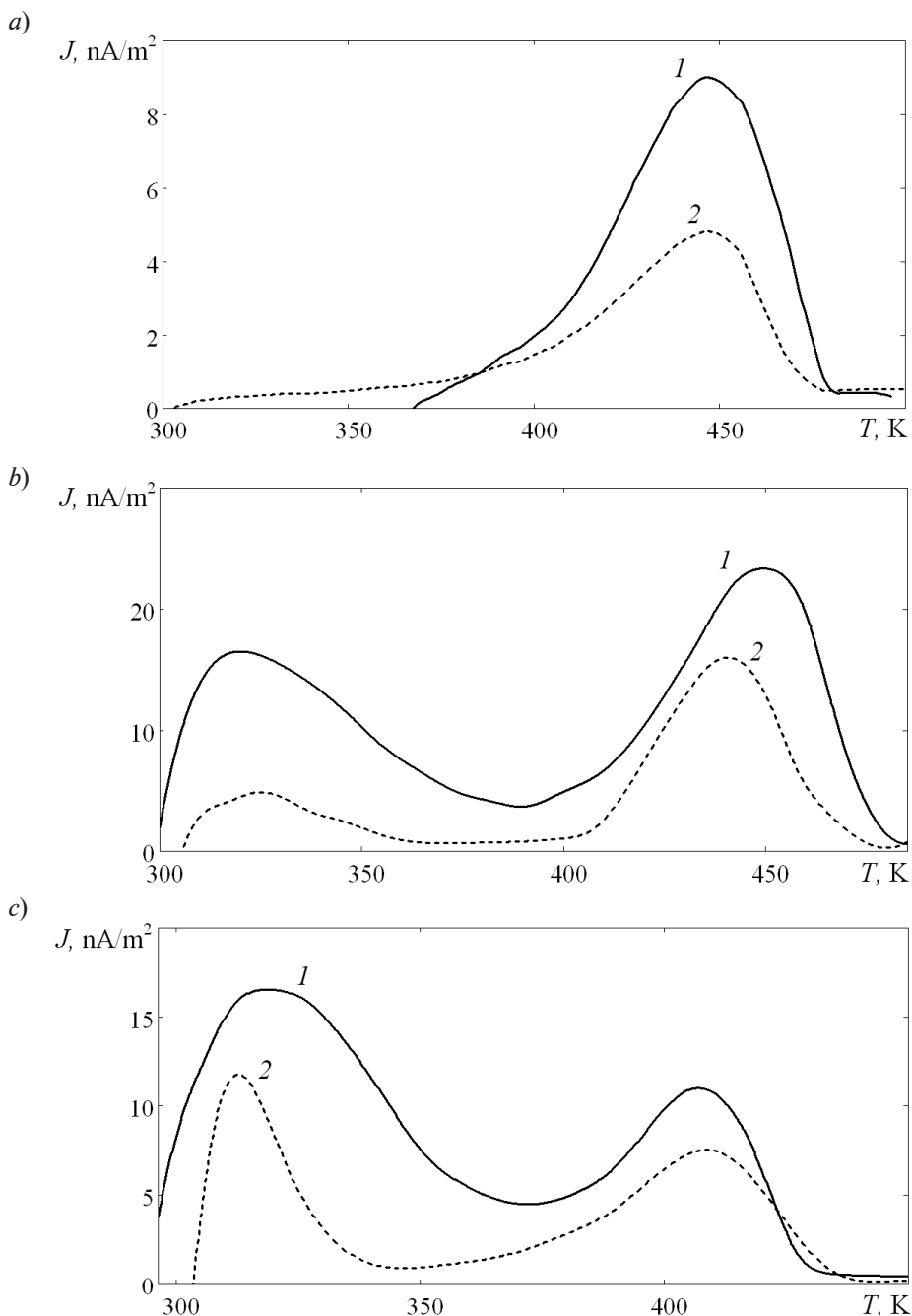


Fig. 4. TSDC spectra of the heated (1) and hydrated (2) polyimide film samples with different degrees of crystallinity, %: 0 (a), 20 (b), 40 (c)

and crystalline phases.

As established in [10], the high-temperature maximum is due to intrinsic conductivity of the R-BAPB polyimide for all polyimide films (with the degrees of crystallinity of 0, 20, and 40%).

It can be seen from the experimental curves in Fig. 4 (dashed lines) that sample hydration leads to reduction in the area under the TSDC curve, i.e., a decrease in the charge accumulated in the sample. The most significant change in the spectrum is observed in the low-temperature region. A possible explanation for this is that the moisture absorbed in the sample creates new traps, localized mainly in the near-surface regions. It is known that sorbed water can exist in polymers in three states: free, moderately and strongly bound. Each of these states affects the charge accumulation and relaxation processes in different ways. Free water in the polymer increases its conductivity, while the water in the moderately and strongly bound states forms new trapping levels resulting from hydrolysis-induced breakdown of cyclic imides. Both negatively charged hydrogen vacancies evolving in benzene rings and COOH groups as a result of hydration can act as such trapping levels. Positively charged NH⁺ groups, which are also formed due to breakdown of cyclic imides in the polymer can act as trapping levels as well

[5, 11 – 15].

Analysis of TSD currents. The obtained TSDC spectra of the dried and hydrated samples were analyzed by “fitting” based on the model of superposition of elementary Debye peaks $\sum_{1,2,3}^n J_n$ governed by first-order kinetics. In this case, the TSD current density J_{TSD} of each peak is described by the expression

$$J_{TSD} = J_m \exp\left[\frac{W}{k}\left(\frac{1}{T_m} - \frac{1}{T}\right)\right] \times \exp\left\{-\frac{W}{kT_m^2} \int_{T_0}^T \exp\left[\frac{W}{k}\left(\frac{1}{T_m} - \frac{1}{T'}\right)\right] dT'\right\},$$

where the peak current density J_m is calculated as

$$J_m = \frac{\varepsilon\varepsilon_0\varepsilon_{lay}U_{e0}}{(\varepsilon h_{lay} + \varepsilon_{lay}h)\tau_m} \times \exp\left\{-\frac{W}{kT_m^2} \int_{T_0}^{T_m} \exp\left[\frac{W}{k}\left(\frac{1}{T_m} - \frac{1}{T'}\right)\right] dT'\right\}.$$

Here ε_{lay} and h_{lay} are the dielectric permittivity and the thickness of the insulating layer; k is Boltzmann constant; T_0 and T' are the initial and the final temperatures, respectively; T_m is the temperature in the current density peak J_m ;

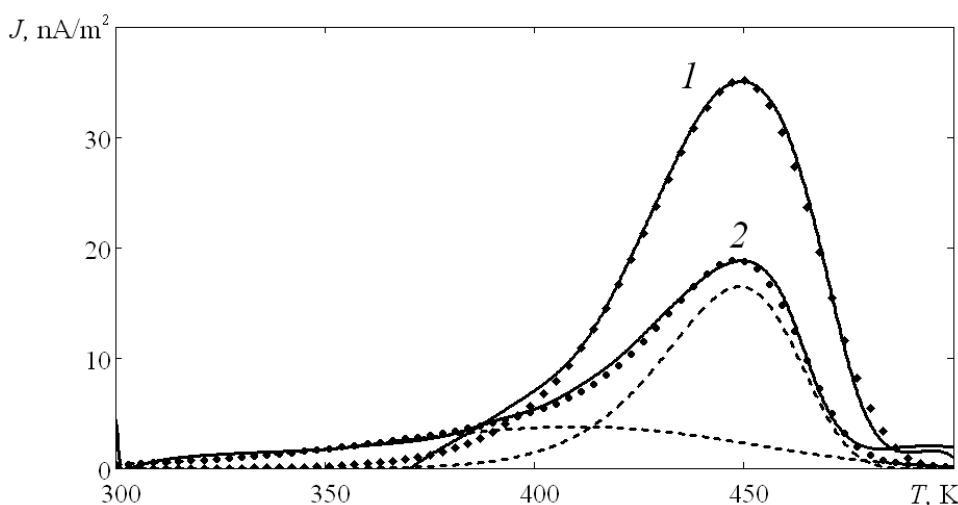


Fig. 5. Experimentally measured (solid lines) and calculated (dotted lines) TSDC spectra for the non-hydrated (1) and hydrated (2) amorphous polyimide films.

The dashed line for spectrum 2 is the result of decomposition into elementary components (see Table 2, data for the second sample)

ε and h are the dielectric permittivity and the thickness of the sample film; U_{e0} is the initial value of the potential difference in the electret; τ_m is the relaxation time at peak temperature, and ε_0 is the dielectric constant.

The relaxation time is described by the expression

$$\tau = \tau_m \exp\left(\frac{W}{kT} - \frac{W}{kT_m}\right).$$

The calculations are based on the characteristic values of the peak current density J_m and the peak temperature T_m , which are determined from the experimental TSDC data; the value of the activation energy W varies in this case.

Table 2 lists the results of calculations using the above-described simulation method. An example of decomposition of the TSDC spectra into elementary peaks is shown in Fig. 5 for

amorphous samples.

As a result of processing the experimental data by mathematical modeling methods, the number of elementary Debye peaks in the TSDC spectra increases. It is established that hydration of polyimide films induces additional relaxation mechanisms, which is accompanied by new elementary current density peaks appearing on the experimental spectra.

Conclusion

Based on the results of the study, the following conclusions can be drawn:

regardless of the degree of crystallinity, the R-BAPB polyimide is less hygroscopic than the industrially used PM polyimide (1.55% for R-BAPB versus 2.30% for PM). Therefore, it is expedient to use this material under high humidity and temperature;

Table 2

Main parameters of the experimental TSDC spectra decomposed into elementary peaks for R-BAPB polyimide films

Film		Peak position T_m , K	Activation energy W , eV
DoC, %	H ₂ O		
0	–	449	0.83
0	+	449	1.05
		410	0.30
20	–	448	0.93
		367	0.58
		337	0.52
		314	0.50
20	+	441	1.10
		367	0.58
		339	0.75
		321	0.70
40	–	407	1.00
		362	0.65
		333	0.61
		313	0.58
40	+	409	0.90
		348	0.50
		320	0.80
		312	1.20

Notes. The zero degree of crystallinity (DoC) corresponds to an amorphous film; a plus in the H₂O column indicates that the film was hydrated

the hygroscopicity of the films increases from 1.07 to 1.55% as the degree of crystallinity of the R-BAPB polyimide increases from 0 to 40%, leading to a decrease in the charge relaxation time. This is likely due to a change in the structure of the film, with a large number of micropores evolving and the free volume of the polymer increasing;

the TSDC spectra become more complex with increasing degree of crystallinity of the samples: low-temperature peaks emerge and grow, indicating that the charge relaxation region shifts towards low temperatures and the electret properties of the material become less stable;

hydration of the material under consideration leads to a change in the charge relaxation mechanisms, accompanied by transformation of the TSDC spectra. For example, the spectrum of an amorphous material gains a shoulder at low temperatures.

To summarize, we have established that moisture affects the charge relaxation process in R-BAPB polyimide films with different degrees of crystallinity, developed at the Institute of Macromolecular Compounds of the Russian Academy of Sciences. We can recommend this material for use under elevated humidity and temperature.

REFERENCES

- [1] **V.E. Yudin, V.M. Svetlichnyy**, Vliyaniye struktury i formy nanochastits napolnitelya na fizicheskiye svoystva poliimidnykh kompozitov [Influence of the structure and the shape of filler's nanoparticles on the physical properties of polyimide composites]. Rossiyskiy khimicheskiy zhurnal. 53 (4) (2009) 75–85.
- [2] **V.E. Yudin, V.M. Svetlichnyi, A.N. Shumakov, et al.**, Morphology and mechanical properties of carbon fiber reinforced composites based on semicrystalline polyimides modified by carbon nanofibers, Composites: Part A. 39 (1) (2008) 85–90.
- [3] **E. Itoh, M. Iwamoto**, Electronic density of state in metal/polyimide Langmuir–Blodgett film interface and its temperature dependence, J. Appl. Phys. 81 (4) (1997) 1790–1797.
- [4] **M.I. Bessonov, V.A. Zubkov**, Polyamide acids and polyimides: Synthesis, transformations, and structure, CRC Press, London, 1993.
- [5] **N.A. Galichin, M.E. Borisova**, The influence of partial discharges on spectra of thermally stimulated depolarization currents, Izvestiya RGPU im. A.I. Gertsena. (79) (2009) 120–127.
- [6] **N.A. Galichin, M.E. Borisova**, Vliyaniye povyshennoy vlazhnosti na stabilnost elektretnogo sostoyaniya v poliimidnykh plenkakh [The influence of elevated humidity on the electretic state stability in polyimide films], Elektrotehnika. (3) (2007) 24–28.
- [7] **Gu Xu, C.C. Gryte, A.S. Nowick, et al.**, Dielectric relaxation and deuteron NMR of water in polyimide films, J. Appl. Phys. 66 (11) (1989) 5290–5297.
- [8] **N.R. Tu, K.C. Kao**, High-field electrical conduction in polyimide films. J. Appl. Phys. 85 (10) (1999) 7267–7275.
- [9] **G.G. Raju**, Dielectrics in electric fields, CRC Press, New York, 2003.
- [10] **M.E. Borisova, A.M. Kamalov, V.E. Smirnova, et al.**, The influence of crystallinity degree on the charge relaxation in R-BAPB polyimides, Polymer Science. 60A (3) (2018) 1–6.
- [11] **Z.Y. He, B.X. Du, J. Li, et al.**, Surface charge behaviors of polyimide/Al₂O₃ nanocomposite films after water absorption, Proc. 1st Intern. Conf. on Dielectrics (ICD 2016), 3–7 July 2016, Montpellier (France) (2016) 301–304.
- [12] **J. Melcher, Y. Daben, G. Arlt**, Dielectric effects of moisture in polyimide, IEEE Trans. Electr. Insulation. 24 (1) (1989) 31–38.
- [13] **N.A. Galichin, M.E. Borisova**, Vliyaniye baryernogo razryada na nakopleniye vlagi v poliimidnykh plenkakh [An influence of a barrier discharge on moisture accumulation in the polyimide films], Proc. of XII All-Russian Conf. on the Problems of Science and Higher School “Basic Research and Innovations in Technical Universities”, May 14, 2008, St. Petersburg, Pp. 237–238.
- [14] **P. Ma, Y. Zhang, F. Zheng, et al.**, Investigation of surface and bulk charge traps of polyimide film by using the photo-stimulated discharge method, Europhysics Letters. 109 (2) (2015) 27006.
- [15] **R. Khazaka, M.L. Locatelli, S. Diahm, et al.**, Broadband dielectric spectroscopy of BPDA/ODA polyimide films, J. Phys. D, Appl. Phys. 46 (6) (2013) 065501.

Received 27.03.2018, accepted 29.03.2018.



THE AUTHORS

BORISOVA Margarita E.

Peter the Great St. Petersburg Polytechnic University

29 Politechnicheskaya St., St. Petersburg, 195251, Russian Federation
vladimirl.borisov@gmail.com

KAMALOV Almaz M.

Peter the Great St. Petersburg Polytechnic University

29 Politechnicheskaya St., St. Petersburg, 195251, Russian Federation
l.almaz.kamalov@gmail.com

ORLOV Ivan D.

Peter the Great St. Petersburg Polytechnic University

29 Politechnicheskaya St., St. Petersburg, 195251, Russian Federation
ivaorlov@yandex.ru

SMIRNOVA Valentina E.

Institute of Macromolecular Compounds RAS

31 Bolshoy Ave. V.O., St. Petersburg, 199004, Russian Federation
ves@hq.macro.ru

THE ION EMISSION DURING THE FRACTURE OF POLYMERS

V.A. Pakhotin¹, V.A. Zakrevskii¹, N.T. Sudar², A.A. Apaseyev²

¹ Ioffe Institute of the Russian Academy of Sciences, St. Petersburg, Russian Federation;

² Peter the Great St. Petersburg Polytechnic University, St. Petersburg, Russian Federation

The results of the study of charged particle emission in the course of the rupture of polymer film samples in the high vacuum have been presented. Regularities of ion emission at the last stages of the stretching are associated with peculiarities of the main crack's intergrowing. Calculations of ion-motion trajectories within the crack were carried out. It was established that the ions emitted from the crack tip on the sample surface were recorded experimentally while the crack growing. The emitting region size and the emission current level were estimated. Mechanisms of formation of low-molecular ions during polymer fracture were discussed.

Key words: emission, ion, mechanoemission, ionization of macromolecules, crack

Citation: V.A. Pakhotin, V.A. Zakrevskii, N.T. Sudar, A.A. Apaseyev, The ion emission during the fracture of polymers, St. Petersburg Polytechnical State University Journal. Physics and Mathematics. 11 (2) (2018) 96 – 105. DOI: 10.18721/JPM.11210

Introduction

Experimental and theoretical study of the processes occurring during the propagation of a main crack in polymers has long attracted the attention of researchers [1 – 7]. The thermophysical properties of a growing crack are discussed in [1 – 3]. Ref. [1] presented a physical model of a polymer heated near the crack tip and described experiments whose results were in good agreement with theoretical predictions. The change in temperature with time in polymethylmethacrylate is due to sequential stretching and breaking of polymer chains in micro-regions about 130 μm in size, located along the trajectory of crack propagation [2]. The effect of heat released under viscoplastic shear on polymer strength was considered in [3]. Refs. [4, 5] were dedicated to the propagation rate of the main crack; Ref. [4] established the role of strain hardening in the process of macroscopic crack propagation in polyolefins. Non-uniform motion of a crack in a polymethyl methacrylate plate was observed experimentally using an ultrafast streak camera both for quasi-static and impulse loading [5]. The fracture regions at the crack tip of glassy polymers were investigated by optical interferometry [6]; it was revealed that the size of these regions can reach tens of microns. The nature of polymer strength remains an important issue, and new methods should be used to study the processes occurring during polymer fracture

(in particular, at the molecular level).

Deformation and fracture of polymers in vacuum are accompanied by emission (mechanoemission) of charged particles (electrons and ions). Emission of electrons during the deformation of polymers has been studied in sufficient detail [7 – 9]; considerably less attention has been paid to mechanoemission of ions. Emission of charged particles was investigated in [9 – 13] both in the pre-fracture stages of sample loading and under fracture. The studies in [9] were mostly limited to filled polymers where fracture occurs at the interface and leads to long-lasting post-emission of positive ions after sample failure. Emission of positive ions during the deformation of polyethylene at the pre-fracture stage was detected in the experiments described in [10, 11]. Ref. [12] reported on the emission of both positive and negative ions during the propagation of a main crack in a number of polymer films. The emission of positive ions was also detected under fracture of auto-adhesive compounds of amorphous polymers formed at temperatures below the bulk glass-transition temperature [13].

It was revealed in [8, 14, 15] for mechanically stressed polymers that a transition of electrons to deep traps may occur with subsequent decay of weak interatomic bonds in the generated positive macroions due to a decrease in the ionization energy of elongated macromolecules. The observed mechanoemission of



cations is likely associated with this separation of charges and with the rupture of interatomic chemical bonds in the macromolecules under stress. It is assumed in [12] that anions form because electrons in polymers can be captured by atomic groups with a positive electron affinity. Ref. [16], reporting on polypropylene fracture in a ball mill at 77 K, found using the EPR method that the electrons were captured by the molecules of the acceptor (tetracyanoethylene), specially embedded into the bulk of the polymer. This indicates that some of the electrons attach to neutral molecules, with negative ions forming, in the regions where fracture occurs.

Apparently, positive ions are emitted in the form of low molecular weight fragments of molecules. It was discovered in [17], where a loaded atomic chain was studied by the molecular dynamics method and the Morse potential was used to describe the interatomic interaction, that a stretched chain of atoms breaks into several fragments upon release, as a result of propagation of a relaxation wave. The chain consisted of forty atoms and was stretched with a force equal to 0.99, corresponding to the tensile strength of the interatomic bond. The first fracture of the chain was associated with superposition of tensile pulses (the incident and the reflected from the fixed end). Fracture of the fragments that broke away occurred due to reflection of waves from the free ends formed and their interference.

A polymer near a growing crack heats up to a temperature $T = 500$ K [18, 19], and up to $T > 1000$ K according to the data of [20, 21]. Thermal degradation of polyethylene terephthalate occurs at a sufficiently high rate at a temperature $T \approx 560$ K [22]. The emission of ions might be caused by thermal desorption of low molecular weight fragments of molecules from the polymer surface.

This study is dedicated to measuring the intensity of ion emission that occurs under fracture of polymer films of different thicknesses in vacuum; the trajectories of ions have been calculated. Our goal has been to determine whether the emission of ions from a crack can be detected, and to assess the sizes of the emitting region and the level of the emission current.

Experimental procedure

The experimental samples were industrial films of polyethylene terephthalate (PET) and PM-1 polyimide (PI). The dumbbell-shaped samples were mounted in a vacuum chamber using metal clamps and insulating sleeves. The widths of the working part of the samples were 1.0; 1.8 and 8 mm, and their length was 5 mm. The thicknesses of the samples were 20 and 100 μm for the PET films, and 40 μm for PI. The samples were deformed at room temperature at a constant rate of 25 mm/s (the samples were not notched). The samples were stretched in a stainless steel chamber at a residual gas pressure no more than 10^{-7} mm Hg and at room temperature.

The emission intensity was measured in the particle-counting mode using a VEU-6 secondary electron multiplier with a grounded cathode. The multiplier was located at a distance $L = 0.28$ m from the sample so that a magnetic field could be generated between the sample and the particle detector. As we measured mechanoemission, a transverse magnetic field was induced with two flat permanent magnets in order to separate the ionic component in the current of negatively charged particles through deflecting the electrons by this field.

The magnetic induction in the central region between the magnets was 0.036 T.

To separate the emission current, the particles were accelerated in the gap between the insulated electrode and the grounded grid installed at the input of the drift space (flight tube). For this purpose, a potential of 1000 V, whose sign coincided with the sign of the charge of the detected particles, was applied to the electrode. The distance between the electrode and the grid was $l = 22$ mm (Fig. 1, *b*). Since the setup had only one detection channel, particles with the charge of only one sign could be detected in testing one sample. The pulses from the particle detector were amplified and simultaneously fed to an intensity meter with a resolution of 1 ms and a time analyzer with a resolution of 1 μs . The intensity meter and the time analyzer, the tools for tuning and adjusting them, and the means for visualizing the time dependences, including the sample loading curves were implemented via a personal computer with the corresponding

software. The experimental setup and the emission detection system are described in more detail in [12]. To assess the actual duration and nature of the emission under sample fracture, the signal was simultaneously fed to the time analyzer with a resolution of $1 \mu\text{s}$, triggered by pulses corresponding to the intergrowth of the main crack.

Experimental samples and discussion

A typical dependence of the emission of negative particles on time t under deformation

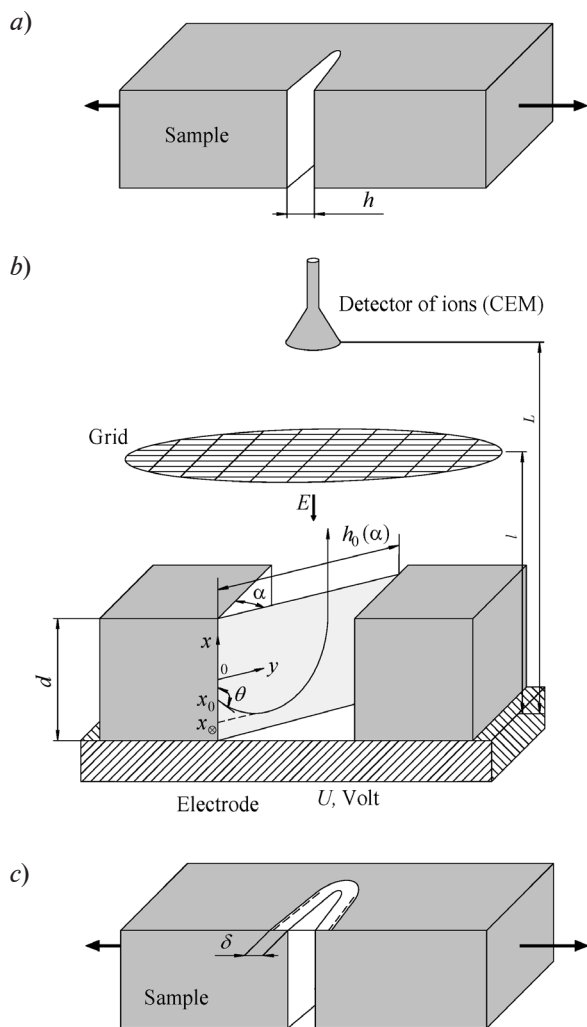


Fig. 1. Schematics illustrating sample fracture and ion emission from a crack in the polymer: *a* is a stretched sample with the main crack; *b* is the layout of the experimental setup and the parameters of the ion trajectory; *c* is the emitting region of width δ on the surface of the film

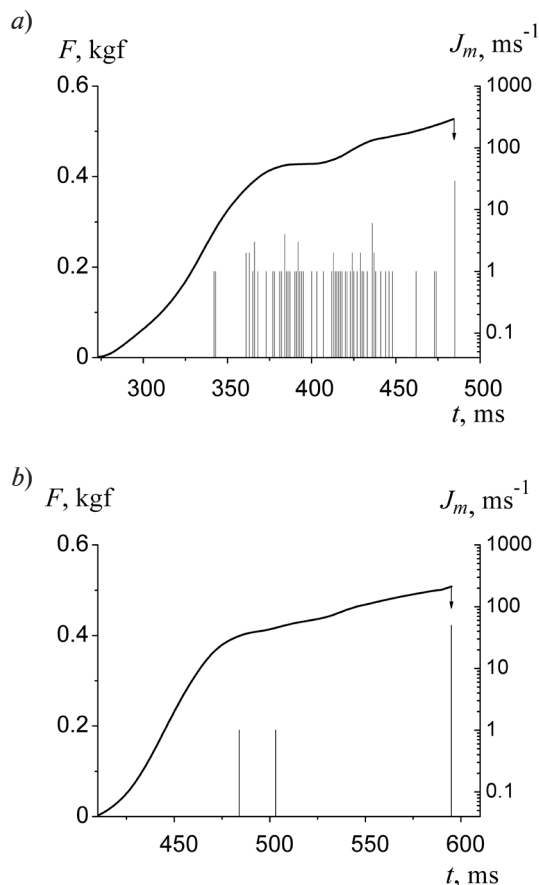


Fig. 2. Loading kinetics F for a polyimide film sample (lines with arrows) and the dynamics of the emission of negative particles from the sample under stretching (the vertical segments are the number of pulses J_m recorded per 1 ms), without (*a*) and with (*b*) a magnetic field applied. The thickness of the sample was $40 \mu\text{m}$, the width was 1.8 mm . The tensile speed was 25 mm/s

of a PI film is shown in Fig. 2. This emission was detected by the number of pulses J_m generated per 1 ms.

Arrows indicate rupture times. Similar $J_m(t)$ dependences were observed for other polymers. Evidently, only individual negative ions are emitted in the presence of a magnetic field until the film ruptures (electrons do not enter the multiplier). The number of negatively charged particles emitted at the time of rupture practically does not depend on the absence or presence of the magnetic field. This means that negative ions are emitted during crack propagation, and the electron emission component is absent.



The dependences similar to those shown in Fig. 2,*b* were also recorded for positive ions. In this case, a positive potential was applied to the electrode, and the corresponding retarding electric field stopped the negative particles. Thus, both positive and negative ions are emitted during polymer rupture. It can be seen from Fig. 2 that the emission burst at the instant of rupture lasts no longer than 1 ms.

The results of determining the actual duration and nature of the emission under sample rupture for PET films of different thicknesses, conducted simultaneously with the above-described experiments (see Fig. 2), are presented in Fig. 3 as the dependence of the emission intensity J_μ of negative ions on time. Apparently, the samples whose thicknesses differed by a factor of five had the same emission intensity. Only the duration of the emission and, accordingly, the total number of detected ions differed, since the samples had different widths. The duration of the emission increased with increasing sample width. For example, emission lasted three times longer for the samples with a width of 8 mm than for the samples with a width of 1 mm. Pauses in emission, whose number increases for wider samples, are also clearly visible. As established in [12], a sharp decrease in ion emission intensity is associated with the retardation of the main crack. The times of occurrence and the duration of the pauses in emission depend on the physico-mechanical properties of the polymer.

These results confirm the conclusion made earlier in [12], where it was found that the observed ion emission occurs only when the crack moves. That study also proposed a method for calculating the emission current taking into account the cross-sectional area of the sample. The emission intensity determined using this method was in good agreement with the experimental results.

Let us now discuss the absence of the dependence of ion emission intensity on film thickness that we have observed (see Fig. 3).

Calculation of the coefficient of ion emission from the crack

The coefficient of ion emission from the crack has to be determined to calculate the ion emission current. It follows from our experi-

ments that ion emission follows the motion of the crack without inertia. This is confirmed, in particular, by the fact that the pauses in emission intensity shown in Fig. 3 start and end quickly. Emission is observed in the first microseconds after fracture evolves in the sample (the start of the intergrowth of the main crack). The crack opens to $h = V_d t_0 = 0.025 \mu\text{m}$ in time $t_0 = 1 \mu\text{s}$ at a tensile speed $V_d = 25 \text{ mm/s}$. Since approximately the same number of ions is emit-

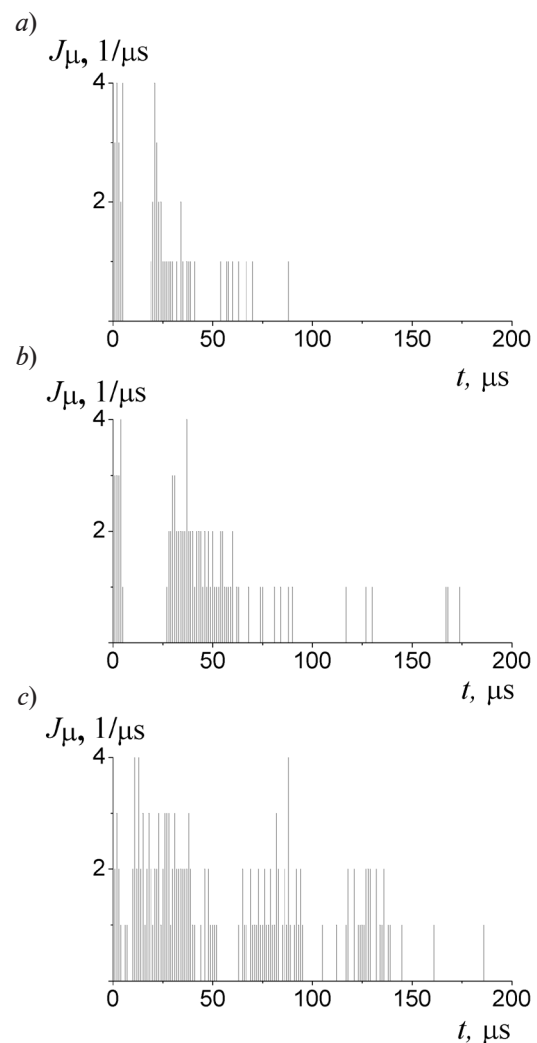


Fig. 3. Dynamics of emission intensity of negative ions (J_μ is the number of pulses recorded per $1 \mu\text{s}$) during crack propagation in PET samples with different thicknesses d and widths B : *a* – $d = 100 \mu\text{m}$, $B = 1.0 \text{ mm}$; *b* – $d = 20 \mu\text{m}$, $B = 1.8 \text{ mm}$; *c* – $d = 20 \mu\text{m}$, $B = 8 \text{ mm}$.

The tensile speed for the film stretching was 25 mm/s

ted each microsecond during the intergrowth of the crack, we assume that the distance between the walls of the crack near its tip is $h = 0.025 \mu\text{m}$. The crack propagation velocity in PET was found in [12] to be $V_c = 40 \text{ m/s}$ (the duration of ion emission was used in the calculations). Thus, the crack should move by $40 \mu\text{m}$ each microsecond, (see Fig. 1, *a, b*).

In order to determine whether the ions that have escaped from the walls of the crack are detected, we calculated all possible trajectories of the ions emitted from different points of the crack wall at different angles. Since the trajectory of an emitted ion lies in a plane passing through the vectors of initial velocity and electric field strength, the three-dimensional problem can be reduced to a two-dimensional one by searching through the ion trajectories lying in these planes. For this purpose, we solved the equation of motion of an ion in a plane parallel to the vector \mathbf{E} and making an angle α with the wall of the crack. As a result, we obtained an equation for the particle trajectory in rectangular coordinates x, y with the origin at $(d/2, 0)$ (see Fig. 1, *b*):

$$x(y) = x_0 + y \operatorname{ctg}\theta + \frac{y^2}{4 \sin^2 \theta} \frac{qE}{W}, \quad (1)$$

where x_0 is the initial exit coordinate, θ is the angle between the vector of the initial particle velocity and the x axis, q is the unit charge, $E = U/l$ is the retarding electric field strength (U is the electrode potential, l is the distance between the electrode and the grid), $W = kT$ is the initial particle energy (k is the Boltzmann constant).

Next, we determined the number N_e of particles that escaped from the crack. Let us denote the total number of the emitted particles as N_s , which is expressed as

$$N_s = n_x n_\theta n_\alpha, \quad (2)$$

where the numbers n are equal to the number of points taken for calculation by the corresponding coordinates. The variation ranges of the numbers n with respect to the coordinates x_0 and θ are obvious.

The greatest value of the angle α is determined by the crack propagation velocity V_c :

$$\operatorname{tg}\alpha_m = \frac{2h}{V_c t_0} = \frac{2V_d}{V_c}. \quad (3)$$

We assumed that only those ions whose trajectories did not intersect the opposite wall of the crack and the surface of the electrode escaped from the crack. Therefore, the first condition for determining the number of ions escaped from the crack is the following: $x(h_0) > d/2$. The second is the condition for the turning point: $x_\otimes > -d/2$. With these conditions in mind, the following formula holds true for the relative number of emitted ions:

$$\eta_e(\alpha, \theta) = \frac{1}{N_s} \sum_1^{n_x} \Phi \left\{ \left[x[h_0(\alpha)] - \frac{d}{2} \right] \right\} \times \Phi \left[x_\otimes(\theta) + \frac{d}{2} \right], \quad (4)$$

where Φ is the unit step function, and

$$x_\otimes(\theta) = x_0 - \frac{dW}{Uq} \cos \theta, \quad (5)$$

$$h_0 \alpha = \frac{V_d \cdot t_0}{\sin \alpha}. \quad (6)$$

Then the coefficient of ion emission from the crack can be defined as

$$\eta = \frac{1}{N_s} \sum_1^{n_x} \sum_1^{n_\theta} \eta_e(\alpha, \theta). \quad (7)$$

The results of calculating the values for $n_x = n_\theta = n_\alpha = 800$ are given in Fig. 4, which shows the angular dependences of the ion emission coefficient. It can be seen that mainly the ions escaping at an acute angle to the surface of the wall can escape the crack. The initial energy of the ions has a noticeable effect on $\eta_e(\alpha, \theta)$, while the retarding field is weak. The potential $U = 1000 \text{ V}$, for which η_e is about 10^{-5} , is typically used in the experiments. Ion emission at grazing angles is energetically unfavorable because ions are attracted by their own images. Apparently, however, ions also cannot be extracted from the crack at angles approaching $\pi/2$ even with a thermal initial velocity. In addition, since the charges formed on the walls of the crack are distributed unevenly, electric fields directed perpendicular to the walls can be generated between them, preventing charged particles from escaping the crack (regardless of the direction of these fields). If the field accelerates the ion, then it most likely falls on

the opposite wall. The retarding field generates an additional potential barrier that prevents ion emission from the surface of the crack wall.

Even though we chose favorable conditions for ion emission from the crack, the calculated value of the emission coefficient turned out to be very small: $\eta \approx 0.01$:

To correctly estimate the intensity of ion emission from the crack, we need to multiply the intensity value calculated in [12] (equal to 10 ions/ μ s) by the value of η . Thus, we can conclude that it is practically impossible to capture ions from the crack by a detector located at a distance $L = 0.28$ m from the sample. Consequently, we mostly detected the particles that escaped from the surface of the sample through the tip of the crack during polymer rupture.

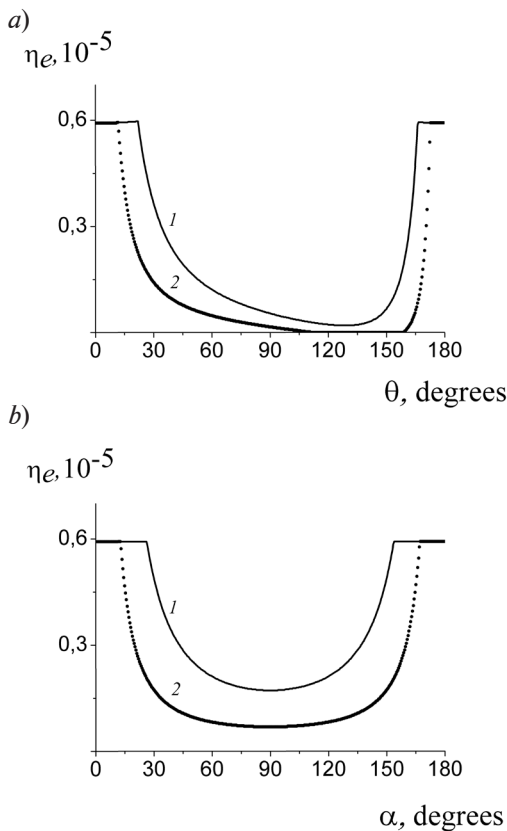


Fig. 4. Calculated angular dependences of the coefficients $\eta_e(\theta)$ (a) and $\eta_e(\alpha)$ (b) of ion emission from the crack with fixed values of the second angle: $\alpha = 0.52^\circ$ (1), 0.97° (2) (a) и $\theta = 0.52^\circ$ (1), 0.97° (2) (b). The electrode potential $U = 1$ kV, the initial ion energy $W = kT$, $T = 580$ K

Calculation of the intensity of ion emission and estimation of the size of the emitting region

Since intense processes of macromolecular rupture and heat generation generally occur near the crack tip, we can assume that ion emission also takes place in this region. The region where intense rupture, deformation, and heating evolve during crack propagation is known to be several tens of microns thick [6].

Let us assess whether our data are in agreement with these concepts. Let us denote the width of the emitting region of the polymer adjacent to the edge of the crack (see Fig. 1,c) as δ . Suppose that each rupture of a macromolecule produces one fragment (ion) with a low molecular weight. If we regard ion emission as the thermal desorption of low molecular weight fragments from the surface of the polymer, then the following equation holds true for the emission intensity J [23]:

$$J = \nu \cdot N_0 \cdot \exp\left(-\frac{\varphi}{kT}\right), \quad (8)$$

where ν is the frequency factor, N_0 is the number of ions produced, φ is the activation energy (ion detachment energy).

Let us assume that ions only escape from a layer with the width approximately equal to the diameter of the macromolecule ($\phi = 1$ nm) from the surface facing the detector. To estimate the value of N_0 , we assume that the emission occurs from the polymer volume ΔV formed during the time Δt as the crack moves with the velocity V_c :

$$\Delta V = 2V_c \Delta t \phi \delta.$$

To detach from the polymer surface, the ion has to acquire an energy exceeding the energy of the interaction between the charge and the induced dipoles. The energy it takes to remove a unit charge q from the dielectric surface is expressed as follows [24]:

$$\varphi \approx \frac{\varepsilon - 1}{16\pi\varepsilon_0(\varepsilon + 1)} \frac{q^2}{\hat{y}}, \quad (9)$$

where ε is the relative permittivity of the dielectric, ε_0 is the electric constant, and \hat{y} is the average distance between the electric charge and the surface.

In case of isotropic emission, the fraction of particles K entering the detector is equal to the ratio of the area S_d of the detector's entrance window to the area of a sphere with the radius L :

$$K = \frac{S_d}{4\pi L^2}. \quad (10)$$

The estimate of the concentration of macromolecular ruptures made in [25] for oriented (by 5.5 times) polymers yielded the value $n \approx 10^{25} \text{ m}^{-3}$. In our experiments, non-oriented samples ruptured at an approximately double elongation. In addition, a plastic deformation developed at the tip of the crack, reaching 60% in PET [26]. Therefore, we can assume that the concentration of macromolecular ruptures was of the same order for the rupture of our experimental polymer samples. Then the quantity $N_0 = n\Delta V$ and only $N_0 K$ ions fall into the detector. Equating this value to the detected N_μ value (the number of ions emitted per 1 μs), we obtain for δ the expression

$$\delta = \frac{N_\mu}{2n\nu\Delta t V_c l_0 K} \cdot \exp\left(\frac{\varphi}{kT}\right). \quad (11)$$

It follows from the data in Figs. 2 and 3 that the detected ion emission intensity is $1 - 4 \mu\text{s}^{-1}$. Therefore, for $Dt = 1 \mu\text{s}$, $\hat{y} \approx 0.1 \text{ nm}$, $\varepsilon = 3$, $\nu = 10^{13} \text{ s}^{-1}$ and for the temperature $T = 580 \text{ K}$ (the onset of thermal degradation in PET [22]), we obtain value $d \approx 20 \mu\text{m}$. From this we can conclude that the area of the fractured material near the surface of the rupture extends to tens of microns around the crack. Consequently, as the main crack propagates, a narrow fracture region adjacent to the crack's edges forms on the surface of the sample.

Results and discussion

Comparing Figs. 2, *a* and *b*, we can see that electrons make the main contribution to the current of negatively charged particles at the pre-rupture stage of polymer deformation. The ionic component becomes dominant in the current of negatively charged particles at the instant of rupture (when the main crack is propagating), i.e., when the fracture process is localized, as evidenced by the weak effect of the magnetic field on the emission intensity at the

time of sample rupture. It was noted above that charges in the polymer are formed by oppositely charged pairs, so the number of positive ions is equal to the number of electrons. Not all ions and electrons are emitted from the surface of the heated polymer. The emission intensities of positive and negative ions are the same. Electrons that could be emitted are not detected during crack intergrowth. Therefore, if the fracture is localized, the probability of electron capture by neutral macromolecular fragments increases practically to unity, apparently due to an increase in the concentration of decay products of strained polymer chains. The lifetimes for autodetachment states of negative ions of complex molecules formed as a result of electron attachment to the corresponding molecules depend on the number of vibrational degrees of freedom for these molecules and amount to tens of microseconds [27]. Therefore, a considerable fraction of the negative ions emitted during propagation of the crack reaches the particle detector. Electrons can get captured by molecules both in the condensed and in the gas phase. The attachment of electrons to molecules in the condensed phase is facilitated by an increased number of possible energy transfer channels generated by molecular interactions. Therefore, the cross-section of electron attachment to molecules is much larger in the condensed phase than in the case of free molecules. In addition, the transition from autodetachment to stable states is facilitated, since the excess energy during the transition of the ion from the autodetachment to the stable state is expended on excitation of the molecule's vibrational degrees of freedom. It is also known that the cross-section of electron attachment to a vibrationally excited molecule is much larger than for a molecule in the ground state. This means that the increase in temperature during polymer fracture and the associated vibrational excitation of the molecules lead to an increase in the cross-section and in the electron attachment rate constant. Importantly, energy redistribution can facilitate the desorption of negative ions in the process of electron attachment to the surface molecules of the polymer [27].

The processes of electron attachment to atomic systems are resonant and occur in the



electron energy range from tens of meV to eV. In our experimental conditions, with the voltage $U = 1000$ V and a 22-mm distance between the grid and the electrode (see Fig. 1, *b*), the electrons manage to acquire the necessary energy near the surface of the polymer, where the emission of volatile products is the highest [28]. For this reason, electrons can also attach to molecules in the gas phase. In this case, due to a decreased number of possible energy transfer channels, the ion may have no time to self-stabilize and decay. As a rule, however, complex electronegative molecules have stable negative ions.

The fractured polymer acting as a new ion source can provide the opportunities for studies of negative ions that are unavailable with traditional ion sources used in negative ion mass spectrometry, limited by the vapor pressure of the test substance [29].

Conclusion

We have carried out experimental and theoretical studies on polymer rupture, establishing that the emitting regions near the tip of the main crack act as the ion sources. These regions have a width of about $20\ \mu\text{m}$ and a length depending on the propagation velocity of the crack. The ion emission from the depth of the crack is less than 1%, and

the cross-sectional area of the sample has little effect on the emission intensity as a result. The kinetics of ion emission under rupture of a polymer sample is governed by the process of macrocrack propagation, which is determined by the properties of a specific polymer.

The method of mechanoemission of ions proves to be extremely effective and makes it possible to obtain new data on the characteristics of the processes that occur during polymer fracture.

Measuring the current-voltage characteristics of ion emission should provide a better understanding of its mechanisms, as generation of negative ions has a resonant character. To gain more insight into the phenomenon, we also plan to carry out two-channel measurements on simultaneous detection of oppositely charged particles and their mass analysis using a special ultrafast time-of-flight mass spectrometer.

Study of the mechanoemission phenomenon has both a purely academic significance for physics of polymer strength and an important value for applications in field sensors, since ionization of stressed macromolecules can affect the operation of various electronic devices [30, 31].

The study was partially funded by the Russian Foundation for Basic Research. Grant no. 18-08-00401 A.

REFERENCES

- [1] **Y.T. Chen, K.X. Liu**, Crack propagation in viscoplastic polymers: Heat generation in near-tip zone and viscoplastic cohesive model, *Appl. Phys. Lett.* 106 (6) (2015) 061908.
- [2] **L.S. Zarkhin, L.I. Manevich**, Thermophysics of a crack propagating in poly(methylmethacrylate), *Polymer Sci. Ser. A.* 52 (9) (2010) 942–948.
- [3] **R. Estevez, S. Basu, E. van der Giessen**, Analysis of temperature effects near mode I cracks in glassy polymers, *Int. J. Fract.* 32 (3) (2005) 249–273.
- [4] **R. Deblieck, D.J.M. van Beek, K. Remerie, I.M. Ward**, Failure mechanisms in polyolefines: The role of crazing, shear yielding and the entanglement network, *Polymer.* 52 (14) (2011) 2979–2990.
- [5] **I.V. Smirnov, Yu.V. Sud'enkov**, Crack dynamics in polymethyl methacrylate plates under quasi-static and dynamic loading, *Techn. Phys.* 56 (12) (2011) 1811–1814.
- [6] **W. Döll**, Optical interference measurements and fracture mechanics analysis of crack tip craze zones, In: Kausch H.-H. (ed.) *Crazing in Polymers*, *Advances in Polymer Science*, Springer, Berlin, Heidelberg, 52/53 (1983) 105–168.
- [7] **A.M. Polyakov, N.A. Krotova**, An investigation of mechanoelectron emission intensity when polymer films are torn off and deformed, *Dokl. Akad. Nauk SSSR.* 151 (1) (1963) 130–133.
- [8] **V.A. Zakrevskii, V.A. Pakhotin**, Mechanism of polymer mechanoemission, *Phys. of the Solid State* 20 (2) (1978) 371–377.
- [9] **J.T. Dickinson, E.E. Donaldson, M.K. Park**, The emission of electrons and positive ions from fracture of materials, *J. Mat. Sci.* 16 (10) (1981) 2897–2908.
- [10] **J. Fuhrmann, G.H. Scherer, R. Hofmann**, Exoemission of polymers induced by deformation and fracture: Description of the experimental method and preliminary results on polyethylene, *Polymer Communications.* 27 (6) (1986) 164–166.
- [11] **V.A. Zakrevskii, V.A. Pakhotin**, Emissiya polozhitelnykh ionov pri rastyazhenii polietilena

[Emission of positive ions during polyethylene tension], Collection of sci. papers (in Russian), Tver State University, Tver, (7) (2001) 112–115.

[12] **V.A. Zakrevskii, V.A. Pakhotin**, Emission of negative and positive ions at rupture of polymers, *Phys. of the Solid State*. 52 (6) (2010) 1155–1161.

[13] **Yu.M. Boiko, V.A. Zakrevskii, V.A. Pakhotin**, Chain scission upon fracture of autoadhesive joints formed from glassy poly(phenylene oxide), *J. Adhesion*. 90 (7) (2014) 596–606.

[14] **V.A. Zakrevskii, V.A. Pakhotin**, Autoionization mechanism of the rupture of chemical bonds in macromolecules, *Polymer Sci., Ser. A*. 23 (3) (1981) 741–746.

[15] **V.A. Zakrevskii, V.A. Pakhotin**, Ionizatsionnyye protsessy pri razrushenii polimerov [Ionization processes in the polymers' rupture], *Mechanics of Composite Materials*. (1) (1981) 139–142.

[16] **M. Sakaguchi, H. Kinpara, Y. Hori, et al.**, Ionic products from the mechanical fracture of solid polypropylene, *Polymer*. 25 (7) (1984) 944–946.

[17] **A.I. Melker, A.I. Mikhaylin, T.E. Kuznetsova**, Drobleniye anгармонической tsepochki atomov [Breaking the anharmonic atomic chain], *Mechanics of Composite Materials*. (4) (1979) 720–723.

[18] **E.A. Yegorov, V.V. Zhizhenkov, A.Ya. Savostin, et al.**, Exothermal effects during polymer fracture, *Phys. of the Solid State*. 17 (1) (1975) 111–117.

[19] **E.A. Yegorov, V.V. Zhizhenkov, S.N. Bezladnov, et al.**, Local exothermal heats of polyethylene terephthalate (pet) decomposition. The temperature profile in the heated zone, *Polymer Sci., Ser. A*. 22(3) (1980) 643–658.

[20] **J.T. Dickinson, L.C. Jensen, S.C. Langford, R.P. Dion**, Temperature measurements of the gaseous emission during the fracture of polystyrene: A determination of the fracture energy and fracture surface temperature, *J. Polym. Sci., Part B: Polym. Phys.* 32 (4) (1994) 779–784.

[21] **L.S. Zarkhin**, Energetics of low-molecular-mass products of mechanical fracture of poly(methyl methacrylate), *Polymer Sci. Ser. A*. 48 (10) (2006)

1086–1097.

[22] **S.L. Madorsky**, Thermal degradation of organic polymers, National Bureau of Standards Washington, D.C., Interscience Publishers, A Division of John Wiley & Sons, Inc. New York . London . Sydney, 1964.

[23] **D.P. Woodruff, T.A. Delchar**, Modern techniques of surface science, *Solid State Sci. Series*, Cambridge University Press, Cambridge, 1986.

[24] **L.N. Dobretsov, M.V. Gomoyunova**, Emission electronics, Transl. by I. Schechtman, Ed. by Y. Freundlich, T. Kom, Israel Program for Sci. Transl., 1971.

[25] **Yu. K. Godovskiy, V.S. Papkov, A.I. Slutsker, et al.**, Energetic effects bound up with the polymer's rupture process, *Phys. of the Solid State*. 13 (8) (1971) 2289–2294

[26] **H.-H. Kausch**, Polymer fracture, 2nd ed., Springer-Verlag, Berlin, Helderberg, New York, 1987.

[27] **E. Illenberger, B.M. Smirnov**, Electron attachment to atomic systems, *Phys. Usp.* 41 (4) (1998) 651–658.

[28] **V.R. Regel, T.M. Muinov, O.F. Pozdnyakov**, Primeneniye metoda mass-spektrometrii dlya issledovaniya mekhanicheskogo razrusheniya polimerov [An application of mass-spectrometry to studies in the mechanical polymer failure], *Phys. of the Solid State*. 4 (9) (1962) 2468–2473.

[29] **R.F. Tuktarov**, Slow decay of negative molecular fluorofullerene ions in the electron autodetachment process, *JETF Letters*. 90 (7) (2009) 515–518.

[30] **V.A. Zakrevskii, V.A. Pakhotin**, Effect of mechanically induced ionization processes in polymer insulators on the noise of cable sensors of physical fields, *J. Commun. Techn. Electronics*. 58 (1) (2013) 56–61.

[31] **V.A. Zakrevskiy, V.A. Pakhotin**, The intrinsic noise of towed cable combined receiving antenna and evaluation of possibilities of its use as a sensor seismic waves, *Fundamental and Applied Hydrophysics*. 8(4) (2015) 61–66.

Received 12.12.2017, accepted 14.12.2017.

THE AUTHORS

PAKHOTIN Vladimir A.

Ioffe Institute of the Russian Academy of Sciences
26 Polytekhnicheskaya St., St. Petersburg, 194021, Russian Federation
v.pakhotin@mail.ioffe.ru

ZAKREVSII Vladimir A.

Ioffe Institute of the Russian Academy of Sciences
26 Polytekhnicheskaya St., St. Petersburg, 194021, Russian Federation
v.zakrevsky@mail.ioffe.ru



SUDAR Nikolay T.

Peter the Great St. Petersburg Polytechnic University
29 Politechnicheskaya St., St. Petersburg, 195251, Russian Federation
sudar53@mail.ru

APASEYEV Aleksey A.

Peter the Great St. Petersburg Polytechnic University
29 Politechnicheskaya St., St. Petersburg, 195251, Russian Federation
aapaseev@bk.ru

PHENIX EXPERIMENT: STUDY OF THE JET QUENCHING EFFECT IN THE ULTRARELATIVISTIC U+U COLLISIONS

**P.V. Radzevich, A.Ya. Berdnikov, Ya.A. Berdnikov,
S.V. Zharko, D.O. Kotov**

Peter the Great St. Petersburg Polytechnic University, St. Petersburg, Russian Federation

Extensive study of heavy ion collisions at RHIC has resulted in discovery of a new state of matter – strongly interacting quark-gluon plasma (sQGP). Measurements of high- p_T particles contribute to systematic study of sQGP properties. Yields of leading particle such as π^0 can be measured with high precision at high transverse momenta. Study of π^0 in different collision systems allows investigation of the path length dependence of energy loss in the medium. U+U presents an opportunity to research non-spherical heavy ion collision system with highest energy density in central collisions. This paper presents the most recent PHENIX results on π^0 production in U+U collision system. Results are presented as functions of p_T and centrality.

Key words: quark gluon plasma; nuclear modification factor; jet quenching heavy ion collision

Citation: P.V. Radzevich, A.Ya. Berdnikov, Ya.A. Berdnikov, S.V. Zharko, D.O. Kotov, PHENIX experiment: Study of the jet quenching effect in the ultrarelativistic U+U collisions, St. Petersburg State Polytechnical University Journal. Physics and Mathematics. 11 (2) (2018) 106 – 114. DOI: 10.18721/JPM.11211

Introduction

The 2005 collaboration at the Relativistic Heavy Ion Collider (RHIC) at Brookhaven National Laboratory [1] announced the discovery of strongly interacting quark-gluon plasma [2] formed in central collisions of ultra-relativistic heavy nuclei. Strongly interacting quark-gluon plasma (sQGP) is a state of nuclear matter existing under extreme conditions (at energy densities of the order of $1 \text{ GeV}/\text{fm}^3$ and temperatures of about 170 MeV) where quarks and gluons possessing a color charge are no longer confined inside hadrons and move freely within a volume of the order of 10 fm^3 . It is believed that the Universe was in this state a few microseconds after the Big Bang.

The current goal of the PHENIX experiment [3] is detailed study of the properties of the sQGP, its dynamics and the specifics of production and interaction of different particles.

One of the key indicators pointing to the formation of sQGP is the effect of quenching

of hadronic jets, which manifests itself as the suppression of the yield of high-energy hadrons in central ultra-relativistic collisions of heavy nuclei. The production of hadrons in the region of high transverse momenta ($p_T > 5 \text{ GeV}/c$) is governed by fragmentation processes where high-energy partons escape from the collision region and form hadronic jets [4 – 6]. Thus, studying the degree of suppression of the hadron yield in the region of high transverse momenta is considered to be one of the best ways to study the properties of sQGP.

Using π^0 mesons is the most popular method for studying the degree of hadron suppression in the region of high transverse momenta. This is convenient because the spectra of π^0 mesons can be measured over a wide range of transverse momenta with a small error.

The system of ultra-relativistic uranium nuclei (U + U) is particularly interesting. Uranium nuclei have a pronounced non-spherical shape, and as a result, the U + U system has a peculiar collision geometry

compared to symmetric (Au + Au, Cu + Cu, Pb + Pb) and asymmetric (Cu + Au) systems. In addition, the central (U + U) collisions are characterized by the highest energy density available at the RHIC. Studying the specifics of production of neutral mesons (in particular, π^0 mesons) allows to better discriminate between different theoretical models describing the properties of sQGP.

Problem statement and description

The main goal of this paper was to study the production of π^0 mesons in (U + U) collisions at an energy $\sqrt{s_{NN}} = 192\text{GeV}$. The following data were obtained and analyzed for this purpose:

- invariant spectra of π^0 meson production as a function of their transverse momentum p_T and centrality of (U + U) collisions;

- nuclear modification factors of π^0 mesons as a function of p_T and centrality.

The transverse momentum p_T characterizes the interaction energy in the system of colliding nuclei. Centrality serves as one of the basic characteristics of interaction; it indicates the degree of overlap of the colliding nuclei with a fixed impact parameter. The maximum degree of overlap corresponds to central collisions (0 – 20%), and the minimum overlap corresponds to peripheral ones (60 – 80%).

Experimental procedure

The results of the study were obtained using the PHENIX spectrometer (RHIC, BNL) [7]. The measuring system of the PHENIX experiment consists of four spectrometer arms. Two muon arms (the north and the south) cover the rapidity range $1.2 < |\eta| < 2.4$, detecting muon radiation. The east and west central arms (Fig. 1) detect electrons, photons and charged hadrons. The central arms consist of two drift chambers 5, three layers of pad chambers 7, eight sectors of electromagnetic calorimeter 2 and 3, RICH detector 4, time-of-flight chambers 6, nucleus-nucleus collision counter 1, and other elements.

The electromagnetic calorimeter measures the energy and positions of photons, electrons and hadrons emitted into its acceptance. The PHENIX detector uses two types of calorimeters:

- scintillation sampling calorimeter PbSc (4 sectors in the west arm and 2 sectors in the east arm);

- lead-glass Cherenkov calorimeter PbGl (2 sectors in the east arm).

Each of these calorimeters has both advantages and disadvantages, and using them simultaneously allows to carry out measurements with the required accuracy and to assess the systematic effects. Each sector of the calorimeter is divided into identical towers determining its segmentation.

The π^0 meson yields are measured in the $\pi^0 \rightarrow \gamma\gamma$ channel. The photon energies and momenta are measured in the electromagnetic calorimeter. However, hadrons may lose energy and form hadronic showers upon falling into the active volume of the detector. Electron showers produced by photons can be binned in many ways, and in this paper we have chosen the discrimination method based on determining the shape of the shower for this purpose.

Different types of quantitative methods are used for different types of detectors. Analysis of the shape of the showers produced in the PbSc electromagnetic calorimeter consists of comparing the energy release within the towers with the data obtained by the Monte Carlo simulation. The comparison is carried out by the χ^2 -fitting procedure correlating the energies deposited in the towers of the same cluster with the data obtained by Monte Carlo simulation. The electromagnetic nature of the clusters reconstructed with the PbSc calorimeter is established using the inequality $\chi^2 < 3$. Analysis of the shape of the showers produced in the PbGl calorimeter is carried out using cluster dispersion analysis. The electromagnetic nature of the clusters reconstructed with the PbGl calorimeter is established using the discrimination inequality.

Additional energy constraints are used to discriminate between hadron clusters. A lower threshold is established for the energy of the reconstructed clusters:

$$E_\gamma > 400 \text{ MeV},$$

since the mean energy deposited in the calorimeter by charged hadrons $E \approx 300 \text{ MeV}$.

The criteria for selecting events include the following conditions:

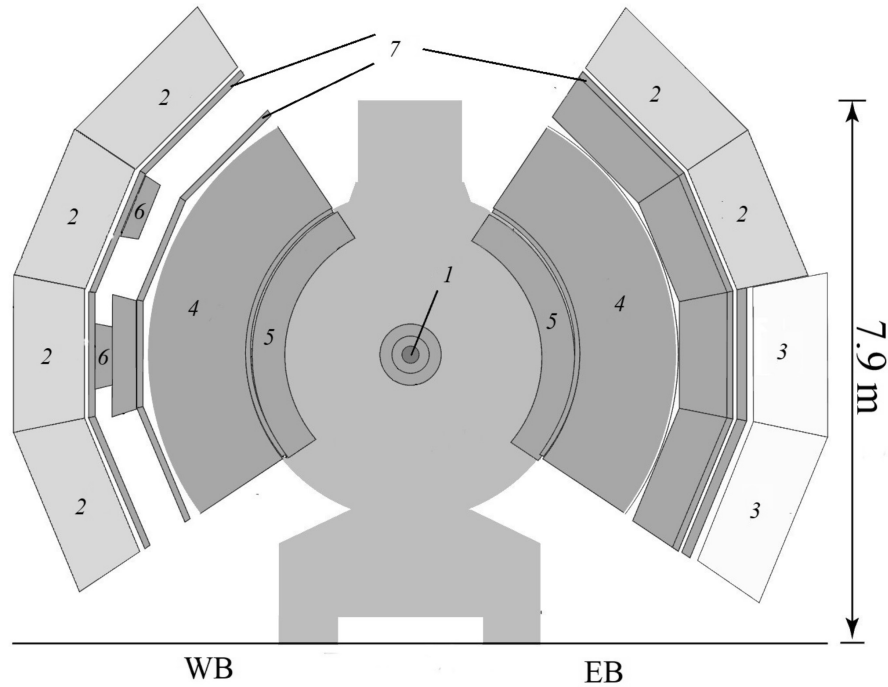


Fig. 1. Schematic of the central part of the PHENIX detector:

nucleus–nucleus collision counter 1, electromagnetic calorimeter 2, 3 (8 sectors), RICH detector 4, drift chambers 5, time-of-flight chambers 6, three layers of pad chambers 7, WB and EB are the west and east branches of the detector

data segments that have not passed the calorimeter’s quality control are excluded;

in this paper, the constraint of the interaction vertex was determined by the inequality

$$-20 < z_v < +20.$$

The efficiency of the trigger in this interval was constant in the cycle of (U + U) collisions.

The π^0 meson yields were measured by combining photonic clusters reconstructed in the sectors of the calorimeter, by reconstructing the effective masses of these mesons as a function of their transverse momentum and by constructing phase distributions of the decay products of these particles.

Data processing was performed using the ROOT CERN 5.34 mathematical library. Monte Carlo simulations of meson production were carried out in the Geant 3 package.

The collective effects of the nucleon interaction in colliding ($A + A$) nuclei can be conveniently described using the nuclear modification factor R_{AA} , equal to the ratio of invariant hadron yields in the collisions of

($A + A$) nuclei to the invariant yields of the same hadrons in proton-proton interactions ($p + p$) This ratio is normalized to the number of inelastic nucleon-nucleon pair collisions $\langle N_{coll} \rangle$:

$$R_{AA} = \frac{1}{\langle N_{coll} \rangle} \frac{dN_{AA}}{dN_{pp}}, \quad (1)$$

where dN_{AA} , dN_{pp} are the respective hadron yields in the collisions of ($A + A$) nuclei and ($p + p$) protons in a given range of transverse momenta.

The number of inelastic nucleon-nucleon pair collisions is determined through calculation by the Monte Carlo method according to the Glauber theory which takes into account the geometry of the colliding nuclei. Normalization to this number is based on the assumption that hadrons are produced in elementary parton-parton interactions (the interactions are described by perturbative quantum chromodynamics). If the value of the nuclear modification factor is equal to unity, collective interaction effects are not observed in the system of colliding nuclei. If the nuclear modification factor differs from



unity, it indicates either a suppression or an excess of the particle yield.

The data that satisfy the constraints on photon clusters reconstructed in the electromagnetic calorimeter and constraints on nuclear collision events are used to measure the π^0 meson yields. The neutral pion yields are measured separately in the PbSc and PbG subsystems in the $\pi^0 \rightarrow \gamma\gamma$ channel

The first step in measuring meson yields is the construction of the effective mass distribution of two gamma quanta depending on the centrality of the colliding U + U nuclei and on the total transverse momentum of the two γ quanta. The effective mass distributions contain a useful meson signal and a combinatorial background (uncorrelated and correlated). The correlated background contains the decay channels of other particles whose final state is accompanied by production of gamma quanta, and the uncorrelated background consists of random combinations of γ pairs.

The form of the uncorrelated background can be reconstructed using the event-mixing technique that involves combining gamma pairs with similar characteristics (vertex and centrality) taken from two different events.

Next, effective mass distributions with event mixing (background) are constructed for each centrality class and normalized to the effective mass distribution for real events (background + signal) and subtracted from it.

Results and discussion

The neutral π^0 meson yields in uranium nuclei collisions (U + U) at $\sqrt{s_{NN}} = 192\text{GeV}$ were measured in five centrality classes (0 – 20 %, 20 – 40 %, 40 – 60 %, 60 – 80 %, 0 – 80 %) and different transverse momentum ranges. The effective mass distribution $M_{\gamma\gamma}$ with event mixing was normalized to the effective mass distribution for real events in the intervals

$$0.080 < M_{\gamma\gamma} < 0.085 \text{ (GeV}/c^2\text{)},$$

$$0.036 < M_{\gamma\gamma} < 0.040 \text{ (GeV}/c^2\text{)}.$$

The combinatorial background decreases sharply with an increase in the transverse momentum, allowing to subtract the distribution over the effective mass of two γ quanta of the

signal + background and background types in the interval

$$1 < p_T < 10 \text{ GeV}/c$$

with respect to the transverse momentum, and the uncorrelated background in the remaining interval is described well along with the residual correlated background.

The result of subtraction of two distributions is approximated by a Gaussian function for describing the signal from reconstructed π^0 mesons and a linear function for describing the residual correlated background, in the interval

$$0.07 < M_{\gamma\gamma} < 0.25 \text{ GeV}/c^2.$$

The π^0 meson yield is measured by counting the number of samples and subtracting the integral under the linear function; this integral describes the residual correlated background. The region of counting the number of samples under the Gaussian function and integrating the linear function lies in the interval

$$0.10 < M_{\gamma\gamma} < 0.17 \text{ GeV}/c^2.$$

An example of the effective mass distribution of two gamma quanta after subtracting the combinatorial background and approximation is shown in Fig. 2.

Analysis of the experimental data obtained provides information only on the π^0 mesons whose decay products have fallen into the detector acceptance. To determine the true spectra of the particles produced in nucleus-nucleus collisions, the efficiency of reconstruction of these particles in the detector has to be estimated. This is achieved through Monte Carlo simulation of the meson flux through the detector system and recording the meson decay products. In this case, the reconstruction efficiency is the ratio of the number of particles reconstructed in the detector during the simulation to the number of the initial particles.

The efficiencies of reconstructing neutral pions in the sectors of the electromagnetic calorimeter that we have estimated for different centralities of copper and gold nuclei collisions are shown in Fig. 3.

The dependence of invariant differential yields of π^0 mesons on the transverse momentum is calculated using the following formula:

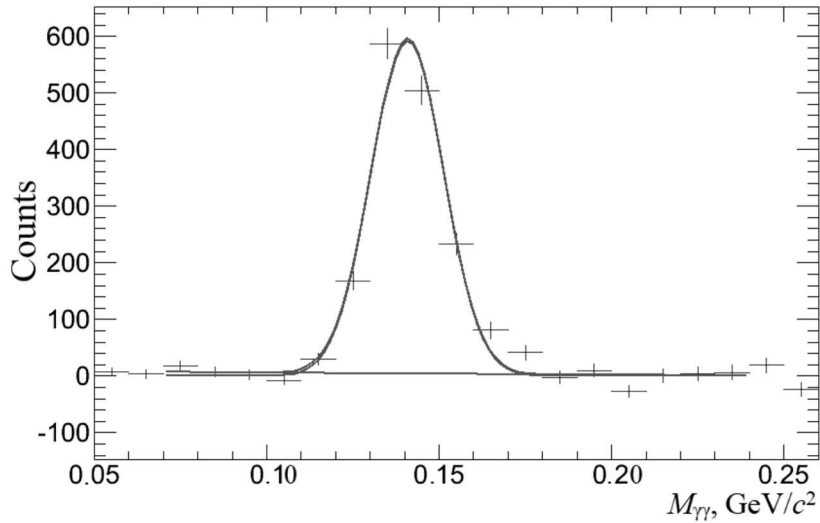


Fig. 2. Effective mass distribution of two gammas after subtraction of the combinatorial background and approximation; the distribution was measured in the range from 9.5 to 10.0 GeV/c (in central collisions) in the PbPb subsystem

$$dN_{AA}(p_T) = \frac{1}{2\pi p_T} \frac{N_{\pi^0}(p_T)}{N_{event} \Delta p_T \varepsilon_{rec}(p_T)}, \quad (2)$$

where N_{π^0} is the yield of neutral π mesons (π^0), ε_{rec} is the recording efficiency, N_{event} is the number of analyzed events.

The invariant spectra of π^0 mesons as a function of the transverse momentum are shown in Fig. 4 for different centrality classes. Because it is impossible to discriminate the signal at the background level in the region of

low transverse momenta, the neutral pion (π^0) spectrum starts at 2 GeV/c. Due to limited amount of statistical data available, the π^0 meson spectra could be measured only up to 16 GeV/c.

The nuclear modification factors of neutral π^0 mesons were calculated by formula (1) using two different sets of the number N_{coll} of the nucleons participating in the interaction in different centrality ranges of (U + U) collisions in a wide range of transverse momenta, up to 16

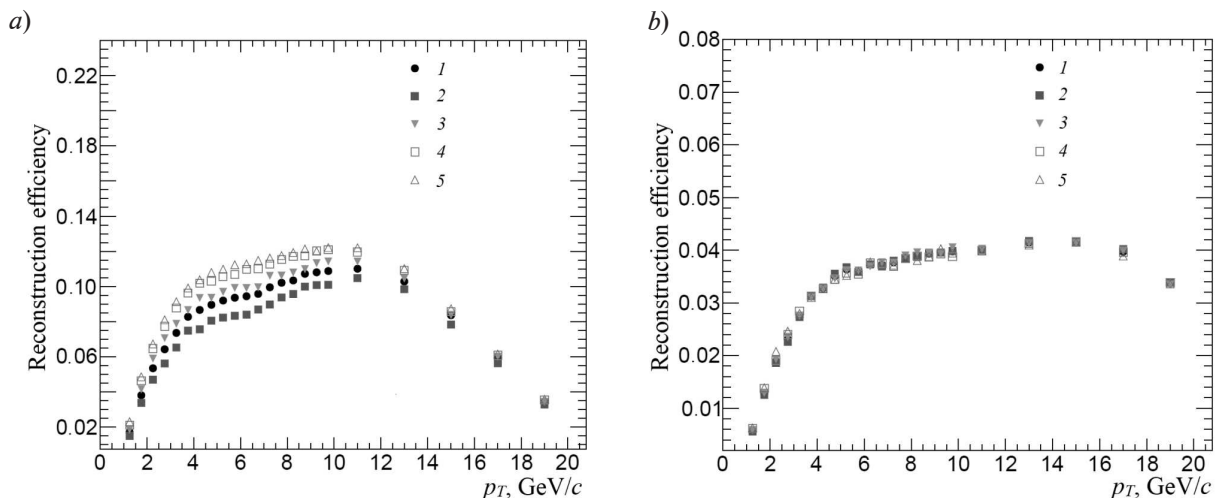


Fig. 3. Reconstruction efficiencies of π^0 mesons in the PbSc (a) and PbPb (b) electromagnetic calorimeters as a function of the transverse momentum for different centrality classes, %: 0 – 80 (1), 0 – 20 (2), 20 – 40 (3), 40 – 60 (4), 60 – 80 (5)

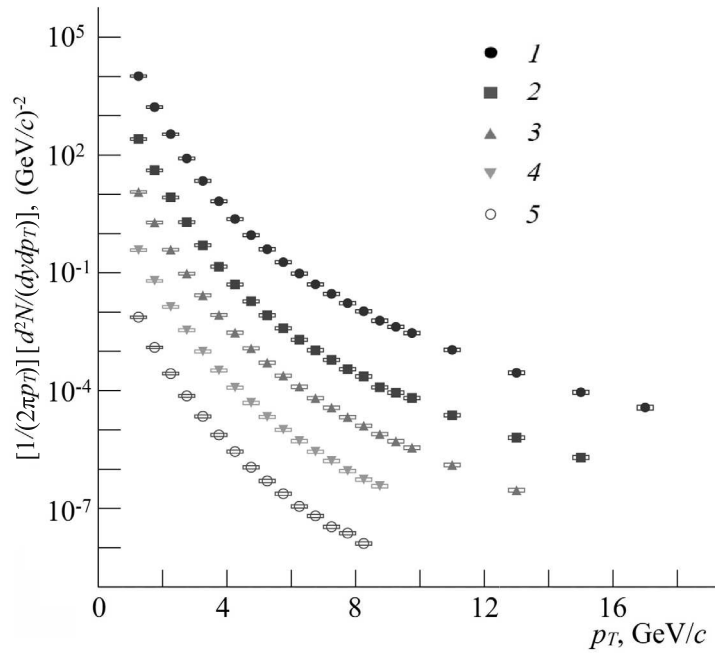


Fig. 4. Invariant spectra of π^0 mesons with respect to the transverse momentum for different centrality classes of (U + U) collisions at an energy $\sqrt{s_{NN}} = 192$ GeV (the curve numbers correspond to those in Fig. 3).

The vertical bars and the horizontal grey rectangles on the points here and below correspond to statistical and systematic measurement errors, respectively

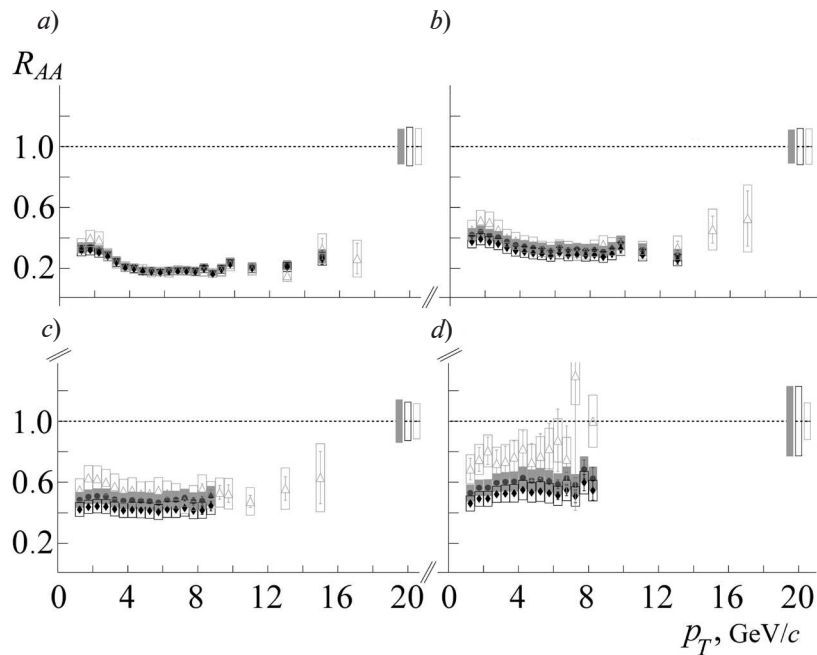


Fig. 5. Dependences of the magnitude of the nuclear modification factor R_{AA} on the transverse momentum p_T for neutral pions in (U + U) interactions (circles and diamonds) and (Au + Au) interactions (triangles) for energies of 192 and 200 GeV, respectively (see the table).

Rectangles over the dashed lines indicate the systematic error for N_{coll}

GeV/c. Two different sets of N_{coll} values are used because uranium nuclei have different degrees of deformation when the nucleon number N_{coll} is calculated in the Glauber model [8 – 10].

Fig. 5 shows the dependences of the nuclear modification factors on the transverse momentum of neutral pions, measured in (U + U) and (Au + Au) collisions [11, 12] at energies $\sqrt{s_{NN}} = 192$ and 200 GeV, respectively, and at close N_{coll} values. The N_{coll} values corresponding to the centrality classes for which the nuclear modification factors are shown are given in the table.

The nuclear modification factors measured in the (U + U) and (Au + Au) systems coincide within the error at large N_{coll} values, which indicates that the degree of neutral pion suppression does not depend on the geometry of the nuclear overlap region. There is a slight difference in the values of nuclear modification

factors obtained in collisions of uranium and gold nuclei at small N_{coll} values.

Conclusion

The PHENIX experiment uncovered the reconstruction efficiencies of π^0 mesons for each type of electromagnetic calorimeter and each centrality range as a function of the transverse momentum. The invariant differential spectra and the nuclear modification factors of π^0 mesons were measured as a function of the transverse momentum in four centrality classes of (U + U) collisions with the energy in the center-of-mass frame equal to 192 GeV. The yields of neutral pions measured in the (U + U) and (Au + Au) collisions at energies of 192 and 200 GeV were equally suppressed with a larger number of nucleon-nucleon collisions ($N_{\text{coll}} > 90$), which indicates that the degree of suppression does not depend on the shape of

Table
Collision numbers N_{coll} as a function of the collision centrality for different types of interactions (see Fig. 5)

Centrality, %	N_{coll}	Fig. 5
Au + Au (200 GeV)		
0 – 5	1065.4 ± 105.3	a)
20 – 30	373.8 ± 39.6	b)
40 – 50	120.3 ± 13.7	c)
60 – 80	20.4 ± 5.9	d)
U + U (variant I), 192 GeV		
0 – 20	934.5 ± 97.5	a)
20 – 40	335.0 ± 33.0	b)
40 – 60	95.9 ± 13.0	c)
60 – 80	17.5 ± 3.8	d)
U + U (variant II), 192 GeV		
0 – 20	999.0 ± 114.0	a)
20 – 40	375.0 ± 45.0	b)
40 – 60	110.0 ± 14.6	c)
60 – 80	19.7 ± 4.4	d)

Note. Different variants possible in the collisions of uranium nuclei are due to different degrees of deformation of the uranium nucleus in calculations of the number N_{coll} of nucleons in the Glauber model [8 – 10].



the overlap region of the colliding nuclei. The yield of π^0 mesons in peripheral ($N_{\text{coll}} \approx 20$) (U + U) collisions may be suppressed more strongly than that in (Au + Au) collisions. Nevertheless, it does not seem possible to reliably discriminate between the results obtained

in the peripheral collisions of uranium and gold for the given measurement accuracy.

The results of this study were obtained within the framework of state task 3.1498.2017/4.6 of the Ministry of Education and Science of the Russian Federation.

REFERENCES

- [1] **K. Adcox, S.S. Adler, S. Afanasiev, et al.** (PHENIX Collaboration), First three years of operation of RHIC, Nucl. Phys. A. 757 (1–2) (2005) 184–283.
- [2] **E. Shuryak**, Physics of strongly coupled quark-gluon plasma, Prog. Part. Nucl. Phys. 62 (Jan.) (2009) 48–101.
- [3] **A. Adare, S. Afanasiev, C. Aidala, et al.** (PHENIX Collaboration), PHENIX Collaboration, Nuclear Physics. A. 967 (Nov.) (2017) 996–1003.
- [4] **C. Andrés, N. Armesto, M. Luzum, et al.**, Energy versus centrality dependence of the jet quenching parameter \hat{q} at RHIC and LHC: a new puzzle? Eur. Phys. J. C: Part Fields. 76 (9) (2016) 475.
- [5] **J. Casalderrey-Solana, Y. Mehtar-Tani, C.A. Salgado, K. Tywoniuk**, New picture of jet quenching dictated by color coherence, Phys. Lett. B. 725 (4–5) (2013) 357–360.
- [6] **Guang-You Qin, A. Majumder**, Parton transport via transverse and longitudinal scattering in dense media, Phys. Rev. C. 87 (2) (2013) 024909.
- [7] **M. Harrison, T. Ludlam, S. Ozaki**, RHIC project overview, Nucl. Instr. Meth. 499 (2–3) (2003) 235–244.
- [8] **H. Masui, B. Mahanty, Nu Xu**, Predictions of Elliptic flow and nuclear modification factor from 200 GeV U + U collisions at RHIC, Phys. Lett. B. 679 (5) (2009) 440–444.
- [9] **A. Adare, S. Afanasiev, C. Aidala, et al.** (STAR Collaboration). Azimuthal anisotropy in U + U and Au+Au collisions at RHIC, Phys. Rev. Lett. 115 (22) (2015) 222301.
- [10] **Q.Y. Shou, Y.C. Ma, P. Sorensen, et al.**, Parameterization of deformed nuclei for Glauber modeling in relativistic heavy ion collisions, Phys. Lett. B. 749 (7 October) (2015) 215–220.
- [11] **A. Adare, S. Afanasiev, C. Aidala, et al.** (PHENIX Collaboration) Suppression pattern of neutral pions at high transverse momentum in Au+Au collisions at $\sqrt{s_{NN}} = 200$ GeV and constraints on medium transport coefficients, Phys. Rev. Lett. 101 (23) (2008) 232301.
- [12] **M.L. Miller, K. Reygers, S.J. Sanders, P. Steinberg**, Glauber modeling in high energy nuclear collisions, Ann. Rev. Nucl. Part. Sci. 57 (2007) 205–243.

Received 12.01.2018, accepted 29.01.2018.

THE AUTHORS

RADZEVICH Pavel V.

Peter the Great St. Petersburg Polytechnic University
29 Politechnicheskaya St., St. Petersburg, 195251, Russian Federation
radzevichp@gmail.com

BERDNIKOV Alexander Ya.

Peter the Great St. Petersburg Polytechnic University
29 Politechnicheskaya St., St. Petersburg, 195251, Russian Federation
alexber@phmf.spbstu.ru

BERDNIKOV Yaroslav A.

Peter the Great St. Petersburg Polytechnic University
29 Politechnicheskaya St., St. Petersburg, 195251, Russian Federation
berdnikov@spbstu.ru

ZHARKO Sergey V.

Peter the Great St. Petersburg Polytechnic University
29 Politechnicheskaya St., St. Petersburg, 195251, Russian Federation
zharkosergey94@gmail.com

KOTOV Dmitriy O.

Peter the Great St. Petersburg Polytechnic University

29 Politechnicheskaya St., St. Petersburg, 195251, Russian Federation

dmitriy.kotov@gmail.com

PHASE SHIFT CONTROL USING WAVEGUIDE-SLOT PHASE SHIFTER

D.V. Dikiy, V.P. Akimov, A.A. Sochava, A.S. Cherepanov

Peter the Great St. Petersburg Polytechnic University, St. Petersburg, Russian Federation

Some specific electrical properties of a waveguide-slot phase shifter have been studied in the paper. We propose to use waveguide-slot phase shifter as a controlled coupler in the switchgears of phased arrays with series feeding and $p-i-n$ -diodes control. The characteristics of the waves transmitted through the waveguide and their dependences on the slot's position and dimensions were considered. The slot of special form was cut through the waveguide wide wall. We succeeded in obtaining the phase shift up to 360 degrees by the lengthwise variation in the slot's position in a coupling window and by the slot's displacement specularly relative to the waveguide's axis line. The study of the problem was conducted experimentally and by simulation technique. The simulation results were verified by experimental data. The proposed phase-shifter can be also used in switchgears of phased arrays with a locked beam.

Key words: waveguide; slot in waveguide; antenna; phased array; phase shifter

Citation: D.V. Dikiy, V.P. Akimov, A.A. Sochava, A.S. Cherepanov, Phase shift control using waveguide-slot phase shifter, St. Petersburg Polytechnical State University Journal. Physics and Mathematics. 11 (2) (2018) 122 – 128. DOI: 10.18721/JPM.11212

Introduction

Phased arrays (PAs) are increasingly used as radar antennas for different ranges and applications. Series-fed arrays are one possible configuration for these devices. Examples of antennas with series feeding serving as PAs were proposed in [1 – 7]. Any phased array includes a switchgear that supplies power to the radiating elements with the required phase and amplitude.

In most cases, phase shifters with individual driver circuits for each element are used to control PAs. A series-fed PA uses a ferrite phase shifter to form an amplitude-phase distribution of the field of radiating elements. The driver circuit of a ferrite phase shifter is usually cumbersome and power-consuming [6, 8 – 10], which limits potential applications of such devices.

In this paper, we have studied the characteristics of a slot-waveguide phase shifter which at the same time can be used as a controlled coupler in PA switchgears with serial feeding and $p-i-n$ -diode control.

Design of the phase shifter and its operating principles

The design of the slot-waveguide phase shifter is shown in Fig. 1. Two waveguides are connected by a longitudinal slot similar to

that used as the radiating element of the slot-waveguide array.

The concept we propose in this study is that varying the position of the slot allows controlling the phase shift of the electromagnetic field. If the longitudinal position of the slot is changed, then the phase of the field changes. An additional phase shift of 180 degrees is achieved when the slot is moved to the other side of the center line. If the slot detuned from resonance, it should be possible to gain some extra phase shift. Slots are formed by turning $p-i-n$ -diodes on or off.

Thus, we have an opportunity to control the phase of the coupled electromagnetic field.

Simulation results

In this section we present the simulation results for a slot-waveguide phase shifter. Fig. 2, *a* shows the frequency dependences of the coupling coefficient S_{31} from the source port to the radiator for different positions of the slot. The S_{31} magnitudes are usually from -20dB to -10dB . The exact value is determined by the number of elements in the series-fed antenna, as well as by the shape of the required amplitude distribution. The coupling coefficient S_{31} can be varied by shifting the slot from the center line of the waveguide, and also by detuning it from the resonance. It

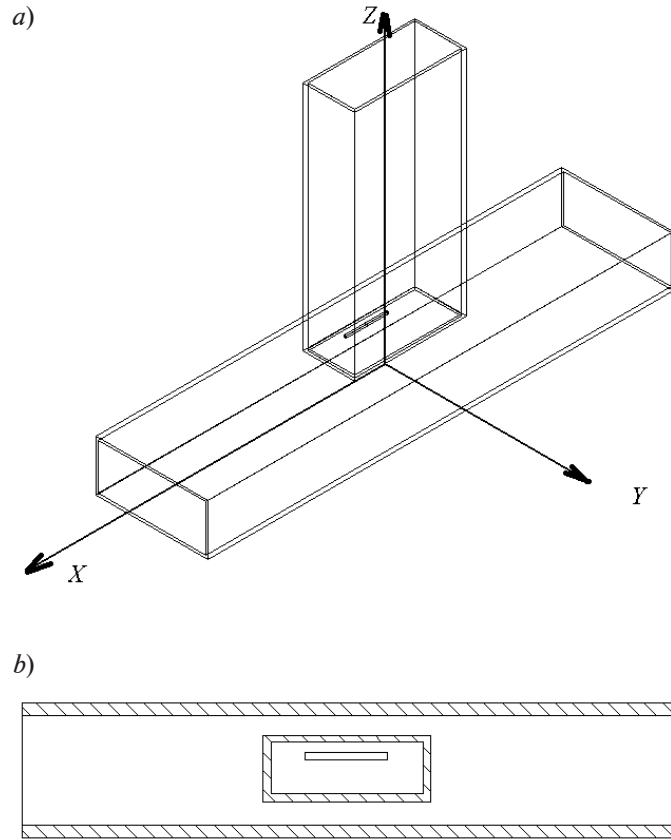


Fig. 1. Schematic of the slot-waveguide phase shifter: general view *a*, cross-section in the *xy* plane (plane of contact of the waveguides) *b*

can be seen from below Fig. 2 that the resonance frequency slightly increases when the center of the slot is shifted relative to the symmetrical position.

Fig. 2, *b* shows the frequency dependences of the phase shift of the electric field (relative to the input port) for the fixed position of the slot. It can be seen that the maximum phase shift is 62° at 9.50 GHz.

To increase the phase shift, we propose using an inverted-L-shaped slot near the edges of the waveguide's cross-port. Fig. 3 shows a sketch of the slot of the phase shifter being considered. The radiating inverted-L-shaped slots are formed by turning the *p-i-n*-diodes in the inverted-U-shaped slot on or off. We simulated different positions of the slot, including two near-edge positions.

Fig. 4 shows the simulation results of the E field distribution along the slot. It can be seen that the distribution of the electric field

amplitude over the inverted-L-shaped slot is close to sinusoidal, the same as for the rectangular slot.

Fig. 5, *a* shows the phase shift of two inverted-L-shaped slots against the radiation frequency. The maximum phase shift is 177° , which is enough to create a fully functioning phase shifter for a scanning PA (taking into account a 180° -degree shift of the slot that is symmetric with respect to the waveguide axis, the maximum phase shift obtained is about 360°).

The transmission coefficients S_{31} (Fig. 5, *b*) varies less than 10 dB over the operating range for two slot positions.

Experimental results and discussion

To test the simulation results, we have built two models of phase shifters and two sets of slots. Laser cutting and milling were used to cut the slots in the first and the second sets, respectively.

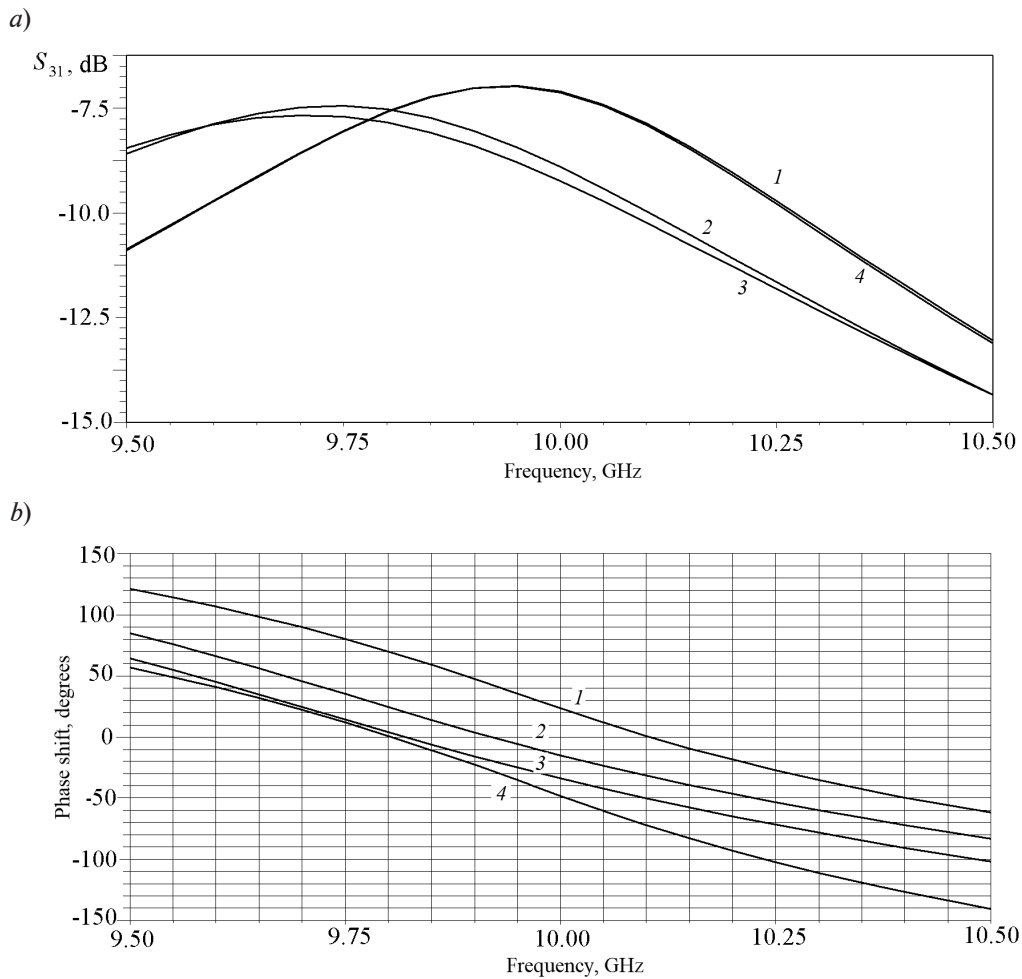


Fig. 2. Frequency dependences of the coupling coefficient S_{31} (a) and the phase shift relative to the input terminal $\arg(S_{31})$ (b) for different shifts of the slot center along the x axis with respect to the origin:
 -4 mm (curve 1); 0 mm (2); +2 mm (3); +4 mm (4)

Fig. 6 shows the experimental dependences of the phase shift against the position of the slot for model 1. The curves depicted in Fig. 6, b, are the results of measurements for the slots located on the other side of the waveguide's center line (bottom row),

compared to the slots in Fig. 6, a (top row). This produces an additional phase shift of 180° . This phase shift was taken into account in the results shown in this figure (180° were subtracted from the data in Fig. 6, b). Therefore, according to theory, the

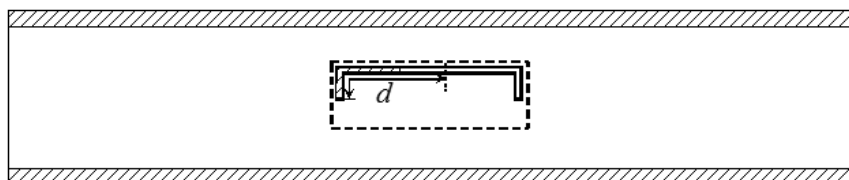


Fig. 3. Schematic of the proposed shape of the radiating slot of the given phase shifter (the non-radiating part of the slot is shaded)

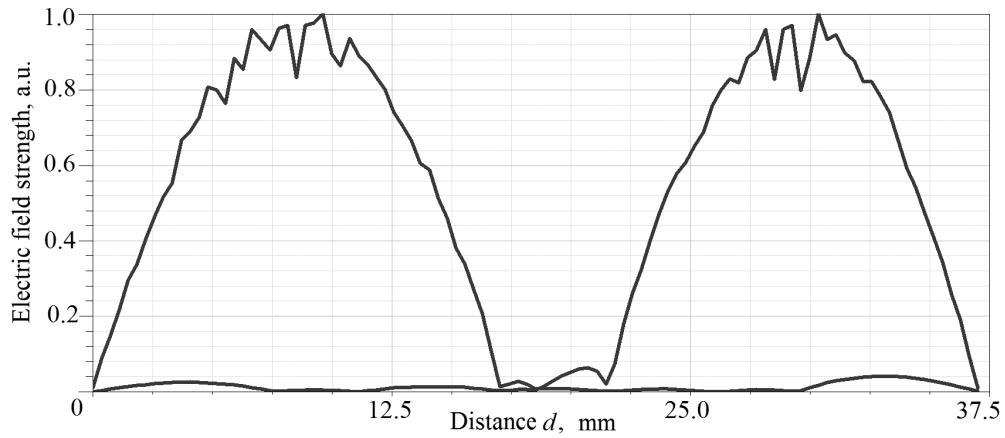


Fig. 4. Distribution of the electric field strength along the inverted-L-shaped slot for two states of $p-i-n$ -diodes (the distance d is shown in Fig. 3)

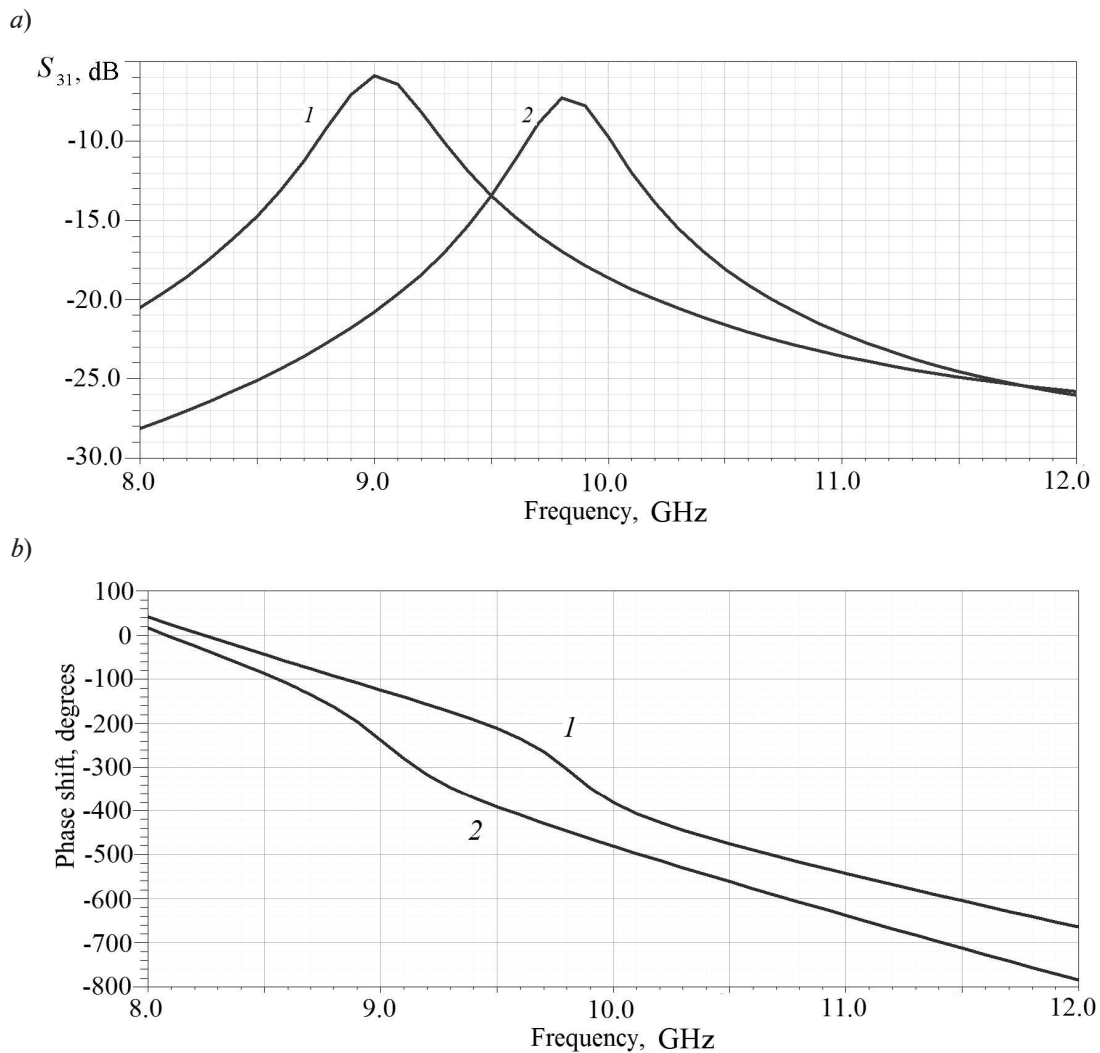


Fig. 5. Frequency dependences of the transmission coefficient (a) and the phase shift (b) of two inverted-L-shaped slots for their extreme left (curve 1) and extreme right (curve 2) positions

curves in Fig. 6, *b* should coincide with the curves in Fig. 6, *a*. The differences in these graphs can be used to estimate the error in the measurements, as well as the error of positioning the aperture.

Photos of both models are shown in Fig. 7. The results of measurements for model 2 turned out to be close to those for model 1, which proves that both laser cutting and milling are suitable technologies for cutting inverted-L-shaped slots.

Conclusion

We have studied some specific properties

of a slot-waveguide phase shifter, which is proposed to be used as a controlled coupler in switchgears of phased array antennas with serial feeding and *p-i-n*-diode control. We have considered the characteristics of the wave transmitted through the waveguide and their dependences on the position and size of the slot cut in the waveguide's wide wall. To test the simulation results, we have built experimental models of the phase shifter, equipped with inverted-L-shaped slots. We have measured the characteristics for two types of phase shifter layouts.

The experimental data obtained generally

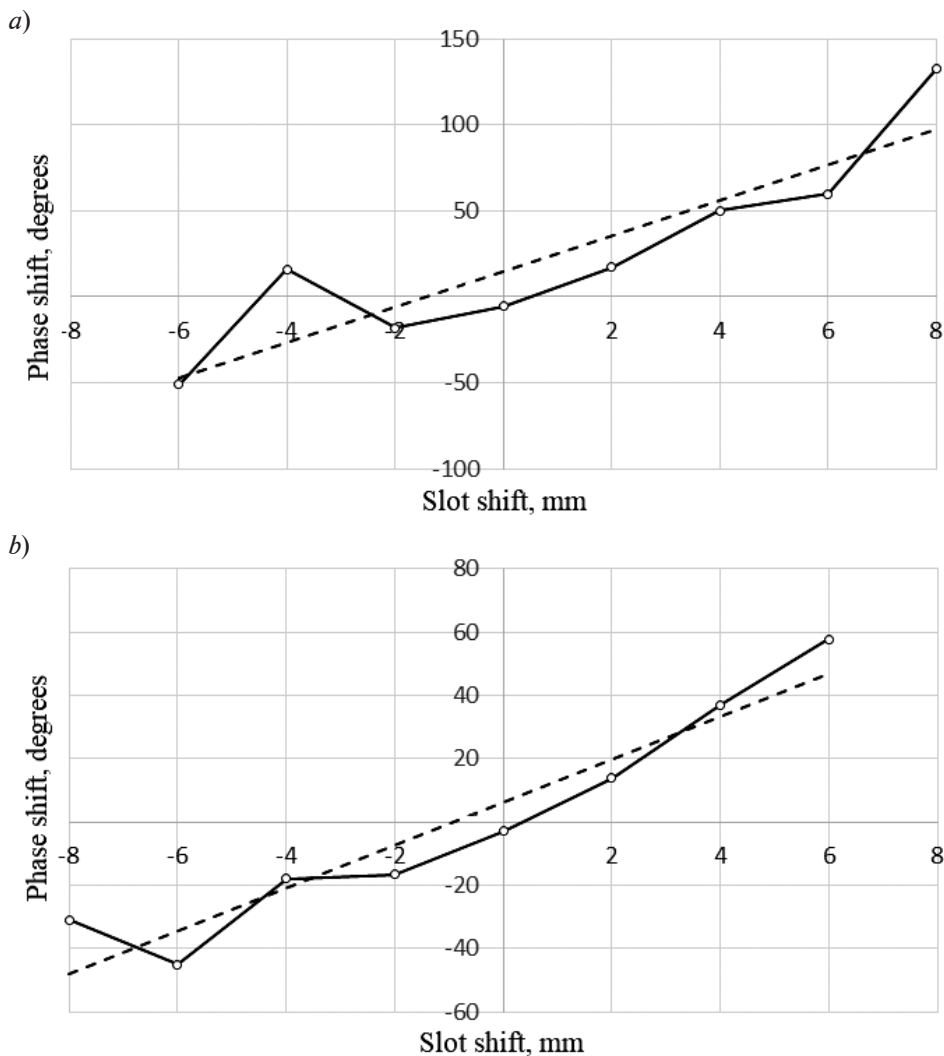


Fig. 6. Experimental dependences of the phase shift on the position of the inverted-L-shaped slot for the top (*a*) and bottom (*b*) rows (see the explanations in the text) for experimental model 1 (see Fig. 7, *a*), and linear approximations of the data (dashed lines).

The frequency of microwave radiation is 10 GHz

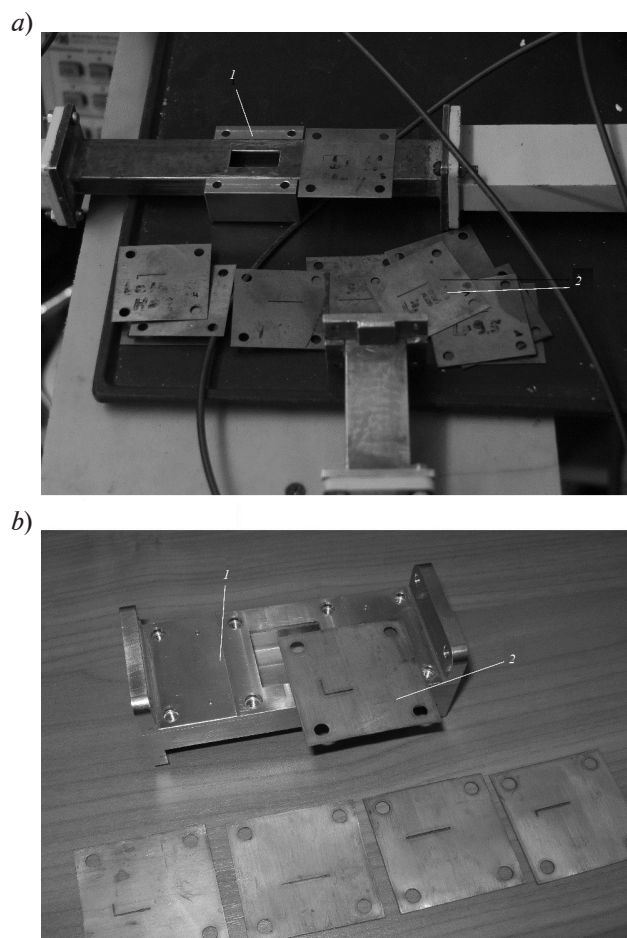


Fig. 7. Photographs of models 1 (a) and 2 (b) of the phase shifters (1) and inverted-L-shaped slots (2) attached to the phase shifters

confirmed the simulation results. Thus, we have proved that it is possible to use a slot-

waveguide phase shifter as a switchgear element of a phased array with series feeding.

REFERENCES

- [1] G.A. Gurevich, N.A. Bogomaz, Nonreciprocal phase shifts and a decay factor in the phase-plate-loaded waveguide, *J. Commun., Techn. & Electron.* 3 (9) (1958) 1133–1343.
- [2] A.G. Gurevich, *Ferrity na sverkhvysokikh chastotakh* [Microwave ferrite devices], Fizmatgiz, Moscow, 1960.
- [3] E.F. Zaytsev, A.S. Cherepanov, A.B. Guskov, New electrically scanning antennas of millimeter wave range, *Radioelectronics and Communication Systems.* 46 (4) (2003) 3–12.
- [4] A.S. Cherepanov, K.V. Guzenko, I.A. Kroutov, The slot integrated phased array, *St. Petersburg State Polytechnical University Journal. Computer Science, Telecommunications and Control Systems.* No. 2 (145) (2012) 41–45.
- [5] E.F. Zaytsev, A.S. Cherepanov, A.B. Guskov, New millimeter-wave electrically scanned antennas, *St. Petersburg State Polytechnical University Journal.* (2) (2001) 47–52.
- [6] D.I. Voskresenskiy, R.A. Granovskaya, N.S. Davydova, et al., *Antenny i ustroystva SVCh. Proyektirovaniye fazirovannykh antennykh reshetok* [Antennas and microwave devices. Designing the phased arrays], Radio i svyaz, Moscow, 1981.
- [7] O.G. Vendik, M.D. Parnes, *Antenny s elektricheskim skanirovaniem. Vvedeniye v teoriyu.* Pod red. L.D. Bakhrakha [Electrically scanned antennas, An introduction to the theory, Ed. by L.D. Bakhrakh], Science-Press, Moscow, 2002.
- [8] O.G. Vendik, M.D. Parnes, *Fazovrashchateli skaniruyushchikh antenn dlya radarov obzora*

territoriy [Phase shifters of scanning antennas for territory-looking radars], *Wireless Technologies (Rus.)*. (2) (2006) 26–28.

[9] **O. Vendik, A. Vasiliev, M. Parnes**, Low cost ferroelectric phase shifter for a higher microwave power level, *IEEE COMCAS 2009, The International IEEE Conference on Microwaves, Communication,*

Antennas and Electronic Systems, Tel-Aviv, Israel (2009).

[10] **A.A. Bezuglov, A.V. Litvinov, S.E. Mishchenko, V.V. Shatskiy**, The evolutionary method of multi-criteria phase synthesis of linear array antenna, *Radioengineering*. (6) (2017) 251–260.

Received 16.01.2018, accepted 30.01.2018.

THE AUTHORS

DIKIY Dmitriy V.

Peter the Great St. Petersburg Polytechnic University
29 Politechnicheskaya St., St. Petersburg, 195251, Russian Federation
diwil@mail.ru

AKIMOV Valeriy P.

Peter the Great St. Petersburg Polytechnic University
29 Politechnicheskaya St., St. Petersburg, 195251, Russian Federation
valeri_akimov@mail.ru

SOCHAVA Alexander A.

Peter the Great St. Petersburg Polytechnic University
29 Politechnicheskaya St., St. Petersburg, 195251, Russian Federation
sochava@mail.ru

CHEREPANOV Andrey S.

Peter the Great St. Petersburg Polytechnic University
29 Politechnicheskaya St., St. Petersburg, 195251, Russian Federation
ASCherSPb@mail.ru

CHANNELING OF ULTRARELATIVISTIC PARTICLES IN A DIAMOND CRYSTAL

K.B. Agapev¹, V.K. Ivanov¹, A.V. Korol², A.V. Solov'yov²

¹ Peter the Great St. Petersburg Polytechnic University, St. Petersburg, Russian Federation;

² MBN Research Center UG, Frankfurt am Main, Germany

The numerical simulation results on the channeling of ultrarelativistic electrons and positrons with the energy of 270 MeV in a diamond crystal are presented in the paper. Using the pack of applied codes MBN Explorer [1, 2], the trajectories of the charged particles have been determined for the particles' falling on the 20 μm -length crystal, along (110) crystallographic plane. The channeling parameters and radiation spectra of electrons and positrons were obtained computationally for the cases of the charged particles' incidence on a straight diamond crystal and a periodically bent one.

Key words: periodically bent diamond crystal; channeling; ultrarelativistic particle; channeling radiation

Citation: K.B. Agapev, V.K. Ivanov, A.V. Korol, A.V. Solov'yov, Channeling of ultrarelativistic particles in a diamond crystal, St. Petersburg State Polytechnical University Journal. Physics and Mathematics. 11 (2) (2018) 129 – 137. DOI: 10.18721/JPM.11213

Introduction

The processes of interaction of charged particles with matter, in particular, crystalline solids, have been long studied both experimentally and theoretically. The goal of these studies is to determine such characteristics of the interaction as the mean free path traveled by particles in the material, their energy losses, emission spectra, and others [2].

Channeling in crystals, when charged particles falling into a potential channel shaped by electrostatic forces propagate along crystallographic planes or axes, has become the focus of much attention in recent years. The particles trapped in a channel of a straight crystal can travel long distances exceeding the mean free path in an amorphous target, since such particles lose considerably less energy along their path [3]. For electrons, the channel lies along atomic rows or ion chains of the crystal, while for positrons it lies in the space between atomic rows. The stability of particle motion along the channels depends on the energy of the transverse motion that is low compared with the height of the potential barrier.

A particle trapped in the channel experiences oscillations in a plane transverse to the direction of the particle's propagation, inducing radiation during its channeling [4]. This radiation is determined by the transverse energy of the channeled particle, and its intensity varies depending on the type of crystal and its orientation. Oscillatory radiation is incoherent and has a broad energy spectrum [5 – 9].

Channeling can also occur in bent crystals, which are often used to rotate charged particle beams accelerated to relativistic energies [10]. The motion of a particle consists of two components: its oscillatory motion in the channel and its propagation along the centerline of the bent channel. The stability of the second component of motion in such a bent channel is provided by an additional condition, namely, that the bending radius R should significantly exceed the critical value R_c determined by the longitudinal energy of the particle [10]. This motion of a relativistic particle trapped in a bent channel induces additional synchrotron radiation. The intensity and frequency of synchrotron radiation depend on the type and en-

ergy of the channeled particles, as well as on the characteristics of the crystal [11 – 18].

Synchrotron radiation is certainly an interesting subject to explore in connection with the concept of the crystal undulator (see, for example, Ref. [18] and references therein). Channeling of charged relativistic particles in a periodically bent crystal (a crystal undulator) can produce a new source of monochromatic radiation with energies ranging from hundreds of keV to several MeV.

There has been a number of experiments in the recent years with a view to create the crystal undulator, measuring the channeling parameters and the characteristics of the emission spectra of ultrarelativistic positrons [19 – 21] and electrons [22, 23] in straight and bent crystals of silicon and diamond. Theoretical studies on channeling in these crystals are carried out using the newly developed MBN Explorer package [1, 2]. Simulations for amorphous and crystalline silicon have verified that this package is applicable for describing the channeling of electrons and positrons [2, 24 – 26].

Since experiments are currently being carried out to measure the emission spectra of electrons in a periodically bent diamond crystal [27], theoretical interpretation of the experimental results is clearly an interesting problem.

In view of the above, the goal of this study is theoretical analysis of channeling of ultrarelativistic electrons and positrons with an energy of 270 MeV both in a straight diamond crystal oriented along the (110) crystallographic plane and in a periodically bent diamond crystal.

We have performed simulations of electron and positron channeling in straight, bent and periodically bent channels using the versatile MBN Explorer software package [1, 2].

Simulation procedure with the MBN Explorer package

Three-dimensional simulation of ultrarelativistic particles passing through a crystalline medium is carried out using a molecular dynamics algorithm implemented in the MBN Explorer software package [2]. The characteristics of the motion of high-energy particles inside the crystal were obtained by integrating the relativistic equations of motion.

Step-by-step dynamic simulation of the crystalline medium was performed to construct the particle trajectory [2].

A quasiclassical approximation is applicable to describing the motion of ultrarelativistic particles, and, since the quantum corrections are small, it is sufficient to use the equations of classical relativistic mechanics:

$$\dot{\mathbf{p}} = q\mathbf{E}(\mathbf{r}). \quad (1)$$

Here $\mathbf{E}(\mathbf{r})$ is the external electrostatic field; q is the particle charge, and p is its relativistic momentum, determined by the standard expression:

$$\mathbf{p} = m\gamma\dot{\mathbf{r}} = m\gamma\mathbf{v},$$

where m , \mathbf{r} , \mathbf{v} are the mass of the particle, its position vector and velocity, respectively; γ is the relativistic factor,

$$\gamma = (1 - v^2/c^2)^{-1/2} \gg 1$$

(c is the speed of light).

The initial conditions for the coordinates of the incident particle and its velocity, $\mathbf{r}_0 = \mathbf{r}(0)$ and $\mathbf{v}_0 = \mathbf{v}(0)$, are used for integrating Eq. (1).

In the MBN Explorer channeling module, the electrostatic field is calculated as

$$\mathbf{E}(\mathbf{r}) = -\nabla U(\mathbf{r}). \quad (2)$$

Here the electrostatic potential $U(\mathbf{r})$ is the sum of atomic potentials U_{ar} :

$$U(\mathbf{r}) = \sum_j U_{ar}(\boldsymbol{\rho}_j), \quad (3)$$

where $\boldsymbol{\rho}_j = \mathbf{r} - \mathbf{R}_j$ (\mathbf{R}_j is the position vector of a j^{th} atom, $\boldsymbol{\rho}$ is the coordinate in the plane perpendicular to the direction of motion).

Formally, summation is carried out over all the atoms of the crystal. However, given that $U_{ar}(\boldsymbol{\rho}_j)$ rapidly decreases with distance, we can introduce the maximum distance ρ_{max} , beyond which the contribution of the atomic potential $U_{ar}(\boldsymbol{\rho}_j)$ is negligible. Therefore, for a given observation point \mathbf{r} , the sum can be limited to the atoms located inside a sphere with the radius ρ_{max} . The linked cell algorithm implemented in the MBN Explorer is used to search for such atoms. This algorithm involves dividing the crystal into cells and considering only the atoms closest to the particle. The described scheme is used to calculate the force $q\mathbf{E}$ acting



during each integration step.

The motion of particles along a crystallographic plane with the Miller indices $(k\ l\ m)$ is simulated by the following procedure [28]. A simulation box with the dimensions $L_x \times L_y \times L_z$ is introduced, containing a crystal lattice. The z axis is oriented along the direction of beam propagation and is parallel to the $(k\ l\ m)$ plane, the y axis is directed perpendicular to this plane. The position vectors $\mathbf{R}_j^{(0)}$ ($j = 1, 2, \dots, N$) of the lattice sites are generated in accordance with the type of the Bravais cell of the crystal, using predefined values of the translation vectors [18].

Once the nodes inside the simulation box are determined, the position vectors of the atomic nuclei are generated taking into account the thermal vibrations of these nuclei resulting in a random displacement Δ_j from the nodal positions; these positions are determined by the normal distribution with respect to the root-mean-square amplitude of thermal vibrations [29].

Integration of the equations of motion begins at $t = 0$, when the particle enters the crystal at $z = 0$. A random number generator is used to choose the initial coordinates x_0 and y_0 lying in the (xy) midplane, within the range $\Delta x = 2d$, $\Delta y = d$ (d is the interplanar spacing of the $(k\ l\ m)$ planes). The initial velocity \mathbf{v}_0 of the particle is oriented along the z axis, i.e., has the components $\mathbf{v}_0(0, 0, v_{0z})$.

Particle propagation through a crystal with a finite thickness L is simulated in MBN Explorer using the so-called dynamic simulation box [2, 18] as a new type of boundary conditions. A particle moving inside the box interacts with atoms lying inside the cutoff sphere. To optimize the numerical procedure, the dimensions of the box L_x, L_y, L_z are chosen to be 3 to 5 times larger than ρ_{\max} . As soon as the distance l from the particle to the nearest face approaches ρ_{\max} ($l \approx \rho_{\max}$), a new simulation box of the same size is generated, its geometric center approximately coinciding with the position of the particle. To avoid spurious changes in the force acting on the particle, the positions of the atoms located at the intersection of the old and the new simulation boxes are not changed. The positions of the atomic nuclei in the rest of the new box are generated according to the

above-described scheme. Simulation is interrupted when the z coordinate of the particle becomes equal to the crystal thickness L .

A similar process is performed for simulation of channels in a bent crystal.

Simulation of electron and positron trajectories

The MBN Explorer package was used to simulate the trajectories of electrons and positrons with the energy of 270 MeV, incident on diamond crystals along the (110) crystallographic planes. The calculations were performed for a straight crystal and for a crystal with periodical cosine-like bending; the crystal length was 20 μm in both cases. The bending amplitude of the crystal was 2.5 E, and the length of the bending period was 5 μm . A random number generator was used to construct 6,000 trajectories for electrons in a straight diamond crystal oriented along the (110) crystallographic plane and in a periodically bent crystal. The same number of trajectories was obtained for positrons in the same crystals. The trajectories were analyzed and averaged to calculate the channeling parameters in the crystal.

An ordinary diamond crystal has straight channels due to the periodic arrangement of its atoms. The width of the channel is determined by the interatomic distance and amounts to $d = 1.26$ E. Particles trapped in straight channels with a low transverse energy leave such channels less often. Since the crystal is short, positrons most often move through the entire straight crystal while staying in the channel, and electrons are more likely to collide with lattice atoms and leave the channel. This is because positrons move between the crystal atoms, where they are confined by repulsive interaction with the lattice ions. On the other hand, electrons move along helical trajectories in the immediate vicinity of the nuclei, so they are much more likely to collide with them and escape the channel.

The trajectories of charged particles channeled in bent crystals become more complex and diverse. As an example, Fig. 1 shows several typical trajectories of electrons and positrons in periodically bent diamond crystals. Thin solid lines in the figure indicate the boundaries of the channels; the distance y is plotted along the vertical axis in a plane

perpendicular to the direction of motion (the distance is measured in units of the interatomic spacing d). The main features and characteristics of particle motion in a crystal, such as the channeling, dechanneling, and rechanneling modes, are shown in the figures [18]. Rechanneling is a process when a particle moving outside a channel can experience a collision and get trapped into some channel as a result.

Fig. 1, *a* shows only one trajectory of an electron passing through a crystal in one channel. Statistically, such trajectories are an exception, as the rest of the trajectories

presented correspond to the more typical motion of electrons in dechanneling and irregular rechanneling modes in short segments of different channels.

Comparison of the trajectories shown in Fig. 1, *a* and *b*, indicates that positrons channel much better than electrons, and this pattern is observed for both straight and bent crystals. Only a small part of the positrons originally trapped in the channel escapes it, while most of them move through the entire crystal while staying in one channel. Therefore, the intensity of synchrotron radiation should be higher in a periodically bent crystal.

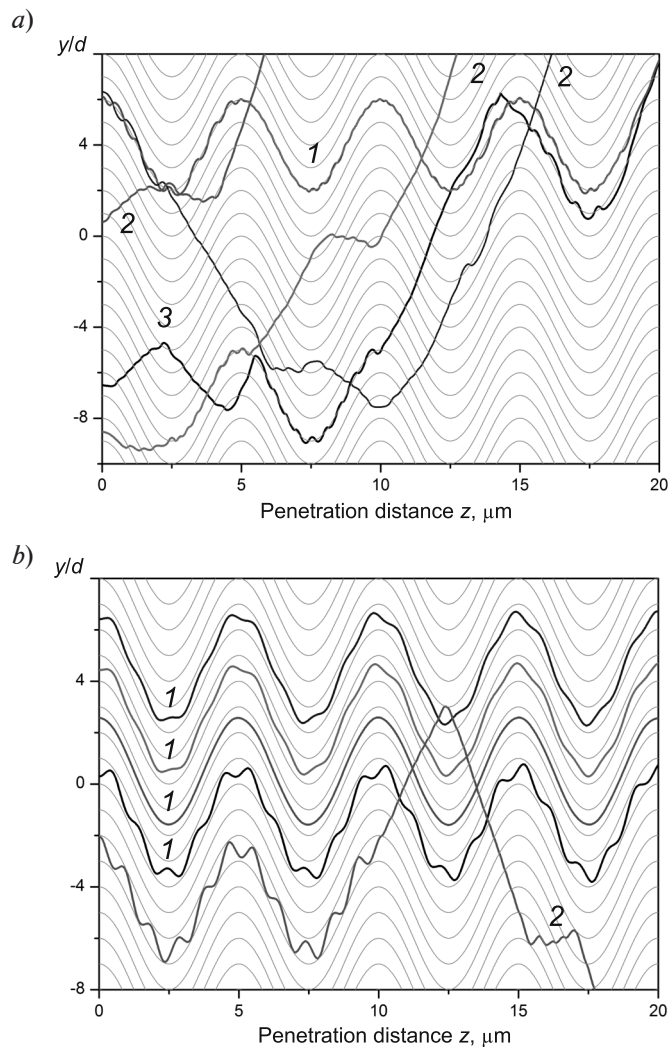


Fig. 1. Trajectories of electrons (*a*) and positrons (*b*) with energies of 270 MeV in a periodically bent 20 μm long diamond crystal. Channeling (curves 1), dechanneling (2) and rechanneling (3) modes are shown. The interatomic spacing in the crystal $d = 1.26 \text{ \AA}$



Notably, positrons may have different oscillation amplitudes inside the channel, but transverse oscillations are practically isochronous and their period remains almost unchanged, which corresponds to harmonic oscillations. Consequently, all positrons emit energy at approximately the same wavelength, and their channeling radiation peak is narrower and more intense, in contrast to the maximum radiation intensity for electrons.

Statistical analysis of the calculated trajectories allowed to obtain the main parameters characterizing the channeling of charged particles (given in the table).

The particle trapping coefficient A (acceptance) is the ratio of the number N_{acc} of the particles trapped in the channel upon entering the crystal to the number N_0 of all incident particles:

$$A = N_{acc} / N_0 .$$

The values given in the table refer to the acceptance for the particles falling along the z axis.

The remaining parameters are related to the mean distances or the times during which the charged particles stay in one or several channels. The channeling length L_{ch} is defined as the mean distance traveled by a particle in the channel throughout the entire time it moved in the crystal. The rechanneling length L_{rech} is

the mean distance traveled by particles in the channels during rechanneling (i.e., falling into a new channel as a result of a collision).

The table lists two more parameters, the so-called penetration lengths [1, 18]. The first, denoted as L_{p1} , describes the mean distance traveled by a particle fallen into the initial channel at the entrance to the crystal, that is, the distance from the entrance to the dechanneling point inside the crystal. The second penetration length, L_{p2} , describes the mean distance traveled by a particle in one channel, including the channels into which the particle is trapped through rechanneling.

Since the crystal is rather short (20 μm), the positrons trapped in a channel travel through almost the entire crystal while staying in the same channel; they have greater penetration, channeling and rechanneling lengths, as well as a greater acceptance A .

Electrons are much more likely to experience collisions with lattice ions, since their trajectories pass in the immediate vicinity of the ions, and often escape the channel as a result.

Emission spectra of electrons and positrons

Analysis of the obtained time dependences of the particle coordinates $\mathbf{r} = \mathbf{r}(t)$ and velocities $\mathbf{v} = \mathbf{v}(t)$ allows to determine the spectral characteristics of the radiation emitted by these particles.

Table

Channeling parameters of the particles in the straight and the periodically bent diamond crystal

Parameter	Notation	Straight crystal		Periodically bent crystal	
		E	P	E	P
Particle acceptance	A	0.695	0.957	0.511	0.888
Channeling length	L_{ch} , μm	9.039	18.664	6.058	17.173
Rechanneling length	L_{rech} , μm	4.184	6.083	5.979	7.529
Penetration length	L_{p1} , μm	5.431	19.068	4.303	18.819
	L_{p2} , μm	4.551	18.013	3.599	16.373

Notations: E and P are electrons and positrons, respectively.

Notes. 1. The length of both diamond crystals is 20 μm . 2. Particles of both types fall on crystals with an energy of 270 MeV along the (110) crystallographic plane. 3. The straight crystal is oriented along the (110) crystallographic plane.

The spectral angular distribution of the radiated energy $d^3E / (\hbar d\omega d\Omega)$ (ω is the frequency of the emitted photon, Ω is the solid angle) is calculated by the semiclassical approximation developed by Bayer and Katkov (see [30] for more details).

Within the semiclassical approximation, the spectral distribution of the energy emitted by an ultrarelativistic particle in the direction \mathbf{n} is determined by the following expression [30]:

$$\frac{d^3E}{\hbar d\omega d\Omega} = \alpha \frac{q^2 \omega^2}{8\pi^2} \int_{-\infty}^{\infty} dt_1 \int_{-\infty}^{\infty} dt_2 e^{i\omega'(\psi(t_1) - \psi(t_2))} \times \left[\left(1 + (1 + u^2) \left(\frac{v_1 v_2}{c^2} - 1 \right) \right) + \frac{u^2}{r^2} \right], \quad (4)$$

where $\alpha = e^2/\hbar c$ is the fine-structure constant, q is the particle charge in elementary charge units,

$$\psi(t) = t - \mathbf{nr}(t)/c.$$

The quantities ω' and u take into account the radiative recoil:

$$\omega' = (1 + u)\omega, \quad u = \frac{\hbar\omega}{\varepsilon - \hbar\omega}. \quad (5)$$

The spectral distribution of the radiated energy $dE / (\hbar d\omega)$ is obtained by numerically integrating the values of $d^3E / (\hbar d\omega d\Omega)$ over the given ranges of the angles φ and θ . In the results below, we confined ourselves to taking into account the photons emitted within the aperture of 0.2 mrad. In other words, the photon beam that we took into account in the emission spectra lies within a cone with the parameters $\varphi[0; 2\pi]$ and $\theta[0; \theta_0]$.

Thus, we have obtained the emission spectrum for each calculated trajectory and can average over the ensemble of these trajectories.

Fig. 2, *a* shows the emission spectra of electrons in the straight and in the bent crystal. The broad peak (curve 1) at an energy greater than 0.4 MeV is determined by the contribution to the radiation intensity associated with the electron oscillations in a plane transverse to the direction of particle motion (CR). The decrease in the intensity of this peak in a periodically bent crystal (curve 2) is associated with greater losses of channeling

electrons.

Fig. 2, *b* show the emission spectra of positrons in the straight and in the bent crystal. The CR maximum (curve 1) here is narrower and higher because the transverse oscillation frequency of all positrons is approximately the same during propagation in the channel.

It can be seen from Fig. 2, *a* and *b* (curves 2) that a radiation intensity peak is observed for channeling in a bent crystal at a photon energy of the order of 130 keV, which is absent in the straight crystal. This peak appears due to motion of the particle in the periodically bent crystal, with the charged particle moving along the centerline of the bent channel. The particle radiation frequency is related to the period of the channel curvature and the longitudinal energy of the charged particle. This radiation is coherent, has a narrow spectral width and, since it is similar to the radiation of free electrons and positrons passing through a periodically oriented magnetic field in accelerators, it is called undulator radiation. Since the study deals with electrons and positrons with the same energy, the position of the undulator peak on the emission spectra is the same. However, radiation intensity is higher for positrons than for electrons by an order of magnitude, because positrons experience harmonic oscillations and longer channeling.

Conclusion

We have numerically simulated the trajectories of ultrarelativistic charged particles in straight and bent diamond crystals, with electrons and positrons incident on the (110) crystallographic plane, using the MBN Explorer software package [1, 2]. The coordinates of the particles upon entering the crystal in the transverse plane were chosen with a random number generator. Statistical processing of the obtained trajectories made it possible to determine the channeling parameters of electrons and positrons with an energy of 270 MeV in a 20 μm long diamond crystal. We have established that channeled positrons have a larger acceptance and run substantially longer distances in the crystalline channel as compared to electrons.

The calculated emission spectra of electrons

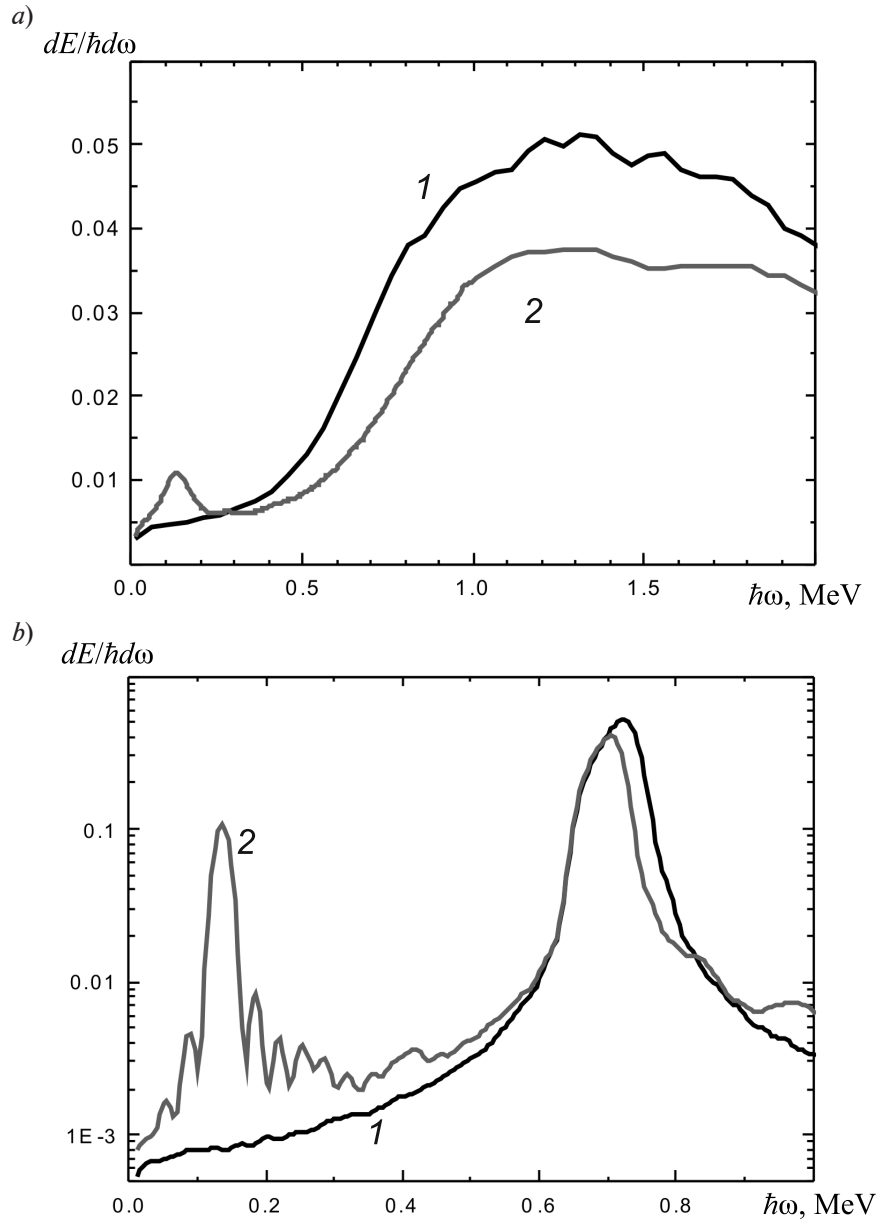


Fig. 2. Emission spectra $dE / (\hbar d\omega)$ of electrons (a) and positrons (b) in a straight (1) and a periodically bent (2) diamond crystal of length $L = 20 \mu\text{m}$ oriented along the (110) crystallographic plane

and positrons in the semiclassical approximation under channeling in a periodically bent crystal contain two main regions. The high-energy intensity peak is associated with synchrotron radiation induced by oscillatory motion of the particles in the channel; the same peak was obtained under channeling in a straight crystal. A low-energy peak in the 130 keV region

occurs when particles move in a periodically bent channel and has an undulatory nature. This radiation is coherent and, even though the bent crystal has a small number of periods (only 4), the radiation is characterized by a noticeable intensity, which is significant for potential applications in lasers [17, 18, 31].

The obtained channeling parameters and

the calculated emission spectra are of interest in view of the experiments on electron channeling in straight and bent crystals currently under way at the University of Mainz (Germany) [27].

Acknowledgment

We express our gratitude to the team of the Polytechnic Supercomputer Center for providing computing resources for the simulations.

REFERENCES

- [1] **I.A. Solov'yov, A.V. Yakubovich, P.V. Nikolaev, I. Volkovets, A.V. Solov'yov**, MesoBioNano explorer – a universal program for multiscale computer simulations of complex molecular structure and dynamics, *J. Comp. Chem.* 33 (30) (2012) 2412–2439.
- [2] **G.B. Sushko, V.G. Bezchastnov, I.A. Solov'yov, et al.**, Simulation of ultrarelativistic electrons and positrons channeling in crystals with MBN explorer, *J. Comp. Phys.* 252 (2013) (November 1) 404–418.
- [3] **J. Lindhard, A. Winther, K. Dan**, Influence of crystal lattice on motion of energetic charged particles, *Vidensk. Selsk. Mat. Fys. Medd.* 34 (14) (1965) 1–64.
- [4] **M.A. Kumakhov**, On the theory of electromagnetic radiation of charged particles in a crystal, *Phys. Lett. A.* 57 (1) (1976) 17–18.
- [5] **J.U. Andersen, E. Bonderup, R.H. Pantell**, Channeling radiation, *Ann. Rev. Nucl. Part. Sci.* 33 (1983) 453–504.
- [6] **J. Bak, J.A. Ellison, B. Marsh, F.E. Meyer, ..., M. Suffert**, Channeling radiation from 2–55 GeV/c electrons and positrons: (I). Planar case, *Nucl. Phys. B.* 254 (1985) 491–527.
- [7] **J. Bak, J.A. Ellison, B. Marsh, F.E. Meyer, ..., M. Suffert**, Channeling radiation from 2 to 20 GeV/c electrons and positrons (II): Axial case, *Nucl. Phys. B.* 302 (1988) 525–558.
- [8] **V.A. Bazylev, N.K. Zhevago**, Intense electromagnetic radiation from relativistic particles, *Sov. Phys. Usp.* 25 (8) (1982) 565–595.
- [9] **M.A. Kumakhov, F.F. Komarov**, Radiation from charged particles in solids, AIP, New York, 1989.
- [10] **E.N. Tsyganov**, Estimates of cooling and bending processes for charged particles penetration through a monocrystal, Fermilab preprint TM-682, Fermilab, Batavia, 1976. Fermilab Preprint TM-684. Fermilab, Batavia, 1976.
- [11] **V.V. Kaplin, S.A. Vorobev**, On the electromagnetic radiation of channeled particles in a curved crystal, *Phys. Lett. A.* 67 (2) (1978) 135–137.
- [12] **Yu.A. Bashmakov**, Radiation and spin separation of high energy positrons channeled in bent crystals, *Radiat. Effects and Defects in Solids.* 56 (1-2) (1981) 55–60.
- [13] **A.M. Taratin, S.A. Vorobiev**, Quasi-synchrotron radiation of high-energy positrons channeled in bent crystals, *Nucl. Instrum. Methods Phys. Res. B.* 42 (1) (1989) 41–45.
- [14] **V.A. Arutyunov, N.A. Kudryashov, V.M. Samsonov, M.N. Strikhanov**, Radiation of ultrarelativistic charged particles in a bent crystal, *Nucl. Phys. B.* 363 (1991) 283–300.
- [15] **A.M. Taratin**, Particle channeling in a bent crystal, *Physics of Elementary Particles and Atomic Nuclei.* 29 (5) (1998) 437–462.
- [16] **A.V. Korol, A.V. Solov'yov, W. Greiner**, Coherent radiation of an ultrarelativistic charged particle channeling in a periodically bent crystal, *J. Phys. G.: Nucl. Part. Phys.* 1998. Vol. 24 (5) (1998) L45–L53.
- [17] **A.V. Korol, A.V. Solov'yov, W. Greiner**, Photon emission by an ultrarelativistic particle channeling in a periodically bent crystal, *Int. J. Mod. Phys. E.* 8 (1) (1999) 49–100.
- [18] **A.V. Korol, A.V. Solov'yov, W. Greiner**, Channeling and radiation in periodically bent crystals, 2nd ed., Springer-Verlag, Berlin, Heidelberg, 2014.
- [19] **V.T. Baranov, S. Bellucci, V.M. Biryukov, G.I. Britvich., ..., V.N. Zapolsky**, Preliminary results on the study of radiation from positrons in a periodically deformed crystal, *Nucl. Instrum. Methods Phys. Res. B.* 252 (1) (2006) 32–35.
- [20] **H. Backe, D. Krambrich, W. Lauth, et al.**, Future aspects of X-ray emission from crystal undulators at channeling, *Nuovo Cimento. C.* 34 (4) (2011) 175–180.
- [21] **H. Backe, P. Kunz, W. Lauth, A. Rueda**, Planar channeling experiments with electrons at the 855 MeV Mainz Microtron MAMI, *Nucl. Instrum. Methods Phys. Res. B.* 266 (17) (2008) 3835–3851.
- [22] **H. Backe, D. Krambrich, W. Lauth, et al.**, X-ray emission from a crystal undulator – experimental results at channeling of electrons, *Nuovo Cimento. C.* 34 (4) (2011) 157–165.
- [23] **H. Backe, D. Krambrich, W. Lauth, et al.**, Channeling and radiation of electrons in silicon single crystals and Si_{1-x}Ge_x crystalline undulators, *J. Phys.: Conf. Series.* 438 (2013) 012017.
- [24] **G.B. Sushko, A.V. Korol, W. Greiner, et al.**, Sub-GeV electron and positron channeling in straight, bent and periodically bent silicon crystals, *J. Phys.: Conf. Series.* 438 (2013) 012018.
- [25] **R.G. Polozkov, V.K. Ivanov, G.B. Sushko, et al.**, Channeling of ultrarelativistic positrons in bent



diamond crystals, St. Petersburg State Polytechnical University Journal. Physics and Mathematics. No. 2(218) (2015) 167–178.

[26] **A.V. Korol, V.G. Bezchastnov, G.B. Sushko, A.V. Solov'yov**, Simulation of channeling and radiation of 855 MeV electrons and positrons in a small-amplitude short-period bent crystal, Nucl. Instrum. Methods Phys. Res. B. 387 (2016) 41–53.

[27] **W. Lauth, H. Backe, R. Barrett, et al.**, Channeling experiments with electrons at the Mainz Microtron MAMI, In: 4th Intern. Conf. “Dynamics of Systems on the Nanoscale” (DySoN 2016), October 03–07, 2016, Bad Ems, Germany, Book of Abstracts, 2016, P. 63.

[28] **G. Molière**, Theorie der Streuung

schneller geladener Teilchen I Einzelstrahlung am abgeschirmten Coulomb-Feld, Z. Naturforschg. A 2 (1947) 133–145.

[29] **D.S. Gemmel**, Channeling and related effects in the motion of charged particles through crystals, Rev. Mod. Phys. 46 (1) (1974) 129–227.

[30] **V.N. Baier, V.M. Katkov, V.M. Strakhovenko**, Electromagnetic processes at high energies in oriented single crystals, World Scientific, Singapore, 1998.

[31] **A.V. Korol, A.V. Solov'yov, W. Greiner**, Channeling of positrons through periodically bent crystals: on the feasibility of crystalline undulator and gamma-laser, Int. J. Mod. Phys. E. 13 (5) (2004) 867–916.

Received 23.03.2018, accepted 23.03.2018.

THE AUTHORS

AGAPEV Kirill B.

Peter the Great St. Petersburg Polytechnic University
29 Politechnicheskaya St., St. Petersburg, 195251, Russian Federation
cyr96@mail.ru

IVANOV Vadim K.

Peter the Great St. Petersburg Polytechnic University
29 Politechnicheskaya St., St. Petersburg, 195251, Russian Federation
ivanov@physics.spbstu.ru

KOROL Andrey V.

MBN Research Center UG
Altenhoferallee 3, 60438 Frankfurt am Main, Germany
korol@mbnexplorer.com

SOLOV'YOV Andrey V.

MBN Research Center UG
Altenhoferallee 3, 60438 Frankfurt am Main, Germany
solovyov@mbnresearch.com

AERODYNAMICS AND HEAT TRANSFER OVER THE SURFACE OF A SINGLE CIRCULAR FIN

A.A. Gusakov, M.A. Grekov, V.V. Seroshtanov

Peter the Great St. Petersburg Polytechnic University, St. Petersburg, Russian Federation

In the paper, it has been proposed to unite the heat flux measurements with thermal imaging and the PIV diagnostics for studies in aerodynamics and heat transfer over the surface of a circular fin. The hollow fin under consideration was heated by saturated steam from within; meanwhile the isothermal external surface simulated an ideal fin. The surface flow and heat transfer of the solid fin sized and shaped identically, and made of titanium alloy, was investigated in the same regimes. Gradient heat flux sensors were placed on the fin surface. The velocity field near the fin, the temperature field and the heat flux per unit area over its surface were obtained. The data analysis gave an impartial piece of information. The proposed method allows examination of a flow and a heat transfer over the fin surface in the real-time processing.

Key words: heat flux measurement; PIV diagnostics; circular fin; heat flux; heat transfer coefficient

Citation: A.A. Gusakov, M.A. Grekov, V.V. Seroshtanov, Aerodynamics and heat transfer over the surface of a single circular fin, St. Petersburg Polytechnical State University Journal. Physics and Mathematics. 11 (2) (2018) 138 – 148. DOI: 10.18721/JPM.11214

Introduction

The principal elements of most convective heat exchangers are circular tube bundles in cross-flow, typically with finned surfaces. The structure of the flow near finned tubes has been well-studied. The Reynolds number Re , calculated by the diameter of the tube and the velocity of the external flow, is the parameter governing the flow structure. Heat transfer efficiency in the first rows of tubes, where there is practically no effect from the tube pitch and the type of tube bundle, is of primary importance for studying hydrodynamics in finned tube bundles [1]. We selected our experimental model based on this consideration.

Study of flow and heat transfer in cross-fin tubes is a multifactorial problem associated with a number of difficulties. For example, [5, 6] described three-dimensional flow at the base of a fin. A pressure drop occurred along the tube axis in the flow over the tube wall because of the difference in velocities near the fin surface and in the core of the flow. Due to such a drop, the fluid moved from the center of

the channel between the fins to the base of the fin. It was also established that the influence of the tube as a barrier blocking the main flow increased if the height of the fin was relatively small [1]. In this study, the flow was visualized using a kerosene soot suspension.

Recalculating the velocity field by the measurements of the static pressure field is also a widespread method of studies on this subject. Particle Image Velocimetry (PIV), introduced with the expansion of laser technologies, is based on measuring the velocity of the particle image; the method has opened up new opportunities for the development of this field.

The local heat transfer coefficient α serves as the objective function in heat transfer studies. Numerous papers have been dedicated to measuring this quantity, based on various methods with a wide range of geometric conditions and flow regimes. For example, a method based on the similarity between the processes of heat and mass transfer [1] allowed to determine the mass transfer coefficients by the photometric method. The coloring intensity of different



regions of the fin in the images presented was proportional to the local heat transfer coefficient. Since interpreting experimental data is complicated, and there are other difficulties in using the photometric method as a whole, it was not developed any further.

More popular methods involve using heat flux sensors (HFS). The measurements in [1] were performed on fully heated models of finned tubes. HFS were mounted on the fin and on the surface of the supporting cylinder, and their position relative to the direction of the incident flow was varied by rotating the tube around the axis. Studies of local heat transfer coefficients were carried out for single tubes [1, 15] and for tube banks [7, 9].

The findings of these and other studies are contradictory, with discrepancies in both quantitative and qualitative characteristics of the local heat transfer coefficient distribution. Some authors note (see, for example, Ref. [1]) that the distribution of the heat transfer coefficient over the fin surface is non-uniform, and the coefficient α is higher near the tip of the fin than at the base, where a thicker boundary layer is formed. It was also found that the maximum values of the objective function α fall on the azimuthal rotation angle $\varphi = 70 - 90^\circ$. Similar results were obtained in [5, 9].

However, other studies [6, 15] found local maxima of the heat transfer intensity at the base of the fin in similar regimes. In addition, the results obtained in [1] indicate that heat transfer intensity peaks exist in the region $\varphi = 100 - 130^\circ$, which the authors attribute to the separation of the boundary layer from the surface of the tube.

Despite the wide variety of cross-fin heat transfer surfaces used, there is currently no universal and accurate method for simulating these surfaces. This is because the distribution of the heat transfer coefficient over the surface of the fin is non-uniform [1, 2, 4, 8]. Analysis of the results presented in the literature led us to conclude that a combined study of heat transfer and flow around the fin by gradient heat flux measurement, PIV and thermal imaging diagnostics can yield substantially new and useful results and allow to refine the existing simulation methods and computational models.

The goal of this study was to explore the effect of the flow regime, the height of the fin and the flow incidence angle on the distribution and the averaged values of the heat transfer coefficient by a hyphenated method.

We present the results of experiments on heat transfer and air flow around a single circular fin, obtained for the first time by combined use of PIV and thermal imaging diagnostics, as well as by the unique method of gradient heat flux measurement.

Experimental procedure

The flow was visualized by the PIV method, the heat flux was measured by gradient heat flux measurement, and the temperature at the surface of the fin in the locations where the GHFS were mounted was measured by thermal imaging diagnostics. We have already tested the combination of gradient heat flux measurement and PIV diagnostics and used it in experiments; the results of these measurements were generalized in [12, 16, 17]. Complementing these methods with thermal imaging diagnostics should allow to extend this approach to studies of non-isothermal heat transfer surfaces.

Heat flux measurements. Gradient heat flow sensors (GHFS) have been developed and introduced into experimental studies at the Department of Thermophysics of Power Units of Peter the Great St. Petersburg Polytechnic University. Record-low time constants ranging from 10^{-8} to 10^{-9} s are a unique feature of these sensors [9], making them practically inertia-free devices for measurements in most heat transfer problems.

The operating principle of the GHFS is based on Seebeck's transverse effect: as a heat flux passes through a plate with anisotropic thermal and electrophysical properties, a thermo-emf normal to the heat flux vector and proportional to its magnitude evolves in the plate [9, 10].

Five GHFS made of a single crystal of bismuth were used in the study (Fig. 1). Three of them had the dimensions of 2×2 mm, the fourth 4×7 mm, and the fifth 5×5 mm. All GHFS were 0.2 mm thick. The volt-watt sensitivity of the GHFS, determined using absolute calibration by the Joule – Lenz heat flux, was about 10 mV/W. The signal generated

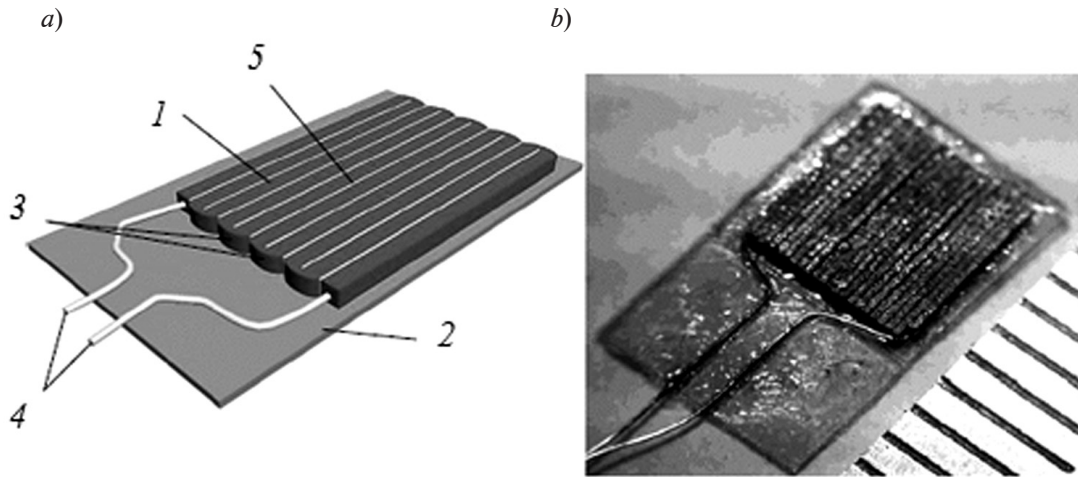


Fig. 1. Schematic model (a) and photograph (b) of the gradient heat flux sensor (GHFS): bismuth strips 1; mica substrate 2; bismuth solder joints 3; current outputs 4; lavsan spacers 5

by the sensors was recorded with a V7-78/1 digital voltmeter by AKIP (Russia).

PIV diagnostics. PIV technology in the POLIS system [11] allowed to visualize the airflow near the surface of the fin by a non-contact method. PIV (Fig. 2) involves seeding air flow I with tracer particles 2 – 3 μm in diameter, illuminated by double flashes of a laser sheet (obtained by reshaping laser beam 2 with a system of cylindrical lenses). Digital camera 3 captures images of the tracers during flashes. The camera is synchronized with the laser (the synchronization unit is not shown in the figure). The system allows to adjust the

supply of tracer particles and the frequency with which photographs are taken in accordance with the flow regime in order to minimize the effects due to inertia and buoyancy forces.

Next, the photographs were processed with the ActualFlow software, which calculates the velocity and vorticity fields. The software uses correlation methods of image processing to determine the motion of particles. The PIV method allows to detect the instantaneous velocity fields and calculate the time-averaged ones in the plane of the laser sheet. The classical (2D) configuration of the method was used in our experiments, and the number of

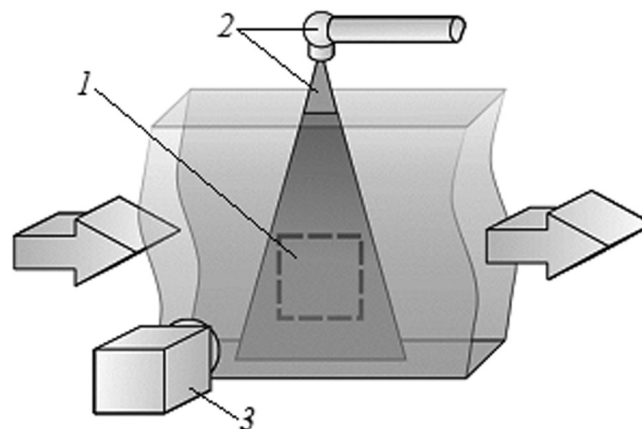


Fig. 2. General schematic of PIV measurements: detected flow with tracers 1; laser and laser sheet 2; digital camera 3; arrows indicate the direction of the flow

photographs was 1000 pairs.

It was found for PIV of the flow around heated models that the smoke generated by a standard device was not suitable [12]. Weighted oil tracers 1 – 5 μm in diameter had time to evaporate above the heated surface, making it impossible to visualize the flow in the wall layer. For this reason, we used solid particles of wood smoke from a fog machine as tracers.

To suppress glare from the laser, the fin and the supporting cylinder were treated with a mixture of industrial oil, alcohol and fluorescent rhodamine 6G which makes the reflected laser beam change the wavelength compared to the incident one. Reflected light was filtered by a narrow-band green filter mounted on the camera.

Thermal imaging. A FLIR P640 infrared thermal camera was used to measure the surface temperature of the fin. Bodies whose temperature is different from absolute zero emit thermal electromagnetic radiation. The spectral power density of this radiation has a maximum whose wavelength depends on the temperature. The position of the maximum in the emission spectrum shifts towards smaller wavelengths with increasing temperature. Bodies heated 40 – 100°C are characterized by a radiation maximum in the mid-infrared range. The camera software allowed to simultaneously measure the temperature at several points on the surface of the fins with practically no time delay and with an accuracy of 1 K. As an

example, Fig. 3 shows two thermal images.

Experimental setup

Experimental models. The initial model was a finned cylinder with a diameter of 66 mm and a length of 600 mm, made of a 0.1 mm thick steel sheet. Two circular fins with the diameter $D = 106$ mm were mounted on the cylinder. The first fin was hollow and simulated an ideal (isothermal) fin, and the second, made of a titanium alloy (thermal conductivity $\lambda = 9 \text{ W}/(\text{m}\cdot\text{K})$), simulated a non-isothermal fin.

The second model was constructed similarly, but the outer diameter of the fins was $D = 186$ mm. The GHFS were installed on the surface of the fins (Fig. 4). The GHFS were calibrated at the test bench described in [10], providing sufficient accuracy for measuring the heat flux per unit area vector [14], while the combined standard uncertainty did not exceed 1 %.

The model was heated from within by saturated steam at atmospheric pressure with a temperature close to 100°C. The cylinder was rotated around the axis so that the GHFS could be moved circumferentially. The temperature at the surface of the ideal fin was $T_w = \text{const}$ for all values of the rotation angle $0 \leq \varphi \leq 180^\circ$ (Fig. 4, *a*); it was additionally controlled by the thermal imager. The temperature T_w of fin 3 (made of a titanium alloy), which depends on the fin height H and the angular coordinate φ , was also measured by the thermal imager.

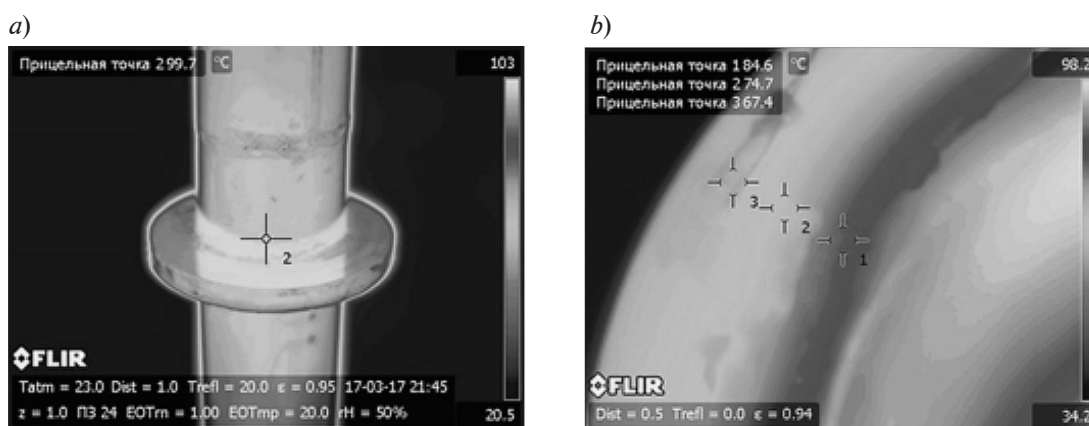


Fig. 3. Thermal images of the cylinder with an isothermal fin (*a*) and a fragment of a non-isothermal fin (*b*); the temperature points in the locations where the sensors were mounted are shown

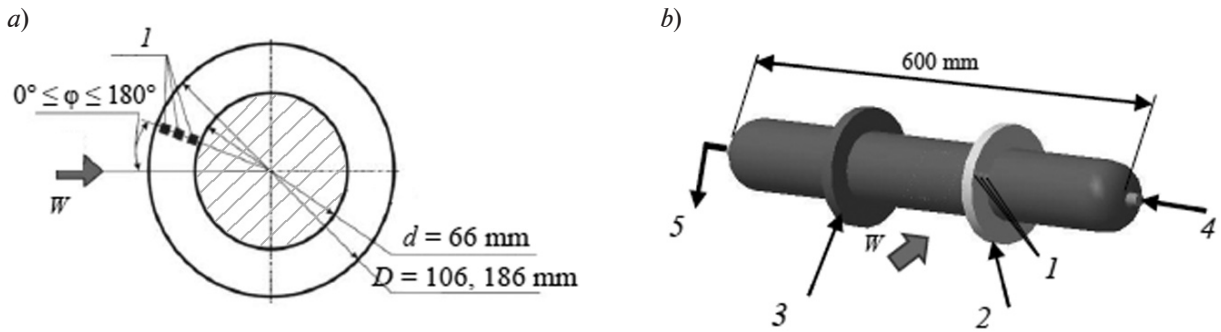


Fig. 4. Schematics of the experimental model of a finned cylinder: cross-sectional drawing *a*; overall appearance *b*; three GHFS *1*; isothermal and non-isothermal fins 2 and 3, respectively; steam inlet 4; condensate outlet 5. The height of the fins is $H = 20$ and 60 mm; W is the incident airflow vector

The model was mounted on a turntable allowing to change the angle β between the incident airflow vector W and the cylinder axis.

Wind tunnel. The experiments were carried out in the subsonic wind tunnel (Fig. 5) developed, built and tested at the Department of Thermophysics of Power Units of the Polytechnic University [9].

The open-type tunnel is equipped with an Eiffel camera made of acrylic glass, which made it possible to use the PIV. The air flow from the centrifugal blower enters the return passage through the cooler. The turning vanes direct the air into a settling chamber with a honeycomb. The contraction cone has a 1 to 7 contraction ratio; the air is fed into the

Eiffel chamber through a circular outlet with a diameter of 450 mm and then to the blower inlet.

The tunnel has two specific features:

a thyristor drive and a reversed fan allow to conduct experiments at velocities that do not exceed 0.1 – 0.2 m/s;

a cooler connected to the cold-water supply system maintains an almost constant air flow temperature in the tunnel (the spread in the values is $\pm 0.1 \text{ K}$).

The cooler increases the resistance of the wind tunnel by 500 Pa, decreasing the velocity in the operating area as a result; for this reason, the cooler is a plate that can be removed and replaced with a guide vane for short-term experiments.

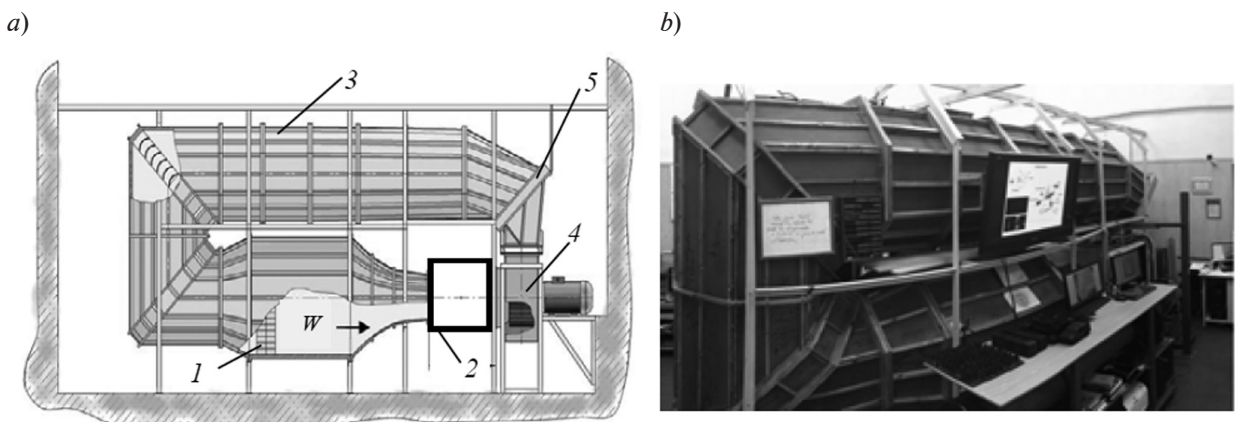


Fig. 5. Schematic layout (*a*) and appearance (*b*) of the wind tunnel used in the experiments: settling chamber *1*, Eiffel chamber *2*, return passage *3*, blower *4*, heat exchanger *5*; incident airflow vector W

Turning vanes, a honeycomb and a contracting cone were installed in bends to reduce turbulence of the airflow in the tunnel. The degree of turbulence did not exceed 1 % over the entire velocity range [9].

Experimental results and discussion

Aerodynamic studies were carried out for Reynolds numbers $Re = (0.4 - 4.1) \cdot 10^4$. This number is expressed as follows:

$$Re = \frac{W \cdot d}{\nu},$$

where W , m/s, is the flow velocity; d , m, is the diameter of the supporting cylinder; ν , m^2/s is the kinematic viscosity.

We also found the local heat flux per unit area q_φ (W/m^2) at different points along the height of the fins with the angular coordinate φ , the local heat transfer coefficient α_φ ($W/(m^2 \cdot K)$) and the local Nusselt number Nu_φ . These characteristics are determined by the following formulae:

$$q_\varphi = \frac{E}{S_0 \cdot F},$$

where E , mV, is the GHFS signal; S_0 , mV/W, is the volt/watt sensitivity of the sensor; F , m^2 , is the plan area of the GHFS;

$$\alpha_\varphi = \frac{q_\varphi}{T_f - T_w},$$

where T_f and T_w , $^\circ C$, are the temperatures of the air flow and the fin surface, respectively;

$$Nu_\varphi = \frac{\alpha_\varphi d}{\lambda_f},$$

where d , m, is the diameter of the supporting cylinder; λ_f , $W/(m \cdot K)$, is the thermal conductivity of air;

$$Nu = \frac{\alpha d}{\lambda_f},$$

where α is the value of α_φ , averaged over the fin height.

Fig. 6 shows the dependences of the local heat transfer coefficient α_φ on the fins of height $H = 20$ mm (isothermal and non-isothermal) at different angles φ and for different regimes. Apparently, the quantity α_φ

changes significantly less along the height of an isothermal fin than the same quantity for fin made of a titanium alloy. The value of α_φ near the root turns out to be less for a solid fin than for a hollow one for all values of the angle φ .

Fig. 6 also shows the dependences of the local heat transfer coefficient for a fin with the height of 60 mm. The α_φ distributions for ideal and non-ideal fins differ significantly more than for fins with the height of 20 mm.

The distribution of the heat transfer coefficient turns out to be more filled for an ideal fin than for non-ideal one, but heat transfer is much lower at the tips of the fins than in the remaining part. This is because the fin has a sufficiently wide ($\delta = 10$ mm) sharp edge. A stagnation region forms near the fin, as evidenced by the flow patterns presented below.

Interestingly, there is an extremum on the dependence of the heat transfer coefficient α versus the coordinate h , corresponding to the location where the sensor was mounted; the extremum is observed at $h = 20$ mm for both ideal and non-ideal fins; further study is required to explain this. It is also noteworthy that the heat transfer coefficient is extremely low near the root of the fin made of a titanium alloy: $\alpha = 1 - 4$ $W/(m^2 \cdot K)$ in the region $\varphi = 120 - 180^\circ$ with the free flow rate $W = 0.9$ m/s. This can be attributed to the difference in the temperatures on the surface of the supporting cylinder heated by steam ($100^\circ C$), and at the root of the fin ($85 - 92^\circ C$); the latter temperature is lower by $8 - 15^\circ C$ due to substantial contact thermal resistance.

Fig. 7 shows the averaged velocity fields of the airflow over fins of different heights. The vectors show the direction of the flow in the cross-section of the light sheet.

The flow patterns obtained for a fin with the height $H = 20$ mm are in good agreement with the results of the studies in [1]. Averaged flow patterns alone are insufficient for explaining the distribution of the local heat transfer coefficient along the height of the fin. An experiment simultaneously recording flow patterns, heat flux and temperature values has to be carried out to explain the differences in the behavior of the quantity α for ideal and non-ideal fins. The method of combining calorimetry and PIV diagnostics was developed and applied in [5].

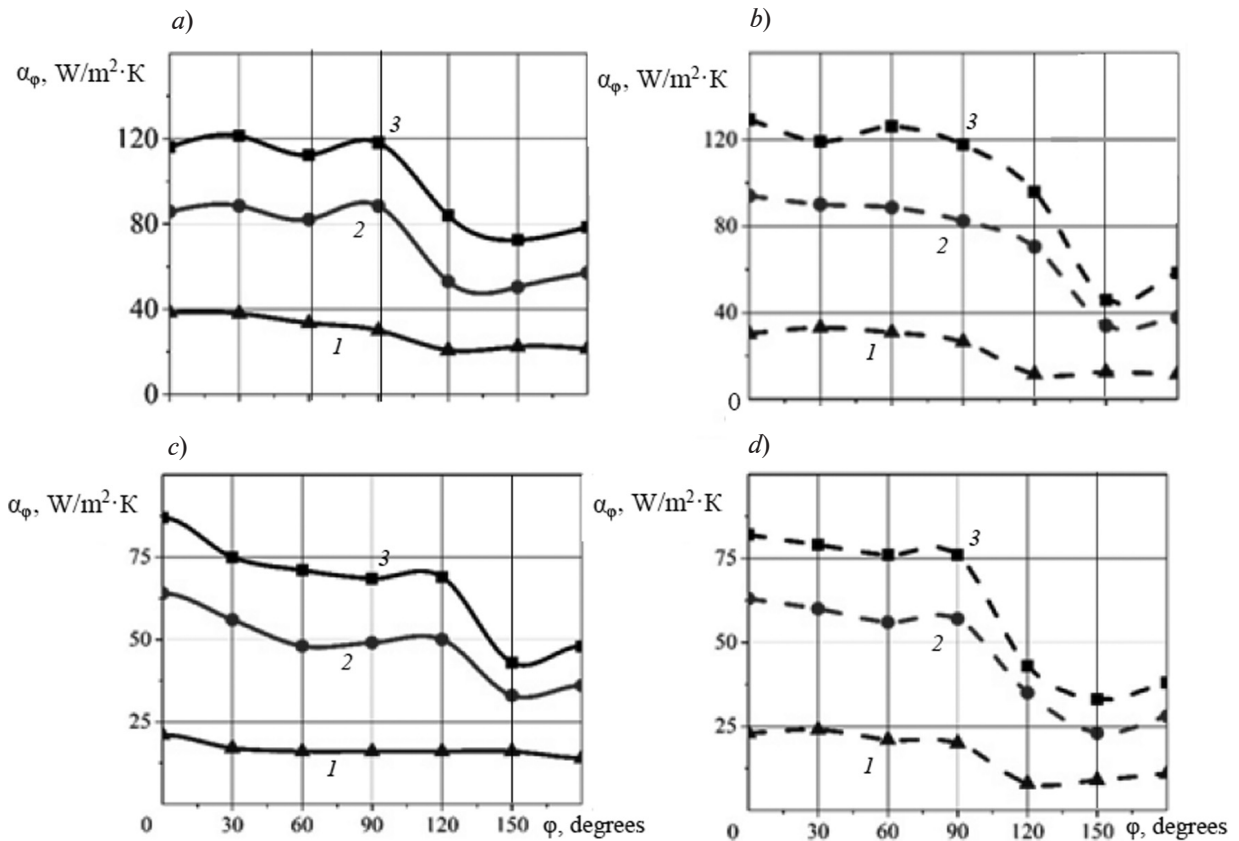


Fig. 6. Dependences of the local heat transfer coefficient for isothermal (a, c) and non-isothermal (b, d) fins with the heights of 20 mm (a, b) and 60 mm (c, d) versus the cylinder rotation angle ϕ for different Reynolds numbers Re , 10^4 : 0.9 (1), 2.2 (2), 4.1 (3)

Visualization of the flow near the fin with the height of 60 mm in Fig. 7, b, d illustrates the stagnation zone at the tip of the fin and the vortex at its mid-length. We can conclude that the shape of the skin layer follows the general structure of the flow in these cases, which corresponds to the results in [1]. Our PIV studies for a 60 mm high fin revealed the presence of a vortex, shown in Fig. 8. Maximum heat dissipation is achieved at the coordinate $h = 20$ mm; it is due to a return vortex formed as the flow is separated [3, 17].

At the next stage of the study, we examined the effect of the yaw angle β between the air flow velocity vector W and the cylinder axis on the characteristics of the air flow around a finned cylinder. We considered a fin with the height of 20 mm at a yaw angle $\beta = 5 - 15^\circ$, in the same Reynolds number range [15].

The flow at an angle to the horizontal plane

XZ in the Cartesian coordinate system is asymmetric. The cylinder was tilted at a negative yaw angle: $\beta = (5 - 15)^\circ$ (Fig. 8). The heat transfer coefficients were thus measured on both sides of the fin, making it possible to average them over the whole heat transfer surface.

Fig. 8 shows that the contribution of the mean heat transfer coefficient is larger on the trailing edge (II) than on the leading edge (I), and increases with increasing yaw angle. The opposite picture is observed with increasing flow rate: the largest contribution to the mean heat transfer coefficient is made by the leading edge of the fin (I). We have also obtained the distribution of the local heat transfer coefficient along the height of the isothermal and non-isothermal fins.

Analysis of the velocity fields obtained by PIV diagnostics proves that the stagnation region and the region with separated vortices

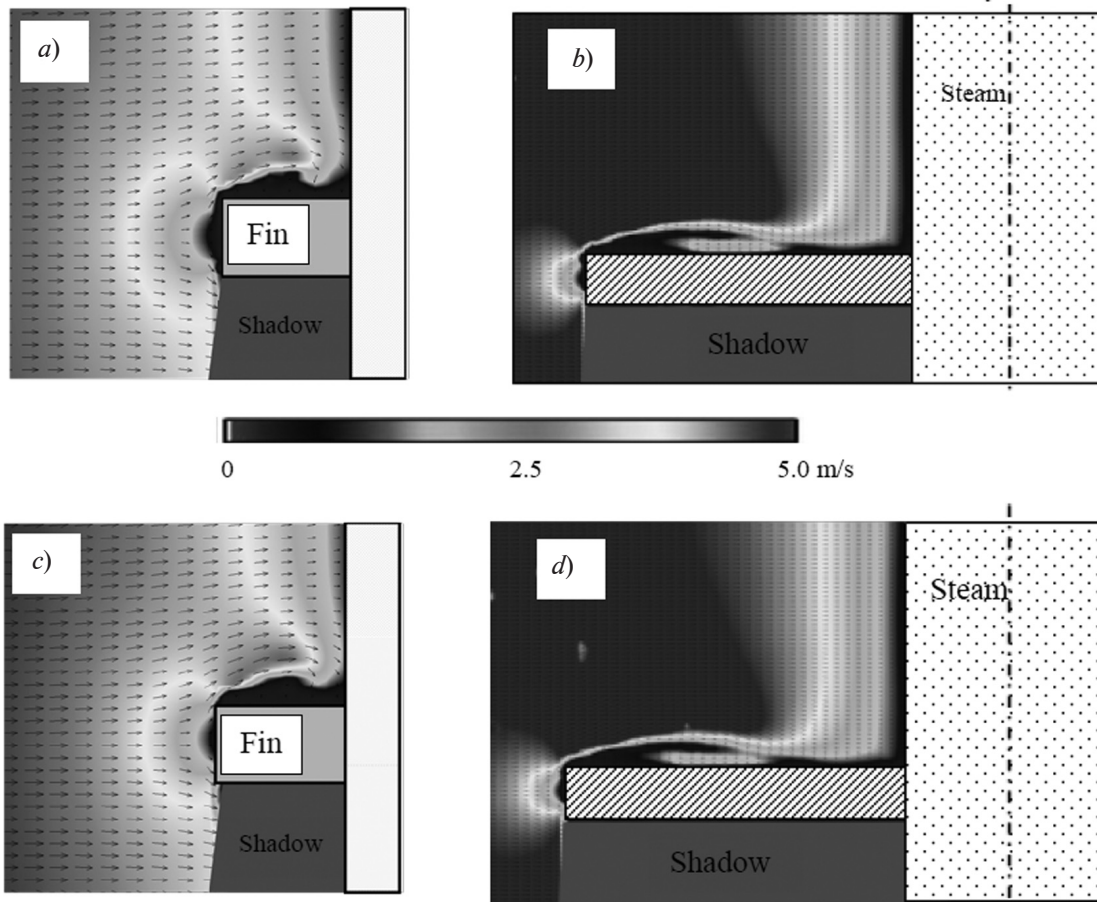


Fig. 7. Velocity fields near fins with the heights $H = 20$ mm (*a, c*) and 60 mm (*b, d*) for Reynolds numbers $Re = 2.2 \cdot 10^4$ (*a, b*) and $4.1 \cdot 10^4$ (*c, d*)

shift (see Fig. 9) from the leading to the trailing edge and vice versa with the changing angle β , and in sum give approximately the same mean heat transfer coefficient.

Fig. 9, *b, c* also shows the heat transfer coefficient distributions along the height of the non-isothermal fin in the measurement range of the GHFS (5, 10 and 15 mm from the root of the fin) for an angle $\beta = 5^\circ$ and the Reynolds number $Re = 2.1 \cdot 10^4$. The distributions are shown separately for the leading (*b*) and trailing (*c*) edges of the fin, since it is asymmetric for $\beta \neq 0$.

Conclusion

We have constructed two special models for the purpose of carrying out a comprehensive study of the aerodynamic and thermal characteristics of a finned metal cylinder with

internal heating and air flow around it. As a result of the measurements, we have obtained flow velocity fields near the isothermal and the non-isothermal fins, the temperature field on the cylinder surface, and the heat flux densities. Analysis of these data revealed important information on the aerodynamic and thermal properties of flows near the surface of the fin. The main findings of the study are as follows:

- we have revealed the effect of the fin height on the flow structure and the distribution of the heat transfer coefficient;

- we have established that with a varying yaw angle, the mean heat transfer coefficient practically did not change throughout the given range of Reynolds numbers on the surface of an isothermal fin, while on the surface of a non-isothermal fin it increased up to 6.5 %;

- for the Reynolds number $Re = 4000$, the

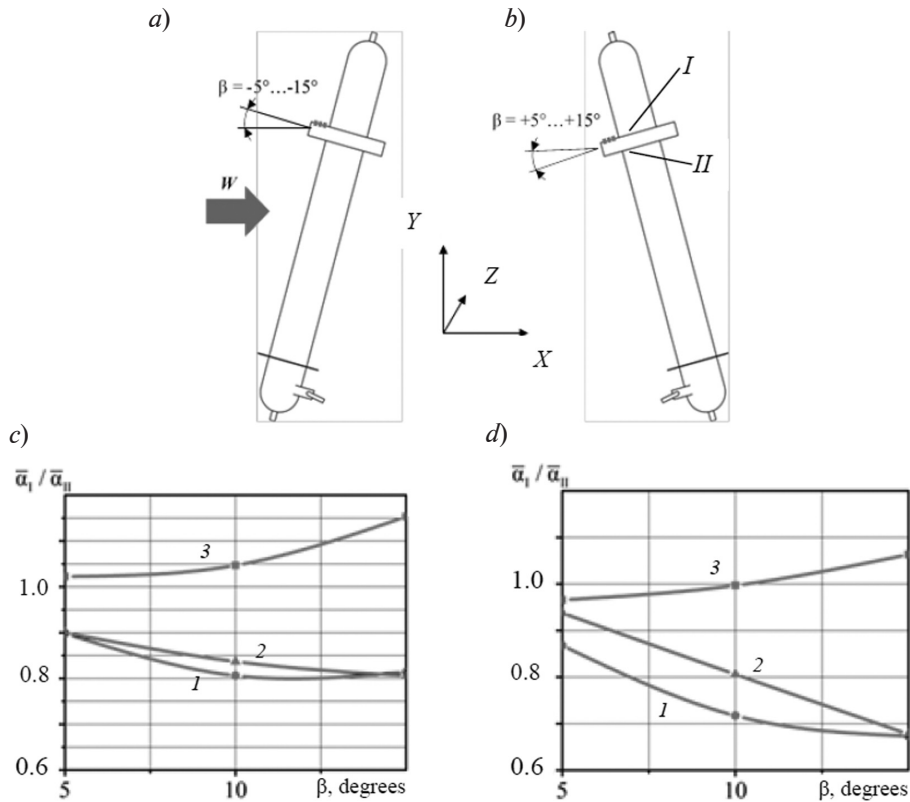


Fig. 8. Schematic of the cylinder model with the fin in two positions (a, b) and the dependences of the dimensionless heat transfer coefficient on the angle β for the isothermal (c) and the non-isothermal (d) fin, and for different values of the Reynolds number Re , 10^4 : 0.9 (1), 2.2 (2), 4.1 (3)

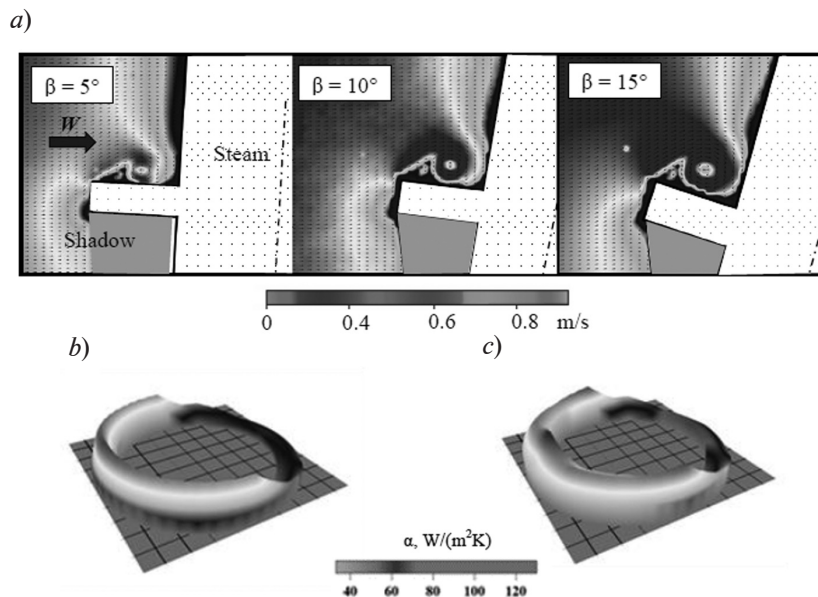


Fig. 9. Velocity fields near the isothermal fin for $Re = 0.4 \cdot 10^4$ at different yaw angles β (a), and the distribution of the heat transfer coefficient α at the leading (b) and trailing (c) edges of the non-isothermal fin at $\beta = 5^\circ$ and $Re = 2.1 \cdot 10^4$



mean heat transfer coefficient is higher at the leading edge of the fin than at the trailing edge and increases with increasing yaw angle (if $\beta > 0$). As the incident flow velocity increases, the highest mean heat transfer coefficient is reached at the trailing edge of the fin;

the heat transfer coefficient decreases sharply for all regimes in the range of cylinder rotation angles $\varphi = 120 - 240^\circ$.

We have confirmed for the first time that it is possible to combine gradient heat flux mea-

surement, PIV and thermal imaging diagnostics for measuring the heat transfer coefficient on a non-isothermal surface. This approach allows to examine the flow and heat transfer on the surface of a fin in real time and opens up new opportunities for aerodynamic and thermal studies. For example, in the future we should consider a similar model containing segmented fins, in particular, those opened at an angle $\varphi = 120 - 240^\circ$ along the path of the major arc.

REFERENCES

- [1] **E.N. Pismenny**, Teploobmen i aerodinamika paketov poperechno-orebrennykh trub [Heat exchange and aerodynamics of packages of cross-finned tubes], Alterpres, Kiev, 2004.
- [2] **H. Hamakawa, H. Matsuoka, K. Hosokai, et al.**, Characteristics of aerodynamics sound radiated from two finned cylinders, In: Proc. of the ASME 2014, Pressure Vessels and Piping Conference, Anaheim, California, USA, ASME. (4) (2014) V004T04A073.
- [3] **M. Bansal**, Experimental and numerical investigation of three equispaced cylinders in cross-flow, Master's thesis, University of Waterloo, Waterloo, Ontario, Canada, 2014.
- [4] **G.A. Dreytser**, O nekotorykh problemakh sozdaniya vysokoeffektivnykh trubchatykh teploobmennyykh apparatov [On some problems of creating high-efficiency tubular heat exchangers], Novosti teplosnabzheniya. (5(45)) (2004) 37–43.
- [5] **V.M. Legkii, Ya.S. Zholudov, O.A. Gerashchenko**, Local heat exchange of a single transversely round tube with external circular fins, Journal of Engineering Physics and Thermophysics. 30 (2) (1976) 178–182.
- [6] **A.A. Zhukauskas, R.V. Ulinskas, F.V. Zinyavichyus**, Mestnyye kharakteristiki teplootdachi i obtekaniya shakhmatnykh puchkov rebristykh trub [Local characteristics of heat transfer and flow around the staggered banks of finned tubes], Trudy AN Lit. SSR, Ser. B. 2 (141) (1984) 46–53.
- [7] **Jeff.E.J. McClure**, On the planar flow development and structural loading of cylinders with circular fins in cross-flow, University of Waterloo, Waterloo, Ontario, Canada, 2015.
- [8] **R.L. Webb, Nae-Hyun Kim**, Principles of enhanced heat transfer, Taylor&Francis Group, New York, 2005.
- [9] **S.Z. Sapozhnikov, V.Yu. Mityakov, A.V. Mityakov**, Gradiyentnyye datchiki teplovogo potoka [Gradient heat flux sensors], Izd-vo SPbSPU, St. Petersburg, 2003.
- [10] **O. Heinz, B. Ilyushin, D. Markovich**, Application of a PDF method for the statistical processing of experimental data, International Journal of Heat and Fluid Flow. 25 (5) (2004) 864–874.
- [11] **A.A. Gusakov, A.S. Kosolapov, D.M. Markovich, et al.**, Simultaneous PIV and gradient heat flux measurement of a circular cylinder in cross-flow, Appl. Mech. Mater. 629 (2014) 444–449.
- [12] **A.I. Pokhodun**, Eksperimentalnyye metody issledovaniy. Pogreshnosti i neopredelennosti izmereniy [Experimental methods of research. Errors and uncertainties in measurements], SPbGU ITM, St. Petersburg, 2006.
- [13] **E.M. Sparrow, J.M. Gorman, K.S. Friend, J.P. Abraham**, Flow regime determination for finned heat exchanger surfaces with dimples/protrusions, Numerical Heat Transfer, Part A: Applications. 63(4) (2013). 245–256.
- [14] **F. Samie, E.M. Sparrow**, Heat transfer from a yawed finned tube, Journal of Heat Transfer. 108 (2) (1986) 479–482.
- [15] **D. Sumner**, Flow above the free end of a surface-mounted finite-height circular cylinder, A review, Journal of Fluids and Structures. 43 (2013) 41–63.
- [16] **A. Mityakov, A. Babich, A. Bashkatov, et al.**, Investigating heat transfer augmentation using gradient heat flux measurement and PIV method, MATEC Web of Conferences, 2017, 3rd Siberian Thermophysical Seminar, STS 2017, 115 (10 July) (2017), No. 02006, 1–4.
- [17] **A. Mityakov, V. Mityakov, S. Sapozhnikov, et al.**, Hydrodynamics and heat transfer of yawed circular cylinder, Int. J. Heat Mass Transf. 115A (December) (2017) 333–339.

Received 27.02.2018, accepted 03.05.2018.

THE AUTHORS

GUSAKOV Andrey A.

Peter the Great St. Petersburg Polytechnic University
29 Politechnicheskaya St., St. Petersburg, 195251, Russian Federation
a.gusakov.spb@mail.ru

GREKOV Mikhail A.

Peter the Great St. Petersburg Polytechnic University
29 Politechnicheskaya St., St. Petersburg, 195251, Russian Federation
grekov66@yandex.ru

SEROSHTANOV Vladimir V.

Peter the Great St. Petersburg Polytechnic University
29 Politechnicheskaya St., St. Petersburg, 195251, Russian Federation
vladvik1992@gmail.com